70

Characterization of Air-Sea Gas Exchange Processes and Dissolved Gas / Ice Interactions Using Noble Gases

By

Eda Maria Hood

B.S., magna cum laude, Marine Sciences
Texas A&M University at Galveston
(1991)

SUBMITTED IN PARTIAL FULFILLMENT OF THE REQUIREMENTS FOR THE DEGREE OF

DOCTOR OF PHILOSOPHY

at the

MASSACHUSETTS INSTITUTE OF TECHNOLOGY

and the

WOODS HOLE OCEANOGRAPHIC INSTITUTION

September 1997

Signature of Author _____

Joint Program in Marine Chemistry and Geochemistry
Massachusetts Institute of Technology /
Woods Hole Oceanographic Institution

Certified by _____

Dr. William J. Jenkins
Thesis Supervisor

Accepted by _____

Dr. Edward A. Boyle
Chairman, Joint Committee for Marine Chemistry and Geochemistry
Massachusetts Institute of Technology /
Woods Hole Oceanographic Institution

Characterization of Air-Sea Gas Exchange Processes and Dissolved Gas / Ice Interactions Using Noble Gases

by

Eda Maria Hood

Submitted to the Massachusetts Institute of Technology -
Woods Hole Oceanographic Institution
Joint Program in Oceanography
on September 30, 1997, in partial fulfillment of the
requirements for the degree of
Doctor of Philosophy

Abstract

In order to constrain the processes controlling the cycles of biogeochemically important gases such as O_2 and CO_2, and thereby infer rates of biological activity in the upper ocean or the uptake of radiatively important "greenhouse" gases, the noble gases are used to characterize and quantify the physical processes affecting the dissolved gases in aquatic environments. The processes of vertical mixing, gas exchange, air injection, and radiative heating are investigated using a 2 year time-series of the noble gases, temperature, and meteorological data from Station S near Bermuda, coupled with a 1-dimensional upper ocean mixing model to simulate the physical processes in the upper ocean. The rate of vertical mixing that best simulates the thermal cycle is $1.1\pm0.1 \times 10^{-4}$ m s^{-1}. The gas exchange rate required to simulate the data is consistent with the formulation of Wanninkhof (1992) to $\pm$ 40%, while the formulation of Liss and Merlivat (1986) must be increased by a factor of $1.7\pm$ 0.6. The air injection rate is consistent with the formulation of Monahan and Torgersen (1991) using an air entrainment velocity of 3 ± 1 cm s^{-1}. Gas flux from bubbles is dominated on yearly time-scales by larger bubbles that do not dissolve completely, while the bubble flux is dominated by complete dissolution of bubbles in the winter at Bermuda. In order to obtain a high-frequency time-series of the noble gases to better parameterize the gas flux from bubbles, a moorable, sequential noble gas sampler was developed. Preliminary results indicate that the sampler is capable of obtaining the necessary data. Dissolved gas concentrations can be significantly modified by ice formation and melting, and due to the solubility of He and Ne in ice, the noble gases are shown to be unique tracers of these interactions. A three-phase equilibrium partitioning model was constructed to quantify these interactions in perennially ice-covered Lake Fryxell, and this work was extended to oceanic environments. Preliminary surveys indicate that the noble gases may provide useful and unique information about interactions between water and ice.

Thesis Supervisor: William J. Jenkins
Title: Senior Scientist, Woods Hole Oceanographic Institution

Acknowledgements

I am sincerely grateful to many people who have made this work possible and enjoyable. I am especially thankful to have had the opportunity to work closely with Bill Jenkins, who has been a source of inspiration, encouragement, and guidance. I am eternally indebted to Dempsey Lott for his mentorship, dedication, patience, and friendship over the last 6 years. None of the work presented in this thesis would have been possible without his contributions. The staff of the Helium Isotope Lab (Scot Birdwhistell, Josh Curtice, Marcia Davis, Peter Landry, Mike Mathewson, and Sheila Clifford) have all contributed to my work and well-being, and have made my time here very entertaining. I am also thankful for the skillful work and dedication of Rich Zuck and Charlie Clemshaw. My committee, Ed Boyle, Nelson Frew, Jim Ledwell, and Bruce Johnson, provided many useful insights, comments, and direction for this work. I am particularly thankful to Dave Glover and Scott Doney, who have helped to guide me through the mysterious world of upper ocean modeling. I am grateful to a number of people who have provided samples and insights for several of the projects presented in this thesis; Brian Howes, Dale Goehringer, Kunio Shirasawa, Tom Trull, and Lisette Robertson. Most of all, I am indebted to my family and friends, who have given me the strength and encouragement to continue.

This work has been supported by the National Science Foundation - OCE 9302812 and DPP 9118363, the Ocean Ventures Fund (Ditty Bag Fund and Wescott Fund) and the WHOI Education Office.

Contents

List of Figures

List of Tables

Preface

Air-Sea Gas Exchange - In the early years of the debate on the role of anthropogenic CO_2 in global warming, it was believed that the ocean represented a vast sink for CO_2 and would remove approximately 95% of all the CO_2 pumped into the atmosphere. However, later work by Suess, Revelle, Keeling, and others showed that the removal of atmospheric CO_2 by the oceans was much slower than originally expected, and that there was indeed a measurable increase in the level of atmospheric CO_2 (Weart, 1997). It became clear that we had only a tentative grasp on the mechanisms of the exchange of gases between the atmosphere and the ocean. Today, measurements of atmospheric CO_2 show that about 60% of the anthropogenic CO_2 released resides in the atmosphere, with the remainder being taken up by the ocean and terrestrial biosphere. However, the relative sizes of these sinks and the rate of gas exchange between the reservoirs is a matter of debate and the focus of much research (e.g. Tans et al., 1990; Sarmiento and Sundquist, 1992; Siegenthaler and Sarmiento, 1993; Keeling et al., 1996).

Part of the difficulty in assessing the exchange of gases between the atmosphere and the upper ocean results from the fact that the concentrations of dissolved gases in the surface ocean change spatially and temporally, responding to a range of complex biological, chemical, and physical processes. The direct measurement of the air-sea fluxes of these gases is technically possible only over relatively small space and time-scales. We are thus faced with the task of establishing relationships between the fluxes of the gases and observable parameters that can be measured over large space and time-scales, which will then provide the predictive capability to determine global gas fluxes under all oceanic conditions.

The relations between hydrodynamics, meteorological forcing, and gas fluxes are typically investigated using a suite of gases with different physicochemical properties as tracers of the exchange process. Estimates of gas exchange rates have been made using a combination of wind tunnel and wave tank experiments, field observations, and heuristic modeling. Although progress in our understanding of the mechanisms of air-sea gas exchange has been made using these techniques, we still do not have a sufficiently firm understanding of the processes over the spectrum of oceanic conditions to make large-scale flux calculations with much certainty. Observational data from several studies (Wallace and Wirick, 1992; Farmer, et al., 1993) have shown that there is a considerable enhancement in the transfer of gases during bubble injection from breaking waves, and that typical parameterizations of gas exchange during high wind/wave conditions

considerably underestimate the true flux. While these intense forcing episodes may occur sporadically, data collected from major field programs such as GEOSECS and WOCE suggest that these events leave a lasting imprint on the concentrations of the dissolved gases in the surface ocean, and that gases exist in a dynamic, rather than static, equilibrium with the atmosphere. Air injection has been shown to be an important control in the concentrations of dissolved gases in the upper ocean, and parameterization of these processes is necessary for modeling not only the short-term concentrations, but also the seasonal cycles of gases (Musgrave et al., 1988; Schudlich and Emerson, 1996). Clearly, gas exchange processes in high energy conditions constitute an important link in the steady-state, dynamic balance between the atmosphere and the upper ocean.

Ultimately, our understanding of air-sea gas exchange is limited by the lack of observational data over the spectrum of oceanic conditions. The intensity and combination of high energy conditions that force the exchange process in the open ocean cannot be adequately simulated in laboratories, and in situ sampling under these conditions is difficult. One approach for studying these processes is the observation of a time-series of gases as they respond to physical forcing (Spitzer and Jenkins, 1989; Wallace and Wirick, 1992; Farmer et al., 1993; Schudlich and Emerson, 1996). While observations of these processes at one location in the ocean cannot provide a full range of oceanic conditions, this approach provides a means of utilizing a wide variety of "natural laboratories" in the ocean, and elucidates the responses of gases to physical forcing over seasonal and yearly time-scales. More detailed information about the mechanisms of the

high energy exchange process requires sampling of an appropriate frequency to observe the immediate response of the gases to the conditions. Additionally, appropriate gases must be used as tracers to avoid ambiguity of competing biological, chemical, and physical processes.

The noble gases (He, Ne, and Ar) represent powerful probes of air-sea gas exchange processes. They are biogeochemically inert, making them excellent tracers of the physical processes controlling the dissolved gases. The noble gases have a broad range of solubilities, solubility temperature dependencies, and molecular diffusivities (see Figure 1.1), and therefore respond to gas exchange and air injection processes to varying degrees, creating characteristic "finger-prints" of these mechanisms. High-frequency time-series observations of noble gases in the upper ocean as they respond to changes in physical forcing could provide much-needed information about air-sea gas exchange processes over the broad range of physicochemical parameters of the gases and sea-surface conditions.

Interactions between dissolved gas concentrations and ice formation - The processes of ice formation and melting constitute another mechanism of exchange of gases between the atmosphere and the oceans. During ice formation, salt and gases are largely rejected from the ice matrix, increasing the concentrations of salt and gas in the residual water. Gas saturations build to a point where the total dissolved gas pressure exceeds the local hydrostatic pressure, either at the ice water interface or in brine pockets within the ice,

and bubbles nucleate. The gases partition between the various phases of the ice, the bubbles in the ice, and the residual water depending on the solubility of the gas in each phase. The gases in this residual, dense water are transported into the interior and deep ocean as the water sinks to a level of neutral buoyancy, and the gas ratios created by the process of ice formation leave a unique fingerprint on the resulting water mass. In questions of how much of an atmospheric gas the ocean can remove from the atmosphere, the limiting rate factor is not gas exchange across the air-sea interface, but rather the transport of gases from the surface to deep oceans.

During melting, a low salinity surface layer is created, which acts as an impedance to gas exchange. In addition, this melt layer is, for most gases, undersaturated with respect to atmospheric equilibrium, and is thus capable of absorbing more gas from the atmosphere. Like the residual water from ice formation, this melt-water has unique concentrations of the dissolved gases, although the signal may be quickly lost to the atmosphere during equilibration.

Together, freezing and melting constitute a type of dissolved gas pump that serves to transport gases from the surface to deep ocean. It has been suggested that ice formation can have a profound effect on dissolved gas concentrations, either through direct interaction of the gases with the ice, or through formation of dense water. However, our understanding of the effects of the cryosphere on the exchange of dissolved gases in the aquatic environment is limited by the lack of adequate tracers.

Recent work (Top et al., 1988; Schlosser et al., 1990; Moore and Spitzer, 1990; Hood et al., 1997) suggests that the noble gases could be excellent tracers of ice-gas-water interactions. In addition to the physico-chemical properties that make them such useful tracers of gas exchange processes, He and Ne are soluble in the ice, whereas Ar is rejected from the ice lattice as water freezes. This property creates a unique fingerprint of the noble gases in the residual water that may provide useful insights into these processes.

This work encompasses projects that address both the exchange of gases across the air-sea interface and the influence of the cryosphere on air-sea gas exchange processes. The work is presented in two separate parts:

Part 1. Air-Sea Gas Exchange

- *The Effects of Gas Exchange and Air Injection Processes on Seasonal Dissolved Gas Cycles* - Dissolved gas concentrations in the surface ocean are the result of the complex interplay between biological, chemical, and physical processes. I have modified an upper ocean, one-dimensional vertical mixing model with recent formulations of gas exchange and air injection processes to simulate the seasonal cycles of the dissolved gases. I use observations from a two year, approximately monthly data set of He, Ne, and Ar from Station S near Bermuda, along with synoptic wind speed data from NCEP, to constrain the model and test the current formulations of gas exchange and air injection processes. In addition, the gas exchange

formulations of Wanninkhof (1992) and Liss and Merlivat (1986) are tested and compared. Using the simulations and data, I quantitatively estimate the processes of vertical mixing, gas exchange, air injection, and the mode of bubble trapping occurring over this time period at Station S.

- *Noble Gas Sampler* - Studies of air-sea gas exchange are currently limited by the lack of observational data over the spectrum of oceanic conditions, but sampling and measurement of dissolved gases under high wind/ wave conditions is problematic. Additionally, observations of the gases as they respond to physical forcing requires high frequency (every 12-24 hours) sampling over time-scales of days to weeks for a single event of interest. While information of this frequency and over this spectrum of conditions is often obtainable from moored instrumentation, samples of dissolved gases of this type are problematic. Samples of the noble gases, which are very useful tracers of air-sea gas exchange processes, are particularly difficult to obtain because of the need to store the very diffusive gases He and Ne over long time-periods. We have designed and developed a moorable, sequential noble gas sampler that is capable of obtaining a time-series of the noble gases in the upper ocean over a period of days to months. I discuss here the design, operation, and testing of the noble gas sampler, and illustrate its capabilities for studies of air-sea gas exchange studies.

Part 2. Ice-Water Interactions

- *Lake Fryxell, Antarctica* - It has long been recognized that ice formation and melting can significantly influence dissolved gas concentrations, but quantitative treatments of

these processes do not exist. Lake Fryxell, a permanently ice-covered Antarctic lake, offers a natural laboratory for studies of ice influences on dissolved gas concentrations in natural systems. I have measured the dissolved noble gases (^{3}He, ^{4}He, Ne, and Ar), and have constructed a 3-phase partitioning model of the gases between the ice, air bubbles in the ice, and the surrounding water that predicts observations of the saturations at the ice-water interface. In addition, by reconstructing the tritium input history for the surface waters of the lake, I characterized the mechanisms and rates of ventilation for the bottom of the lake. The noble gases in the bottom waters can be used to constrain the past hydrographic balance of the lake, and provide further evidence of a near-desiccation event that occurred approximately 2000 ybp.

- *Saroma-Ko Lagoon*- This seasonally ice-covered salt water lagoon off the coast of Hokkaido, Japan offers a natural extension to the investigations of ice-formation effects on the concentrations of dissolved gases. Seawater ice is considerably different than ice formed from fresh water, and the structure and composition of the ice can significantly influence the concentrations of the gases in the surrounding water. In addition, this system is more open to mixing than the lake environment, but still quiescent enough to provide an environment where strong signals are likely. The concentrations and saturations of the noble gases show pronounced anomalies that are related to ice melting. Using estimates of the temperature, salinity, and density of the ice, I constructed a model of the ice composition (i.e. relative volumes of ice, bubbles,

and brine) and estimated the concentrations of the gases in each phase of the ice. The model predictions of N_2, Ar, and O_2 in the bubbles were in excellent agreement with measured concentrations in sea ice from the area, and suggest that an adequate representation of the gas composition in the various phases of ice may be constructed from basic information about the system. Using this model, I estimated the concentrations of the noble gases that would exist in undiluted melt-water from this ice, and then estimated the melt-water addition to the lagoon based on the measured concentrations and saturations. This work provides further evidence that the noble gases have potential as tracers of ice-water interactions in oceanic systems.

- *Prydz Bay, Antarctica* - I have measured the concentrations of He, Ne, and Ar from a 3-station, meridional transect across Prydz Bay in Antarctica. The saturations of the noble gases show large deviations from solubility equilibrium, with large supersaturations of He and Ne, and undersaturations of Ar. Further, the individual water masses of the bay can be distinguished by unique noble gas ratios. While there is not sufficient data to quantitatively estimate the effects of water-ice interactions on the concentrations of the noble gases, it can be qualitatively demonstrated that interactions with the ice are largely responsible for the anomalous saturations of the dissolved noble gases. This work provides further support that the noble gases, due to their unique interactions with ice, could potentially provide useful information about the interactions between ice and water.

CHAPTER 1

Air-Sea Gas Exchange Introduction

1.1 *Introduction*

One of the main goals of air-sea gas exchange studies is to be able to parameterize the transfer velocity as a function of the physical properties of the gas and one or several of the typically-measured hydrodynamic or meteorological parameters over the entire spectrum of oceanic conditions. This has been accomplished with moderate success for gas exchange across the air-sea interface at low to moderate wind speeds (Section 1.2), but in conditions of wave breaking, current parameterizations fail to adequately represent the flux (Section 1.3). Our understanding of air-sea gas exchange processes is severely limited by the lack of observational data in these conditions. While much may be learned from laboratory wave tank simulations, there is a limit to their utility in high energy conditions. The observational data that do exist are often ambiguous, or do not provide

sufficient information to determine the flux as a function of the physico-chemical properties of the gases (Section 1.4). This information can be obtained by utilizing a high-frequency (1-2 measurements per day) time-series of measurements of a suite of gases with a wide range of solubilities, solubility temperature dependencies, and diffusivities, such as the noble gases (Section 1.5). Chapter 3 describes the results of a one-dimensional, upper ocean vertical mixing model used to simulate the seasonal cycles of dissolved gases to investigate the longer-term (weekly to seasonal) effects of air-sea gas exchange processes on the cycles of gases in the upper ocean. A 2 year time-series of temperature, He, Ne, and Ar from Hydrostation S in Bermuda is used to constrain the model and validate the recent parameterizations of air injection and gas exchange processes. In Chapter 4, I describe the development of a moored, automated sampler that may be used to obtain a high-frequency time-series of a suite of noble gases over the spectrum of oceanic conditions..

1.2 *Gas exchange across the air-sea interface*

Gas flux across the air-sea interface is typically parameterized as:

$$F = K (C_s - C) \tag{1.1}$$

where K = the transfer velocity of the gas in units of m s^{-1}, C_s is the concentration of the gas in solubility equilibrium with the atmosphere (equal to P α, the partial pressure, in atm, of the gas in the air multiplied by the solubility of the gas, in units of moles m^{-3} atm^{-1}), and C is the *in-situ* concentration of the gas in the water. A positive flux represents

transfer from the atmosphere into the ocean. The transfer velocity, K, is a complicated function of the physico-chemical properties of the gas, and meteorological and hydrodynamic factors, such as wind speed, fetch, near-surface turbulence, surfactants, and bubbles, and is the focus of much research (see Jähne and Monahan, 1995 for a thorough review). Because the relations between these parameters and the transfer velocity have not yet been firmly established, K is most often parameterized solely in terms of the diffusivity of the gas and the wind speed, or wind friction velocity (Wanninkhof, 1992). While several studies (Jähne et al., 1984; Wallace and Wirick, 1992; Jähne and Monahan, 1995) have demonstrated that surface wave characteristics are more closely correlated to gas transfer than wind speed, these parameters are not easily measured over large space and time-scales. Recently, however, there has been a growing trend towards utilizing satellite data, such as scatterometry data, to provide information directly related to the state of the sea surface, thus providing a better determinant of transfer velocity (Etcheto and Merlivat, 1988; Wanninkhof and Bliven, 1991). These relations are still rather tenuous, however, and more research is needed to establish firm links between transfer velocity and these parameters. Thus at present, the transfer velocity as a function of wind speed is the most widely used and accepted parameterization (Wanninkhof, 1992).

The transfer velocity, K, is given by:

$$K \propto Sc^{-n} U^* \qquad (1.2)$$

where Sc is the Schmidt number of the gas (Sc = ν /D, kinematic viscosity of the water divided by the molecular diffusion coefficient of the gas), and U* is the friction velocity, equal to $\sqrt{\frac{\tau}{\rho}}$, where τ is the surface wind stress, and ρ is the water density.

For a rigid surface free of surface waves, the transfer velocity has been shown to be a function of the -2/3 power of the Schmidt number (Deacon, 1977). For a free wavy surface, the dependence changes to n = -1/2 (Ledwell, 1984). These power law dependencies have been confirmed for wind tunnel and wave tank experiments (Jähne, 1984; Ledwell, 1984; Asher, 1992), but have not yet been confirmed for the open ocean (Keeling, 1993). Watson et al. (1991) showed n = -0.51 $\pm$ 0.01 at low to moderate wind speeds using dual tracers in a small lake, and Wanninkhof (1993) showed the lowest wind speeds to have a power law dependence of -0.56 $\pm$ 0.01 using dual tracers in a small lake and applied to the coastal ocean.

The relation between transfer velocity and windspeed over a range of hydrodynamic regimes is given in Liss and Merlivat (1986) as a combination of three linear relations with break-points associated with the onset of capillary waves (at windspeeds <=3.6 m/s) and the onset of breaking waves (at > 13 m/s). The relation given for the breaking wave regime is an extrapolation from lower windspeeds and is not based on any observational data. The data used in the formulation come from wind tunnel studies and evasive tracer studies from a lake (Wanninkhof et al., 1985). While estimates of gas flux in the

literature exhibit considerable scatter, the formulation of Liss and Merlivat (1986) predicts the fluxes reasonably well at low wind speeds, and has been widely used. More recently, however, several studies have demonstrated that this parameterization is inadequate for the breaking wave regime (Wallace and Wirick, 1992; Farmer et al., 1993), and that the considerable scatter in estimates of gas fluxes at moderate wind speeds may be related to the averaging period of the wind speeds used (Wanninkhof, 1992). Wanninkhof (1992) presents a quadratic dependence of gas transfer velocity with wind speed for both short term winds and long term averages of wind speed. These parameterizations have yet to be confirmed by open ocean data.

Discrepancies are largely due to the fact that gas transfer is controlled by many factors other than windspeed which are not accounted for in these simplified parameterizations (Jähne et al, 1984; Wallace and Wirick, 1992; Wanninkhof, 1992; Farmer et al., 1993). Individual transfer velocity estimates have an uncertainty of about ± 30% before the onset of breaking waves (Liss, 1988; Wanninkhof, 1992). The uncertainty in the transfer velocity term often constitutes the majority of the uncertainty in studies involving dissolved gas cycles or air-sea fluxes of dissolved gases (Musgrave et al., 1988; Jenkins and Wallace, 1992).

1.3 *Bubble-mediated gas flux*

In conditions of wave breaking, bubbles are injected into the water, which increases gas transfer through direct exchange of gas across the bubble, and through near-surface

turbulence generated by the bubbles and breaking waves (Thorpe, 1982; Merlivat and Memery, 1983; McGillis et al., 1995). Observational data from several studies of gas exchange in conditions of breaking waves have shown that there is a considerable enhancement of gas transfer associated with bubbles, and that current parameterizations of the exchange process underestimate this flux by as much as a factor of 4 (Wallace and Wirick, 1992; Farmer et al., 1993). While these intense forcing episodes may occur sporadically, data collected from major field programs such as GEOSECS and WOCE suggest that these events leave a lasting imprint on the concentrations of the dissolved gases in the surface ocean. Characterization of the gas exchange process in these conditions is complicated by several factors. There are obvious logistical problems with obtaining data in these conditions in the open ocean, and laboratory wave/wind tanks cannot adequately simulate the combination of hydrodynamic and meteorological conditions that force the system in the ocean under these conditions. While several recent parameterizations of gas transfer from bubbles have been made (Keeling, 1993; Woolf, 1993; Asher et al., 1995), there is not sufficient observational data with which to constrain or validate the models, and the exchange mechanism remains poorly understood.

The net flux of gas from bubbles is described by the same general equation:

$$F=K_n\alpha(P_g-P_l) \tag{1.3}$$

where K_n is the net transfer of gases from the bubble, and P_g and P_l are the partial pressures of the gases in the gas and liquid, respectively. However, unlike exchange

across the interface, the partial pressure of the gas in the bubble is controlled by many factors, and is not strictly governed by solubility equilibrium. Hydrostatic pressure and surface tension on the bubble will tend to increase P_g relative to P_l. Because this combination of forces on the bubbles generally drives the gases from the bubbles into the water, gas exchange from bubbles can lead to supersaturations of gases in the water (Merlivat and Memery, 1982; Thorpe, 1982; Broecker and Siems, 1984; Keeling, 1993; Woolf, 1993) The partial pressure of the majority gases in the bubble, N_2 and O_2, will control the size of the bubble, and thus affect the transfer of the other gases (Woolf and Thorpe, 1991).

The transfer velocity of a gas across a bubble boundary layer is a function of the solubility of the gas as well as the diffusivity (Keeling, 1993; Woolf, 1993; Asher et al., 1995), which is a function similar to the permeability of the gas. In general, the net transfer of gases from bubbles is inversely proportional to the solubility of the gas, and directly proportional to the diffusivity, or the Schmidt number of the gas (Woolf, 1993). The power of the Schmidt number dependence is governed by the condition of the bubble boundary layer. If the bubble is coated with surface-active material, as is common in the ocean, the power dependence is given as the 2/3 power of the diffusivity (Clift et al 1978, Woolf, 1993). If the surface of the bubble is "clean", the Schmidt number dependence is proportional to the 1/2 power of the diffusivity (Levich, 1962).

The transfer velocity is also a function of the size of the bubble. For gas transfer parameterizations, bubbles may be divided into 2 size classes; small bubbles that dissolve completely, adding their entire gas load to the water, and larger bubbles that only exchange a fraction of their gas load before resurfacing (Fuchs et al., 1987; Jenkins, 1988; Keeling, 1993). While this is an oversimplification of the bubble size spectra and exchange from injected bubbles, the essential nature of the exchange process can be described as a linear combination of these two end-member conditions (Jenkins, 1988; Keeling, 1993; Schudlich and Emerson, 1996; Woolf, 1993). In the case of small bubbles that dissolve completely, the complete flux (gas exchange across the air-sea interface and bubble flux contribution) is given by:

$$F = K(C_s - C) + V_{inj} \cdot \chi \cdot \left(\frac{P_T}{RT}\right) \tag{1.4}$$

where V_{inj} is the volume flux of gas from the bubbles (in units of m^3 of air m^{-2} s^{-1}), χ is the mole fraction of the gas in air, P_T is the total atmospheric pressure (in atm), and R is in units of $\frac{atm \cdot m^3}{K \cdot mol}$.

At steady-state, the flux goes to zero, and the equation becomes:

$$-K(C_s - C) = V_{inj} \cdot \chi \cdot \left(\frac{P_T}{RT}\right) \tag{1.5}$$

By defining the saturation deviation from solubility equilibrium, ΔC, as $\frac{C - C_s}{C_s}$, the equation further reduces to

$$\Delta C = \frac{V_{inj} \cdot \chi}{K \cdot \alpha \cdot P} \cdot \left(\frac{P_T}{RT} \right) \tag{1.6}$$

The volume flux of air injected is a function of the hydrodynamic conditions, and has been related to wind speed and whitecap coverage (Monahan and Torgersen, 1990; Keeling, 1993). In addition, as mentioned previously, the transfer velocity, K, is a function of the diffusivity of the gas (parameterized here as $K \propto D^{0.5}$) as well as wind speed and other hydrodynamic parameters. However, by expressing the resulting saturations in terms of the saturations of a *pair* of gases, the dynamic terms, which act on all the gases in the same manner, cancel, and the equation becomes:

$$\frac{\Delta C_1}{\Delta C_2} = \frac{\alpha_2 \cdot D_2^{0.5}}{\alpha_1 \cdot D_1^{0.5}} \tag{1.7}$$

This parameterization is particularly useful for eliminating many of the unknown, hard-to-measure hydrodynamic terms, and relates the saturations to the physico-chemical properties of the gases.

For the partial trapping case, the total flux is given by:

$$F = K(C_s - C) + V_{exch} \cdot N_B \cdot \chi \cdot \left(\frac{P_T}{RT} \right) \tag{1.8}$$

where V_{exch} is the volume of gas exchanged during the lifetime of the bubble in the water in units of m^3 of gas m^{-2}, and N_B is the rate of injection of bubbles in s^{-1}. At steady-state, the equation becomes:

$$\Delta C = \frac{V_{exch} \cdot N_B \cdot \chi}{K \cdot \alpha \cdot P} \cdot \left(\frac{P_T}{RT} \right) \tag{1.9}$$

The volume of gas exchanged from a bubble is a function of the diffusivity and the solubility of the gas ($V_{exch} \propto \alpha K_b$, where K_b is the transfer velocity of the gas across the bubble), as well as hydrodynamic influences acting on the bubble. Again, by expressing the resulting saturations as the saturations of a pair of gases (denoted by the subscripts 1 and 2), the equation reduces to:

$$\frac{\Delta C_1}{\Delta C_2} = \frac{K_{b1}}{K_1} \cdot \frac{K_2}{K_{b2}} \tag{1.10}$$

For K_b, I use a proportionality of $D^{2/3}$ to describe the diffusive flux across the bubble boundary layer appropriate for dirty bubbles (Clift et al., 1978; Woolf, 1993). The equation thus reduces to:

$$\frac{\Delta C_1}{\Delta C_2} = \frac{D_1^{0.17}}{D_2^{0.17}} \tag{1.11}$$

The average transfer of gas from a cloud of bubbles injected would have intermediate values between the two extreme end-member conditions described by equations 1.7 and 1.11. Several recent parameterizations based on wave tank experiments or modeling studies (Keeling, 1993; Woolf, 1993) give single transfer velocities that are a function of some exponential power of both the diffusivity and solubility terms. For example, Keeling (1993) suggests that the flux from bubbles should scale as $\alpha^{0.7} D^{0.35}$, which in the fractional supersaturation form becomes:

$$\frac{\Delta C_1}{\Delta C_2} = \frac{D_2^{0.15} \cdot \alpha_2^{0.3}}{D_1^{0.15} \cdot \alpha_1^{0.3}} \tag{1.12}$$

as given in Schudlich and Emerson (1996). Additionally, these new parameterizations relate the flux as a function of the area of whitecap coverage of the surface water rather than wind speed (Monahan and Torgersen, 1991; Keeling, 1993; Woolf, 1993). However, validation of these models has only been possible using wave tank data (Wanninkhof et al., 1995), and it is difficult to identify the cause of discrepancies between the model predictions and the observations due to the constraints and limitations of wave tank simulations. No adequate data set is available to fully test these parameterizations.

There have been several studies of dissolved gases using the time-series approach at a few sites in the open ocean (Jenkins and Goldman, 1985; Spitzer and Jenkins, 1989; Schudlich and Emerson, 1996). While these parameterizations provide valuable insights into the longer term (weeks to seasons) effects of air injection processes and dissolved gas cycles, the sampling frequency of these studies is too low to adequately characterize the response of the dissolved gases specifically to breaking waves and bubble injection. Within the last few years, several studies have obtained high-frequency observations of dissolved gas concentrations during storm events (Wallace and Wirick, 1992; Farmer et al, 1993). These studies provide a glimpse into the responses of dissolved gases to conditions of wave breaking, and clearly show that the gas flux is much greater than predicted by previous parameterizations. In addition, these studies, using high-frequency,

automated sampling techniques from moorings and drift-buoys demonstrate the type of approach that must be used to advance our knowledge of these processes. It seems clear that while we are still some distance from establishing the predictive capability to accurately determine gas fluxes of large space and time-scales, we have identified the major controlling factors of the exchange process, and progress is currently limited by the lack of observational data over the spectrum of real oceanic conditions that are required to constrain and validate the parameterizations.

1.4 *Necessity of in situ, observational data*

The necessary data to further our understanding of gas exchange processes is difficult to obtain. Collection of samples in storm conditions has obvious logistical problems, and moorable or drifting sensors have not yet been developed to provide the range of gas data required. While wave tank simulations are useful for identifying the basic relations between gas flux and various physical and hydrodynamic factors, they do not adequately simulate the conditions that occur in the open ocean. For example, because of the size limitations imposed by wave tanks, experiments often fail to realistically reproduce many of the meteorological and hydrodynamical features that drive gas transfer, especially in the high wind / breaking-wave regime. Wave tanks may seriously fail to reproduce realistic near-surface turbulence, and as a result, may also fail to simulate the appropriate production rate, size spectrum, and lifetime of bubbles (Johnson and Cooke, 1979; Wu, 1981; Thorpe, 1984). The bubbles that are produced are not subjected to realistic turbulent conditions, and thus are not advected to a depth at which the pressure becomes

most effective in enhancing gas transfer from the bubble (Thorpe, 1984). One of the largest wind tunnel facilities is the large IMST Wind-Wave Facility, which has a water depth of only 0.75-1.0m (Jähne et al., 1985). Mean vertical profiles of bubble concentrations in the ocean decrease roughly exponentially with depth, with a penetration depth range of 4-12 meters for wind speeds of 12 m/s (Crawford and Farmer, 1987), and it has been shown that during storm conditions, bubbles may be swept to depths of 20 meters or more (Kanwisher, 1963; Thorpe, 1982). Clearly, the wind/wave tanks that have been used do not have the dimensions necessary to study these high energy processes. Many wind/wave tank studies of gas exchange only extend up to the point of breaking waves and bubble production, and those that have addressed the role of bubbles report inconsistent results at high wind speeds (Merlivat and Memery, 1983).

It is difficult to compare the results of studies from different wave tanks because the wave fields that are created are a function of the dimensions of the tank which vary among the facilities (Memery and Merlivat, 1983; Liss and Merlivat, 1986). Frew et al.(1995) and Hara et al. (1995) have shown that when gas transfer is parameterized as a function of the mean square slope of the wave, rather than windspeed, results from wave tanks of differing dimensions are in excellent agreement, provided that the water is surfactant-free. However, the concentrations of naturally occurring surfactant material present in the water causes variability in the relation between the transfer velocity and windspeed (or wave slope), and the concentrations present in wave tanks is very difficult to control (Frew et al., 1995). No single wave tank study has yet managed to cover the full range of

wind speeds that typically occur in the open ocean, and amalgamating data from several studies is problematic. Liss and Merlivat (1986) synthesized an idealized plot of transfer velocity as a function of wind speed based on data from lake experiments and wave tank observations. While the predicted values show reasonable agreement with the field results averaged from larger data sets at moderate wind speeds (e.g. the GEOSECS results), the parameterization was created without oceanic field results or high wind speed data. The authors also state that the data sets used show considerable variations in both transfer velocity and wind speed (Liss and Merlivat, 1986), and there are many suggestions (Thorpe, 1982; Merlivat and Memery, 1983; Thorpe, 1984; Woolf and Thorpe, 1991; Wallace and Wirick, 1992; Farmer et al., 1993) that this parameterization may be inappropriate when air injection occurs.

Models of air-sea gas exchange are, of course, limited by the available data on the relations of the many parameters that drive gas transfer. To adequately parameterize gas flux from bubbles, knowledge of bubble populations, size spectra, and hydrodynamic behavior over the range of turbulent conditions is vital. Many studies have addressed the issue of bubble populations and size spectra through direct observations (Blanchard and Woodcock, 1957; Kolovayev, 1976; Johnson and Cooke, 1979; Walsh and Mulhearn, 1987; Medwin and Breitz, 1989), *in situ* acoustic measurements (Medwin, 1970; Thorpe, 1982; Thorpe, 1986; Crawford and Farmer, 1987), and laboratory studies (Hwang et al., 1990). However, the distribution of bubbles in the upper ocean and its relation to hydrodynamic conditions is still poorly understood and thus poorly modeled (Woolf and

Thorpe, 1991). In theoretical treatments of gas exchange from bubbles, mass flux and transport equations are derived for a single bubble and then a link is established between the hydrodynamics and the bubble size spectra over which the equations may be integrated (Thorpe, 1982; Merlivat and Memery, 1983). This link is only a tenuous one, however, and at present the only reliable data on the bubble size spectra is for bubbles with radii between 50 and 150μm (Woolf and Thorpe, 1991). The omission of the smaller bubbles is potentially a serious one (Medwin and Breitz, 1989), but data in this size range is difficult to obtain with current techniques. Conversely, modeling studies based on laboratory experiment data suggest that bubbles larger than 0.05cm in radius may contribute significantly to the gas flux (Keeling, 1993). The effects of these larger bubbles is often ignored.

Another problem with air-sea gas exchange models exists when trying to compare the observational data with the model predictions. Several parameterizations of gas exchange and air injection processes under high wind/wave conditions have been proposed (Memery and Merlivat, 1983; Thorpe, 1984; Jähne et al., 1984; Fuchs et al., 1987; Spitzer and Jenkins, 1989; Woolf and Thorpe, 1991). However, these air injection models are forced by wind speed (or friction velocity) and therefore require that gas invasion episodes be driven by wind events, whereas the observational data show a stronger relationship between air injection events and the wave parameters (Wallace and Wirick, 1992). In many areas of the ocean, waves are often not in equilibrium with the wind, and

further, air injection is not a simple function of wind speed (e.g. Jähne et al.,1987; Wanninkhof, 1992).

The observational data that do exist fail to provide the information necessary to predict transfer velocities as a function of wind speed over the entire range of oceanic conditions. Estimates of oceanic gas exchange rates based on the distribution of either natural or bomb-produced ^{14}C (Broecker and Peng, 1974) and the radon deficit method (Peng et al., 1979) have several limitations. While numerous ^{14}C and radon measurements have been made, the values of transfer velocity are averaged temporally over all oceans (Liss and Merlivat, 1986), and they fail to show any clear dependence of gas exchange with meteorological or hydrodynamic parameters (Memery and Merlivat, 1983). They do, however, provide a vital constraint on transfer velocity estimates obtained by other methods.

Observational data from several recent studies (Wallace and Wirick, 1992; Farmer et. al., 1993) have shown that there is a considerable enhancement in the transfer velocity of gases during bubble penetration, and that current parameterizations of gas exchange during high wind/wave conditions underestimate the true flux by as much as a factor of 4 (Farmer et al., 1993). While these studies provide clear evidence of the importance of gas exchange in high energy environments, they all fail to provide a link between the physicochemical properties of the gas and the exchange over the spectrum of wind and

wave conditions. These parameters are essential in order to apply the established relationships between measured hydrodynamic and meteorological conditions and the transfer velocity to any gas of interest.

1.5 *The noble gases as tracers of air-sea gas exchange mechanisms*

In order to establish relations between the physical properties of a gas and the transfer velocity, it is necessary to use several gases as tracers. The noble gases (He, Ne, Ar, Kr, Xe) represent powerful probes of air-sea gas exchange processes, and they have been used as tracers of these processes for more than 20 years (e.g. Bieri, 1971; Craig and Weiss, 1971). The noble gases have a broad range of solubilities, solubility temperature dependencies, and molecular diffusivities (Figure 1.1), and therefore respond to gas exchange and air injection processes in different ways. The noble gases are inert and are not directly affected by chemical or biological processes.

As an illustration of the approach of using the noble gases to differentiate between complete and partial trapping, a comparison of the effects of the two modes of injection on the concentrations of the noble gases is shown in Table 1.1.

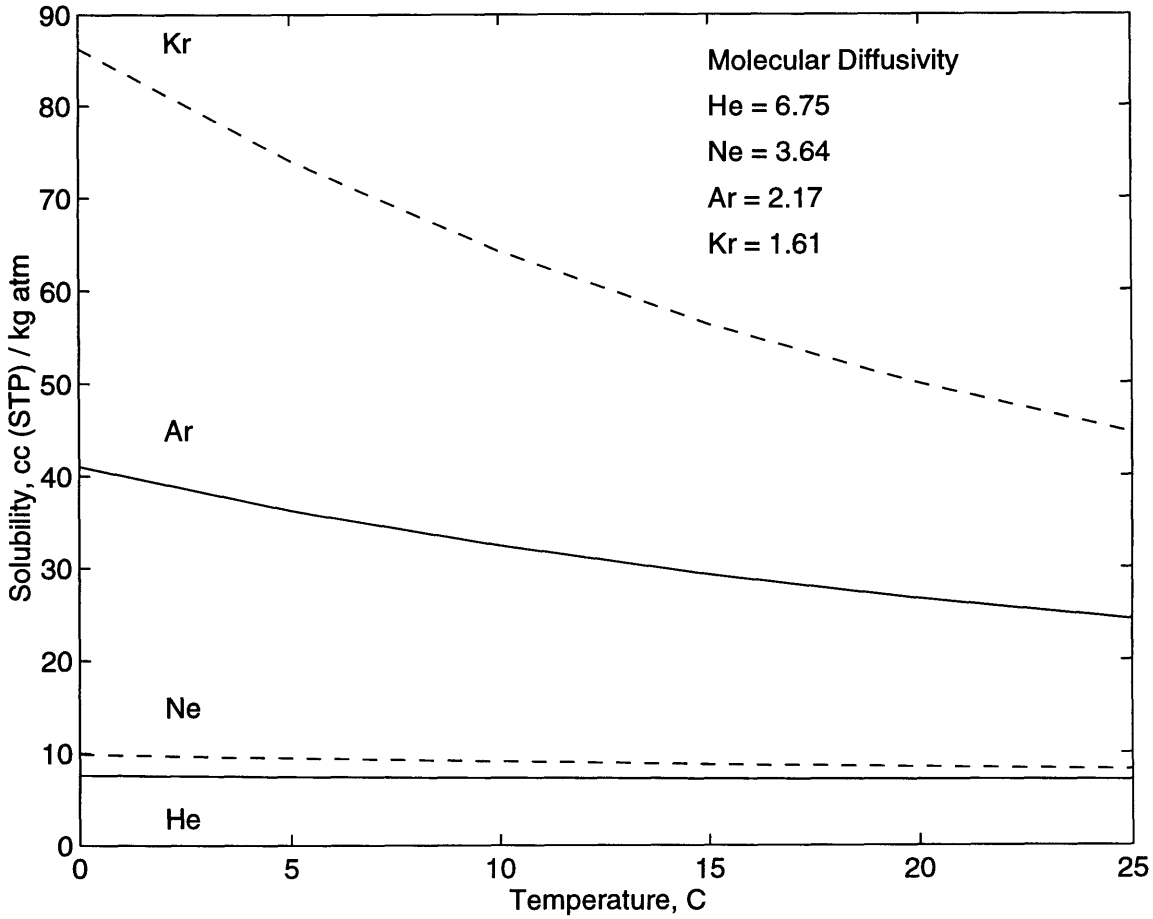

Figure 1.1 Solubility temperature dependencies and diffusivities at 20°C (inset text) of the noble gases.

	Complete Trapping	Partial Trapping	Large Bubbles
He / Ne	0.862	1.85	0.96
He / Ar	2.11	3.11	1.25
Ne / Ar	2.45	1.68	1.31

Table 1.1 Saturation ratios of noble gases resulting from complete bubble trapping, partial bubble trapping, and air injection from large bubbles (Keeling, 1993) in seawater at 20°C, 34ppt.

Shown are the relative supersaturations $\frac{\Delta C_1}{\Delta C_2}$ of the gases for complete and partial trapping modes. Also included is the bubble transfer velocity estimate of Keeling (1993) for large bubbles,

$$K_b \approx \alpha^{0.7} D^{0.35}$$

which, when in balance with flux across the air-sea interface and put in terms of fractional supersaturation, becomes:

$$\frac{\Delta C_1}{\Delta C_b} = \frac{D_2^{0.15} \cdot \alpha_2^{0.3}}{D_1^{0.15} \cdot \alpha_1^{0.3}} \tag{1.13}$$

The partial trapping mode affects helium more strongly than neon, whereas neon is more sensitive to the complete trapping mode, making the helium-neon pair an excellent diagnostic of the air injection process. The He/Ar and Ne/Ar pairs offer stronger contrasts. These two trapping modes represent the boundary conditions of the air injection process, and the total injection of air via bubbles is represented by a linear combination of the two endmembers.

Using this approach, Jenkins (1988) determined the optimal mixture of the two modes for GEOSECS Atlantic upper ocean gas concentrations to be partial trapping = 63 % ± 13%. Using a similar approach, Schudlich and Emerson (1995) determined that observations of upper ocean Pacific supersaturations at Station ALOHA were largely controlled by complete trapping. Bubble size spectra are controlled by many hydrodynamic processes, and will vary both temporally and spatially. While a linear combination of the two

boundary conditions may not be truly representative of the flux from a spectrum of bubble sizes, it allows for constraints to be placed on the process. As illustrated in the earlier equations, the approach considers the bubbles to be either dissolved completely, or that the flux is diffusively limited across the bubble boundary layer. As long as the mechanism of gas flux across the bubble boundary layer is the same for all sizes of bubbles that do not dissolve, and no other fractionations of the gases occur as a result of exchange across the bubble boundary layer, the linear combination approximation should provide an adequate representation of the relative supersaturations of gases generated by this process.

Observations of a time-series of noble gas concentrations in the upper ocean as they respond to changes in physical forcing can provide useful information about air-sea gas exchange processes over a broad range of physicochemical parameters of the gases and sea-surface conditions. This approach was implemented by Spitzer and Jenkins (1989) who used a time-series of monthly Ar, He, and O_2 measurements in the upper ocean near Bermuda to examine gas exchange, vertical mixing rates and new primary production on seasonal and annual time-scales. Seasonal supersaturations of biogeochemically important gases are caused by a combination of air injection, radiative heating, and biological processes. Argon and oxygen have very similar molecular diffusivities and solubilities, thus making argon an abiogenic tracer of oxygen. By comparing the cycles of Ar and O_2, it is possible to account for the relative contributions of physical and biological processes to the overall supersaturations, thus constraining the biological

signal and allowing for estimates of new primary productivity. Further, by using an upper ocean seasonal gas cycle model (Musgrave et al., 1988) to account for the radiative heating and mixing-induced supersaturations, the air injection contribution to the concentrations can be constrained (Jenkins, 1988). Spitzer and Jenkins (1989) demonstrated that the differences in chemical and physical characteristics of the noble gases result in clear and measurable contrasts in their concentrations, and were able to make quantitative determinations of average rates of gas exchange and air injection.

The study of Spitzer and Jenkins illustrated the strength of the noble gas time-series approach and ways in which the method could be extended. In order to more accurately characterize air injection processes, a time-series over a greater range of wind speeds is required. A time-series approach to observe physical forcing processes (i.e. the passage of a storm) requires a higher sampling frequency than that implemented in the Spitzer and Jenkins study. Also, it has long been recognized that wave characteristics are important in air-sea gas exchange processes (Kanwisher, 1963; Jähne et al., 1984; Wallace and Wirick, 1992), and an important goal is to develop air injection models in terms of wave characteristics. Further, extending the measurements of the noble gases to include Ne and Kr would place tighter constraints on the solubility and diffusivity dependence on gas exchange, and would extend the range of physical models that could be tested. For example, the large range in the molecular diffusivities between He and Kr suggests a more than a factor of two difference in their transfer velocities, thus making the observed changes a sensitive diagnostic of Schmidt number dependencies and gas flux. The extent

of supersaturation of a gas is dependent upon the product of the solubility of the gas and some power of the molecular diffusivity, depending on the mode of bubble trapping. The range of this product between He and Kr would lead to approximately a factor of four difference in supersaturations caused by complete bubble trapping and as much as a factor of ten difference in the supersaturations caused by partial trapping. Clearly, the ratios of these supersaturations can be useful tracers of air injection and gas exchange processes.

The recent study by Wallace and Wirick (1992) clearly demonstrates the type of approach that can be used to obtain the needed information about air-sea gas exchange over the spectrum of oceanic conditions. Using moored, quasi-continuous oxygen probes, they obtained a long time-series of dissolved oxygen concentrations in the upper ocean in the Middle Atlantic Bight. Also incorporated in this study were time-series of temperature, sensible heat flux, salinity, wind speed, and wave spectrum. Over a four month period, they documented several large increases in the oxygen flux that were associated with surface wave activity. They attributed this to breaking waves with subsequent air injection. The supersaturations of oxygen approached 10%. A numerical simulation that included air injection by bubbles (Thorpe, 1984) showed similar behavior. The results of this study support the idea that air injection is an important mechanism of air-sea gas exchange, and that wave parameters may provide a better correlation with gas flux than wind speed. However, the lack of vertical resolution in this study prohibited them from ruling out water advection and entrainment as a source of the increased gas

concentrations, and because biological processes in the upper ocean can cause supersaturations of O_2, the use of oxygen as the tracer presented some ambiguity in the source of the supersaturations. This study does, however, demonstrate the power of the time-series approach in conjunction with the relevant hydrodynamic and meteorological information for obtaining the information necessary to further our understanding of air-sea gas exchange processes in high energy environments.

Incorporation of a time-series of the noble gases into the framework of a study like that of Wallace and Wirick (1992) could provide the necessary information to characterize gas exchange and air injection processes in high energy environments. There are obvious logistical problems associated with obtaining data on gas fluxes over a range of atmospheric and sea surface conditions, particularly in the high wind/wave regime. A time-series approach requires frequent sampling which extends over a period that is long with respect to the physical forcing and the equilibration time of the system. A moorable, quasi-continuous measurement device, such as the oxygen probe units used by Wallace and Wirick (1992) would be ideal, but unfortunately the development of this type of device for the noble gases is not possible. Instead, we have developed a moorable, automated gas sampler capable of obtaining and storing a time-series of dissolved gas samples over long time-periods, which can be analyzed using conventional techniques in the laboratory (Chapter 4).

By obtaining a time-series of the noble gases along with hydrodynamic and meteorological data, several important pieces of information about air-sea gas exchange processes in high energy environments may be gained:

- basic correlations between gas flux and high wind or wave events
- contribution of bubbles to the flux of a gas based on the physical properties of the gas
- characterization of complete and partial trapping fractions
- parameterization of total gas exchange (direct and bubble-mediated) as a function of wind and/or wave characteristics for high energy environments
- information needed to test and validate the existing air injection models
- along with O_2 measurements, estimates of new primary production on a 1-2 month time-scale

Part 1 of this thesis (Chapters 3 and 4) examines the effects of gas exchange and air injection processes on the seasonal cycles of dissolved gases in the upper ocean, and describes a new sampling device and measurement technique that can provide the type of information necessary to examine the effects of gas exchange and air injection processes on short time-scales over the range of oceanic conditions.

Chapter 2

Methods

2.1 *Introduction*

The concentrations of the noble gases He, Ne, and Ar in seawater were measured by quadrupole mass spectrometry using ion current manometry. The gases were trapped and separated cryogenically. Overall uncertainty of measurements is 0.4% for He, 0.3% for Ne, and 0.2% for Ar, based on reproducibility of replicate samples. Tritium was measured by the ^{3}He ingrowth technique (Jenkins et al., 1983). Helium isotopes were measured on a statically operated, magnetic sector, dual collecting mass spectrometer. Measurement uncertainties are ± 0.25% for helium isotopes, and ± 0.01 T.U. for tritium. Sampling methods are discussed in Section 2.2. Sections 2.3 and 2.4 describe the analytical system and the extraction, purification, and separation of the gases. The automation of the system is discussed in Section 2.5. Sections 2.6 and 2.7 describe the

standards preparation and ion current manometry techniques. The data processing methods are discussed in Section 2.8, and Section 2.9 describes the analytical system and procedures for the analysis of 1 gram samples.

2.2 *Sampling Methods*

Samples are obtained from Niskin bottles or Kemmerer bottles, using tygon tubing to gravity-feed the water to a 3/8" o.d. copper tube, which holds approximately 13 grams of water. After flushing several volumes of water through the copper tube, the copper tube is sealed on both ends by means of specially-designed clamps (Weiss, 1969). Several precautions are taken to avoid trapping bubbles in the copper tubes. The tygon tubing is soaked in water 24 hours prior to sampling to prevent bubble formation in the tubing on contact with water. Figure 2.1 illustrates the basic sampling procedure from a Niskin bottle. The gravity feed of the water from the Niskin bottle is established slowly to prevent creation of bubbles or trapping of air pockets in the tubes. The copper tubes are flushed with several volumes of water, and the channel assemblies holding the tube are tapped as the tube is flushed to release any bubbles that may adhere to the copper tube walls. The clamps are then sealed, and the copper tube channels and clamps are rinsed thoroughly with fresh water to prevent corrosion. Water volumes are determined by weighing the copper tube when it is full, and then again when it is empty after the sample has been analyzed. A Metler PE 1600 balance with a precision of 0.01g was used. Uncertainty in the weights of the water samples is 0.1%. Tritium samples were collected in 1 liter, treated Flint glass bottles fitted with high-density polyethylene caps.

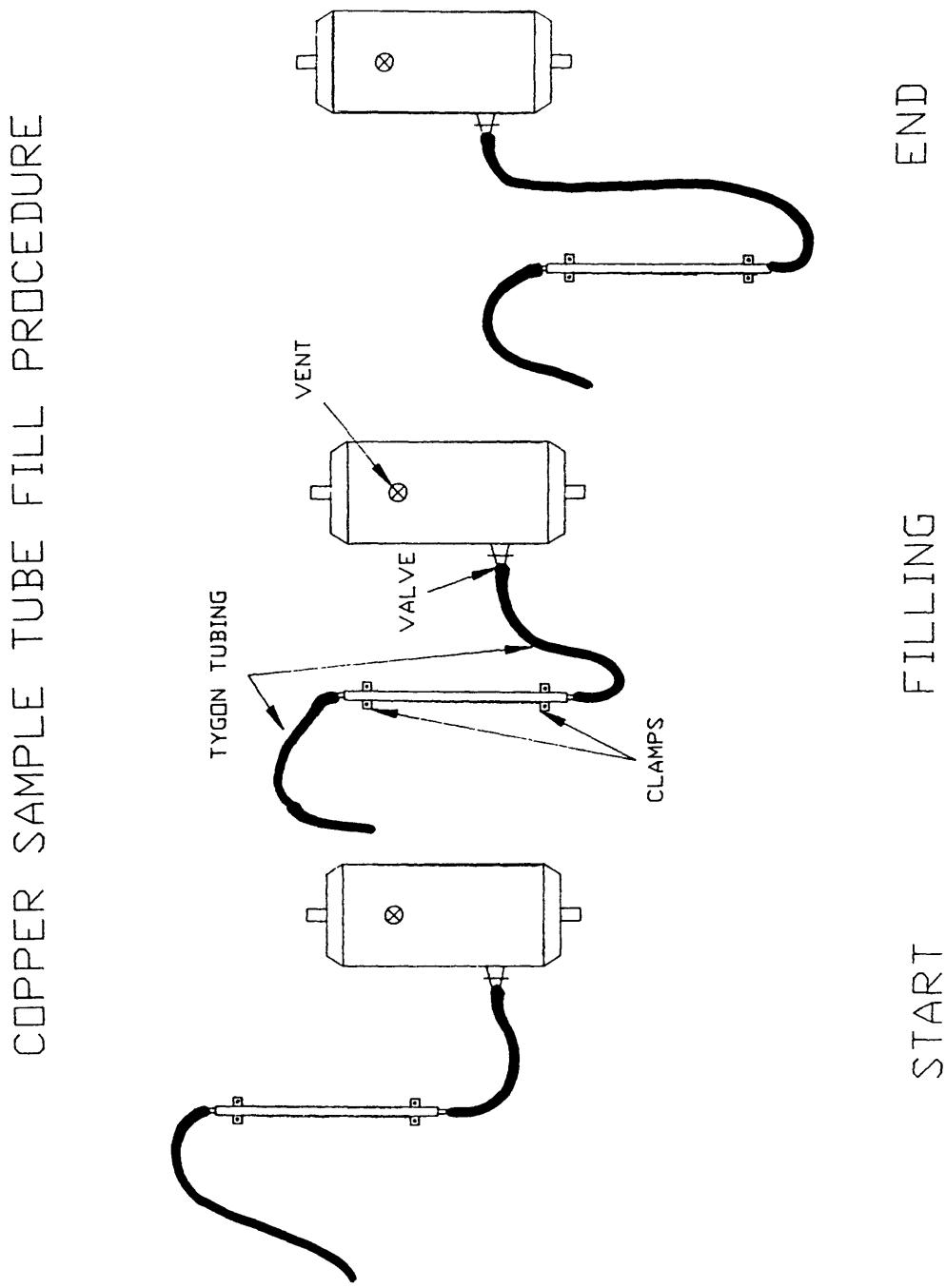

Figure 2.1 Procedure for taking water samples in copper tubes from a Niskin bottle.

Many tests have been conducted to determine the robustness of the sampling and storage technique (Spitzer, 1989). Results indicate that the uncertainty due to sampling procedures is less than 0.5% for He, Ne, and Ar.

The 13 gram sample size provides ample signal for measurement of the noble gases. With the current procedure, the signals of He, Ne, and Ar are approximately $2x10^{-10}$ amps, with pressures in the quadrupole less than $4x10^{-6}$ torr. With the 200 amu, faraday cup-equipped quadrupole system, we are able to routinely measure noble gas signals to approximately $1x10^{-15}$ amps. The reproducibility of the blanks for the system, which ultimately determines the detection limit for each gas, is less than 0.1% of the sample signal for all gases.

2.3 *Analytical System*

Figure 2.2 shows a block diagram of the noble gas processing system. The processing line is an all-metal system, which is necessary to prevent diffusion of helium into the line, and greatly reduces the lingering "memory effects" that other materials such as plastics and glasses have on the gas signals. The processing line is made of stainless-steel, bakeable to 400°C. The line is typically vacuum pumped to a pressure of $1x10^{-8}$ torr with a trapped oil diffusion pump, which is backed by a 195 l/min rotary pump. There is a separate rotary pump to handle large gas and water vapor loads from the extraction section of the line, and pumps the system down to approximately $1x10^{-3}$ torr. There are two SAES® getters operated at 300° C to getter reactive gases. The getter material used

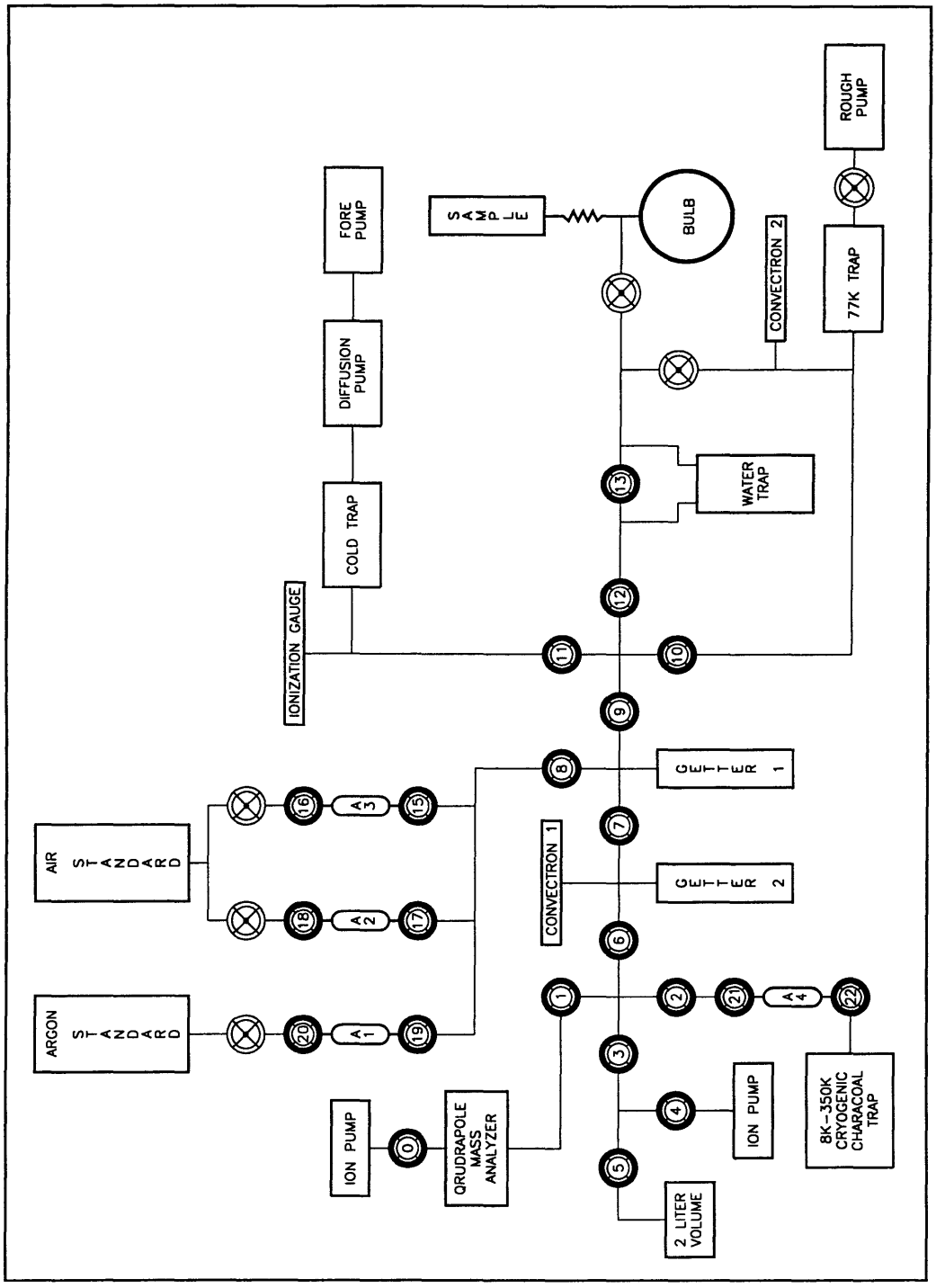

Figure 2.2 Noble Gas Processing Line. See text for details.

is type ST707 pellets (size 6-2), which is a non-evaporable getter alloy in pellet form, having a surface area of $100mm^2$. Each of the traps is filled with approximately 86 grams of this pellet material. The gases are trapped on a closed-cycle cryogenic trap at 8 K, which is controlled to ±0.2K using a Scientific Instruments model SI9650 temperature controller and a PC via RS-232 connection. The standards and aliquot volumes are housed inside a shielded area, and the room temperature is monitored and controlled to ensure thermal equilibrium between the reservoirs and the aliquoting volumes. The system is equipped with a 200 amu Balzers quadrupole mass spectrometer (QMG 112A) with a faraday cup detector, bakeable to 400°C. The quadrupole is pumped to a pressure of $1x10^{-8}$ using a Starcell VacIon Plus 20 ion pump (22 l/sec for N_2). An additional ion pump, a VacIon Plus 25 (20 l/sec for N_2) allows for pumping of the "clean", cryogenics section of the line. The processing, cryogenics cycling, and quadrupole operations are automated using a 486 PC. (see automated operation section).

2.4 *Extraction, Purification, and Separation*

Refer to Figure 2.2 and Table 2.1 for a schematic of the line and the exact timing of the procedures discussed below.

Timing (minutes)	Procedure Step
0-12	Open sample, flame every 3 minutes
12-12.5	Open manual valve to D.I.E. trap
12.5-14.5	Open valves to 1st getter; getter 2 minutes
14.5-17.5	Open valve to 2nd getter; getter 3 minutes
17.5	Close valves; cycle D.I.E. trap; repeat steps 1-4
35-45	Close manual valve to wet section; draw to cryotrap
45-46	Close valve to D.I.E. trap; draw 1 minute
46	Valves close; computer control of processing

Table 2.1 Noble gas extraction procedure (see text for details).

Water samples are attached to the vacuum system by a 3/8" Viton o-ring compression fitting connected to a stainless steel bellows to allow for flexibility and alignment of the sample. A 200 cc aluminosilicate bulb is attached beneath the bellows by a 3/8" viton o-ring compression fitting. Initial analysis (processing of Lake Fryxell samples and Saroma-Ko samples) used a 50 cc aluminosilicate bulb with a 1/4" compression fitting, but the system was altered to the above design to reduce the mechanical transfer of water to the system. The blanks for the wet section of the line are due to diffusion of helium from the viton o-rings in the compression fitting, and desorption of argon from material surfaces after exposure to air. There was no increase in the wet section blanks after changing the bulb size. The section is diffusion pumped for at least 1.5 hours, which is sufficient to reduce the wet section line blank to acceptable levels (see system performance section for details). The section is checked for leaks by measuring the pressure change after the section has been isolated from the pump for 5 minutes.

The system is isolated from the pump, and the bottom seal of the copper tube is re-rounded to allow the water to drain into the bulb. The tube is heated to drive the water down, and the water in the bulb is stirred and gently heated, which additionally drives the gas into the headspace by reducing the solubility of the gases in the water, increasing the diffusion of the gases, and lowering the water viscosity (which thins the air-water boundary layer). In addition, warming the bulb serves to compensate for cooling effects caused by evaporation during the release of the water into the evacuated bulb. At room temperature, the air-to-water partition coefficients for He, Ne, and Ar are approximately

133, 115, and 38, respectively. Given a headspace volume that is approximately 15 times the water volume, the percentage of gas partitioned into the headspace after the first extraction is > 99.9%. The headspace is vapor pumped through a capillary into a water trap at dry-ice ethanol temperatures (-72°C) to trap out water vapor.

The sample is then exposed to two SAES getter traps operating at 300° C for 5 minutes to remove the reactive gases. Results of gettering experiments show that this is sufficient time to getter the active gases. Nitrogen, hydrogen, and CO_2 are routinely measured in the mass spectrometer to monitor gettering efficiency. After the gettering processes, only the non-reactive gases remain. The two trap system allows the first trap to getter most of the gases, while the trap closest to the cryogenic section stays relatively clean. After the 5 minute gettering time, the valve between the water trap and the wet section is closed, and a second cycle of equilibration of the gases and headspace is performed. The dry-ice ethanol trap is cycled to room temperature for two minutes, and cooled back to dry-ice ethanol temperatures over the next 10 minutes. Extraction efficiency experiments of Spitzer (1989) show that the majority of gases left in the wet section is the result of gases being trapped in ice that formed in the D.I.E. trap during transfer. A capillary is installed between the sections to reduce the transfer of water and to prevent "backstreaming" of the extracted gases. Typically, about 2 grams of water are transferred from the bulb to the water trap. The extraction efficiency of the current procedure using two headspace

equilibrations and cycling the D.I.E. trap in between cycles is approximately 99.98 ±.01% for Argon, the most difficult of the gases to extract.

After the gases have been extracted and gettered, they are drawn from the wet section to the cryogenic charcoal trap at 8K over a period of 10 minutes. Analysis of "left-behinds" in the system indicates that this amount of time provides a generous time margin for trapping all of the gas. The gases are released and analyzed sequentially from the cryogenic charcoal trap by warming the trap to the release temperature of each gas.

Release curves and temperatures for release of He, Ne, and Ar were determined experimentally (Figures 2.3a and b). After trapping a gas sample at 8K, the trap was warmed at a rate of 5K/min to specific temperature intervals. The trap was held at the target release temperature for 5 minutes to insure equilibration between the charcoal and the headspace. The helium and neon curves are expressed in percent of gas released at each temperature step, and the argon is shown in terms of the signal size at each temperature step. The release of argon from the charcoal is a kinetically limited process, and the curve demonstrates the release of argon under these particular heating and time conditions. The curves provide an estimate of the temperature of maximum release. The curves show good separation between the gases, and release temperatures of 40K, 75K, and 280K were chosen to give maximum signal and separation between the gases. It is not necessary to release 100% of the gas as long as the fraction released is reproducible, which is borne out in the reproducibility of repeated air standards.

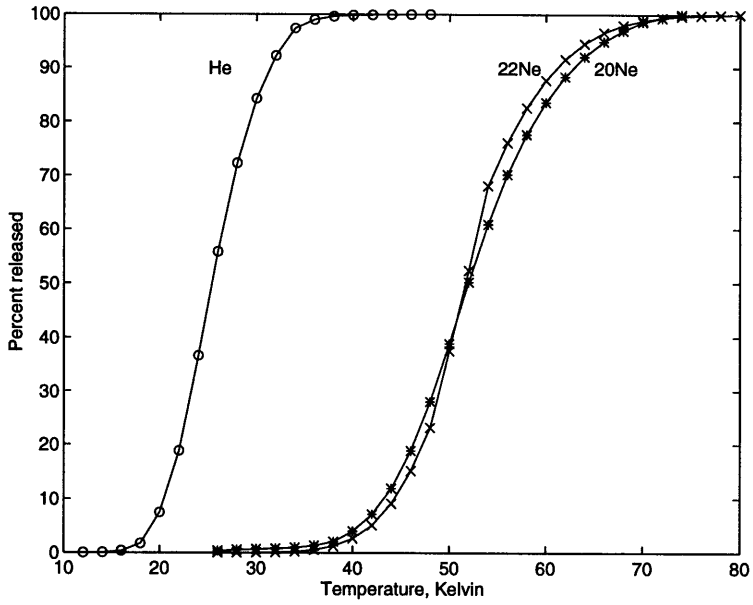

Figure 2.3a Percent of gas released from the cryogenic charcoal trap as a function of temperature for He (circles), ^{20}Ne (crosses), and ^{22}Ne (stars). ^{20}Ne is not corrected for the effects of Ar^{++}.

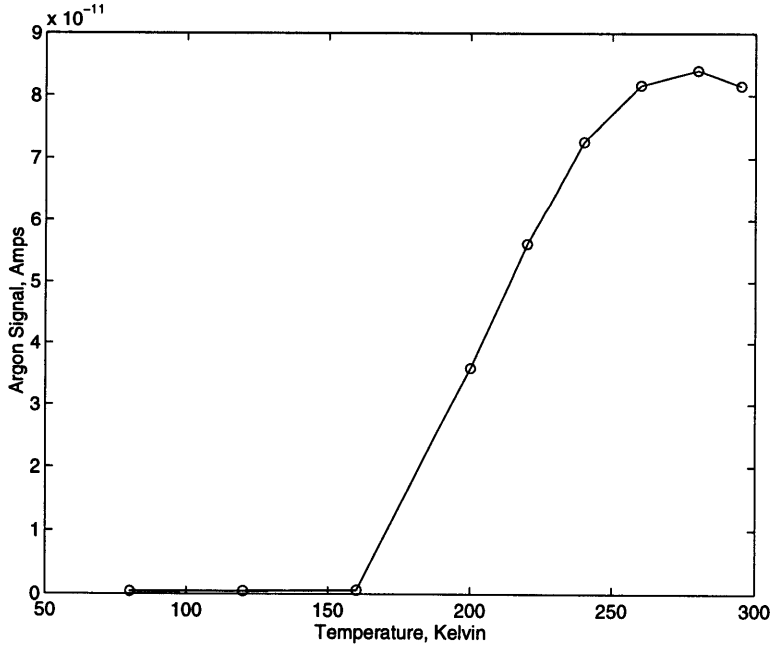

Figure 2.3b Argon signal strength (amps) in the quadrupole during released of Ar from cryogenic charcoal trap as a function of temperature.

The amount of gas introduced into the quadrupole must be sufficient to provide a strong signal, but remain below the maximum stable operating pressure for the quadrupole (approximately 10^{-5} torr). Because of the large size differences of the gases in the samples (see Table 2.2), a separate procedure for expanding the gas from the cryogenic charcoal trap into the quadrupole is used for each gas (Table 2.3).

	cc (STP) / g	atm (STP)
He	3.75×10^{-8}	5.24×10^{-6}
Ne	1.53×10^{-7}	1.81×10^{-5}
Ar	2.49×10^{-4}	9.34×10^{-3}
Kr	5.49×10^{-8}	1.14×10^{-6}
Xe	7.80×10^{-8}	8.70×10^{-8}

Table 2.2 Concentrations of the noble gases in seawater at solubility equilibrium with the atmosphere, and the partial pressures of the noble gases in dry air.

Line Section	Approximate Volume (cc)
Cryogenic Charcoal Trap	7
Aliquot Volume	0.75
Cross Sections	30
Ballast Volume	2000
Quadrupole	200

Helium	Neon	Argon
Direct inlet from cryogenic trap to quadrupole	Inlet from cryogenic trap to 2 cross sections	Expand two aliquot volumes into both cross sections and ballast volume
	Inlet 1 cross section to quadrupole	Close aliquot volume
		Pump away cross sections
		Expand remaining gas in aliquot volume to quadrupole.

Table 2.3 Approximate volumes of the inlet section of the noble gas processing line, and the inlet procedures for He, Ne, and Ar.

Using these expansion procedures, the total pressure in the quadrupole for each gas is less than $5x10^{-6}$ torr (N_2- equivalent pressure). Experiments showed that the pumping time in-between the two Ar expansions necessary to reduce the signals from the expansion section to blank levels was approximately 7 minutes. The reproducibility of He, Ne, and Ar from air standards analyzed using these procedures is 0.1-0.2% over 16 hours.

During the release at 75K to measure Ne at mass 20, a small fraction (0.01%) of argon is also released. While this is insignificant as a loss to the total Ar signal, a fraction of this Ar is doubly-charged (Ar^{++}) during the ionization process in the quadrupole, and interferes with the ^{20}Ne measurement at mass 20. Figure 2.4 shows the effect of the Ar^{++} on the mass 20 signal.

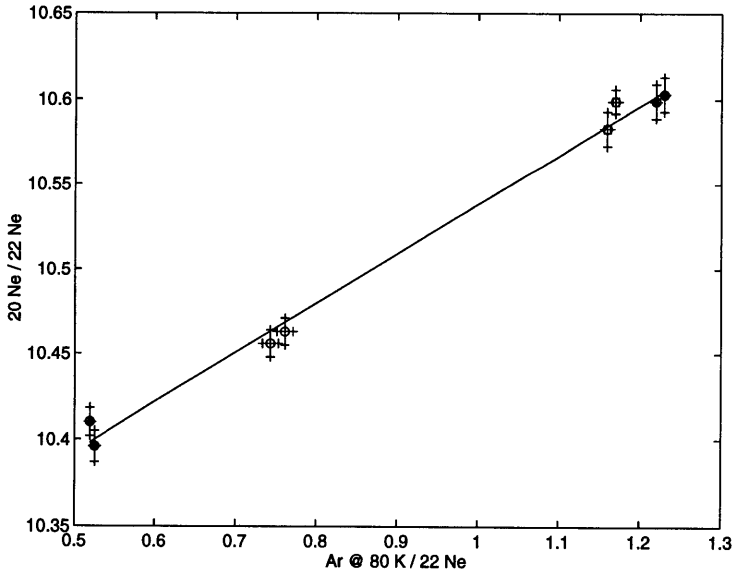

Figure 2.4 The effect of Ar^{++} on the signal at mass 20 at 75 Kelvin release temperature. The line is a least-squares fit to the data points with a slope of 0.29 ± 0.01. The slope represents the amount of signal at mass 20 due to the presence of Ar^{++} in the quadrupole.

Repeated experiments show the Ar^{++} contribution to the mass 20 signal to be 29±1% of the Ar^{+} signal measured at 75 K. This effect was checked periodically and found to be stable with time. The relative sizes of the signals in the quadrupole for a typical sample leads to a correction to the mass 20 signal of approximately 5%. The uncertainty in the correction due to the uncertainty in the Ar^{++} ionization efficiency is approximately 0.17%.

The Argon signal is also affected significantly by a "memory effect" in the cryogenics charcoal trap and the quadrupole from the previous sample in the system. The memory effects for helium and neon are less than the uncertainty in the individual measurements. The effect is a function of the size of the previous sample and the amount of time between samples. This effect is measured and quantified by measuring the lineblank -to-air standard argon ratio for various size samples as a function of time. Figure 2.5 shows a plot of such comparisons over a range of lineblank-to-signal sizes of approximately a factor of 3, and over time periods from approximately 3 hours to over 4 days. A non-linear least squares regression of the data to an equation having the form:

$$Y_f = Y_\infty + Y_1 \cdot e^{(-\alpha \cdot t)} \tag{2.1}$$

was performed, and the coefficients of the fit are: $Y_\infty = 0.00113$, $Y_1 = 0.00189$, $\alpha = 1.8158$. This equation represents the size of the memory effect as a function of time, t, and is multiplied by the previous sample and subtracted from the current sample signal. The stability of this function was checked periodically and found to be stable within the uncertainties of the measurements over periods of several months.

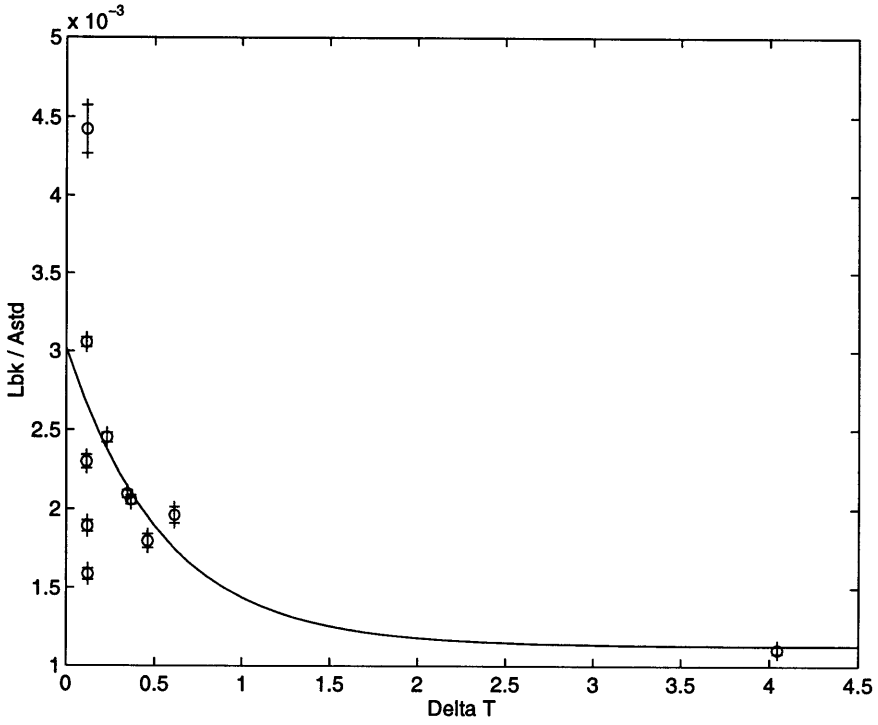

Figure 2.5 Memory effect for Ar in the system. Lbk/Astd is the ratio of the Ar signal (amps) in a lineblank to the Argon signal in an air standard. Delta T is the elapsed time in days between the air standard and the lineblank. The curve is a non-linear least-squares fit to the data points. See text for details.

The release of krypton has considerable overlap with the release of argon, with a maximum release temperature of approximately 300 K (P. Schlosser, pers.comm.). Separation of the two gases is crucial due to the large size discrepancy of the two gases; a sufficient volume of Kr cannot be expanded into the quadrupole without exceeding the pressure limitation of the quadrupole if Ar is not removed . Attempts to separate the gases by pumping away the argon at 250-280K and analyzing the remaining krypton at 325K gave signal sizes at mass 84 that were not significantly greater than the background noise on the most sensitive scale of the quadrupole. Xenon at mass 132, with a release temperature range of 200-320K was similarly undetectable. Separation and analysis of

krypton and xenon would be possible using a two-stage cryogenic trap system. The first trap operating at temperatures around 100K would trap Kr and Xe, while the second trap at 8K would trap the remaining gases. Quantitative separation would not be necessary. The amount of Ar on the first trap would need to be sufficiently small to avoid pressure interferences on inlet of the sample to the quad so that the maximum load of Kr and Xe could be released.

2.5 *Automated Operation*

The operation of pneumatically-actuated valves, the cryogenic trap temperature, and the quadrupole are controlled by 486 personal computer, (66MHz, 8 MB memory). Digital I/O and 16-bit A/D conversion operations are controlled using ComputerBoards 1602/16 A/D board and DIOH-48 boards. The cryogenics temperature is controlled using Scientific Instruments model 9650 temperature controller via RS232 connection. The software to interface and control the system was written using Microsoft Visual Basic 3.0 Professional Edition, and data were then transferred to a UNIX workstation where data processing was done using Matlab, version 4.2c. The sample extraction procedure requires an operator to open and extract the sample, and the process and analysis is fully automated after the draw on to the charcoal trap. During the extraction phase, the computer is used to time and prompt the operations of the procedure. This type of automation and analysis allows for greater reproducibility of conditions and minimizes operator intervention. The total time for the processing and analysis of a sample is 2.8 hours. After a sample is on the charcoal trap and the analysis is under computer control,

the wet section may be prepared for the next sample. The wet section and water trap are cleaned with distilled, deionized water, isopropanol, and dried with N_2. A new sample is attached to the wet section and the section is rough pumped with a liquid nitrogen water vapor trap for the remaining time. The wet section is diffusion pumped for approximately 1.5 hours between samples. Wet section blanks indicate that this is a sufficient time to reduce the signals to acceptable blank levels.

2.6 *Standards Preparation*

Air standards are taken from sea-level at the Woods Hole Oceanographic Institution beach in stainless-steel reservoirs. The volumes of the reservoirs are determined gravimetrically to a precision of 0.05% The reservoirs, fitted with copper stem-tipped Nupro valves, are evacuated on a pumping station to less than $5x10^{-8}$ torr. The reservoir is valved off, and is taken to the beach, placed in the shade, and given 1 hour to reach thermal equilibrium. The air standard is taken by opening the valve during an onshore breeze.

Measurements of barometric pressure (Pennwalt aneroid barometer, ± 0.24 mm Hg), relative humidity (Brooklyn hygrometer, ± 3%), and temperature (Fisher 15140B, ± 0.2°C) are used to calculate the size of each atmospheric gas in standard cubic centimeters (cc at STP). Abundances of the gases in the atmosphere used in the calculations were taken from the Handbook of Chemistry and Physics, 62nd edition. The

uncertainties in the measurement of these parameters and in the tank volumes leads to a total uncertainty of 0.16%.

The maximum stable operating pressure of the quadrupole is approximately 10^{-5} torr, and aliquot volumes from the standard reservoirs are chosen to provide a strong signal at a pressure below this maximum. The aliquot volumes are calculated by determining the volume of the empty chamber, then adding a solid metal rod of known volume to the chamber to achieve the desired aliquot volume. The aliquot volumes are calibrated against glass volumes to 0.07% by connecting them in parallel to the aliquot and air standard, and comparing the signal response to each from the quadrupole. The glass volumes were determined gravimetrically using triple-distilled mercury. Other aliquot volumes may then be calibrated against the originally calibrated aliquot volume. The uncertainty of the aliquot volumes using the calibration standard is a function of the number of measurements made, and the aliquot volumes are generally determined to a precision of between 0.1-0.2 %. The overall uncertainty of the size of the air standards is approximately 0.17%. The integrity of the air standard is checked periodically by taking multiple standards and comparing the calculated sizes and signals to the original. Reproducibility of air standards is approximately 0.2%.

Due to the greater solubility of argon in water relative to helium and neon, a separate argon standard is used to augment the argon concentration in the air standard and to provide a signal of argon similar to that expected in a water sample. The argon standard

was prepared by expanding research grade argon into a reservoir using an MKS Barotron manometer to measure the pressure in the reservoir. This argon standard was calibrated against a known air standard.

2.7 *Ion Current Manometry*

The quadrupole uses a tungsten filament, which is shown to have a longer working life than rhenium filaments (nominal expectancy = 1 year), and provides stable and reproducible ionization for the noble gases. The manufacturer's reported sensitivities for the noble gases are:

He	6.4×10^{-5} A / mbar
Ne	6.4×10^{-5} A / mbar
Ar	24×10^{-5} A / mbar

Measurement of the working sensitivity shows good agreement with these values.

Peaks are scanned by the quadrupole in 0.05 amu increments. A parabolic fit is made to the 9 points over the peak. This procedure compensates for limited mass resolution and drift in the mass spectrometer. The peak shapes (Figure 2.6) are smooth, and the peak position is stable for similarly-sized samples within the resolution of the 16 bit A/D converter over periods of months. The time constant for the quad response is set to 75 msec. Baseline corrections are made by subtracting the ion current measured on the same scale as the sample at mass 5 for He, mass 25 for Ne, and mass 47 for Ar.

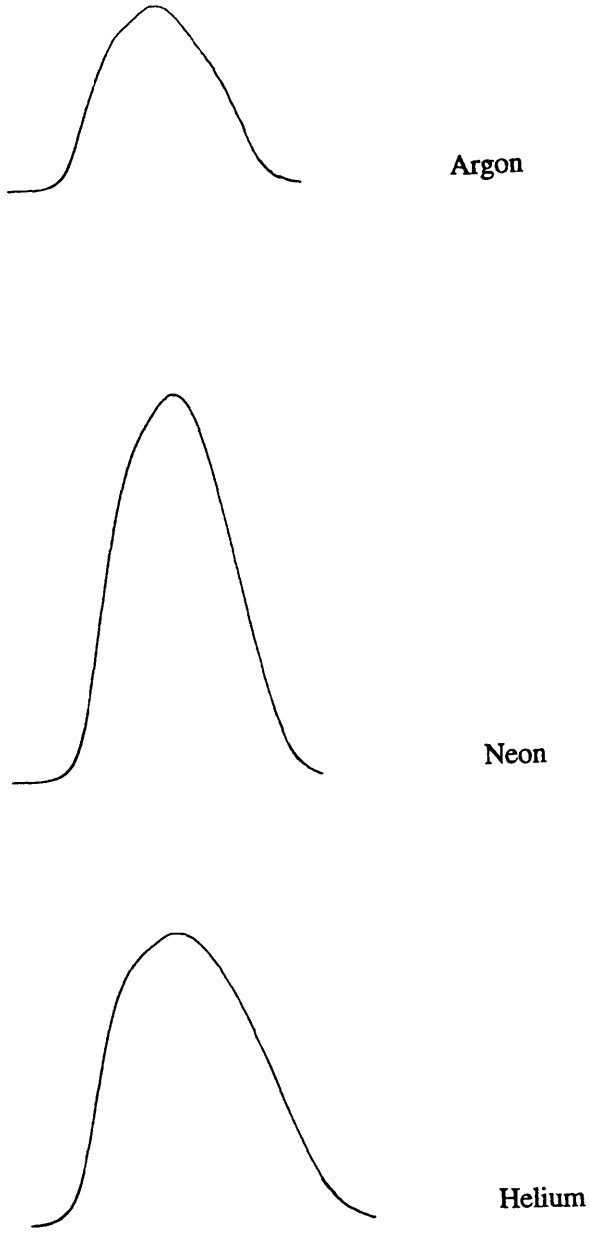

Figure 2.6 The peak shapes of He, ^{20}Ne, and Ar in the quadrupole from a typical air standard. Quadrupole and chart-trace speeds provide scans at a rate of 4 cm / amu. The signal range is 10^{-9} Amps full scale.

There is a reproducible decrease in the helium peak height over the time period of the analysis, possibly due to cooling of the ion source as the quadrupole reaches thermal equilibrium with the gas introduced (Figure 2.7).

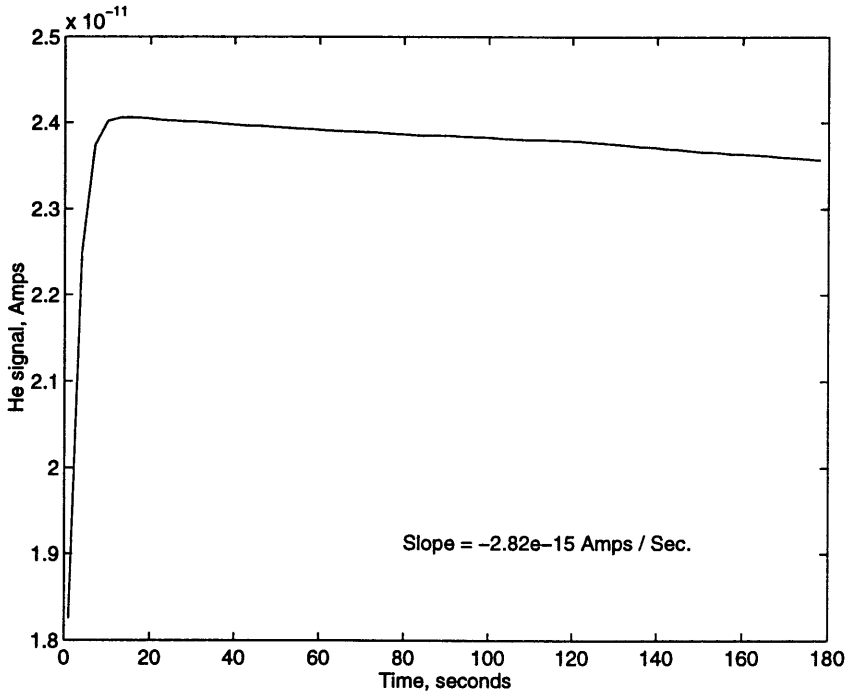

Figure 2.7 Helium signal decrease during the inlet and analysis time in the quadrupole.

The neon peak height also decreases, but the effect is not significant over the time-scale of the measurement. This decrease has a rate of 1.7×10^{-13} amps/min, or 2.0% of the sample peak signal over the 3 minutes of the analysis. The analysis of each gas consists of multiple peak measurements (8-10), each measurement being an average of over 20,000 readings (~ 3 seconds). The peaks are bracketed by measurements of the baseline and corrected over the time of analysis. A least squares fit line is fit to the multiple peak

measurements, and extrapolated to the signal at the time of entry of the sample into the mass spectrometer. The uncertainties of the intercepts of the linear regressions for the three gases are typically about 0.07%. The sensitivity of the quadrupole response for a given sample size (amps / cc) is shown in Figure 2.8 for air standards. The specifications of the drift in the sensitivity are approximately 1% over 8 hours. Measurements of time series of air standards show the quadrupole sensitivity for the noble gases to be extremely stable, with typical variations of less than 0.7% over 24 hours.

2.8 *Data Reduction*

Data reduction and corrections are done using a Matlab program designed to convert the ion current signal information from the quadrupole to concentration values. The data matrix is first corrected for the effects of doubly-charged Ar (see Section 2.4 and Figure 2.4) on the mass 20 signal (amps) to calculate the ^{20}Ne signal:

$$^{20}Ne_{corr} = {}^{20}Ne^{0} - (0.29) \times {}^{40}Ar \qquad (2.2)$$

where $^{20}Ne^{0}$ is the uncorrected signal measured at mass 20, and ^{40}Ar is the Ar^{+} signal measured during the Ne inlet procedure at 75 K.

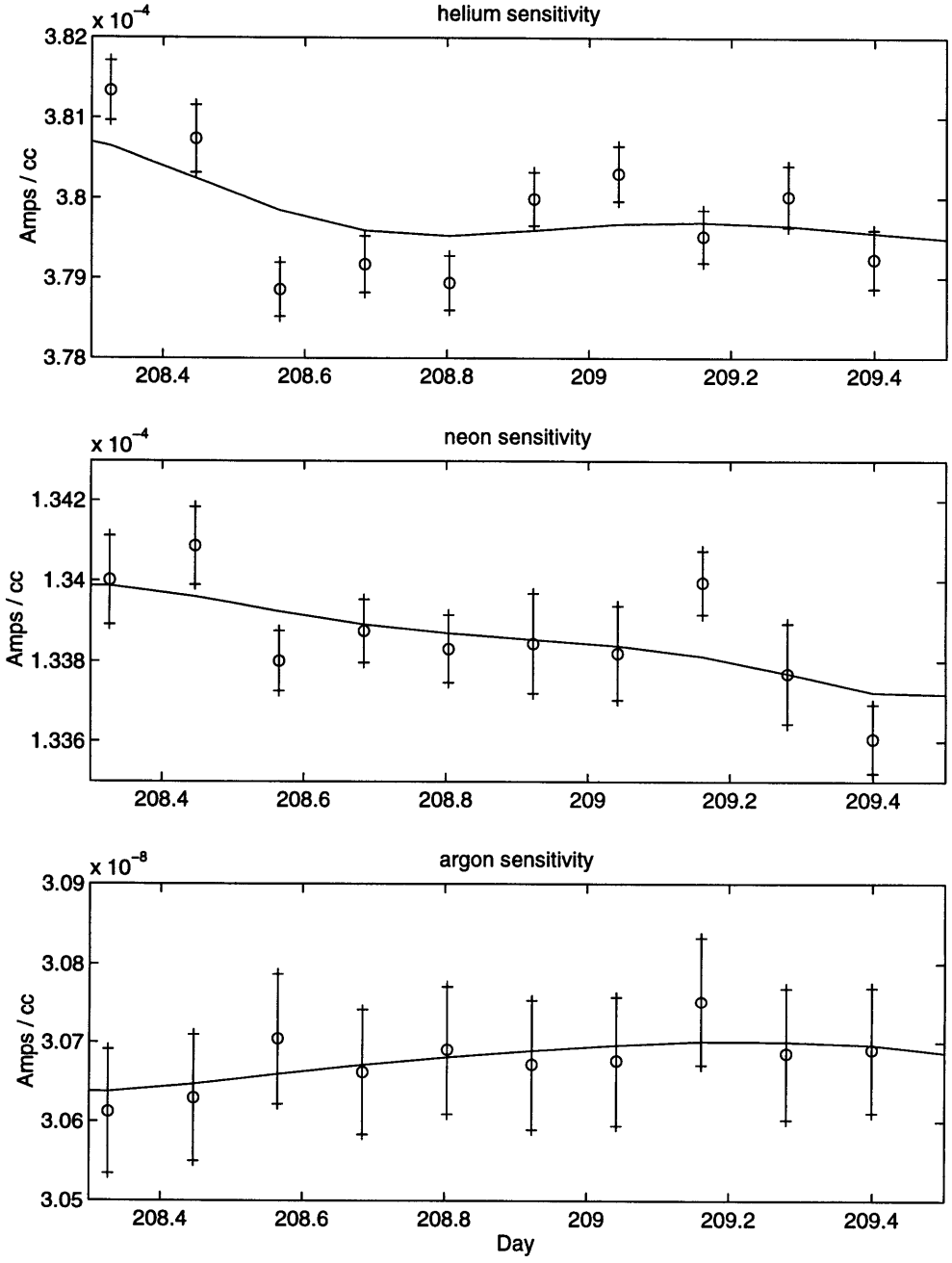

Figure 2.8 He, Ne, and Ar sensitivity (signal strength / volume of gas) in air standards over a 24 hour period.

The matrix is then corrected for the memory effects for Ar (see Section 2.4 and Figure 2.5) by subtracting the memory effect of the previous Ar measurement:

$$Ar^{i}_{corr.} = Ar^{i} - (0.00113 + 0.0019 \cdot e^{(-1.8158 \cdot \Delta T)}) \cdot Ar^{i-1} \quad (2.3)$$

where the superscript i represents the relative position of the measurement in time, and ΔT is the elapsed time (in days) between the current and previous measurement.

A cubic smoothing spline is fit to the lineblank and wet section blank signals for each of the gases and interpolated over the time grid of the data matrix. Air standard signals and sample signals are blank-corrected using the interpolated values of the line blanks and wet section blanks, respectively, at the time of the standard or sample:

$$S_s = S^0 - S_b$$

where S_s is the blank-corrected sample signal, S^0 is the initial signal, and S_b is the signal of the blank. Figures 2.9 and 2.10 show the wet section blanks and line blanks over time.

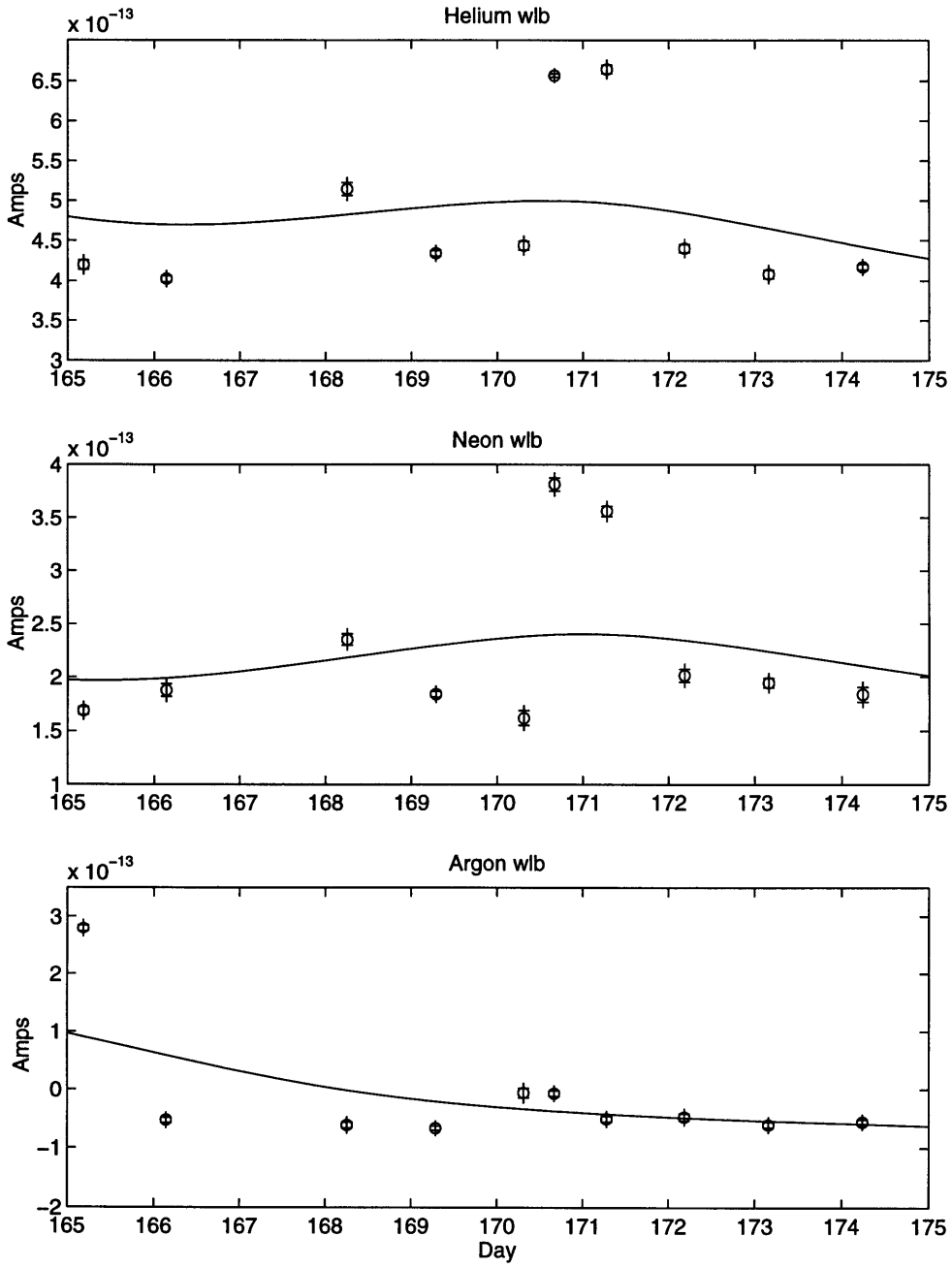

Figure 2.9 He, Ne, and Ar blanks from the wet section of the processing line over a 10 day period.

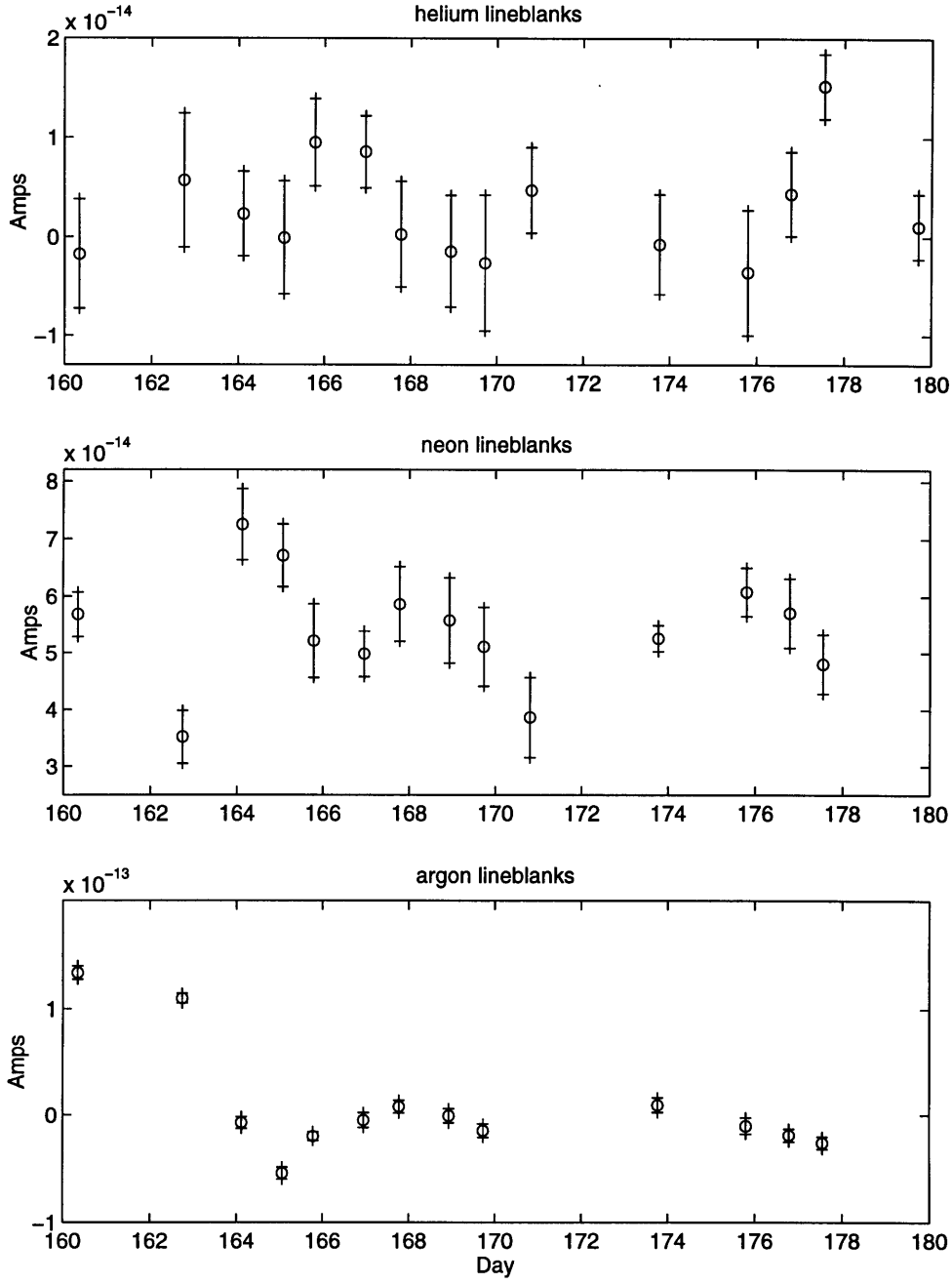

Figure 2.10 He, Ne, and Ar line blanks over a 20 day period.

The sizes of standards is determined based on the initial size of each gas in the standard tank and the number of aliquots removed from the tank (see Section 2.6). The size, S, of each gas in the air standard tank is calculated using:

$$S = \frac{P - P_{H_2O}}{760} \cdot \frac{273.15}{273.15 + T} \cdot P_p \cdot V_A \cdot \frac{V_T}{V_T + V_L} \cdot DF \tag{2.4}$$

where

- P is the barometric pressure when the air standard was taken
- P_{H_2O} is the pressure of water vapor in the air at the measured air temperature, which is determined from relative humidity,
- T is the air temperature (°C)
- P_p is the partial pressure of the gas in air (at STP)
- V_A is the volume of the aliquoting volume used to deliver the gas to the system
- $\frac{V_T}{V_T + V_L}$ is a correction for the volume of the system that connects the air standard tank to the system, where V_T is the volume of the air standard tank and V_L is the volume of the system line connecting the tank to the system
- DF is the depletion factor needed to correct the gas pressure in the tank for the number of aliquots removed from the tank:

$$DF = [1 - (\frac{V_A}{V_A + V_T + V_L}) \cdot (1 - \alpha)]^n \tag{2.5}$$

where α is the volume fraction of the aliquot volume to the volume of the line into which the gas is expanded. Additional corrections are made for the fraction of gas left behind in

the aliquot volume after expansion to the system, and for the effects of this left behind fraction on the gas delivered to the system when taking multiple aliquot volumes for a single analysis.

The amount of each gas in a sample is determined by determining the sensitivity of the machine for each gas (i.e. the signal current to size ratio in Amps /cc gas), and calculating the cc's of the gas in the unknown sample from this ratio and the signal of the unknown. The sensitivity of the quadrupole to each gas is determined by running standards of known sizes that bracket the size of the unknown sample, and the sensitivity is spline fit using a cubic smoothing spline and interpolated over the time grid of the data matrix to provide and estimate of the sensitivity at the time of the processing of the sample. Figure 2.8 shows the sensitivities for each gas from a standard size that is comparable to the sample sizes. The uncertainty of the estimated sensitivity, and thus the estimated size of the sample, is determined by calculating the rms deviation between the cubic spline fit and the known sensitivity from analysis of the standards. This uncertainty is added in quadrature to the uncertainties in the initial size determinations of the gases in the standards. At present, most of the uncertainty is due to the uncertainty in the aliquot volume sizes of the air standard tanks. These volumes are calibrated against standard volumes to approximately 0.1%.

The standards used to bracket the sample size are used to determine the system linearity over the pressure range of the samples and standards. In general, the system is linear to

better than 0.2% over a size range that is approximately ± 20% of the running standard size. The volumes of the aliquot sizes from the standard and spike tanks provide a resolution of the standard sizes that is less than approximately ±10% of the sample size for all gases.

The sample sizes measured are then divided by the weight of the water sample to obtain the concentration of the gases in the sample in units of cc (STP) / gram.

Table 2.4 shows a list of the random and systematic uncertainties associated with sampling and processing.

ANALYTICAL UNCERTAINTIES	
Extraction efficiency	99.98% 0.01%
Blank reproducibility	0.1%
QMS analysis	0.06%
QMS linearity reproducibility	0.2%
Sample weighing	0.1%
TOTAL	**0.25%**
SYSTEMATIC UNCERTAINTIES	
Sampling	<0.5%
Sample Storage	<0.3%
Standards	<0.16%
Solubility values	0.5%
TOTAL	**0.5%**
Reproducibility of Replicate Samples	
He	0.4%
Ne	0.3%
Ar	0.2%

Table 2.4 Analytical and Systematic Uncertainties.

2.9 *One Gram Sample Analysis*

For the preliminary analysis of one gram samples from the noble gas sampler, a very basic, abbreviated procedure was used to measure He, Ne, and Ar. No attempt was made to make precision measurements on the gases for this preliminary analysis. The goal of this first analysis was to determine, in general, the extraction efficiency of the 1 gram samples, the signal to line blank ratio, and to measure the relative sizes and reproducibility of the three gases in the samples. (For details of the noble gas sampler and 1 gram sampling procedure, see Chapter 4).

A diagram of the 1 gram processing line is shown in Figure 2.11, and timing of the procedure is shown in Table 2.5.

Timing (minutes)	Procedure Step
0-10	Open the sample; flame to drive water into bulb
10-15	Warm bulb
15-20	Dry-Ice Ethanol on bulb
20-22	Submerge bulb in D.I.E.
22-24	Open V10 and V7 to LNCT trap section
24-26	Close V10 and V7
26-30	Open V1 and V2; Inlet He and Ne; Analyze.
30-32	Open V10 and V7; Warm bulb
32-36	Shut off titanium getter #1
36-37	Shut off titanium getter #2; Open V5 to SAES getter
37-41	Shut off SAES getter
41-45	Trap an aliquot between V1 and V2; Inlet; Analyze

Table 2.5 Extraction and purification procedures for 1 gram sample analysis.

The crimped ends of the capillary tubing are cut with capillary tubing cutters, and the end pieces measured with vernier calipers for corrections to the volume loss. This volume is

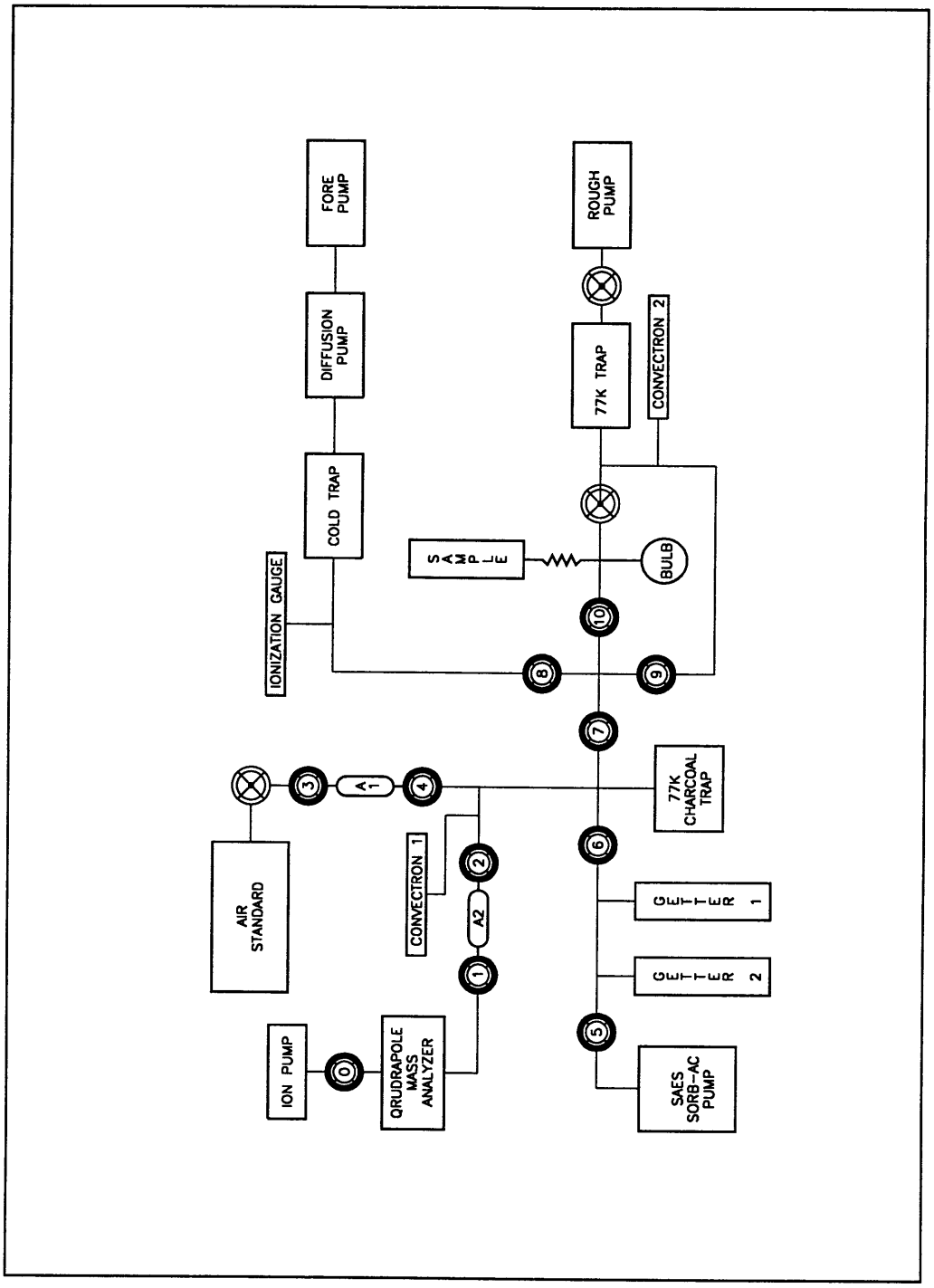

Figure 2.11 The one-gram noble gas processing system. See text for details.

typically less than $5x10^{-4}$ cm^3, which constitutes a volume correction of less than 0.05%. The sample chamber is then mounted on a stainless steel bracket with clamps on either end having gaps of ~0.30" (Figure 2.12), creating a helium leak-tight seal.

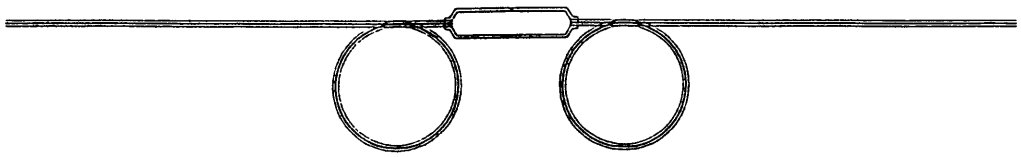

Sample Chamber

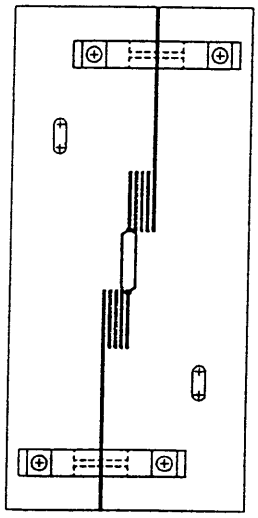

Figure 2.12 A diagram of the sample chamber (upper panel) showing the capillary ends coiled. A top view of the chamber mounted on an extraction mount (lower panel).

The sample is connected to the vacuum system using a 1/16" o-ring compression fitting, and the system is evacuated to less than $5x10^{-8}$ torr. The sample section is isolated from the system, and the lower crimped seal of the capillary tubing is re-rounded using the same procedure as for 13 gram samples. The water is heat-driven into a 25 cc aluminosilicate bulb that is submerged in liquid nitrogen. After the water is in the bulb, the bulb is warmed to a temperature slightly above room temperature to drive the gases into the headspace of the bulb. The bulb is then re-submerged in a dry-ice ethanol slurry to trap the water vapor, leaving the gases in the headspace. The sample is opened to the liquid nitrogen charcoal trap, where Ar is trapped on the charcoal and He and Ne remain in the headspace. The He and Ne are then expanded into the quadrupole and analyzed. After the He and Ne analysis, the liquid nitrogen charcoal trap is warmed to room temperature for several minutes to release the Ar and other gases. The sample is expanded into the getter section and the active gases are removed using two titanium sponge getters and a SAES Sorb-Ac Cartridge pump (ST101 getter material). An aliquot of the remaining gas is expanded into the quadrupole for Ar analysis.

Repeated extractions of the samples demonstrate that the extraction efficiency for the 1 gram procedure is better than 99.7% for Argon, which is the most difficult gas to extract. The samples obtained during the test cruise deployment (see Chapter 4 for details) had signal sizes of approximately $1.1x10^{-11}$ amps for He, $1.9x10^{-11}$ amps for Ne, and $1.6x10^{-10}$ amps for Ar. These signals are approximately 4-5 orders of magnitude above the detection limit for the system. The ratio between the sample signals and the system blank

signals are approximately $\frac{37}{1}$ for He, $\frac{125}{1}$ for Ne, and $\frac{1040}{1}$ for Ar. This trend reflects the relative solubilities of the gases in water, and the diffusion rate of the gases into the system through the o-ring in the compression fitting.

Chapter 3

The Effects of Gas Exchange and Air Injection Processes on Seasonal Dissolved Gas Cycles

3.1 *Introduction*

The net exchange of gases between the upper ocean and the atmosphere has often been interpreted as being driven by the gradient that is established by the saturation of the gas in the water relative to its atmospheric equilibrium concentration. Saturations of the gases in the upper ocean may be modified by biological and chemical processes, mixing, radiative heating, interactions with ice, and injection of bubbles from breaking waves. The dynamic interactions of these processes can lead to *steady-state* supersaturations of the gases in the surface water, implying zero net flux of the gases between the upper ocean and atmosphere despite the existence of a saturation gradient. In order to constrain the processes controlling the cycles of biogeochemically important gases such as O_2 and

CO_2, and thereby infer rates of biological activity in the upper ocean or the uptake of radiatively important "greenhouse" gases, the inert gases are often used to constrain the physical processes affecting gas saturations (Jenkins and Goldman, 1985; Craig and Hayward, 1987; Spitzer and Jenkins, 1989; Emerson et al., 1995; Schudlich and Emerson, 1996). In these studies, the concentrations of the dissolved gases are sensitive to the parameterizations of gas exchange and air injection, and these processes are often the largest source of uncertainty in the models (Musgrave et al., 1988). While air injection from breaking waves occurs only sporadically, surveys of dissolved inert gases in the upper ocean from large hydrographic programs such as GEOSECS and WOCE show that the saturations of these gases exist in a "dynamic equilibrium" with the atmosphere and are supersaturated over large space and time-scales. Because the solubilities of He and Ne are not strongly dependent on temperature, the persistent supersaturations of these gases indicate that air injection plays a role in determining the long-term, steady-state saturations of gases in the upper ocean. However, Farmer et al. (1993) and Wallace and Wirick (1992) found that the parameterizations of gas exchange typically used considerably underestimate the flux of gas during storm events, as inferred from rapid temporal changes in dissolved gas concentrations or partial pressures. Several recent parameterizations of air-sea gas exchange and air injection processes have been proposed (Wanninkhof, 1992;Woolf, 1993; Keeling, 1993), but have yet to be extensively compared to observational data from the open ocean.

The purpose of this study is to investigate the effects of air-sea gas exchange processes on the concentrations of the dissolved gases over seasonal time-scales. It is over these time-scales that the biogeochemical cycles of dissolved gases are of most interest. I use a 2 year, approximately monthly time-series of He, Ne, and Ar, and an adaptation of the Spitzer and Jenkins (1989) 1-D upper ocean bulk mixed layer model to evaluate and constrain several of the current gas exchange and air injection parameterizations, and to quantitatively estimate the effects of vertical mixing, air injection, gas exchange, and bubble trapping modes on the seasonal cycles of the dissolved gases. The model of Spitzer and Jenkins (1989) has been improved in several ways (as discussed in more detail in Section 3.3):

- Neon data has been included, which provides a stronger constraint on the fractions of complete and partial bubble trapping.
- The model is forced using synoptic winds from NCEP data (Kalnay et al., 1996) over the time-period of the noble gas sampling, rather than climatological winds.
- The air injection formulation has been improved by using the air injection parameterization of Monahan and Torgersen (1991)
- The model was run separately using two formulations (Wanninkhof (1992) and Liss and Merlivat (1986)) of the piston velocity of a gas as a function of wind speed, and the effects of the two formulations are compared

- More features of the gas cycles are used to constrain the processes controlling the cycles
- An improved procedure for solving the linearized constraint equations for the necessary parameters is used.

3.2 *Data*

Water samples were taken on a monthly basis between April 1985 and April 1988 at Station S, located 25 kilometers southeast of Bermuda (32 °N 64 °W). Measurements of He and Ar were made for the entire series, while Ne measurements were made only for the last 2 years of the series. The sample profiles extend from the surface to 2700 m, with approximately 10 meter resolution in the upper 100 m. For a thorough review of the sampling details and hydrography of Station S, the reader is referred to Spitzer (1989). In brief, the 35 year hydrographic record at Station S provides a robust framework for interpretation of the seasonal cycles of the dissolved gases. The station is within the tight recirculation region of the North Atlantic subtropical gyre (Worthington, 1976), which tends to homogenize the tracer distributions over a large area. In addition, the area exhibits approximate closure for annual cycles of heat flux (Woods and Barkmann, 1986), and advective features do not appear to significantly bias the seasonal cycles of the dissolved gases, thus making this an appropriate site for application of a 1-D vertical mixing model (Musgrave et al., 1988). A two or three year time-series should be sufficient to resolve the seasonal cycles of the dissolved gases from the influences of mesoscale eddies or cold core rings in the area (Frankignoul, 1981), although longer-term

(decadal) variations are significant (e.g. Jenkins, 1982; Jenkins and Goldman, 1985). The mixed layer concentrations of the dissolved gases respond on the time-scales of gas exchange over the mixed layer, which range from several days in summer, to several weeks in winter.

The 1986-1988 temperature, mixed-layer depth, and gas data are shown in Figures 3.1-3.6. The temperature cycle in the upper ocean is characterized by deep convection in the winter, followed by stratification in the spring and erosion of the seasonal thermocline in the fall. This cycle can be seen more clearly in the seasonal evolution of the mixed-layer depth, shown in Figure 3.2. The mixed-layer depth is defined here as the depth at which the temperature is more than 0.5 °C cooler than the average temperature in the upper 15 meters. While the summer "thermal" mixed-layer depth may shoal above 15 meters over short (~ day) time-scales due to diurnal warming, the defined 15 meter minimum is a realistic mixed-layer depth over the ~week-long time-scales that affect the dissolved gases. The mixed-layer cycle shows the seasonal stratification of the water column resulting from thermal forcing, with deep (>200 meter) mixed-layers in the winter, and rapid shoaling and erosion of the summer mixed-layer depth in the spring and fall.

The Ar concentration cycle (Figure 3.3) is qualitatively similar to that of temperature, due to the strong solubility temperature dependence of Ar, which leads to smaller concentrations in the summer, and larger concentrations in the winter. Comparison of the Ar concentration cycle with the saturation anomaly cycle shown in Figure 3.4 illustrates

the relative influences of thermal effects, mixing, and gas exchange processes on the seasonal evolution of Ar. The concentrations of Ar are highest in the winter due to the increased solubility of Ar at lower temperatures. As the surface water temperature increases in the spring and summer, these winter equilibrium concentrations of Ar become supersaturations in the warmer water. Gas exchange can remove only a fraction of the excess gas, and the supersaturations of Ar persist throughout the summer, even though the concentrations of Ar decrease. Similarly, below the summer mixed-layer, vertical mixing can remove only a fraction of the supersaturations produced by radiative heating, leading to large supersaturations of Ar in the seasonal thermocline. In the fall and winter, as radiative heating decreases, the shallow summer mixed-layer is eroded and the water column is mixed. The Ar concentrations in the water column are rapidly "reset" to near-solubility equilibrium by outgassing and equilibrating with the atmosphere.

The seasonal cycles of He and Ne are not strong functions of radiative heating, and respond more strongly to air injection processes. Figures 3.5 and 3.6 show the saturation anomalies of He and Ne in the mixed-layer. In general, the saturation anomalies of He and Ne are largest in the fall and winter, when air injection is dominant, although there is considerable variability in the strength and timing of air injection processes from year to year. The saturation anomalies of He and Ne show the same general trend for 1986-1988, with lower values in 1986, followed by a maximum in the winter of 1987, and decreasing throughout the summer.

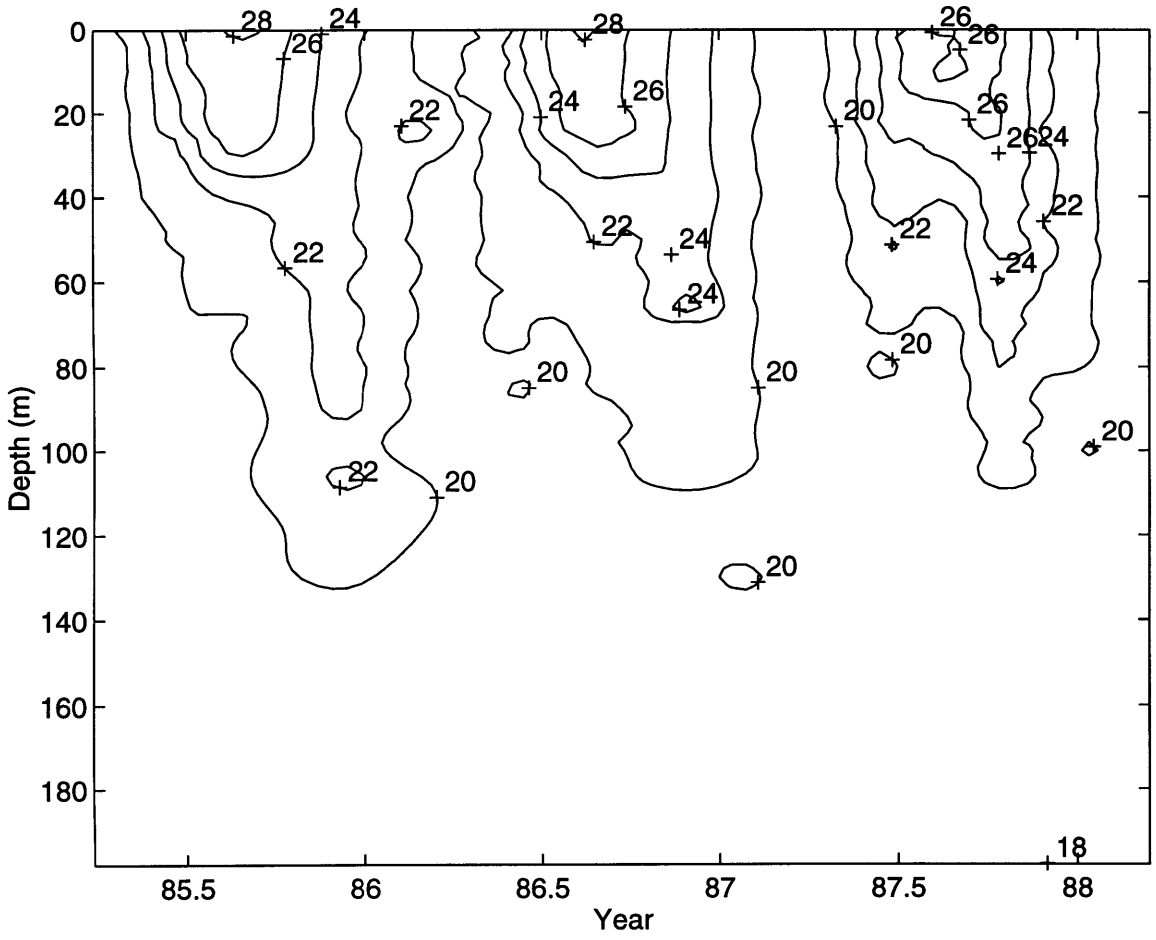

Figure 3.1 Upper ocean temperature cycles from Station S. Temperature contours are in °C.

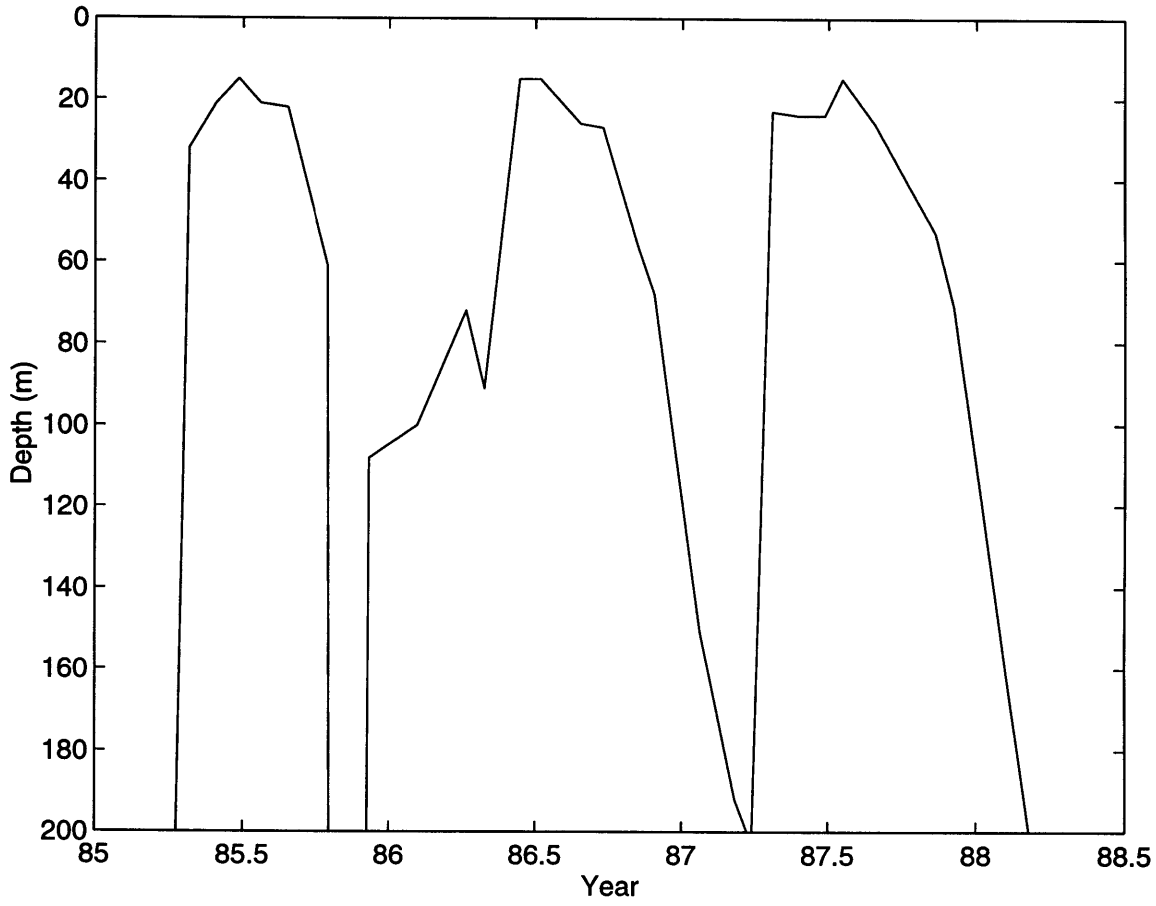

Figure 3.2 Upper ocean mixed-layer depth from Station S. The mixed-layer depth was defined as the depth at which the temperature decreased by ≥ 0.5 °C from the average temperature of the upper 15 meters.

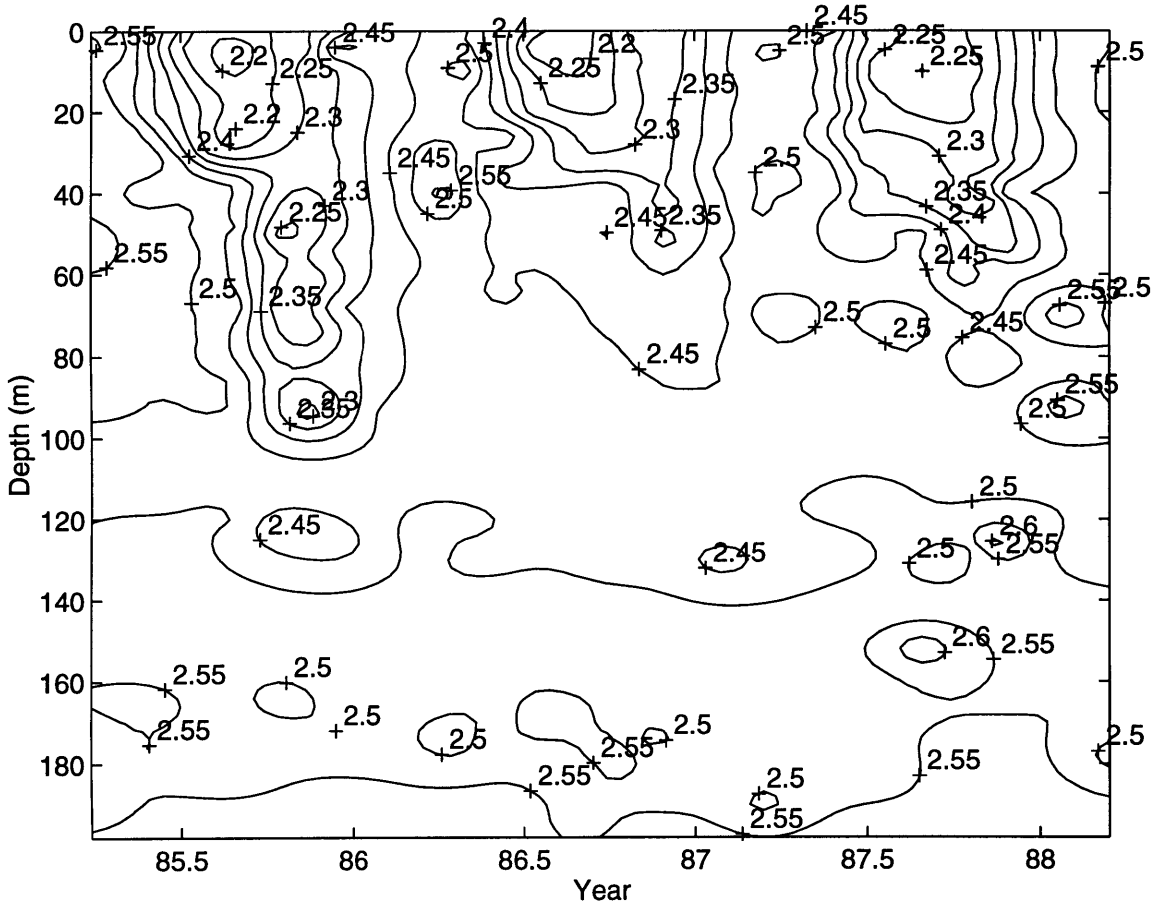

Figure 3.3 Argon concentrations in the upper ocean from Station S. Contours are in 10^{-4} cc (STP) g^{-1}.

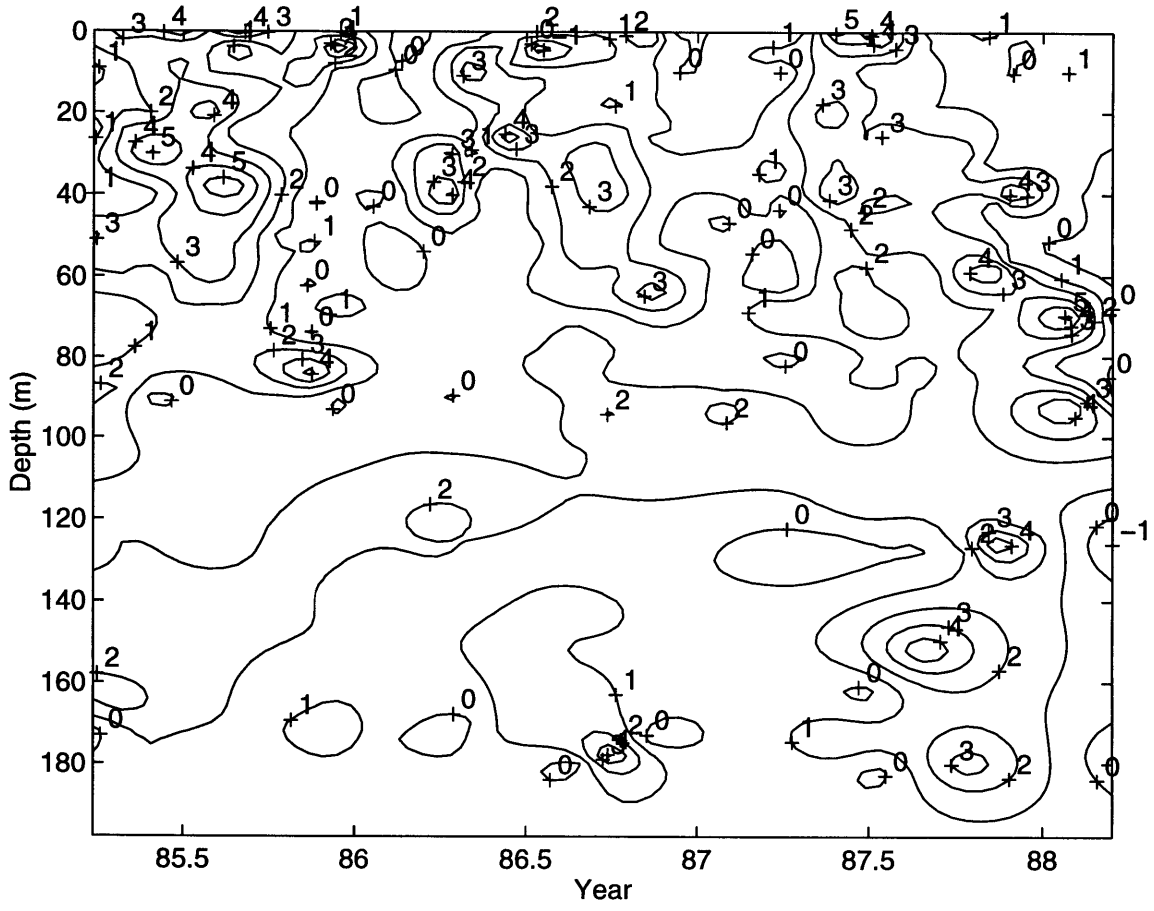

Figure 3.4 Argon saturation anomalies (deviation from solubility equilibrium in %) in the upper ocean from Station S.

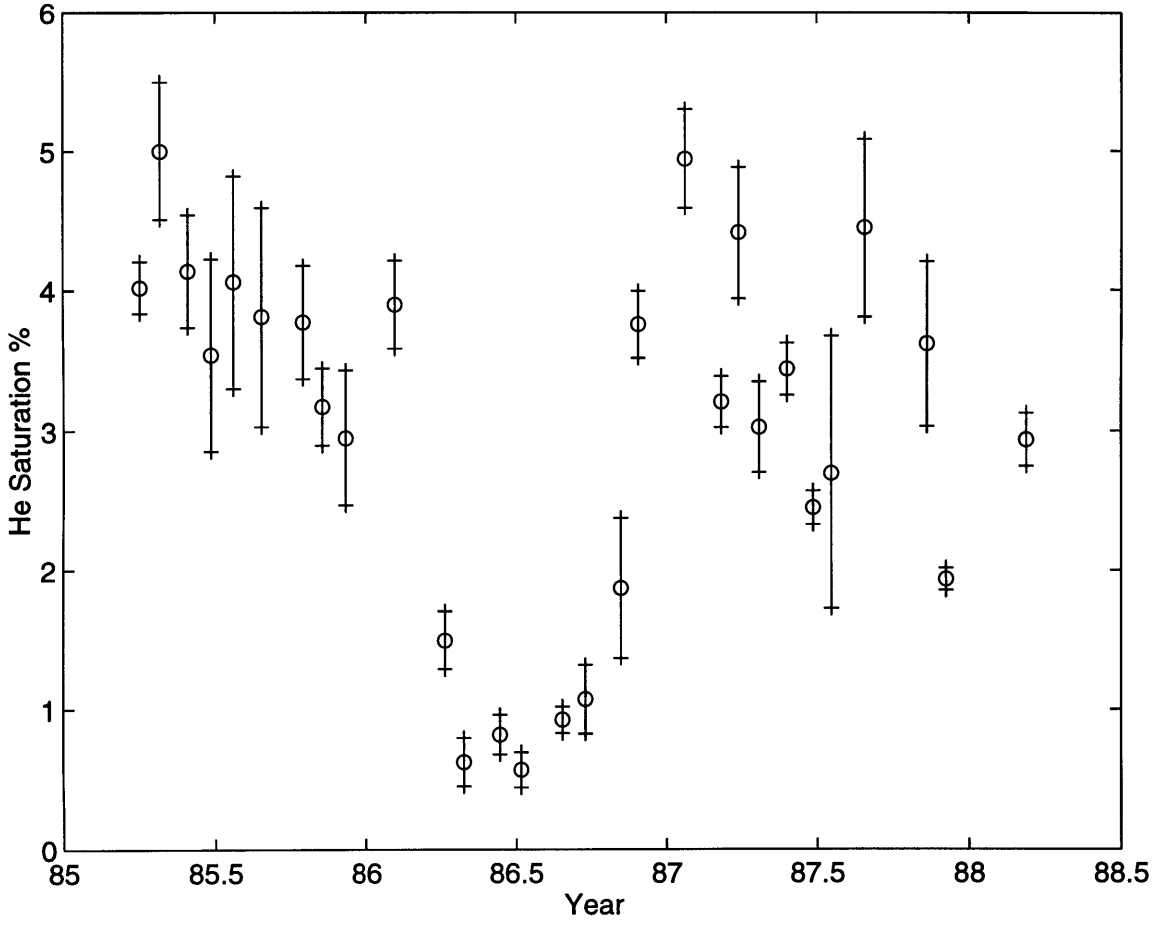

Figure 3.5 Mixed-layer He saturation anomalies (%) at Station S. The uncertainties are the standard deviations from the mean for the samples in the mixed-layer at each sampling date.

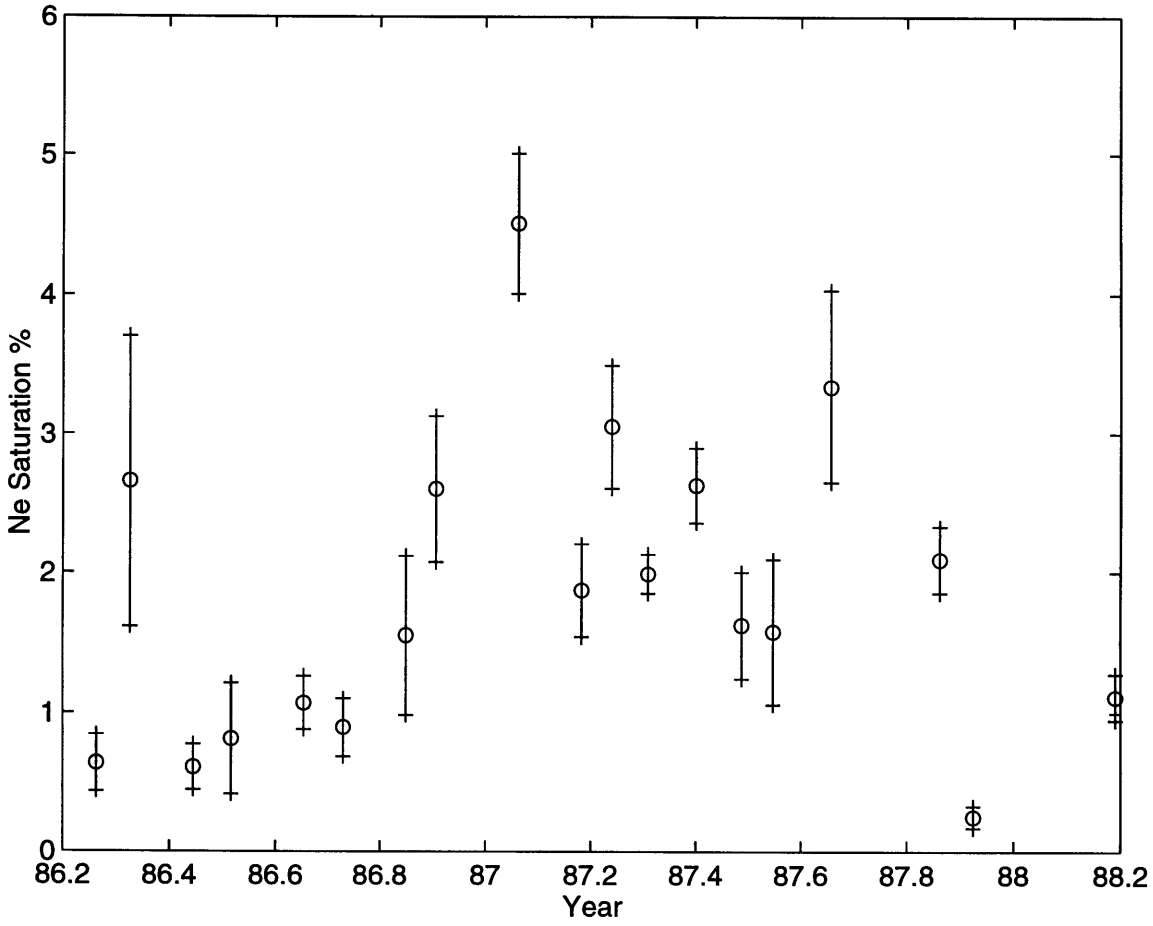

Figure 3.6 Mixed-layer Ne saturation anomalies (%) at Station S. The uncertainties are the standard deviations from the mean for the samples in the mixed-layer at each sampling date.

I use wind speed data from NCEP (Kalnay et al., 1996; S. Doney, pers. comm.) for the Bermuda area (E 63.75° , N 31.4281°) over the time-span of the data. The wind speeds are 6 hourly averages (4 points/day), and are interpolated onto the time-grid of the model (3-4 hours).

3.3 *The Model*

I use an adaptation of the Price et al. (1986) model to simulate the physical processes in upper ocean, with additional parameterizations for gas exchange and air injection similar to those of Chou (1985), Musgrave et al. (1988) and Spitzer and Jenkins (1989).

The Price et al. (1986) model (hereafter referred to as the PWP model) is a one dimensional vertical mixing model designed to simulate the diurnal thermal cycle, and is driven by surface fluxes of heat and momentum. This model has been shown to successfully simulate the seasonal temperature cycle at Station S (Chou, 1985; Musgrave et al., 1988), and simulates diurnal and seasonal cycles as well as or better than most turbulence closure models (Musgrave et al., 1988; Martin, 1986). The model is forced at the surface with heat exchange and wind stress, and the vertical structure is adjusted using vertical mixing predicted by several stability criteria. The static stability criterion is imposed by requiring that the density of the water column increases with depth :

$$\frac{\partial \rho}{\partial z} > 0 \qquad (3.1)$$

where ρ = density, and z = depth (z positive downward).

The dynamic stability criteria include mixed-layer stability, determined by the bulk Richardson number, and shear flow stability, determined by the gradient Richardson number. If the velocity shear at the base of the mixed layer created by the acceleration due to wind stress becomes too great for stability, the mixed layer deepens. This stability requirement is given by:

$$R_b = \frac{g \cdot h \cdot \Delta\rho}{\rho \cdot \Delta v^2} \geq 0.65 \tag{3.2}$$

where g is the gravitational acceleration, h is the thickness of the mixed layer, $\Delta\rho$ is the density contrast between the mixed layer and the underlying water, and Δv is the difference in the horizontal velocity between the mixed layer and the underlying water. The empirical constant, 0.65, has been determined experimentally, and shown to be applicable over a large range of conditions in the ocean (Price, 1979; Price et al., 1978). The shear flow stability criterion, given by:

$$R_g = \frac{g \cdot \frac{\partial\rho}{\partial z}}{\rho_0 \cdot (\frac{\partial v}{\partial z})^2} \geq 0.25 \tag{3.3}$$

determines the point at which the velocity gradient between layers at the base of the mixed layer exceeds the value for stability. This mixing tends to blur the transition between the mixed layer and the water below, creating a more realistic transition zone at the base of the mixed layer.

During periods of net heat loss, the free convection (static stability) is the dominant mixing process, whereas periods of net heat gain are dominated by wind mixing. Over seasonal cycles, static instability is greatest during the cooling part of the cycle due to net heat loss at the surface and convective mixing. During the summer months when the water surface experiences net heat gain and the water column is stably stratified , the shallow mixed layer is strongly influenced by wind stress, and the mixing is dominated by shear instabilities.

The PWP model simulates these upper ocean mixing processes in the following manner at each time-step: Solar insolation is applied to the water column using the relation of Kraus (1972), heat is added or removed from the surface cell, and the fresh water flux is applied. The water column is vertically mixed from the surface downward according to static stability criteria. Wind stress is then applied, and the mixed layer depth is adjusted for dynamic stability.

3.3.1 *Historical Development of PWP Model Used to Simulate Dissolved Gas Cycles*

(i) Musgrave et al. (1988) modified the PWP model to simulate the seasonal cycle of dissolved O_2 at the Panulirus site in the Sargasso Sea. This model calculates the time-dependent *in situ* absorption of solar radiation, turbulent vertical mixing, and surface gas exchange. Vertical eddy diffusivity is added to the model, which is shown to strongly influence the shape of the temperature profile of the model. For gas exchange, a bi-linear

dependence of transfer velocity with wind speed is applied, where the relation of Deacon (1977) is used for wind speeds < 3.9 m/s, and a fit to published field results is used for wind speeds > = 3.9 m/s. The model is run with a tunable parameter for the wind speed dependence to encompass the variability of the published field data. No parameterization was included for air injection processes. The heat flux and wind stress used to drive the upper ocean physics of the model was from the monthly climatology data of Bunker (1976). To simulate stochastic wind events, a 1^{st} order auto-regressive process was superimposed on the climatological cycle that is determined by the monthly averages.

The results of the model predict an annual oxygen production value that is in good agreement with that estimated by Jenkins and Goldman (1985). The results show that the majority of the uncertainty in modeling the seasonal cycle of oxygen is due to the poorly constrained relationship between gas exchange and wind speed. Further, they suggest that the near-surface concentration of oxygen could be largely determined by air injection processes. This model also pointed out that a balance exists between stochastic wind events and turbulent vertical diffusivity for determining the near-surface mixing rates.

(ii) Spitzer and Jenkins (1989) built upon the PWP model and the modifications of Musgrave et al. (1988) by using the gas exchange parameterization of Liss and Merlivat (1986), and by including a simulation of air injection processes. The flux from bubbles (given here in m^3 (STP) m^{-2} s^{-1}) was simulated using:

$$F_i = \alpha_i \cdot a_{inj} \cdot (f_t + \Gamma f_p) \cdot 6 \times 10^{-8} \cdot (\frac{u_{10}}{10})^{\gamma} \quad (3.4)$$

where α_i is the mole fraction of the gas in the air, a_{inj} is a tunable parameter for air injection amplitude, u_{10} is the wind speed at 10 m above the sea surface, γ is a tunable wind speed exponent, and f_t and f_p are complete and partial trapping modes, respectively (see Chapter 1). The air injection flux is normalized to that of helium at 20°C, using:

$\Gamma = (D_i / D_0)^{2/3}$

where D_0 is the molecular diffusivity of helium at 20°C. This relation describes the diffusivity dependence of transport across a "dirty" bubble boundary layer given by Levich (1962). This normalization factor is employed to eliminate the necessity of modeling the complex hydrodynamic parameters that also affect the flux of gases across the bubble boundary layer (see Keeling, 1993; Woolf, 1993; Woolf and Thorpe, 1992). By using ratios of gases, it is not necessary to describe these effects, since the gases will all experience the same forcings and those terms cancel in the equations. (see chapter 1 for details). Further, by normalizing the gas flux to helium and also tuning the fraction of partial trapping to match the helium saturations, the fluxes of other gases can be determined. In essence, the tunable parameter for the air injection amplitude is used to set the amplitude of the model He saturation anomaly to match the observations, and then the saturation anomalies of the other gases are simulated by their relation to He using the normalization procedure in the bubble flux parameterization.

Seasonal averages of gas exchange rates determined from the model appeared to be in good agreement with the Liss and Merlivat (1986) formulation of gas exchange, and the estimates of the rate of bubble trapping and the wind speed dependence of this rate seemed consistent with other estimates (Thorpe, 1984; Thorpe, 1986). However, due to poorly constrained estimates of complete versus partial trapping fractions that resulted from being limited to measurements of He and Ar only, the model predicts an unphysical, negative complete trapping fraction (average = -0.5±0.1). By adding an additional constraint that all solutions be non-negative, the results for other factors are not substantially changed, and the fraction of complete trapping is forced to zero. While this is most likely not a realistic representation of the air injection process, the model provides reasonable estimates of the seasonal gas cycles in temperate regions with moderate wind regimes. For example, the model of Spitzer and Jenkins (1989) predicts the seasonal cycles of N_2 and Ar from the ALOHA site reasonably well, except at periods of high supersaturations observed in the fall (Schudlich and Emerson, 1996). In areas of high wind speeds and over shorter time-scales, however, the Spitzer and Jenkins model fails to reproduce the observations (Wallace and Wirick, 1993).

(iii) Schudlich and Emerson (1996) used the PWP model and recent parameterizations of gas exchange and air injection to study the effects of heat flux, gas exchange, and bubbles on the concentrations of N_2 and Ar at two locations in the Pacific. For gas exchange, they used the relation of Liss and Merlivat (1986), and used the Keeling (1993) formulation for the injection of small bubbles that dissolve completely. The effects of larger bubbles

were not modeled. The model predicted the observations of the gas cycles reasonably well during the summer months, while the fall and winter observations were substantially underpredicted, possibly due to the assumption that all air injection is due to complete trapping of bubbles. This work illustrated the necessity of bubble processes to interpret the observations of seasonal dissolved gas cycles, and the need for parameterizations of air injection processes that more completely describe the combination of complete and partial trapping effects.

3.3.2 *The Model Used in this Study*

I have modified the model of Spitzer and Jenkins (1989) in several important ways to improve the simulation of the seasonal cycles of the dissolved gases:

- *Neon Data* - Neon data for 1986-1987 is incorporated into the analysis and model simulation, which provide powerful constraints on the bubble trapping fractions and air injection processes.
- *Synoptic Wind Data from the National Centers for Environmental Prediction* - Climatological wind speed data used in the previous model was replaced with synoptic wind data from NCEP for the Bermuda area, which is important for the magnitude and timing of gas exchange and air injection events, as well as for the influences of wind-stress on the momentum balance of the upper water column. The NCEP wind speed data is, on average, approximately 30% lower than the climatological data used by Spitzer and Jenkins (1989).

- *Air Injection* - An improved air injection parameterization is used (Monahan and Torgersen,1991), which relates the volume flux of air injected into the water to fractional whitecap coverage (via wind speed), eliminating the variable exponential wind speed dependence of the previous model.
- *Gas Exchange* - The gas exchange formulation of Wanninkhof (1992) is used, which may be more appropriate for open ocean gas exchange rate determinations. The model is also run using the formulation of Liss and Merlivat (1986) for comparison.
- *Additional Constraint Equations* - More features of the dissolved gas cycles are used to constrain the processes of air injection, gas exchange, bubble trapping mode, and vertical mixing that control the gas cycles.
- *Improved Linearization Techniques* - I use a regression technique (singular value decomposition) to solve for the *coefficients* of the variables in the linearized equations relating the seasonal features of the gases to the four tunable variables controlling those features, and use this technique again to solve for the values of the *variables* that provide the best fit, in a least-squares sense, of the behavior of the chosen feature to the controlling processes

Description of Specific Model Features

(i) Air injection and gas flux from bubbles - The volume of air injected into the water can be described using the relation proposed by Keeling (1993):

$$V_{air} = V_A W_A$$

where V_A is the air entrainment velocity having a global average of ~ 0.01 m/s at wind speeds of 10 m/s (Erickson et al., 1986; Monahan and Torgersen, 1991; Keeling, 1993), and W_A is the fractional surface area covered by whitecaps (units = %), and is taken from the formulation of Monahan and Torgersen (1991):

$$W_A = 1.85 \times 10^{-6} (U_{10} - 2.27)^3$$

W_A is taken to be zero for wind speeds less than or equal to 2.27 m/s. Thus, the volume of air entrained as a function of wind speed becomes:

$$1.9 \times 10^{-2} \ (U - 2.27)^3 \qquad \text{cc (STP) } m^{-2} s^{-1}$$

For wind speeds less than 2.27, the air injection flux is set to zero. Using these parameterizations, the gas flux from bubbles is given by:

$$F_i = \alpha_i \cdot P_{cf} \cdot A_{inj} \cdot (1.9 \times 10^{-2} \cdot (U - 2.27)^3) \cdot (f_t + \Gamma f_p) \qquad (3.5)$$

where α_i is the mole fraction of the gas in air, P_{cf} is the barometric pressure correction factor for the gases in air relative to 1 atmosphere (1013.15 mb), taken from the Oberhuber climatology (Oberhuber, 1988), and A_{inj} is a dimensionless, variable air injection parameter used to adjust V_A, and is varied between 2 and 8 in the model.

The boundary condition for gas flux across a bubble surface due to partial trapping of bubbles is given for a gas "*i*" by:

$$\Gamma = D_i^{2/3} / D_{He}^{2/3}$$

where the denominator is the normalization to He (see discussion earlier in this chapter). I have modified this normalization factor used by Spitzer and Jenkins (1989) to normalize the flux to helium at the temperature for each time-step. As stated in Chapter 1, the true flux from bubbles will be a function of some power of the diffusivity, and inversely proportional to some power of the solubility, as expressed in other works (Keeling, 1993; Woolf, 1993). However, what I model here is the *end-member* condition for gas flux across the bubble boundary layer for partially trapped bubbles, and then model the total flux of gases from bubbles as a linear combination of the processes of complete and partial trapping.

(ii) Surface Forcing - The heat flux used to force the model is taken from the climatological monthly averages of Oberhuber (1988). The radiant heating values (also from the Oberhuber climatology) are used with a Jerlov type IA absorption curve (Paulson and Simpson, 1977). The fresh water flux used is an adaptation of the Oberhuber climatological values modified to achieve annual closure of the salt budget. Wind stress and wind speed data are from NCEP (Kalnay et al., 1996) for the Bermuda area (E 63.75° , N 31.4281°) over the time-span of the data. The wind speeds are 6 hourly averages (4 points/day), and are interpolated onto the time-grid of the model (3-4 hours).

(iii) Model Procedure Steps - The model is started in mid-March, when the water column is most uniform, and the gases initially held at solubility equilibrium with the

atmosphere. At each time-step, heat flux and fresh water flux are applied, radiant heating is added to the profile, and adjustments are made to maintain static stability. The wind stress - induced momentum is applied, and the bulk Richardson number adjustment is made. Gas exchange and bubble injection effects on the concentrations of the gases are then calculated, and the gradient Richardson number adjustment is made. Finally, the properties are advected and diffused vertically in the water column.

(iv) Model Variables - The model has 4 "tunable" variables: turbulent vertical diffusivity (K_z), air injection amplitude, gas exchange rate, and the fractions of complete and partial trapping. In the model, K_z was varied between 0.75×10^{-4} and 1.5×10^{-4} m^2 s^{-1}. The simulation of the seasonal cycles of the mixed layer requires time-steps that are capable of resolving the solar heating cycle (Woods and Barkmann, 1986) as well as the inertial period of the horizontal velocity vector (Musgrave et al.,1988). The time-step for the model is a function of the K_z used to maintain stability criteria based on von Neumann stability analysis, and varies between 3 and 6 hours over the range of K_z used. The vertical grid for the model is from the surface to 300 meters, with a resolution of 2 meters. This grid spacing provides adequate resolution of the mixed-layer at the summer minimum of approximately 15 meters, and in general, the spatial scale of the behavior of the dissolved gases is large relative to the chosen grid spacing (Musgrave et al., 1988).

3.4 *Model Application*

Quantitative agreement between the observations of the seasonal cycles of the dissolved gases and those simulated by the model depends critically on the values of these tunable variables. It is the value of each of these variables that is of most interest for understanding the nature of the processes controlling gas cycles in the upper ocean. The approach used to determine the value of these 4 tunable variables consists of four steps (discussed in more detail later in this section):

1. *Identification of diagnostic indices* - Specific aspects of the temperature and gas cycles are strongly controlled by one or more of the variables, making these features of the gas cycles useful diagnostics of the relative strengths of the variables required to produce the observations. The use of specific features of the gas cycles rather than just the annual average behavior of the gases provides an overdetermined system of 14 equations that are used to constrain 4 unknowns.
2. *Running the model over the appropriate ranges of the variables* - Preliminary model runs are used to examine the influence of each variable (Kz, air injection, gas exchange, and bubble trapping fraction) on the gas saturations, and then the range of each variable that creates a good bracket of simulated values around the observed values is chosen. The model is then run over the range of appropriate values.
3. *Linearization of the relations between the variables and the indices* - To quantify the relation between the variables and a specific feature of the gas cycles, a linear equation is constructed for each feature and variable set from the model simulations,

and the set of linear equations is solved for the coefficients of the variables using singular value decomposition.

4. *Solving the set of linearized equations for the variables-* Using the coefficients that describe the behavior of each feature to the variables, a second set of linear equations is constructed from these coefficients and the actual data observations, and singular value decomposition is used to solve for the magnitude of the variables that best fit the data.

3.4.1 *Identification of diagnostic indices*

Sample model runs were used to qualitatively examine the influence of the air injection, gas exchange, bubble trapping mode (complete *vs* partial bubble trapping), and turbulent diffusivity on various aspects of the gas and temperature cycles. Because the noble gases have a wide range of solubilities, solubility temperature dependencies, and diffusivities, the saturations of the gases are controlled to varying degrees by the processes forcing the system, and can thus be used to resolve the relative strengths of these processes. Deviations from solubility equilibrium result from the imbalance between the various processes of air injection, gas exchange, radiative heating, and vertical mixing. In general, air injection will increase the saturations of the gases in the mixed-layer, while gas exchange acts to restore equilibrium. Radiative heating will increase the saturations of the gases according to their solubility temperature dependence. Because the upward flux of gases from below the mixed-layer has a much smaller effect on the mixed-layer saturations than the other processes, changes in K_z do not greatly affect the mixed-layer

saturations. The interplay of these effects can be seen in model simulations of the seasonal cycles of He, Ne, and Ar, which are shown in Figures 3.7-3.9. In the winter, air injection processes increase the saturations of He and Ne in the mixed-layer more rapidly than gas exchange can act to restore equilibrium, resulting in persistent supersaturations. Because of its higher solubility and lower diffusivity, Ar is not as strongly affected by air injection processes. During the spring and summer, the imbalance between strong radiative heating and gas exchange leads to supersaturations of Ar, while He and Ne are less affected due to their lower solubility temperature dependencies. The real strength of using the three noble gases is in the ability to differentiate between these forcing processes. For example, increased air injection and lower gas exchange rates both act to increase the saturations of the gases in the mixed-layer, and would be indistinguishable using only one gas, or a suite of gases that responded to these effects in similar ways. However, He and Ne are more sensitive to air injection processes, whereas Ar is not particularly sensitive to air injection, but is instead controlled more strongly by gas exchange and radiative heating. Specific features of the seasonal gas and temperature cycles (hereafter referred to as "indices") are sensitive indicators of the controlling processes, and can be used to resolve the relative influences of each process.

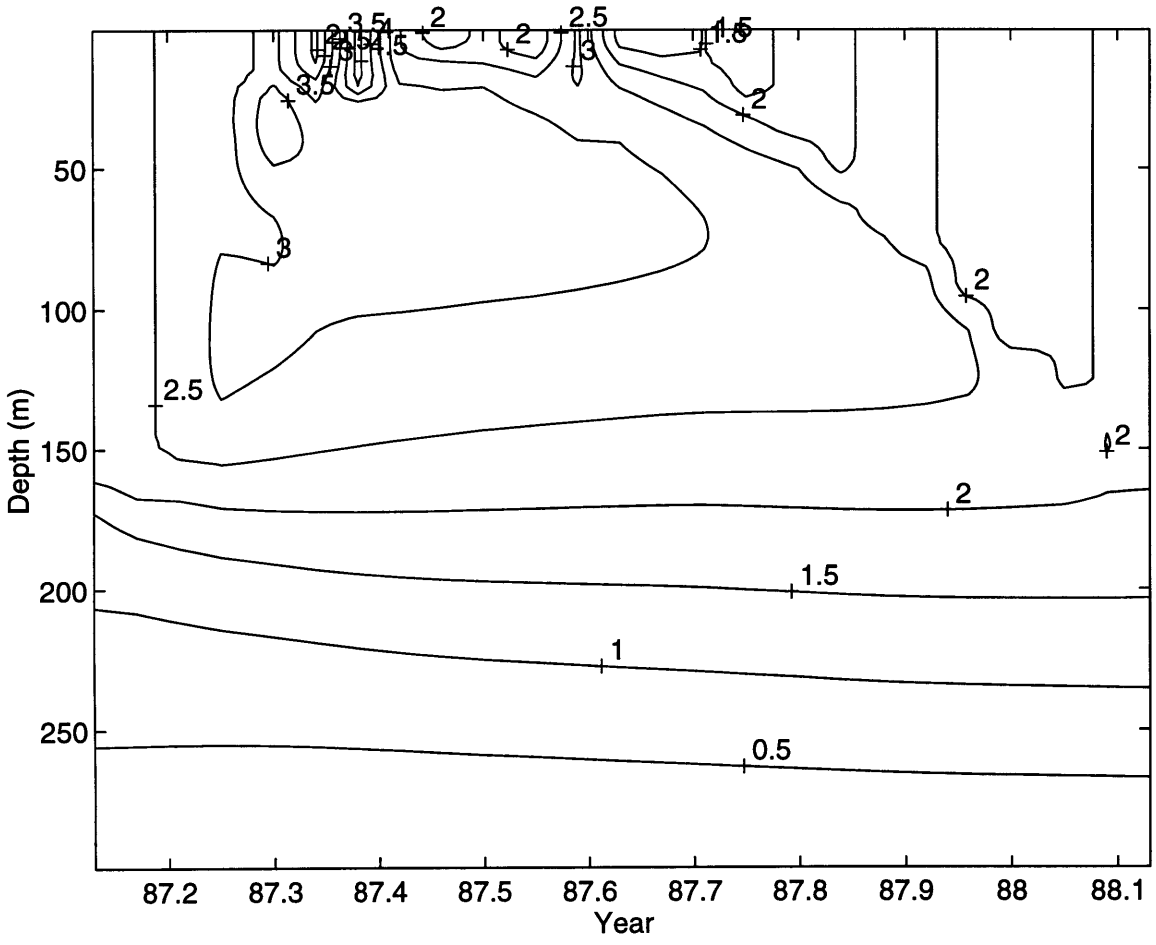

Figure 3.7 Simulation of the seasonal cycle of He saturation anomalies (%) for 1987 using values of air injection, gas exchange, K_z, and bubble trapping fractions calculated from the weighted mean of the inversion solutions from 1986 and 1987.

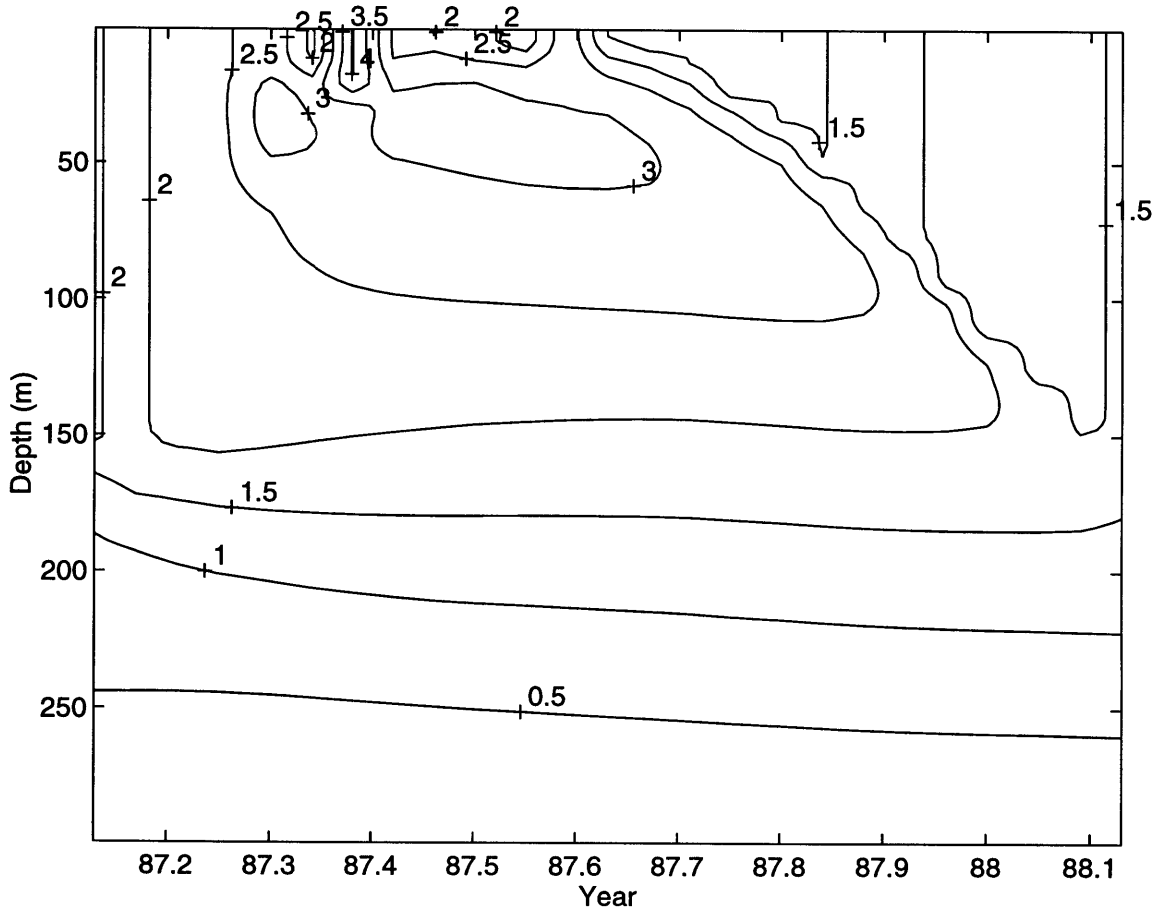

Figure 3.8 Simulation of the seasonal cycle of Ne saturation anomalies (%) for 1987 using values of air injection, gas exchange, K_z, and bubble trapping fractions calculated from the weighted mean of the inversion solutions from 1986 and 1987.

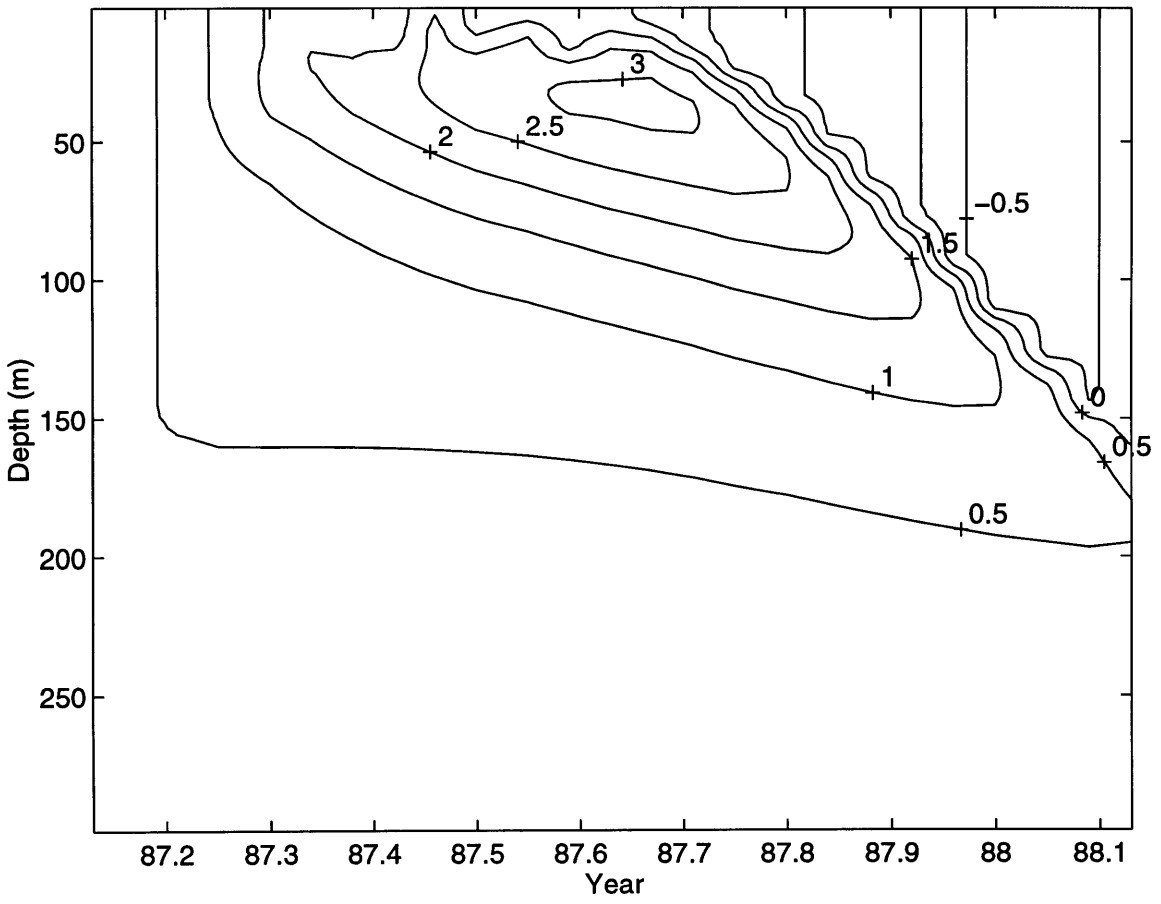

Figure 3.9 Simulation of the seasonal cycle of Ar saturation anomalies (%) for 1987 using values of air injection, gas exchange, K_z, and bubble trapping fractions calculated from the weighted mean of the inversion solutions from 1986 and 1987.

For this analysis, a set of 14 indices were chosen to constrain the magnitudes and interactions of the 4 tunable processes that control the seasonal cycles of the dissolved gases. A larger set of approximately 20 indices was initially chosen, and the weaker constraints were removed until there was a significant change in the inversion results. The values of the indices from the data for 1986 and 1987 are shown in Table 3.1.

	1986	**1987**	
T_{ml} [s - w]	7.06 ± 0.04	8.00 ± 0.01	°C
ΔAr_{max} [s]	4.1 ± 0.2	5.4 ± 0.2	%
ΔAr_{ml} [s]	1.5 ± 0.3	1.4 ± 0.2	%
ΔAr_{ml} [w]	0.3 ± 0.2	0.2 ± 0.1	%
ΔAr_{ml} [s-w]	1.2 ± 0.4	1.2 ± 0.3	%
ΔAr_{ml} [mean]	0.8 ± 0.2	0.9 ± 0.2	%
ΔHe_{ml} [w]	1.4 ± 0.2	3.2 ± 0.2	%
ΔHe_{ml} [mean]	1.1 ± 0.2	2.5 ± 0.2	%
ΔNe_{ml} [w]	0.7 ± 0.3	1.5 ± 0.2	%
ΔNe_{ml} [mean]	0.9 ± 0.2	1.1 ± 0.2	%
ΔHe_{ml} [w] - ΔNe_{ml} [w]	0.7 ± 0.3	1.7 ± 0.3	%
ΔHe_{ml}[mean] - ΔNe_{ml} [mean]	0.24 ± 0.2	1.4 ± 0.2	%
ΔHe_{ml} [mean] - ΔAr_{ml} [mean]	0.3 ± 0.2	1.6 ± 0.2	%
ΔNe_{ml} [mean] - ΔAr_{ml} [mean]	0.07 ± 0.2	0.16 ± 0.2	%

Table 3.1 Observed indices for 1986-1987. Δ = saturation anomaly (% deviation from solubility equilibrium with the atmosphere), *ml* = mixed-layer, *s* = summer, *w* = winter, and *mean* is the mixed-layer average over the annual cycle. Mixed-layer values are calculated using the weighted mean of values occurring in the specified time period (winter, summer, or yearly mean). Uncertainties are calculated from the uncertainties of the weighted means and measurement uncertainties.

The definitions of "summer" and "winter" are based on the mixed-layer temperatures for each of the two years, and the summer and winter gas saturations are the weighted means of the samples collected during those time-periods. Because the system is over-

determined, a single solution that satisfies all the constraint equations may not exist. The regression technique, singular value decomposition, is used to determine the solution that best fits the data in a least-squares sense. The linearized constraint equations were row-normalized by the total uncertainty of the constraint equations (discussed in detail below). The residuals between the inversion results and the observations for each constraint equation are used as a measure of the agreement between the solution for the system and each equation.

Vertical Mixing - Accurately simulating the thermal cycle is crucial for simulating the cycles of the dissolved gases. The concentrations and saturations of the dissolved gases are driven by the thermal cycle due to the temperature dependence of solubility, but perhaps more critically, the thermal cycle largely controls the depth of the mixed-layer, and it is the mixed-layer depth that determines the volume of water that is in direct contact with the atmosphere. The only tunable variable that affects the temperature cycle is K_z, the turbulent vertical mixing coefficient. Figure 3.10 shows sample model runs of the mixed layer temperature cycle as a function of K_z used in the model, and is shown in relation to the measured mixed layer temperature. When the vertical mixing coefficient is weak, heat becomes trapped near the surface, resulting in surface temperatures that are much warmer than the observed values. Similarly, when K_z is strong, too much heat is removed from the surface, resulting in surface temperatures that are too cold. Therefore, a useful diagnostic index of the vertical mixing coefficient effect on the seasonal temperature cycle is the range of the mixed-layer temperature between summer and

winter. When the model simulations are compared to the observed mixed-layer temperature cycle, it can be seen that the optimal range of K_z for this time-series is between $1x10^{-4}$ and $1.5x10^{-4}$ m^2 s^{-1}.

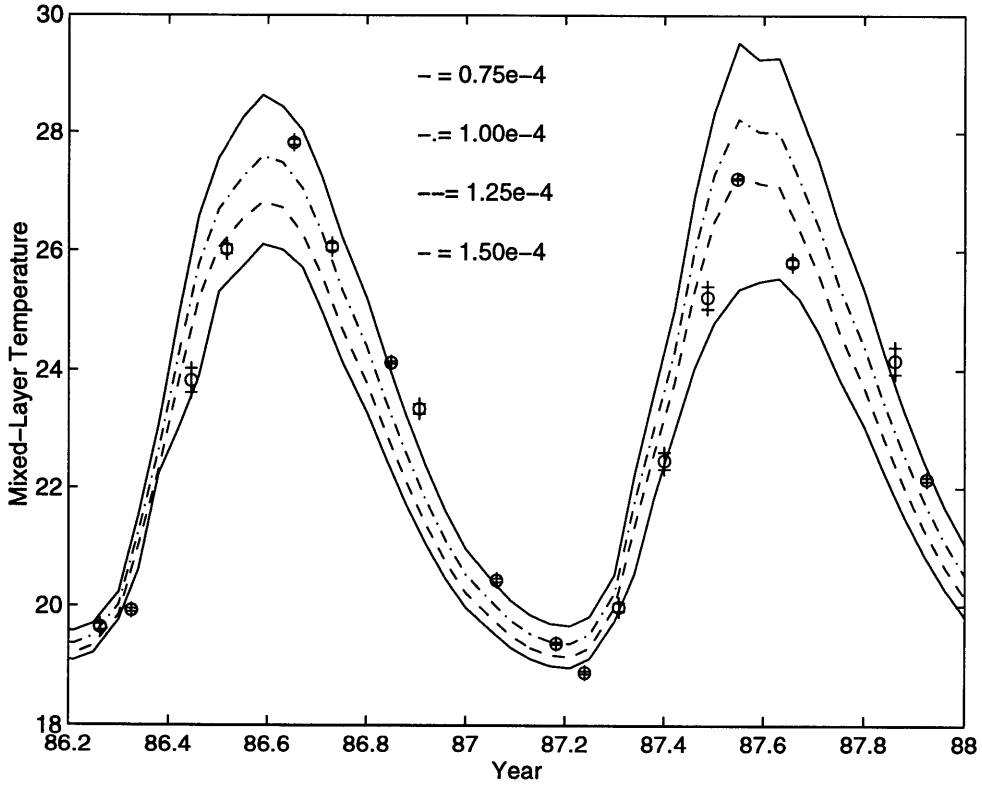

Figure 3.10 Mixed-layer temperature at Station S (symbols), and the seasonal temperature cycles simulated by the W86-W87 simulations with varying K_z: Kz = $0.75x10^{-4}$ (solid top line), Kz = $1.00x10^{-4}$ (dot-dashed line), Kz = $1.25x10^{-4}$ (dashed line), and Kz = $1.50x10^{-4}$ (solid bottom line).

The Ar cycle can also set a marginally useful constraint on vertical mixing. In the summer, the Ar saturation that develops below the mixed-layer is predominantly a balance between radiative heating and vertical mixing. If vertical mixing is too low, the

Ar saturation will become too large. Thus a useful constraint on the magnitude of Kz is the maximum Ar supersaturation below the mixed-layer.

Gas Exchange and Air injection Magnitude - The saturations of gases in the mixed-layer tend to increase proportionally to the air injection rate and inversely to the gas exchange rate, making the control of the diagnostic indices by each process similar, but of opposite sign. Due to the relative response of each gas to air injection and gas exchange, a combination of features of each of the gas cycles can be used to resolve these two processes. For example, the mean mixed-layer saturations of He and Ne are strongly controlled by both air injection and gas exchange processes, whereas Ar is relatively insensitive to air injection, but is strongly controlled by gas exchange. Therefore, the mean mixed-layer saturations of the gases and the differences in the mixed-layer saturations between He-Ar and Ne-Ar provide useful information on the relative strengths of these two processes. Additionally, He and Ne in the winter mixed-layer are predominantly controlled by air injection, while the summer Ar maximum and the summer-to-winter difference in the mixed-layer Ar saturation are strongly controlled by gas exchange.

Bubble trapping fraction - The fractions of complete and partial bubble trapping can be diagnosed by the relative saturations of the three gases, since the *ratios* of the saturation anomalies are predominantly controlled by the relative fractions of complete and partial trapping. The saturations of Ne with respect to He are particularly useful for constraining

this property. Because we have chosen to normalize the total air injection component to He, the saturations of He in the model are independent of the mode of bubble trapping. In a general sense, the tunable air injection variable is used to match the He saturations to the observations, while the mode of bubble trapping determines the saturation ratios of the gases. Thus, the ratios of the gas saturations are useful diagnostics of the mode of bubble trapping. Figure 3.11 shows model simulations of the saturations of He versus Ne in the mixed-layer as a function of bubble trapping fractions (circles = complete trapping, stars = partial trapping), with the values of air injection, gas exchange, and K_z held constant.

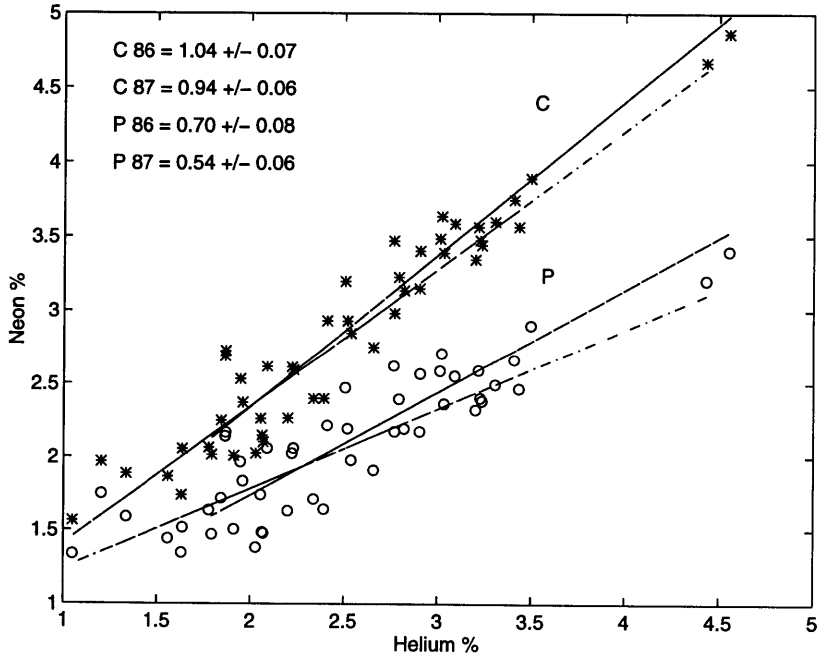

Figure 3.11 Simulations from W86 and W87 of the mixed-layer He and Ne saturation anomalies (%) using 100% complete trapping (C), and 100% partial trapping (P). Stars are the W86 and W87 model values for partial trapping, and circles are the W86 and W87 model values for complete trapping. Lines through the data points are least-squares fits (type 2 linear regression) through the data from 1986 and 1987, where the dashed lines = 1987 simulation results and the dot-dashed lines = 1986 simulation results.

The He-Ne pair offers unique information about the relative fractions of complete or partially trapped bubbles, since Ne is more strongly affected than He by complete bubble trapping (He/Ne <1), while He is more strongly affected than Ne by partial bubble trapping (He/Ne>1). The effects of the two modes are clearly distinguishable, with distinct resolution of the behavior at saturations greater than about 3%. Variations in the slopes of complete and partial trapping between the two years result from changes in wind speeds that drive the air injection parameterization. As shown in the figure inset, the differences in the slopes between the two years are not statistically significant.

3.4.2 *Model Simulations over appropriate ranges for the variables*

After choosing a set of diagnostic indices from preliminary model simulations and the data, ranges for each of the 4 tunable variables were chosen to qualitatively match the observations. The final set of ranges used was determined iteratively by adjusting the variable ranges until the best-fit variable values determined using singular value decomposition were bracketed by the ranges. The set of ranges chosen for the final simulation presented here is:

$$\text{Kz } (\times 10^{-4}\ m^2\ s^{-1}) = [\,0.75 \quad 1.00 \quad 1.25 \quad 1.50]$$

$$\text{Air Injection Multiplier} = [\,2 \quad 4 \quad 8]$$

$$\text{Gas Exchange Multiplier} = [0.5 \quad 1.0 \quad 1.5]$$

$$\text{Fraction Complete Trapping} = [0\% \quad 50\% \quad 100\%]$$

In the preliminary model runs, the air injection multiplier required to match the observed saturations of He and Ne was centered around 4, with values of 2 and 8 bracketing the variations in the annual saturations of the gases. This is consistent with other estimates of the air entrainment velocity (Keeling, 1993) and will be discussed in detail later in this chapter. This set of variable ranges generates 108 (3 x 3 x 3 x 4) separate model simulations that are used to examine the effects of each variable on the chosen diagnostic indices.

3.4.3 *Linearization of the Model Response*

While the exact nature of the relation between a specific feature of the gas cycles and the controlling variables may not be linear, approximating the relations as a linear function introduces very little error over the ranges of the variables used in the simulations, and would simplify the regression techniques required to solve for the variables of interest. The form used here is:

$$Y = a_1X_1 + a_2X_2 + a_3X_3 + a_4X_4 + a_5 \qquad (3.6)$$

where Y is the value of the diagnostic index, X_1-X_4 are the values of the variables over which the model was run, a_1-a_4 are the coefficients of each of these variables, and a_5 is a constant term. For each of the 108 model simulations, the values of the indices generated by the model (Y's) are determined for the given set of the variables (X's) used for each model simulation, and a least-squares regression technique, singular value decomposition, is used to solve the set (108 x 5) of equations to obtain the value of the coefficients of the

variables (a's). These coefficients describe the dependence of each constraint equation on air injection, vertical mixing, gas exchange, and bubble trapping fraction. Because the model is forced by synoptic wind data, the value of the indices generated by the model will be different for each year, and thus the linearization process must be carried out separately for both years of the data set.

Tables 3.2 and 3.3 show the weighted matrices of coefficients for each index from the linearization procedure for 1986 and 1987 using the gas exchange formulation of Wanninkhof (1992). In the tables, the coefficients returned by the linearization process have been weighted (row-normalized) by the reciprocal of the total error of each constraint equation (Tables 3.4 and 3.5). The error introduced by linearizing the model response over the range of variables is determined by calculating the difference in the value of the constraint equation estimated from the linearized equation and the non-linear model simulation for the same set of variables. As can be seen from the tables, the errors introduced by linearizing the equations over the chosen range of the variables are small, and are typically less than the measurement uncertainty of the constraint equations. Tables 3.2 and 3.3 can be used to examine the relative strengths of the individual processes controlling each constraint equation. The values in the tables represent the relative strengths of the variables (columns) in controlling each constraint equation (rows), or conversely, the relative ability of each of the equations to constrain each variable. The set of 14 equations provides a variety of constraints on each variable, and

prevents any particular aspect of the gas or temperature cycles from completely dominating the determination of the parameter.

Constraint Equation	Ainj	F_T	1 / G	1/ K_z
Tml [s - w]	0	0	0	29
ΔAr max [s]	1.2	3.9	5.4	2.5
ΔAr ml [s]	0.8	2.5	4.5	0.1
ΔAr ml [w]	0.9	2.9	-0.3	-3.4
ΔAr ml [s-w]	0.2	0.5	3.9	2.0
ΔAr ml [mean]	1.2	3.9	4.2	1.0
ΔHe ml [w]	2.5	0	9.2	-5.7
ΔHe ml [mean]	3.1	0	12	1.5
ΔNe ml [w]	2.0	3.7	6.5	-4.4
ΔNe ml [mean]	3.1	5.7	12	1.4
ΔHe ml [w] - ΔNe ml [w]	0.08	-3.6	1.1	-0.3
ΔHe ml[mean] - ΔNe ml[mean]	0.05	-6.0	0.6	0.1
ΔHe ml [mean] - ΔAr ml[mean]	2.0	-3.8	8.5	0.5
ΔNe ml [mean] - ΔAr ml[mean]	1.8	1.9	7.6	0.4

Table 3.2 Coefficients of the linearized constraint equations for 1986 model data using the gas exchange formulation of Wanninkhof (1992). The coefficients are weighted by the reciprocal of the total error associated with each constraint equation (see Table 3.4).

Constraint Equation	Ainj	F_T	1 / G	1/ Kz
Tml [s - w]	0	0	0	16
ΔAr max [s]	-2.2	0.8	5.0	5.7
ΔAr ml [s]	0.7	2.2	6.7	1.1
ΔAr ml [w]	0.94	3.2	1.0	3.3
ΔAr ml [s-w]	-0.1	-0.4	6.9	-1.9
ΔAr ml [mean]	1.0	3.2	3.9	1.4
ΔHe ml [w]	2.4	0	10	3.0
ΔHe ml [mean]	3.1	0	12	-4.0
ΔNe ml [w]	2.2	4.2	8.4	3.3
ΔNe ml [mean]	3.0	5.6	12	3.3
ΔHe ml [w] - ΔNe ml [w]	0.04	-4.7	1.0	-0.6
ΔHe ml[mean] - ΔNe ml[mean]	0.02	-5.3	0.21	-0.7
ΔHe ml [mean] - ΔAr ml[mean]	1.6	-3.1	6.5	-4.6
ΔNe ml [mean] - ΔAr ml[mean]	1.6	1.6	6.6	-4.2

Table 3.3 Coefficients of the linearized constraint equations for 1987 model data using the gas exchange formulation of Wanninkhof (1992). The coefficients are weighted by the reciprocal of the total error associated with each constraint equation (see Table 3.5).

Constraint Equation	Measurement Uncertainty	Linearization Error	Total Error	Inversion Residuals
Tml [s - w]	0.04 °C	0.1 °C	0.1 °C	0.03 °C
ΔAr max [s]	0.2 %	<0.1 %	0.2 %	-1.5 %
ΔAr ml [s]	0.3 %	0.1 %	0.3 %	<0.1 %
ΔAr ml [w]	0.2 %	0.1 %	0.2 %	-0.3 %
ΔAr ml [s-w]	0.4 %	0.2 %	0.4 %	<-0.1 %
ΔAr ml [mean]	0.2 %	0.1 %	0.2 %	-0.1 %
ΔHe ml [w]	0.2 %	0.1 %	0.2 %	-0.2 %
ΔHe ml [mean]	0.2 %	<0.1 %	0.2 %	<-0.1 %
ΔNe ml [w]	0.3 %	0.1 %	0.3 %	0.4 %
ΔNe ml [mean]	0.2 %	0.1 %	0.2 %	0.3 %
ΔHe ml [w] - ΔNe ml [w]	0.3 %	<0.1 %	0.3 %	-0.6 %
ΔHe ml[mean] - ΔNe ml[mean]	0.2 %	<0.1 %	0.2 %	-0.3 %
ΔHe ml[mean] - ΔAr ml[mean]	0.2 %	0.1 %	0.2 %	0.1 %
ΔNe ml[mean] - ΔAr ml[mean]	0.2 %	0.1 %	0.2 %	0.4 %

Table 3.4 Uncertainties for 1986 analysis using the gas exchange formulation of Wanninkhof (1992). Measurement uncertainties are calculated from the standard deviation of the mean for the mixed-layer and seasonal averages of each constraint equation, and from the analytical uncertainty. Linearization errors are calculated from the difference of the value of each constraint equation estimated with the linearized equation and the value predicted by the model for a reference model case that is in the center of the ranges for all variables. The inversion residuals are calculated from the difference of the values predicted by the linearized equations for the inversion solution results and the measured observations for each constraint equation. A negative residual is obtained when the constraint equation and inversion results underpredict the observation. Comparison of the inversion residuals to the total error associated with each constraint equation provides a measure of how well the solution satisfies each constraint.

Constraint Equation	Measurement Uncertainty	Linearization Error	Total Error	Inversion Residuals
Tml [s - w]	0.01 °C	0.3 °C	0.3 °C	0.9 °C
ΔAr max [s]	0.2 %	0.3 %	0.3 %	-2.3 %
ΔAr ml [s]	0.2 %	0.2 %	0.3 %	<0.1 %
ΔAr ml [w]	0.2 %	0.1 %	0.2 %	-0.3 %
ΔAr ml [s-w]	0.3 %	<0.1 %	0.3 %	0.4 %
ΔAr ml [mean]	0.2 %	0.1 %	0.2 %	-0.5 %
ΔHe ml [w]	0.2 %	0.2 %	0.2 %	-0.6 %
ΔHe ml [mean]	0.2 %	<0.1 %	0.2 %	-0.3 %
ΔNe ml [w]	0.2 %	0.2 %	0.3 %	-0.5 %
ΔNe ml [mean]	0.2 %	<0.1 %	0.2 %	1.1 %
ΔHe ml [w] - ΔNe ml [w]	0.3 %	<0.1 %	0.3 %	-0.1 %
ΔHe ml[mean] - ΔNe ml[mean]	0.2 %	<0.1 %	0.2 %	-0.1 %
ΔHe ml[mean] - ΔAr ml[mean]	0.2 %	0.1 %	0.2 %	0.3 %
ΔNe ml[mean] - ΔAr ml[mean]	0.2 %	0.1 %	0.2 %	0.4 %

Table 3.5 Uncertainties for 1987 analysis using the gas exchange formulation of Wanninkhof (1992). See Table 3.4 for description.

3.4.4 *Solving the Set of Linearized Equations for the Variables*

The linearized equations provide information about the dependence of each constraint equation on each variable used in the model simulations. These relations are used with the actual data observations (Table 3.1) for the two-year time-series to solve for the value of each variable (air injection, gas exchange, Kz, and bubble trapping fraction) that best fits the *set* of linearized equations. The equation now has the form:

$$Y\text{-}a_5 = a_1X_1 + a_2X_2 + a_3X_3 + a_4X_4 \qquad (3.7)$$

where Y is the value of each constraint equation determined from the data for 1986 and 1987, the a's are the coefficients of the variables (and the constant term) determined in the linearization step, and the X's are the values of the 4 variables for which the system is solved using singular value decomposition.

3.5 *Results and Discussion*

The model was run over the full range of variables using the Wanninkhof (1992) formulation of gas exchange, and then run again using the Liss and Merlivat (1986) formulation. Results from the two model runs for the two-year time-series are hereafter referred to as W86, W87, and LM86, LM87. Information about the data from the two-year time-series used in both analyses is shown in Table 3.1. Tables 3.2-3.6 provide information about the W86 and W87 analyses, and a similar set of tables is shown for the LM86 and LM87 analyses (Tables 3.7-3.11).

Parameter	1986	1987	1986-87 average
K_z ($x10^{-4}$ m^2 s^{-1})	1.3 ± 0.2	0.9 ± 0.2	1.1 ± 0.1
Air Injection	1 ± 2	5 ± 2	3 ± 1
Gas Exchange	0.9 ± 0.4	1.2 ± 0.6	1.0 ± 0.4
Complete Trapping	0.6 ± 0.2	-0.8 ± 0.4	0.2 ± 0.2

Table 3.6 Inversion results using the gas exchange formulation of Wanninkhof (1992).

Constraint Equation	Ainj	F_T	1 / G	1/ K_z
Tml [s - w]	0	0	0	7.8
ΔAr max [s]	0.5	0.9	2.9	1.4
ΔAr ml [s]	0.7	1.1	6.3	-0.1
ΔAr ml [w]	0.3	0.5	-1.8	-30.2
ΔAr ml [s-w]	0.1	0.1	7.0	-0.3
ΔAr ml [mean]	1.0	1.6	3.3	-0.4
ΔHe ml [w]	2.2	0	8.3	0.9
ΔHe ml [mean]	2.7	0	11	0.4
ΔNe ml [w]	1.4	1.4	4.2	0.6
ΔNe ml [mean]	2.7	2.5	11	0.4
ΔHe ml [w] - ΔNe ml [w]	0.04	-1.4	1.4	-0.01
ΔHe ml[mean] - ΔNe ml[mean]	0.01	-2.5	0.5	0.01
ΔHe ml [mean] - ΔAr ml[mean]	1.7	-1.6	7.8	0.7
ΔNe ml [mean] - ΔAr ml[mean]	1.7	0.8	7.3	0.7

Table 3.7 Coefficients of the linearized constraint equations for 1986 model data using the gas exchange formulation of Liss and Merlivat(1986). The coefficients are weighted by the reciprocal of the total error associated with each constraint equation (see Table 3.9).

Constraint Equation	Ainj	F_T	1 / G	1/ K_z
Tml [s - w]	0	0	0	32
ΔAr max [s]	0.7	1.1	4.9	3.6
ΔAr ml [s]	0.8	1.3	10	-0.7
ΔAr ml [w]	0.5	0.8	-1.0	-0.7
ΔAr ml [s-w]	-0.1	-0.2	6.1	0.3
ΔAr ml [mean]	0.7	1.1	2.8	0.9
ΔHe ml [w]	1.3	0	5.4	-1.1
ΔHe ml [mean]	2.8	0	11	-0.05
ΔNe ml [w]	1.3	1.2	4.6	-1.0
ΔNe ml [mean]	2.7	2.5	11	0.4
ΔHe ml [w] - ΔNe ml [w]	0.002	-1.6	1.1	-0.1
ΔHe ml[mean] - ΔNe ml[mean]	0.05	-2.5	0.4	-0.5
ΔHe ml [mean] - ΔAr ml[mean]	1.2	-1.1	4.6	-1.0
ΔNe ml [mean] - ΔAr ml[mean]	1.1	0.6	4.3	-0.7

Table 3.8 Coefficients of the linearized constraint equations for 1987 model data using the gas exchange formulation of Liss and Merlivat(1986). The coefficients are weighted by the reciprocal of the total error associated with each constraint equation (see Table 3.10).

Constraint Equation	Measurement Uncertainty	Linearization Error	Total Error	Inversion Residuals
Tml [s - w]	0.04 °C	0.3 °C	0.3 °C	0.2 °C
ΔAr max [s]	0.2 %	0.3 %	0.4 %	-1.6 %
ΔAr ml [s]	0.3 %	0.1 %	0.3 %	-0.2 %
ΔAr ml [w]	0.2 %	0.4 %	0.5 %	-0.4 %
ΔAr ml [s-w]	0.4 %	<0.1 %	0.4 %	0.1 %
ΔAr ml [mean]	0.2 %	0.1 %	0.2 %	-0.1 %
ΔHe ml [w]	0.2 %	0.1 %	0.2 %	-0.5 %
ΔHe ml [mean]	0.2 %	<0.1 %	0.2 %	0.1 %
ΔNe ml [w]	0.3 %	0.1 %	0.3 %	<-0.1 %
ΔNe ml [mean]	0.2 %	<0.1 %	0.2 %	0.2 %
ΔHe ml [w] - ΔNe ml [w]	0.3 %	<0.1 %	0.3 %	-0.4 %
ΔHe ml[mean] - ΔNe ml[mean]	0.2 %	<0.1 %	0.2 %	-0.1 %
ΔHe ml[mean] - ΔAr ml[mean]	0.2 %	0.1 %	0.2 %	0.2 %
ΔNe ml[mean] - ΔAr ml[mean]	0.2 %	0.1 %	0.2 %	0.3 %

Table 3.9 Uncertainties for 1986 analysis using the gas exchange formulation of Liss and Merlivat (1986). See Table 3.4 for explanation.

Constraint Equation	Measurement Uncertainty	Linearization Error	Total Error	Inversion Residuals
Tml [s - w]	0.04 °C	0.1 °C	0.1 °C	0.08 °C
ΔAr max [s]	0.2 %	0.2 %	0.3 %	-2.6 %
ΔAr ml [s]	0.3 %	<0.1 %	0.2 %	0.1 %
ΔAr ml [w]	0.2 %	0.3 %	0.4 %	-0.6 %
ΔAr ml [s-w]	0.4 %	0.3 %	0.4 %	0.7 %
ΔAr ml [mean]	0.2 %	0.3 %	0.3 %	-0.3 %
ΔHe ml [w]	0.2 %	0.4 %	0.4 %	-1.1 %
ΔHe ml [mean]	0.2 %	<0.1 %	0.2 %	-0.1 %
ΔNe ml [w]	0.3 %	0.4 %	0.4 %	-0.6 %
ΔNe ml [mean]	0.2 %	0.1 %	0.2 %	0.2 %
ΔHe ml [w] - ΔNe ml [w]	0.3 %	<0.1 %	0.3 %	-0.5 %
ΔHe ml[mean] - ΔNe ml[mean]	0.2 %	0.1 %	0.2 %	-0.3 %
ΔHe ml[mean] - ΔAr ml[mean]	0.2 %	0.3 %	0.3 %	0.2 %
ΔNe ml[mean] - ΔAr ml[mean]	0.2 %	0.2 %	0.3 %	0.5 %

Table 3.10 Uncertainties for 1987 analysis using the gas exchange formulation of Liss and Merlivat (1986).

Parameter	1986	1987	1986-87 average
K_z ($x10^{-4}$ m^2 s^{-1})	1.4 ± 0.4	1.1 ± 0.1	1.1 ± 0.2
Air Injection	2.1 ± 0.9	3 ± 2	2.4 ± 0.9
Gas Exchange	2 ± 1	1.5 ± 0.7	1.7 ± 0.6
Complete Trapping	0.2 ± 0.4	-1.7 ± 0.7	-0.3 ± 0.4

Table 3.11 Inversion results using the gas exchange formulation of Liss and Merlivat (1986). The 1986-87 average is the weighted mean of the two years.

The inversion results for the W86 and W87 analyses are shown in Table 3.6, and the results for the LM86 and LM87 analyses are shown in Table 3.11. Also shown in the tables is the weighted average of the results from the two years. The discussion will focus first on the comparisons between the two sets of model runs, followed by a more detailed discussion of the implications of the solutions for each of the variables.

3.5.1 *Comparisons between W86-87 and LM86-87*

Comparison of the inversion results from the mean of the two years from the two sets of model runs (Tables 3.6 and 3.11) provides several insights into the effects of each of the gas exchange formulations on the cycles of the dissolved gases. In general, within the uncertainties of the data, the results are in reasonable agreement for most variables. Specifically, the magnitude of vertical mixing is identical using both sets of model simulations, which results from the fact that the mixed-layer temperature cycle is the strongest constraint on K_z, and is not affected by gas exchange. To a certain extent, the value of the vertical entrainment velocity of the air injection formulation is in good agreement between the two systems. However, the effects of air injection must be viewed

in conjunction with the gas exchange component, because the gas cycles are controlled by the dynamic interactions of both processes. The Wanninkhof gas exchange formulation works quite well in this system, and requires no multiplier to match the observations. The Liss and Merlivat gas exchange function is shown to underpredict the observations, and requires an increase of approximately 70% in the piston velocity to match the observations. By boosting the Liss and Merlivat piston velocity, the air injection flux required is in good agreement with that of Wanninkhof.

The solutions for the relative fractions of complete and partial bubble trapping are the most uncertain in the model, and the solutions of both sets of model runs show negative complete trapping fractions for 1987. Negative complete trapping fractions may be indicative of inadequacies of the bubble trapping end-member processes, or perhaps small inaccuracies in the solubility values of He or Ne. In addition, uncertainties may be introduced from imposing a yearly average of the relative fractions of trapping on the system, whereas the fractions most likely change on seasonal or shorter time-scales (see discussion in section 3.5.2). The evaluation of these influences on the flux from bubbles requires a higher-frequency time-series of the gases than that used in this study.

In general, using the Wanninkhof formulation, the weighted average of the two years is positive, while the weighted average of the two years using the Liss and Merlivat formulation is still negative. Considering only the average values for the two years, the solutions from both formulations of gas exchange are consistent within the uncertainties,

and imply that complete trapping is a very small component of the gas flux from bubbles and that partial bubble trapping is dominant over yearly time-scales.

This illustrates the efficacy of using many constraint equations, which allows the variables to be constrained by different processes and combinations of processes, thus allowing for resolution of interacting processes. For example, even though the bubble trapping fraction formulation depends critically on the volume of air injected into the water, the bubble trapping fractions can be resolved quite distinctly from the air injection component using the He constraint equations, since the bubble trapping fractions have been normalized to He, and its saturation is thus not affected by the relative fractions of complete and partial bubble trapping. Similarly, Ar is not strongly affected by air injection processes, but is strongly dependent on the gas exchange processes.

Spitzer and Jenkins (1989) found good agreement between the gas exchange formulation of Liss and Merlivat and the dissolved gas cycles at Bermuda. That study used climatological wind speed data and a random component to the wind speed with a decorrelation time-scale of 3-4 days to simulate high wind events. Comparison of this wind simulation to the NCEP wind speed data shows that the winds used in Spitzer and Jenkins were approximately 33% higher for average wind speeds and maximum, "storm event" wind speeds. Using these higher wind speeds, the gas exchange formulation of Liss and Merlivat was capable of simulating the observations. However, incorporation of

the synoptic wind speed data shows that the formulation of Liss and Merlivat is too weak to effectively ventilate the surface waters, and must be increased by a factor of 2.

3.5.2 *Solutions of the individual variables*

(i) Vertical Mixing

The value of K_z that best fits the data is 1.1×10^{-4}. This value is in good agreement with the values of K_z required to simulate the observed thermal cycle near Bermuda (Musgrave et al.,1988), but is considerably higher than typical estimates of diapycnal diffusivity of order 1×10^{-5} m^2 s^{-1} in the main thermocline (Ledwell et al., 1993; Gargett, 1984). As discussed in Musgrave et al. (1988) and Spitzer and Jenkins (1989), several processes in the seasonal thermocline can influence K_z in the model simulations. Turbulent diffusivity transports heat downward from the surface layer, and is thus affected by the penetration depth of solar radiation defined by the Jerlov water type used in the simulation. Near Bermuda, measurements of the light attenuation with depth are bounded by Jerlov water types I and Ia. The increase in light attenuation depth by using a Jerlov I water type reduced the required K_z to simulate the thermal cycle. The Ia water type is more typical of the water masses advecting by Station S, and was considered to be the most appropriate for this model (Spitzer, 1989).

It must also be recognized that by using a one-dimensional model, advective processes are not accounted for, and that the high value of K_z required by the model may reflect the effects of these processes. Thus this value should not be regarded as a true estimate of

the turbulent vertical diffusivity in the upper ocean, but rather the value of a perhaps 'fictitious' process that is some combination of the turbulent vertical diffusivity and other processes that are required to transport heat and gases in a realistic fashion within the framework of the model.

The best-fit value of K_z determined from the inversion does a reasonably good job at simulating both the mixed-layer temperature cycle and the evolution of the mixed-layer depth, shown in Figures 3.10 and 3.12. The value of K_z required to simulate the temperature cycle for 1986 was 1.3×10^{-4}, while for 1987, a value of 0.9×10^{-4} was needed. Small annual variations in K_z almost certainly occur due to the dependence of K_z on other factors mentioned above. The model quantitatively simulates both the temperature and the seasonal temperature cycle quite well. The mixed-layer depth and cycle (Figure 3.12) is also well-simulated, although due to the temperature "definition" of the mixed-layer depth, the mixed-layer depth from the data is not allowed to shoal above 15 meters, whereas the model was not constrained. The relatively shallow mixed-layer depths simulated by the model shown in figure 3.12 result from the time at which the 'snap-shot' of the simulated situation was taken and plotted, and are not characteristic of either the true mixed-layer depth or the shorter-term simulated mixed-layer depth. Because the constraint equations use seasonal averages of summer and winter values, the differences between the simulation mixed-layer depth and the calculated mixed-layer depth are minimized.

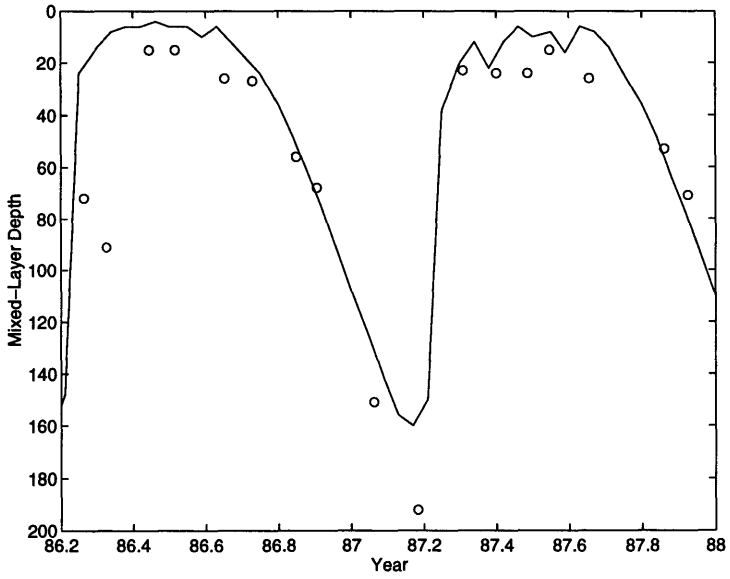

Figure 3.12 Model simulation of the seasonal cycle of the mixed-layer depth using the best-fit solutions for the variables from the W86 and W87 simulations. The symbols are the mixed-layer depths calculated from the temperature data. (see text).

(ii) Air Injection

The model requires a multiplier to the air injection formulation of approximately 3 for both gas exchange simulations to simulate the observed dissolved gas cycles, particularly the winter supersaturations of He and Ne in the mixed-layer. This multiplier is used to adjust the air entrainment velocity (V_A) in the air injection formulation of Monahan and Torgersen (1991) as used in Keeling (1993). The total air entrainment velocity (V_{tot}) is estimated using:

$$V_{tot} = V_A W_A$$

where W_A is the fraction of the sea surface covered with Stage A whitecaps at 20 °C as a function of windspeed (U_{10}>2.27m s^{-1}):

$$W_A = 1.85 \times 10^{-6} (U_{10} - 2.27)^3$$

where U_{10} is the windspeed at 10m in m s^{-1}. Keeling uses a "best guess" case for V_A equal to 1.0 cm s^{-1}, which corresponds to a global-average total air entrainment velocity of 0.001 cm s^{-1} at a windspeed of 10 m s^{-1}. We have adopted this value as the best guess case for our simulation, and the multiplier for our parameterization thus represents the adjustment required to this best-guess V_A used in the model. The mean value for the air injection multiplier for the 1986-87 analyses is in good agreement with that of Keeling (1993),who found that V_A had to be increased by a factor of 3 to match the data of Asher et al. (1992) for the liquid-phase exchange velocity per unit white-cap area for O_2 at 20 °C. This indicates that the average evasion velocity of air vented through Stage A whitecaps that is most consistent with the dissolved gas data from Station S is approximately 3.0 cm s^{-1}.

From the linearized constraint equations, it can be estimated that only about 20% of the annual supersaturation of Ar in the mixed-layer is due to air injection processes, and air injection processes account for less than about 10% of the summer supersaturations . The majority of the supersaturation is due to the imbalance between radiative heating and gas exchange. Because Ar and O_2 have very similar solubilities, solubility temperature dependencies, and diffusivities, the behavior of Ar can be used as an abiogenic tracer of O_2. This suggests that of the pervasive average 3% supersaturation of surface water O_2 seen in O_2 measurements from the GEOSECS program (Broecker and Peng, 1982), only about 0.6% is due to air injection processes (~0.3% in summer), with the rest due to

radiative heating and biological production. Further, the more soluble gases such as CO_2 would be affected even less by air injection processes.

(iii) Gas Exchange

The gas exchange multiplier determined by the W86 and W87 inversions is 1.0 ± 0.4, indicating that the gas exchange formulation of Wanninkhof (1992) works quite well in this simulation. The LM86 and LM87 inversion results, however, suggest that the gas exchange formulation of Liss and Merlivat (1986) must be increased by a factor of 1.7 ± 0.6 to predict the observations. This is in excellent agreement with the findings of Merlivat et al. (1993) and, in part, a result of the fact that the formulation of Liss and Merlivat was initially normalized for lake studies. Merlivat et al. (1993) show that when this formulation is normalized to ^{14}C and the non-linear nature of the relationship between transfer velocity and wind speed is accounted for, the original formulation must be multiplied by a factor of 1.6 to bring the formulation into agreement with oceanic data (Liss and Duce, 1997).

A comparison of the gas piston velocities for the two formulations over a range of wind speeds is shown in Figure 3.13. At the lowest wind speeds, the two formulations predict similar piston velocities, but the predicted values diverge significantly at higher windspeeds, where the formulation of Wanninkhof (1992) predicts values larger than those of Liss and Merlivat (1986) by up to a factor of 2 at the highest windspeeds. The formulation of Wanninkhof must be applied with caution in areas of high windspeeds due

to the quadratic dependence on the windspeed, but in an area with low to moderate wind speed ranges such as Bermuda (shown in the bottom panel), the formulation works quite well.

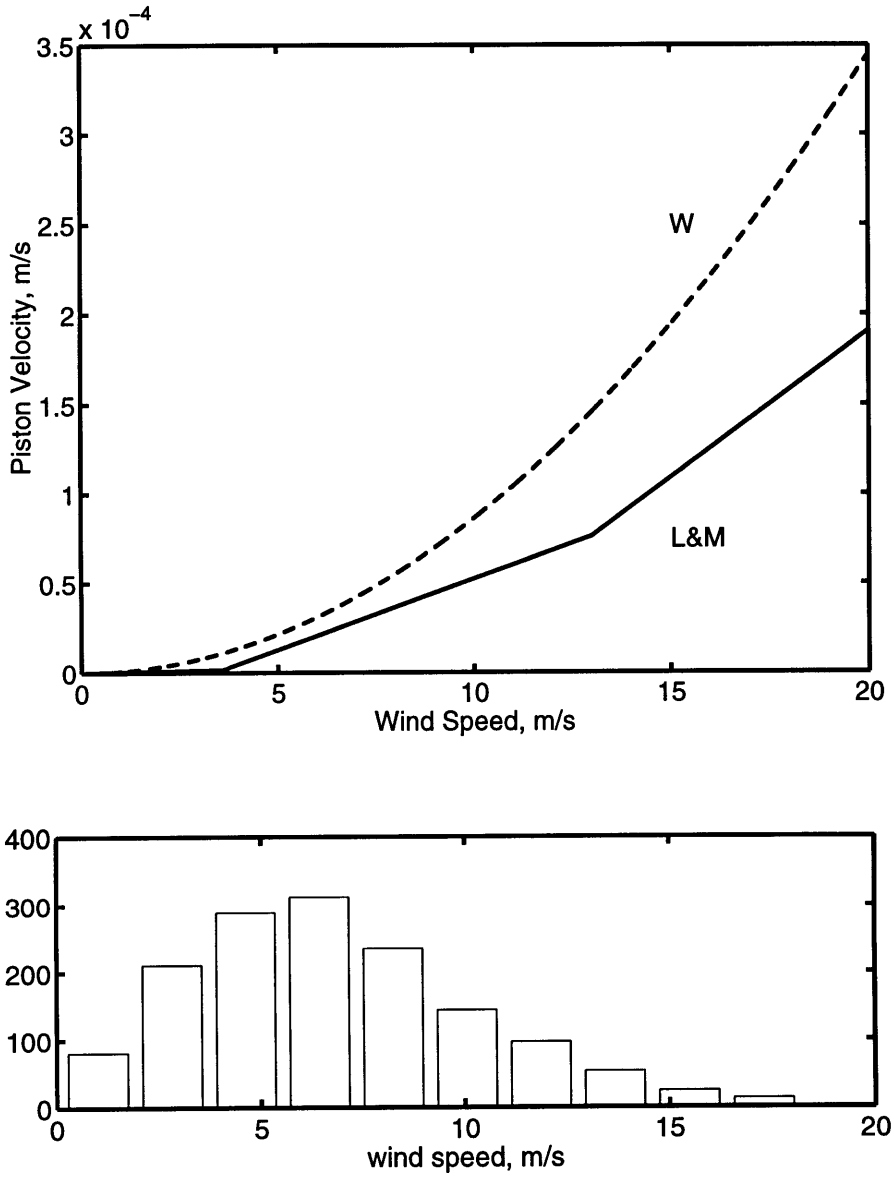

Figure 3.13 Comparison of the piston velocities as a function of wind speed calculated using the formulation of Wanninkhof (1992) (dashed line), and Liss and Merlivat (1986) (solid line). Bottom panel shows a histogram of the wind speed at Station S for 1986 and 1987.

In general, gas exchange works to restore deviations from solubility equilibrium with the atmosphere that result from air injection processes or radiative heating. To a certain extent, an increase in the saturation of a gas may be obtained by increasing the air injection or heating to the system, or by decreasing the gas exchange rate. As discussed earlier, the effects of these competing processes can be resolved by examining the behavior of gases that respond to varying degrees to the forcings on the system. In this study, the same air injection formulation and the same wind speed data are used for both gas exchange cases, and thus the relative efficiency of the gas exchange parameterizations in reproducing the observations can be examined by comparing the two simulations.

Figures 3.14, 3.15, and 3.16 show the mixed-layer He, Ne, and Ar saturations, and the average of the best fit simulations of the saturations for the two years from both gas exchange simulations. The Wanninkhof formulation (solid line) does a slightly better job at simulating the higher saturations of He and Ne in the mixed-layer, and is a slight improvement for the Ar cycle as well. The model is 'tuned' to match the seasonal averages of these cycles, rather than the shorter-term responses shown by the individual data points. This simulation of the longer-term responses, coupled with the use of the model solutions for the average of the two years, is responsible for much of the deviation between the model simulations shown in the figure and the individual data points. Comparison of the inversion residuals for the *seasonal* features shows that the model simulates most of these features within approximately 0.3%.

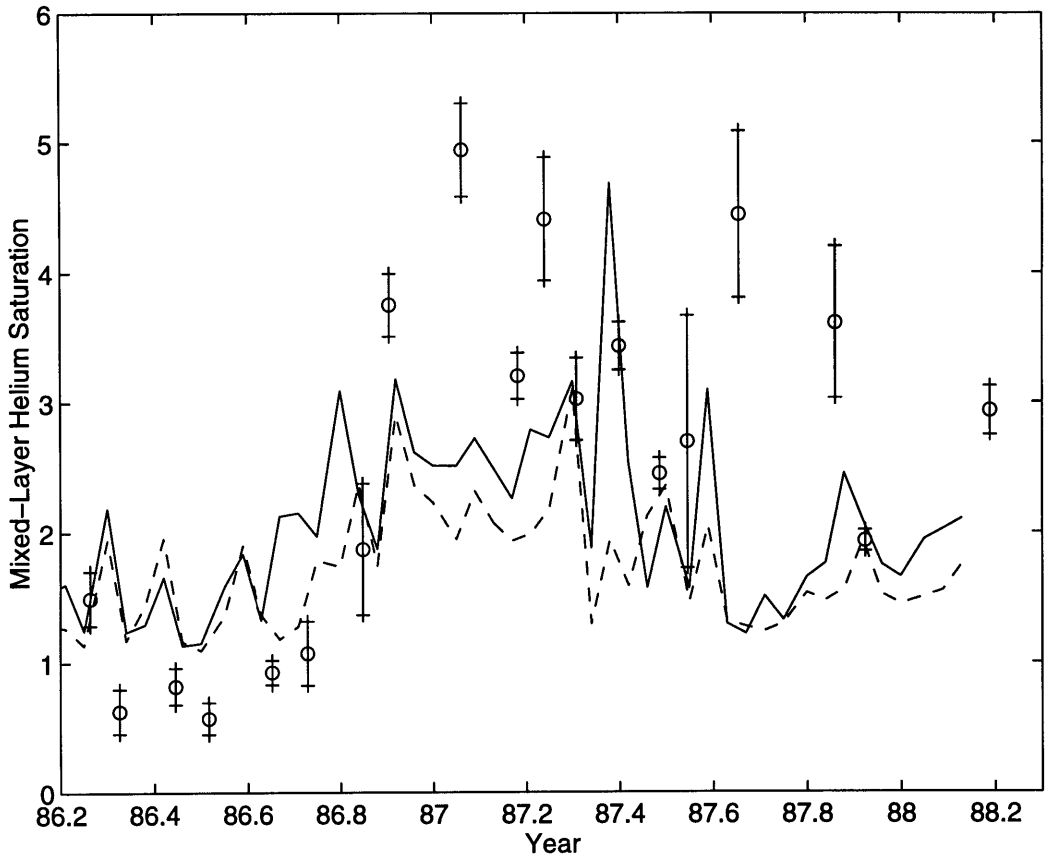

Figure 3.14 Mixed-layer He saturation anomaly data (symbols) and model simulations of the He cycle. Solid line = best-fit W86 and W87; Dashed line = best-fit LM86 and LM87.

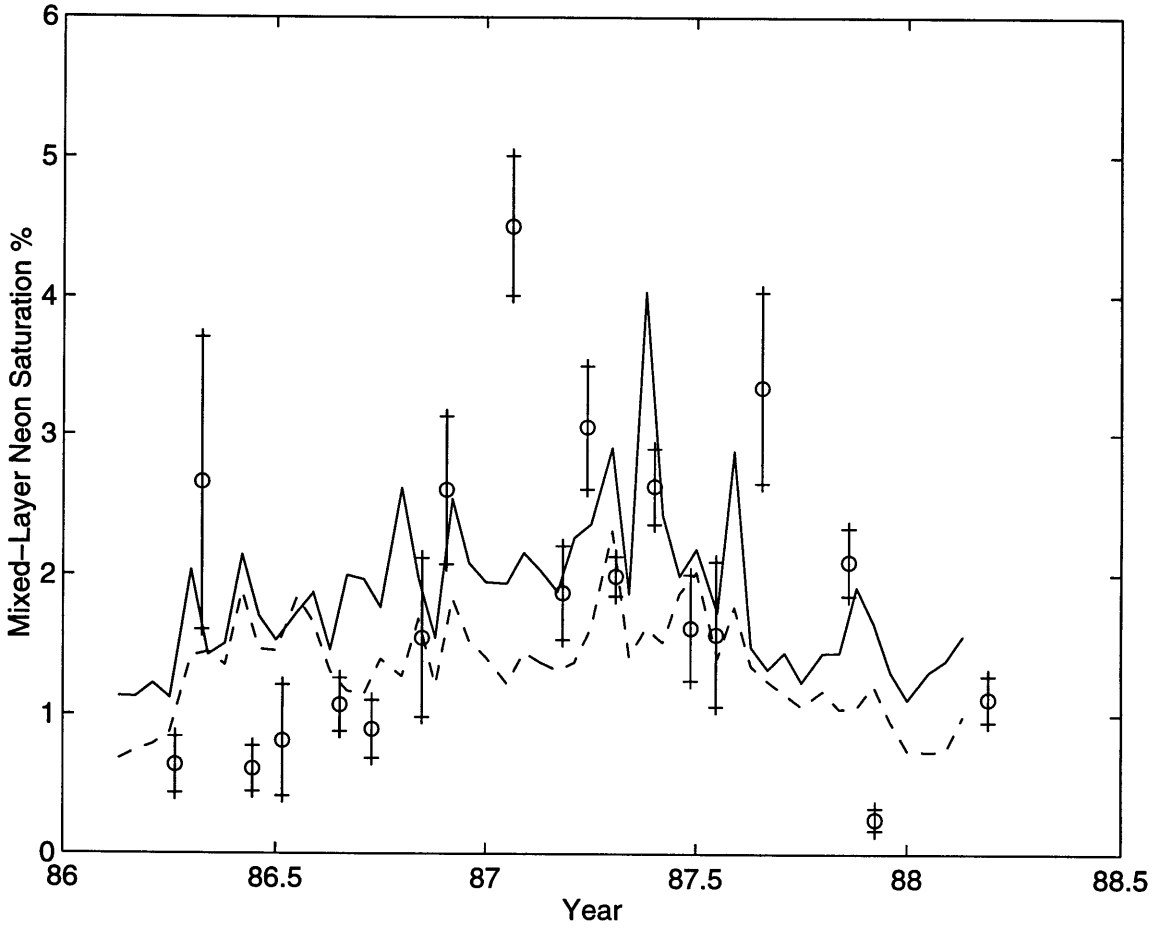

Figure 3.15 Mixed-layer Ne saturation anomaly data (symbols) and model simulations of the Ne cycle. Solid line = best-fit W86 and W87; Dashed line = best-fit LM86 and LM87.

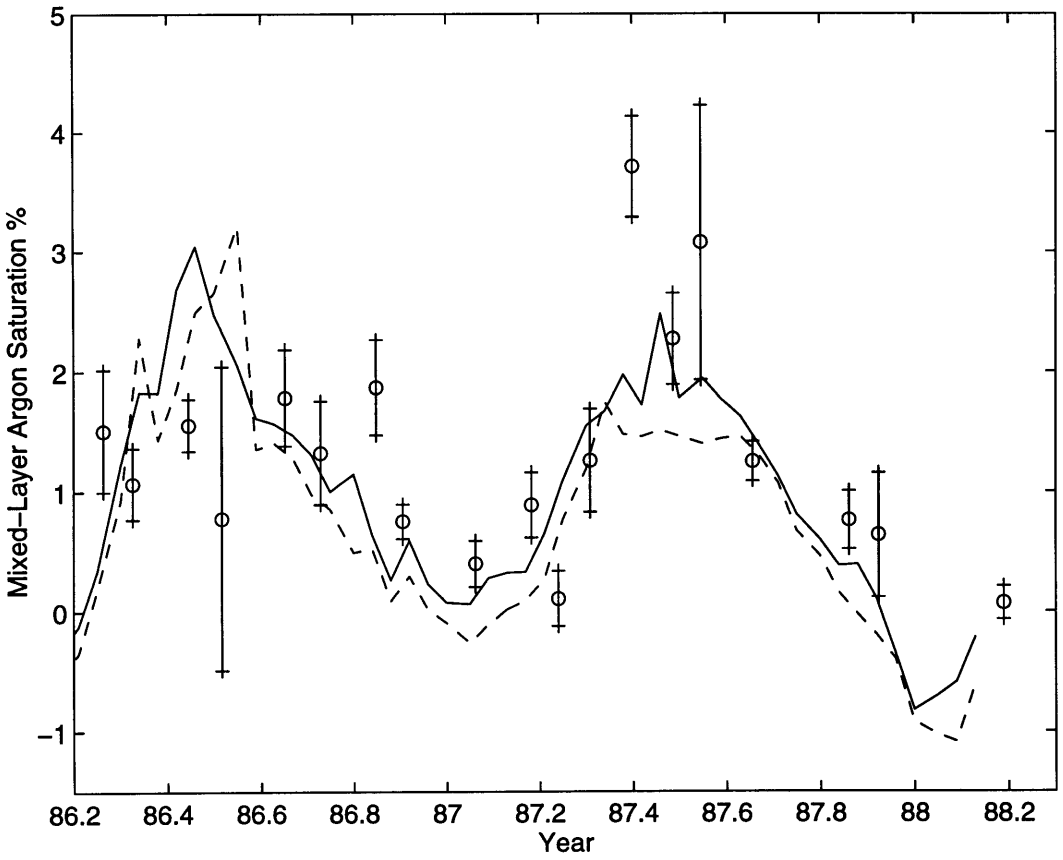

Figure 3.16 Mixed-layer Ar saturation anomaly data (symbols) and model simulations of the Ar cycle. Solid line = best-fit W86 and W87; Dashed line = best-fit LM86 and LM87.

To better evaluate the two formulations, a comparison of the formulations in a region with a larger dynamic range of wind speeds is necessary. With the quality of the data used in this study and the moderate wind speed range, the evaluation is far from definitive.

(iv) Bubble Trapping Fractions

Both sets of simulations indicate that over an annual cycle, bubble trapping is dominated by the partial trapping mode, with an average "mixture" of approximately 20% complete trapping and 80% partial trapping. This is similar to the results of Jenkins (1988) using GEOSECS He and Ne measurements. However, when the measurements are broken down into summer and winter components, a strong seasonal shift can be seen in the relative fractions of complete and partial trapping. Figure 3.17 shows the mixed-layer He and Ne measurements for 1986 and 1987 winter and summer.

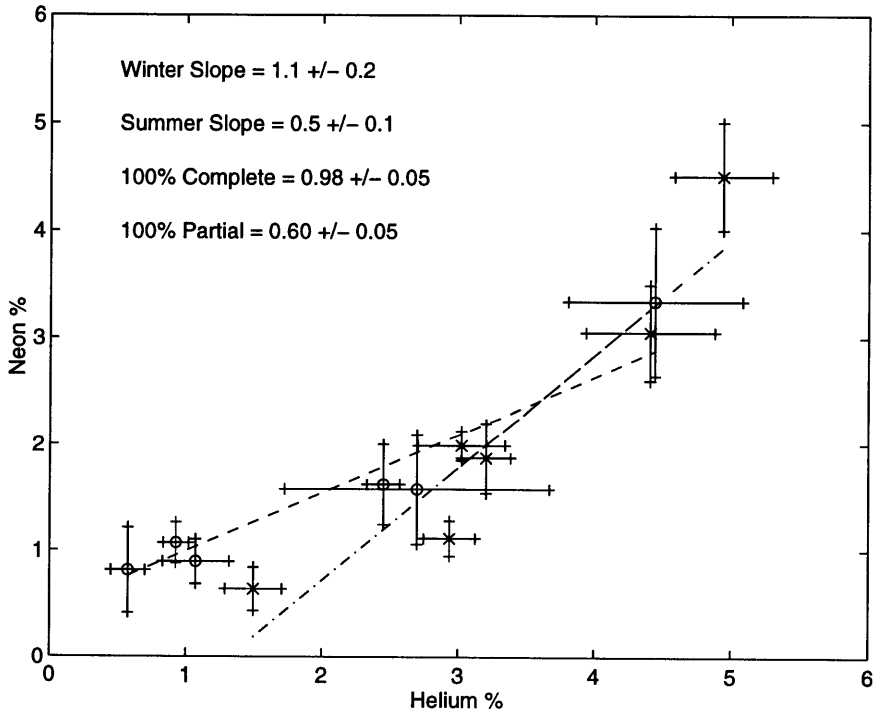

Figure 3.17 Mixed-layer He and Ne saturation anomaly data for summer (circles) and winter (crosses). Slopes are least-squares fits through the data with values shown in the inset text. Given for comparison are the slopes of 100% complete bubble trapping and 100% partial trapping calculated from the best-fit solutions of the W87 simulation.

The slopes of the two relations are least-squares fits to the data. Shown in the inset text of Figure 3.17 are the values of these slopes, and the slopes calculated for 100% complete trapping and 100% partial trapping. These slopes are the weighted means of the slopes calculated from the He and Ne mixed-layer saturations from the W86 and W87 simulations shown in Figure 3.11. The W86 and W87 simulations used are those with the best-fit solution parameters for vertical mixing, air injection, and gas exchange. Vertical mixing and the volume of air injected will not fractionate the saturations of the two gases, while radiative heating will have only a small effect on Ne, and thus the resulting saturation differences between the two gases stem primarily from the effects of bubble trapping modes and gas exchange. Because the *relative* rate at which gases are exchanged across the air-sea interface is independent of the overall piston velocity (i.e. the relative rate of exchange is proportional to the ratio of the square root of the diffusivities of the two gases), the effects of gas exchange alone will not introduce seasonal fractionations in the gas saturation ratios.

The comparisons suggest that while the summer values are dominated by partial bubble trapping, the winter values are controlled by complete trapping. In general, complete trapping is associated with smaller bubbles, while larger bubbles are related to partial trapping (e.g. Jähne et al., 1984; Fuchs et al., 1987; Crawford and Farmer, 1987). An increased fraction of complete trapping in the winter relative to summer may result from the relation between bubble entrainment depth and increased wind speed (e.g. Wu, 1981;

Crawford and Farmer, 1987). As wind speed increases, bubbles are entrained to greater depths where the rate of dissolution of bubbles is significantly enhanced.

Using the parameterization of gas flux from bubbles used in this model (equation 3.5), the relative effects of varying the bubble trapping fractions seasonally can be examined. The calculated gas fluxes (in cc (STP) m^{-2} s^{-1}) for Ne at 20 °C are shown below for 100% complete trapping, 100% partial trapping, and a mixture of 20% complete and 80% partial as suggested by the best-fit inversion results from the W86-W87 model simulations:

100% Complete:	$F = 4.74 \times 10^{-4}$ cc (STP) m^{-2} s^{-1}
100% Partial:	$F = 3.14 \times 10^{-4}$ cc (STP) m^{-2} s^{-1}
20% C, 80% P:	$F = 3.46 \times 10^{-4}$ cc (STP) m^{-2} s^{-1}

If the "average mixture" suggested by the simulation is used, the Ne flux could be underpredicted in the winter (assuming a complete trapping fraction of 100% as suggested by the data) by up to 37%. Further studies are needed to determine how significantly this seasonal change affects calculations of gas fluxes. These seasonal changes may also be responsible for much of the uncertainty in the best-fit solution results for the yearly mean conditions, not only for the bubble trapping fractions, but also for vertical mixing and the air entrainment velocity, V_A in the air injection formulation.

(v) Interannual Variations and Model Weaknesses

Lateral transport is ignored in the model. As discussed in Spitzer (1989) and Spitzer and Jenkins (1989), lateral advection is important for ventilating depths below the mixed-layer, and advective features such as mesoscale eddies may cause significant interannual variations. However, in the upper ~150 -200 m the gas and temperature cycles are largely controlled by forcing at the surface. The inversion results for 1986 and 1987 show that, except for the bubble trapping mode, the best-fit solutions for the two years are identical within the (considerable) uncertainties.

As discussed previously, the model simulates the temperature and mixed-layer cycles reasonably well. From the inversion residuals in Tables 3.4 and 3.5, the solution results from the two year average satisfy most of the constraint equations quite well. However, the maximum summer Ar saturation is not particularly well-constrained by the model using either gas exchange formulation, and the mean mixed-layer Ne saturation is not well-constrained in 1987. The summer maximum of Ar is chosen regardless of depth in the water column, so the "defined" mixed-layer depth in the data observations will have no effect on the observational average of the summer Ar maximum. The cause of the large inversion residual for the maximum Ar may be that the strong temperature cycle constraint on Kz over-powers the weaker constraint imposed by the Ar below the thermocline, thus dissipating the Ar more strongly than the data suggests. This would lead to the negative residuals observed. The large inversion residuals for the mixed-layer Ne are most likely the result of the negative bubble trapping fractions predicted by the

simulations for the 1987 data, and indicate that the simulations are unsuccessful at simulating the He/Ne ratio within the stated constraints of the trapping fractions for that year. The data show considerable variations for He and Ne in 1987, which may be related to sampling errors.

3.6 *Summary*

This analysis of the two-year time-series of He, Ne, Ar, and temperature from Station S using a 1-D vertical mixing model has provided several insights into the processes of gas exchange and air injection that affect the concentrations of dissolved gases in the upper ocean on seasonal time-scales. The gas exchange formulation of Wanninkhof (1992) works well for qualitatively simulating the average seasonal gas cycles, while the formulation of Liss and Merlivat (1986) underpredicts the gas exchange required by the data. Using the air injection formulation of Monahan and Torgersen (1991), both sets of model simulations suggests that a yearly average air entrainment velocity of approximately 3.0 cm s^{-1} is most appropriate for this area. This value is consistent with the air entrainment velocity determined by Keeling (1993) using the laboratory experiments of Asher et al. (1992). The fractions of complete and partial trapping that best predict the yearly average behavior of the gases are consistent with the finding of Jenkins (1988) that bubble trapping is largely dominated by partial trapping of large bubbles. However, this analysis suggests that the optimal mixture of complete and partial trapping fractions changes seasonally, with complete bubble trapping being the dominant mechanism in the winter.

Chapter 4

The Noble Gas Sampler

4.1 *Introduction*

There are obvious logistical problems associated with obtaining data on gas fluxes over a range of atmospheric and sea surface conditions, particularly in the high wind/ wave regime. A time-series approach requires frequent sampling over a period that is long with respect to the physical forcing and the equilibration time of the system. A moorable, quasi-continuous measurement device would be ideal, but unfortunately the development of this type of device for the unreactive noble gases is currently not possible. There are also several designs of moorable water samplers that are capable of obtaining a time-series of water samples, but these are not suitable for the storage and analysis of the noble gases, in particular, helium, which has an appreciable diffusion rate through all types of plastics, polymers, and most glasses that are generally used in constructing the sample

vessels, valves, and seals. The conventional method for collecting samples for analysis of noble gases involves collecting a water sample in a copper tube and clamping the ends to form a seal. Samples can then be stored indefinitely (see Chapter 2). While this method is robust for sampling and storage of water samples for noble gas analysis, it is not feasible to automate for a moorable time-series sampler.

We have designed an automated, moorable dissolved gas sampler that is capable of obtaining a time-series of noble gas concentrations in the upper ocean over periods ranging from several weeks up to a year. The sampler, shown as a block diagram in Figure 4.1, is a closed-loop system filled with distilled water that equilibrates with the dissolved gas concentrations in the surrounding seawater across a gas-permeable membrane. Using a 50-port switching valve and a micropump controlled by a microprocessor, the sample is pumped into a stainless steel sample chamber and stored until recovery. The samples in the chambers are isolated from the rest of the system by means of the diffusion barrier presented by 50 cm lengths of 0.007" i.d. capillary tubing on either end of the chamber. The sample chambers are mechanically sealed upon recovery of the sampler. Sections 4.2 and 4.3 discuss the diffusion barrier and the membrane equilibration techniques, Section 4.4 discusses the system components, operational characteristics and specifications, and Section 4.5 discusses the results of a test deployment.

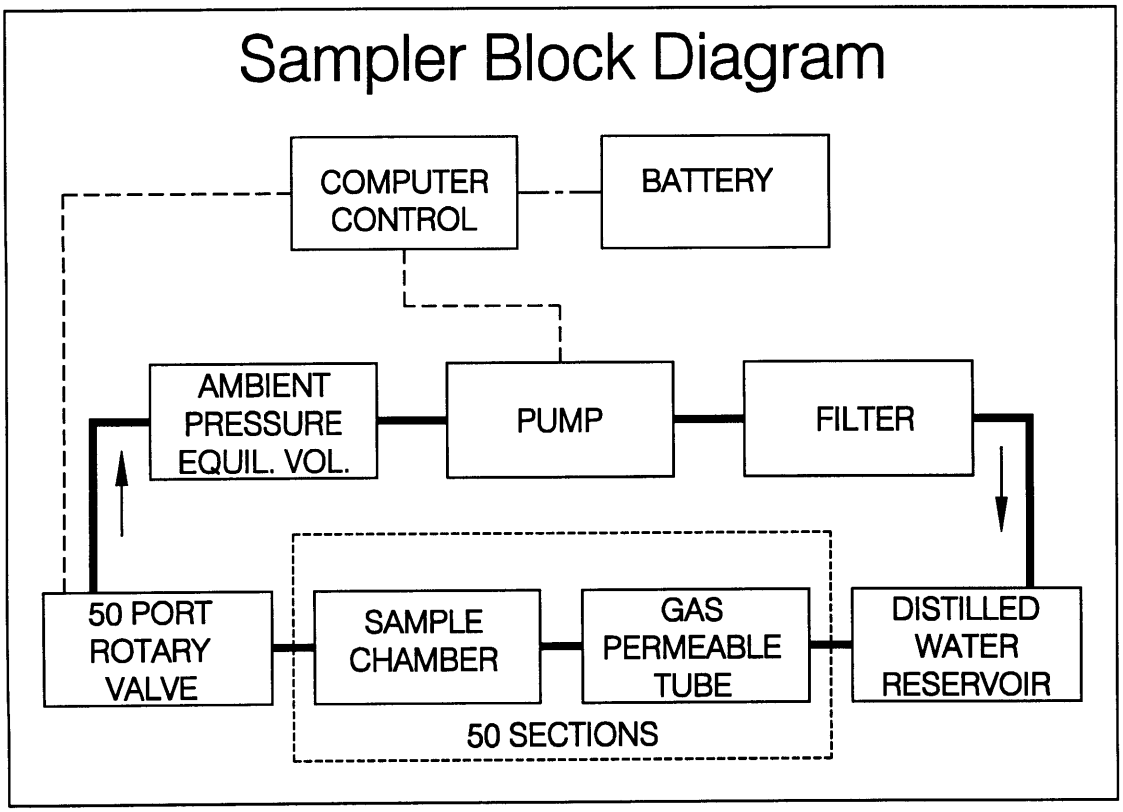

Figure 4.1 Block diagram of the noble gas sampler. See text for details.

4.2 *The sample chambers and diffusion barrier*

The sample chambers, made of type 316L stainless steel, consist of a 1cc cylindrical sample storage volume that is laser welded to 0.5m lengths of 0.007" i.d. stainless steel capillary tubing on either end. The chambers are He leak-checked to $<1x10^{-9}$ std cc atm^{-1} s^{-1}. A sample chamber is shown in Figure 4.2.

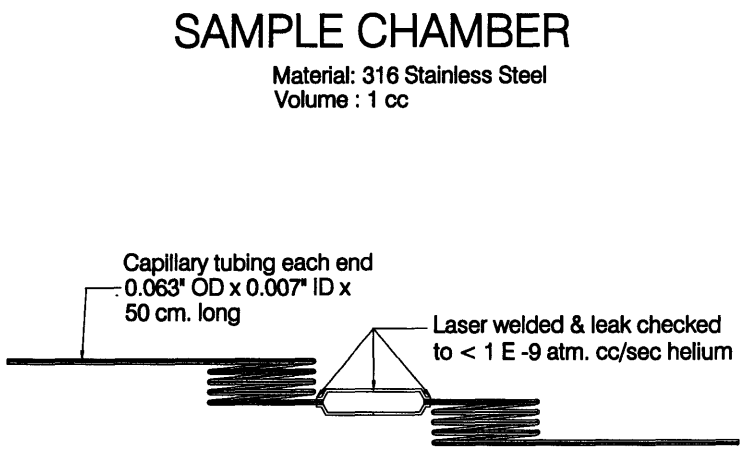

Figure 4.2 Sample chamber from the noble gas sampler.

For ease of handling and space conservation, the capillary tubing is coiled. Volumes of the sample chambers are determined by filling the sample chambers with water (discussed later this chapter) and calculating the weight difference between the full and empty chamber. The reproducibility of the volumes determined is better than 0.1%. The water sample is pumped into the chamber, which is flushed with approximately 8 milliliters of the equilibrated sample water, and the sample is "sealed" against contamination by the

diffusion barrier presented by the long capillaries. On retrieval of the sampler, the ends of the capillary tubing are crimped to form a seal, and the samples are stored in a cool, freshwater bath.

The contamination of the gas concentration in the sample chamber after sampling caused by diffusion through the capillary tubing during the deployment can be modeled using a finite difference technique. The basic equation for the time rate of change of the concentration of the gases in the sample chamber is:

$$\frac{\Delta C}{\Delta t} = \frac{(F_{in} - F_{out})}{V} \tag{4.1}$$

where

$$F_{in} = \frac{a \cdot D(C_{i-1} - C_i)}{\Delta l}$$

$$F_{out} = \frac{a \cdot D(C_i - C_{i+1})}{\Delta l}$$

a = the cross-sectional area of the capillary

D = the diffusion coefficient

C_i, C_{i+1}, and C_{i-1} are the concentrations in the control volume cell, the forward cell, and the preceding cell, respectively.

V= volume of the sample chamber, equal to the area, A, times the length, l.

The equation thus becomes:

$$\frac{\Delta C}{\Delta t} = \frac{a \cdot D(C_{i-1} - 2C_i + C_{i+1})}{A \cdot \Delta l^2} \tag{4.2}$$

The "forward time, centered space" finite difference technique can be used to examine the relative effectiveness of the barrier as a function of the length and diameter of the capillary used. The time derivative is approximated using discrete time-steps, and the model is run for a period of one year. Figures 4.3 and 4.4 show the contamination of He and Kr as a function of various lengths and diameters of capillary tubing as the gases respond to a step-function change in concentration. Contamination is minimized by increasing the length of the capillary tubing and by minimizing the ratio of the cross-sectional area of the capillary tube to the cross-sectional area of the center chamber (i.e. decreasing the i.d. of the capillary tubing). However, the extent to which these factors may be varied is constrained by the operational limitations of the system; namely, the pressure required to force water through a small diameter tubing, and the flow rate needed to flush and fill the sample chambers in a reasonable period of time. The contamination is a stronger function of diameter than length, since a 2-fold reduction in the diameter leads to a 4-fold reduction in the surface area of the capillary, and hence the flux. Experiments showed that 0.007" i.d. tubing was the minimum practical diameter through which water could be pumped at a reasonable flow rate and pressure.

Figure 4.5 shows the fraction of contamination of the dissolved gases in the sample chamber for 50cm lengths of 0.007" i.d. capillary tubing. The maximum contamination for a 3 month time-series is of order 1% or less, depending on the gas. This contamination will be greatest for the oldest samples, and negligible for the samples taken within several weeks of recovery of the instrument. This contamination can also be

corrected for by using the time-series of the dissolved gas concentrations in the water in contact with the capillary ends (via the equilibrated water in the Teflon tubing) and calculating the resulting diffusive contamination to the sample.

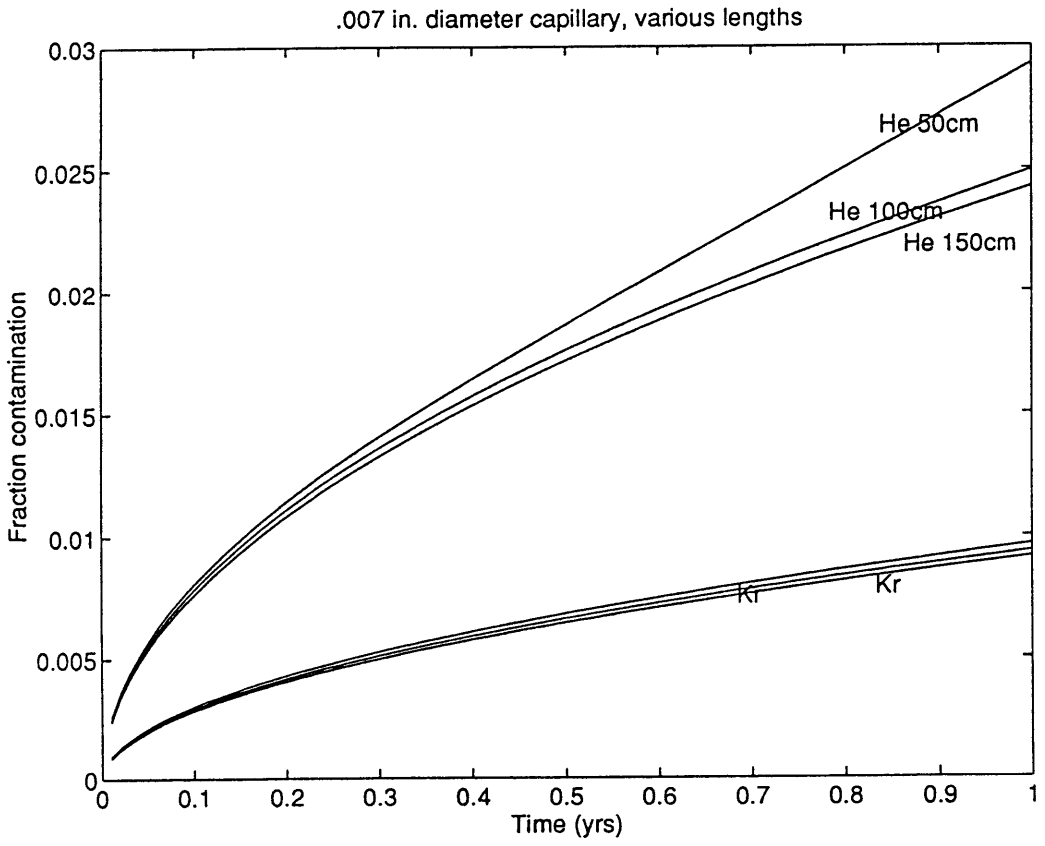

Figure 4.3 Contamination from diffusion over time as a function of the length of 0.007" capillary tubing.

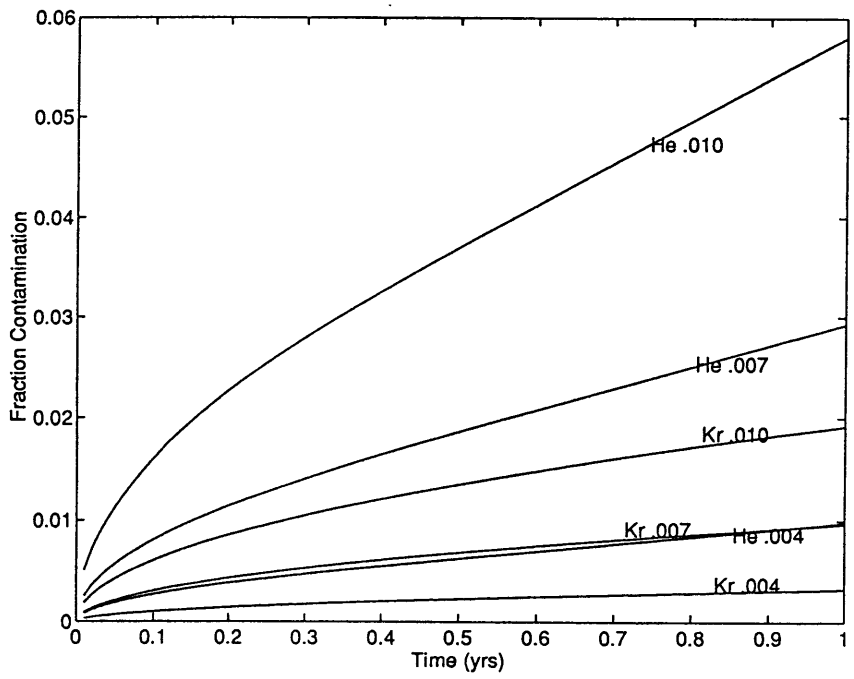

Figure 4.4 Contamination from diffusion over time as a function of the diameter of the capillary tubing.

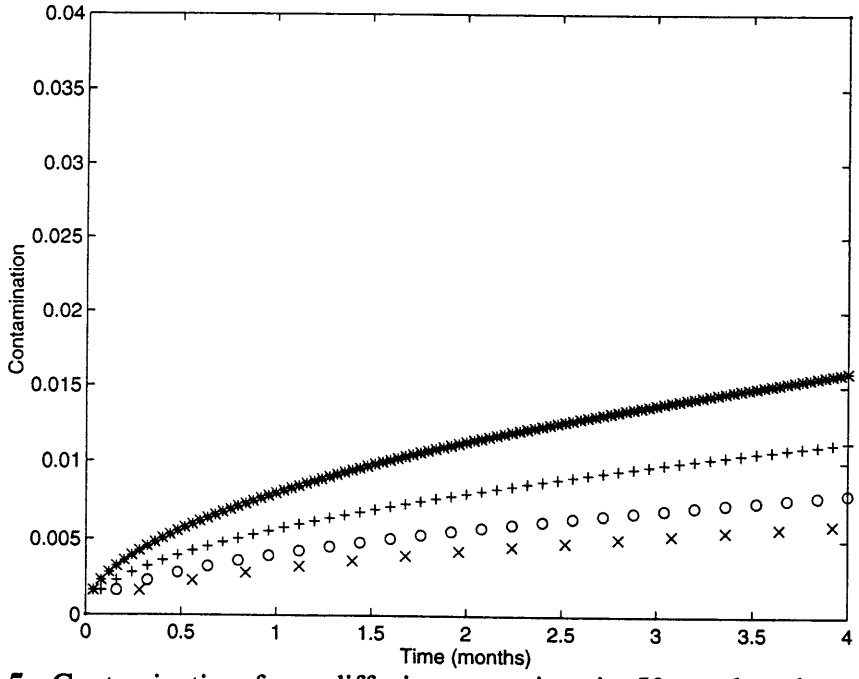

Figure 4.5 Contamination from diffusion over time in 50 cm lengths of 0.007" i.d. capillary tubing. He = * Ne = + Ar = o Kr = x.

4.3 *Gas Permeable Membrane*

The design of the diffusion barrier sample chamber overcomes the problems involved with sampling and storing diffusive gases over long time-periods, but introduces several complications to a typical water sampler design. The small diameter capillary tubing necessary for the diffusion barrier can easily become blocked by particles in seawater. Filtering experiments showed that filters quickly become clogged, considerably reducing the flow rate in the chambers. A constant flow rate is crucial for calculating the volume of water flushed through the chambers during sampling. These problems have been overcome by making the sampler a closed-loop system filled with deionized, distilled water, and utilizing membrane-introduction techniques to equilibrate the dissolved gas in the surrounding seawater with the water in the sampler through a gas-permeable membrane.

Membrane introduction techniques have been used since the early 1960's in analytical chemistry to separate dissolved gases and volatile organic compounds from liquid matrices (Kotiaho et al., 1991; Cooks and Kotiaho, 1992; Kephart et al., 1992; Lauritsen et al., 1992). This type of technique has more recently been used by Anderson and Johnson (1992) in development of a total dissolved gas tension device for measuring dissolved gas pressures in seawater. The basic process of membrane introduction of dissolved gases and volatile organic substances into analytical instruments involves adsorption of the solute into the membrane polymer, diffusion through the polymer, and evaporation or resolubilization on the other side of the polymer. The combined effect of

diffusivity and solubility of the solute in the membrane is referred to as the permeability of the solute in the polymer. The equation describing the permeability, P, of a solute in a polymer is:

$$P = \frac{(quantity\_of\_permeant) \times (film\_thickness)}{area \times time \times (pressure\_drop\_across\_film)}$$

with units of:

$$\frac{cc \cdot cm}{cm^2 \cdot s \cdot atm}$$

The permeability of a solute in a polymer has a temperature dependence typically modeled by the Arrhenius equation:

$$P = P_0 \exp\left[\frac{-E_P}{RT}\right] \tag{4.3}$$

where

P_0 = permeability known at specific temperature

E_p = the permeation activation energy

This equation allows for the calculation of the permeability of the solute in the polymer at any temperature if the activation energy of the gas in the polymer is known. The polymers typically used for these systems are Teflon and polyethylene for dissolved gases, and silicon-based polymers for organic compounds (Kotiaho et al., 1991). The noble gas sampler uses approximately 17 feet of 1/8" o.d., 0.030" wall thickness FEP Teflon tubing for the gas equilibration, providing approximately 10 cc of equilibrated water with which to flush and fill the sample chamber. Teflon tubing is commercially

available in a range of sizes and wall thicknesses, and is rigid enough to withstand the pressures required for pumping water through the capillary tubing.

To estimate the equilibration time between the distilled water and the gases in seawater through Teflon, we use the approach of Anderson and Johnson (1992) to determine the time required for 90% of a concentration step to equilibrate. For this system, the distilled water in the Teflon tubing is stagnant during the equilibration phase, and thus equilibration time is a function of the permeation rate through the membrane and molecular diffusion into the distilled water in the Teflon tube. For these estimates, I use permeability values for He, Ne, and Ar in PTFE (Brandrup, 1975) in 16.5 ft of 1/8"o.d. tubing (0.030" wall thickness). The permeabilities of PTFE Teflon and FEP Teflon are similar, with FEP Teflon having slightly higher permeabilities for the noble gases, making the permeability estimates using PTFE Teflon conservative. Figure 4.6 shows the time for equilibration of the noble gases in this system as a function of water temperature. These values assume no temperature dependence on the activation energy of the membrane, and that the permeability temperature dependence for Ne and Ar is the same as for He. In addition, the type of Teflon used for the noble gas sampler is FEP rather than PTFE, but permeability values were not available for the noble gases in FEP. Although these values can only be viewed as rough estimates, they do provide information about the relative time-scales of equilibration for our system. At 25°C, He and Ne equilibrate within approximately 20 minutes, while Ar requires approximately 1.5 hours. These time-scales are short relative to the time-scale of the response of gases from

physical forcing such as air injection from breaking waves, and the system can adequately resolve the dissolved gas signals with a frequency of 1 sample / 2 hours.

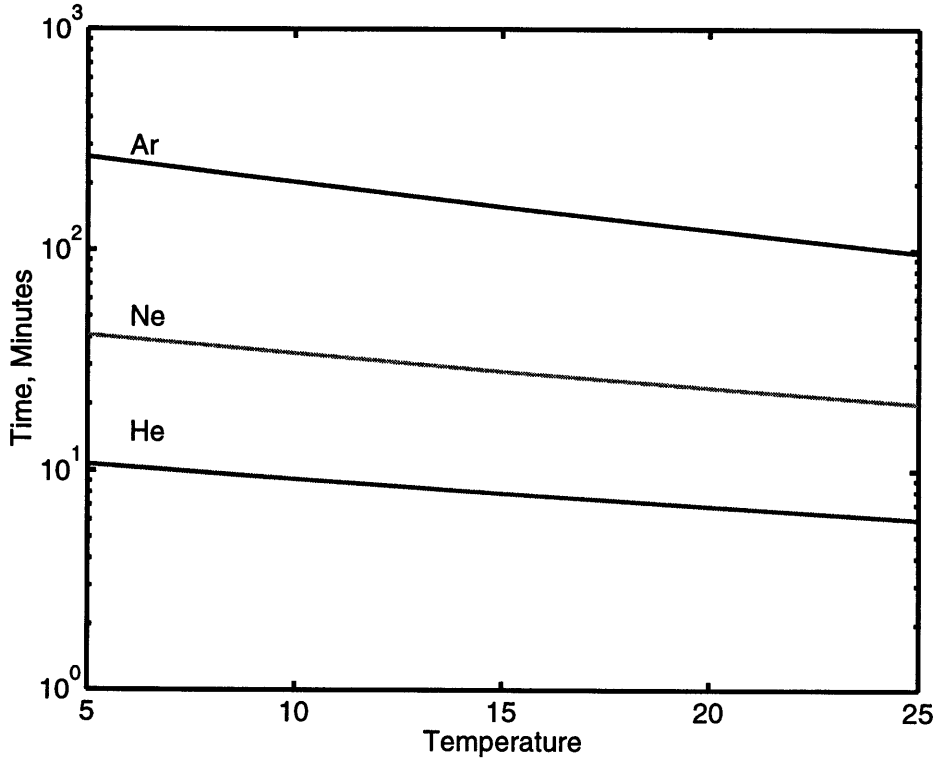

Figure 4.6 Estimated equilibration time of He, Ne, and Ar between surrounding water and water in the equilibration tubing (FEP Teflon) as a function of temperature.

4.4 *System Components and Specifications*

The noble gas sampler is shown in block diagram form in Figure 4.1. The gas permeable membrane used is 0.125" o.d., 0.30" wall thickness extruded FEP Teflon tubing from Upchurch Scientific. Each of the 50 tubes is approximately 5.2 meters long to give an internal volume of at least 10 cm^3. The sample chambers (316L stainless steel), have an

inner volume of approximately 1 cm^3, and have 0.5m lengths of 0.007" i.d. stainless steel capillary tubing laser-beam welded to either end (see Figure 4.2). Each of the 50 sample chambers and the corresponding Teflon tubes form an independent circuit between the reservoir and the 50 port sample selection valve.

The 50 port rotary valve, designed and manufactured by McLane Research Laboratories, is used to select and complete the circuit to the low pressure side of the pump for one sample vessel and Teflon tube circuit. The sample chamber is "flushed" with approximately 8 cm^3 of water from the Teflon tubing that has equilibrated with the surrounding seawater. The ambient pressure equilibration volume allows the internal volume of the closed-loop system to achieve pressure equilibrium with the environment.

The 50 port rotary valve, driven by a stepper motor, has a separate controller card mounted to a Tattletale Model 3 microprocessor controller from Onsett, Inc. Also mounted on the McLane controller card and the Tattletale controller is an in-house designed controller card to control the micropump. The Tattletale controller is programmed using Tattletale Basic, and is used to select a sample circuit by positioning the 50 port rotary valve to complete the loop, and to activate the pump to push water through the sample chamber. The power supply is an alkaline "D" cell battery pack supplying +15 V to the pump and +27 V to the valve, with a common negative terminal. The pump is a modified Micropump, model 188, with a Ryton gear-pump magnetically coupled to a gear-reduction 0-24 VDC motor to produce a flow rate of 0.37 ml / min. at

9V through 0.007" i.d. capillary tubing. Using this flow rate, the time required to take a sample with a flushing volume of 8 cm^3 is approximately 22 minutes. Figures 4.7 a, b, and c show the operational characteristics of the pressure, flow rate, and voltage for the system. The pump body is 316 stainless steel with Teflon case seals. A 316 stainless steel, 60 micron frit is used to filter the pump flow to prevent wear particles from reaching the capillary tubing of the sample chambers. The distilled water reservoir is approximately 105 cm^3 and is common to all 50 Teflon tubes.

The sampler is filled with distilled, deionized water that has been degassed prior to the fill. The degassed water reservoir is attached to the sampler's water reservoir via a valved port. The sampler is first placed under vacuum to approximately 10 millitorr. The valve is rotated during the pump-down to evacuate the system uniformly. During the brief (<1 minute) isolation from the vacuum line prior to filling, gases diffuse into the system through the Teflon equilibration tubing. The degassed water dissolves any gas that may become trapped in the sample chambers during this process. Once the system is filled, the water pump is used to flush the fill water through the sample chambers and switching valve. A small water reservoir with an ambient pressure air headspace is attached to the system between the switching valve and the pressure equilibration housing, through which the fill water is flushed to remove any trapped gas remaining in the system.

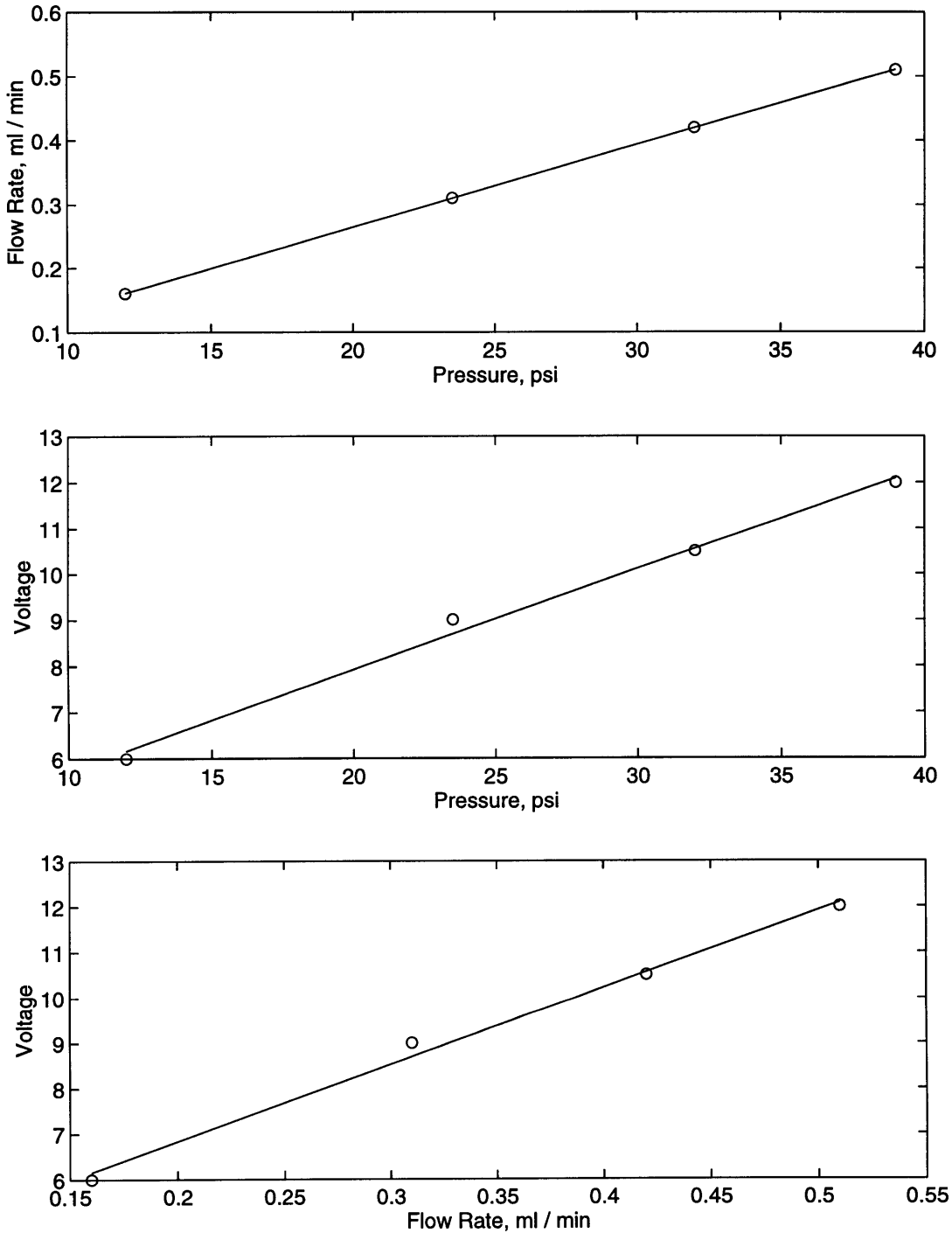

Figure 4.7 Operational characteristics of the noble gas sampler; flow rate vs. pressure (a), voltage vs. pressure (b), and voltage vs. flow rate (c).

4.5 *Test Deployment Results*

A 36 hour test deployment of the noble gas sampler was carried out in August, 1995 on Georges Bank (41°2.5' N, 67° 43.9'W) to perform mechanical tests and to examine the equilibration characteristics of gases across the gas permeable membrane. The sampler was suspended at a depth of 35 meters from the hydrowire of the R/V Cape Henlopen during the 36 hour deployment. The water depth at this location was approximately 60 meters, and the water column was well-mixed throughout the deployment, with a temperature of 14 °C, and salinity of 32.4 psu and a 2.5 knot current. The weather was calm during the deployment, and no whitecaps were visible. The sampler was allowed to reach equilibrium with the surrounding seawater for 12 hours prior to the start of experiments.

Blanks

Because of the diffusion of gases into the system during the fill procedure and dissolution of the gases in the degassed water, the fill water becomes supersaturated with He and Ne, which diffuse into the system very quickly, and undersaturated with Ar and the heavier gases, which diffuse into the system more slowly. Table 4.1 shows the initial He, Ne, and Ar "blanks" after filling the system.

Helium	Neon	Argon
2.97	2.21	0.91
2.55	1.92	0.90
2.18	1.72	0.77
mean = 2.57 ± 0.4	mean = 1.95 ± 0.3	mean = 0.86 ± 0.08

Table 4.1 Saturations of the noble gases in blanks. Saturations are expressed as C / C*, where C is the concentration of the gas in the water and C* is the concentration of the gas at solubility equilibrium with the atmosphere at the temperature and salinity of the fill water.

The values show variation, due to the non-uniformity of gas trapped in individual sample chambers. These initial fill water concentrations are "flushed" from the system at the beginning of the sampler deployment by allowing the system to come to equilibrium with the surrounding seawater for 12-24 hours and then filling the sample chambers with several volumes of the equilibrated water. These initial extreme concentrations in the fill water are used as "tracers" of the flushing and equilibration characteristics of the system.

Volume flushing experiments - Experiments were conducted to determine the optimal volume of equilibrated water that must be used to flush the initial fill water concentrations out of the sample chambers. A series of sample chambers were flushed with 0, 4, 6, and 8 cm^3 of the water from the equilibration tubing. Figure 4.8 shows the flushing characteristics of the sample chambers using Ar as a tracer. The response of the saturation of Ar is in good agreement with the theoretical e-folding displacement of the water in the chambers. Samples for the remaining experiments were flushed with approximately 7.5 cm^3, giving a predicted residual of less than 1%. Although the Teflon

equilibration tubes only have a volume of 10 cm^3, multiple equilibration and flushing cycles may be performed to reduce the residual to less than analytical uncertainty.

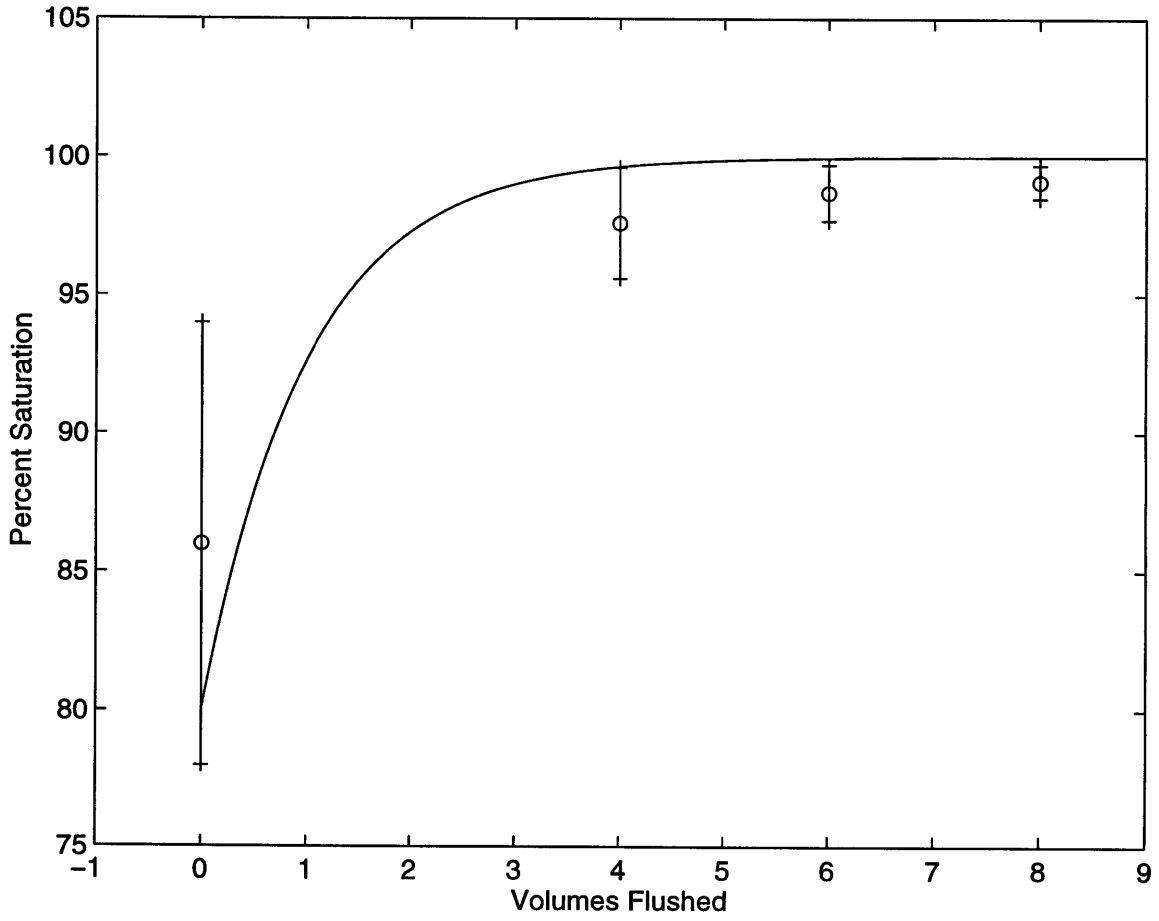

Figure 4.8 Flushing characteristics of water through the sample chambers. Shown is the percent saturation of Ar as a function of the volume of equilibrated water (ml) flushed through the sample chamber containing fill water at the initial fill water saturation. The line is a theoretical curve for the e-folding displacement of the initial fill water.

Replicate sample experiments - Experiments were performed to determine the reproducibility of samples obtained with the noble gas sampler. Using a flow rate of 0.37 ml / min. and a flushing volume of 7.5 cm^3, the minimum time between samples is

approximately 22 minutes. A series of samples was collected every 30 minutes for 4 hours. While some natural variability may occur over this time-period, it was most likely quite small due to the calm weather conditions and well-mixed water column. Table 4.2 and Figure 4.9 show the saturations of He, Ne, and Ar over this time-period.

Sample	Storage method	Helium	Neon	Argon
1	clamped	113	110	100
2	clamped	103	103	100
3	clamped	121	121	101
4	crimped	114	116	101
5	clamped	108	107	99
6	crimped	105	106	101
7	clamped	105	105	100
8	crimped	107	108	100

Table 4.2 He, Ne, and Ar saturations in replicate samples.

While the He and Ne show variability over the four hours, the saturations of the individual samples track each other, with an average saturation difference of less that 1%. They also have identical mean saturations and deviations, suggesting that the variability is the result of incomplete flushing of individual sample chambers rather than natural variability in the water column or errors introduced by analysis. The Ar saturations, with initial fill water saturations that are much closer to the saturations of the surrounding water, show little residual blank effect, and are reproducible to $\pm$ 0.6% over the four hour period. These results suggest that when the sample chambers have been flushed sufficiently to remove the initial fill water, the concentrations of replicate samples are reproducible to better than ~0.5%.

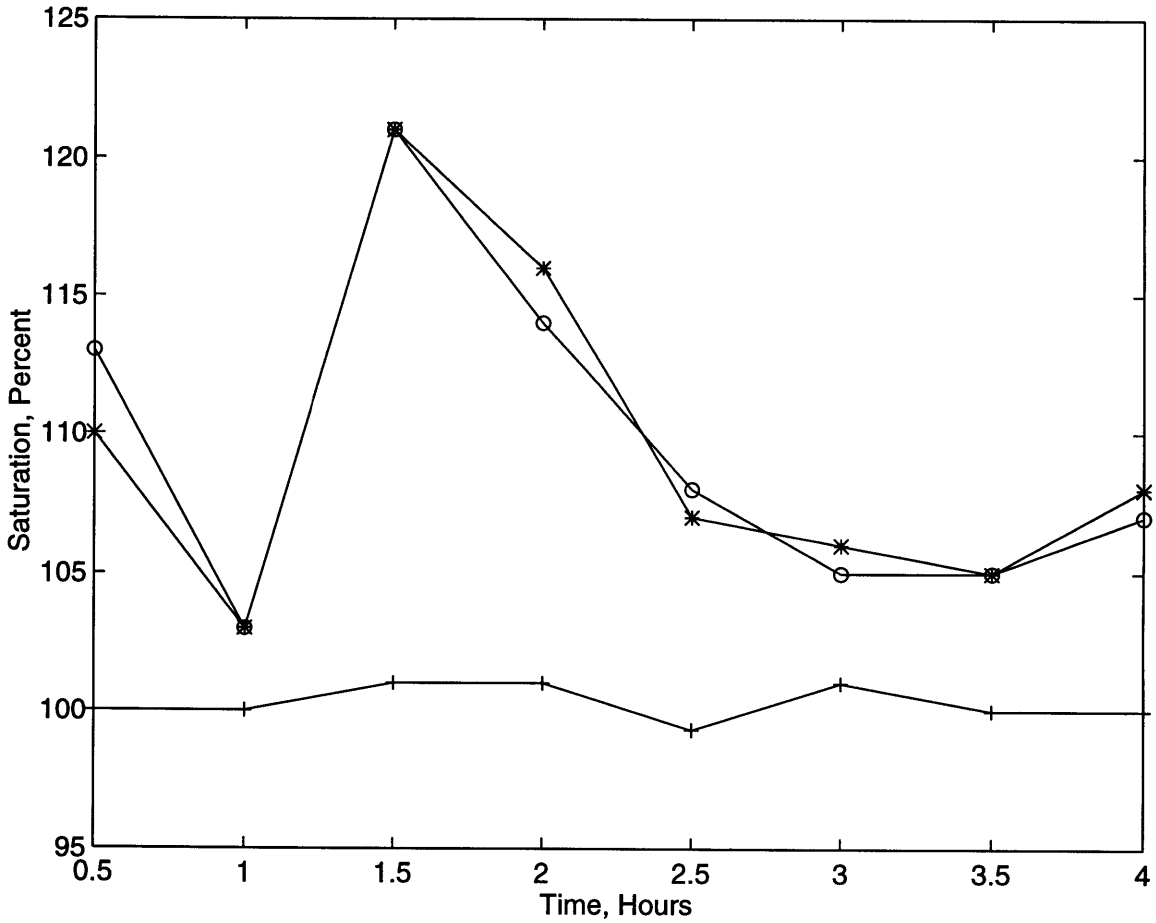

Figure 4.9 Noble gas saturations in "replicate samples" from the noble gas sampler. The sampling rate was one sample every 30 minutes. He = o Ne = * Ar = +.

Sample storage method experiments - Column 2 of Table 4.2 shows the method of sample storage after retrieval of the sampler. The ends of the capillary tubes for each sample chamber were either clamped using the same technique as for copper tube samples, or crimped using a pair of rounded-end vice-grips. Experiments showed that this seal has a leak rate of less than approximately 1×10^{-7} torr atm^{-1}. By storing the sample chamber assemblies under water, the diffusion of helium into the sample is significantly reduced. Prior to attachment on the analytical system, one of the crimped

ends is cut off, and the capillary is clamped to insure a helium tight seal prior to pump down and extraction of the sample. The samples were stored for 5 months in a water bath prior to extraction and analysis. As shown in Table 4.2, there is no detectable difference between the saturations of the samples that were crimped and those that were clamped. In addition, the identical saturations of He and Ne in the samples implies that there was no significant diffusion of the gases between the sample chamber and the surrounding water bath (because the diffusion of He is approximately a factor of 2 faster than that of Ne).

4.6 Summary

Results of the laboratory and field experiments with the noble gas sampler are encouraging, and demonstrate the feasibility of the design for obtaining a time-series of noble gases in the upper ocean. Several important aspects of the sampler performance were demonstrated:

- The sampler can be filled with distilled water and trapped gas can be removed from the system prior to deployment
- Dissolved gases in seawater are exchanging across the Teflon membranes
- The initial fill water of the sampler can be flushed from the sample chambers
- The samples can be removed from the sampler upon retrieval and stored over long time-periods (>5 months) without detectable contamination

- One cc water samples can be extracted and analyzed
- The reproducibility of replicate samples taken over 4 hours is 0.6% (using Ar, which is least likely to change in the water column over the 4 hour period).

Several important tests remain. The mechanical robustness of the sampler over long time- periods in rough conditions must be established. The permeation rates of the dissolved noble gases through the Teflon membrane must be determined experimentally. Comparison of samples obtained by the sampler and those obtained by the conventional copper tube method over a time-series would demonstrate both the accuracy of the samples obtained and provide information on the response time of the sampler to changes in the water column.

Chapter 5

Noble Gases as Tracers of Dissolved Gas / Ice Interactions

5.1 *Introduction*

Ice formation and melting strongly influence a wide range of water properties and processes, such as dissolved gas concentrations and fluxes, dense water formation and ventilation. Dense water formation is a primary mechanism by which atmospheric and surface water properties are transported into the interior and deep ocean, and observation of the effects of this process can answer fundamental questions about global ocean circulation. In questions regarding the ocean's ability to absorb and sequester greenhouse gases, the limiting factor in this exchange process is not the exchange across the air-sea interface, but rather the transport of gases dissolved in the surface waters into the interior and deep ocean. Because dense water formation occurs sporadically in both space and time, information about the rates of water movements and mixing is obtained largely

through the observation of tracers. However, when dense water formation is triggered by ice formation events, interaction of surface water properties with the ice and prevention of equilibration between the atmosphere and the underlying water can significantly modify the concentrations of the tracers. Consequently, the concentrations of these tracers in the interior and deeper layers often provide ambiguous information in ice formation areas. This type of dense water formation occurs in areas of the world's oceans that may be particularly sensitive to changes in regional or global climate, and in areas where the complex coastal circulation and mixing pathways are not fully understood. Our ability to observe and study these processes, however, is currently impaired by our lack of quantitative knowledge about the influences of ice on the tracer distributions.

The interaction of dissolved gases with ice constitutes a type of gas exchange pump, which serves to transport most atmospheric gases into the deep ocean. As water freezes, gases and salt are rejected from the ice lattice and become concentrated in the residual water. In a fresh water, quiescent system, the gas saturations at the ice-water interface may build to a point where the total dissolved gas pressure exceeds the ambient hydrostatic pressure, and bubbles nucleate. The gases partition between the ice, water, and bubble phases according to the solubility of the gases in each phases, and the bubbles become incorporated into the growing ice sheet. In seawater, brine is trapped between the growing ice crystals, and upon further freezing, the gases in the brine are exsolved and create bubbles within the ice. In this case, the gases partition between the ice, residual water, brine and bubbles in the ice. The residual water is made dense through the

rejection of salt, and will thus sink to a level of neutral buoyancy, carrying with it the dissolved gas load. Upon melting, the fresh water released is largely undersaturated with respect to atmospheric equilibrium, and the fresh water cap serves to keep the melt at the surface while at the same time impeding gas exchange between the atmosphere and the water below the melt. The combined processes of melting and freezing thus act as a pump, with freezing transporting dissolved gases into the interior and deep ocean, and the undersaturated melt-water acting as a sponge to absorb more gas from the atmosphere. For CO_2, the additional mechanism of precipitation of $CaCO_3$ during brine formation could lead to an additional transport of CO_2 equal to approximately 1% of the total amount of CO_2 entering the deep ocean (Jones and Coote, 1981).

In recent years, much attention has been paid to the possible effects of global warming on sea ice production and melting, which can lead to dramatic changes in the efficiency of this pumping mechanism (Johannessen et al., 1995; Wadhams, 1995). The links between melt-water input to the North Atlantic and large-scale climate changes have been examined over the last decade (Broecker and Denton, 1989; Birchfield and Broecker, 1990; Broecker, 1990; Keigwin et al., 1991) and it has been demonstrated that even small-scale changes in the salinity of the surface ocean may have profound effects on bottom water formation (Jones, 1991). Over the last several decades, deep convection in the Greenland Sea has significantly slowed or ceased (Wadhams, 1995; Schlosser et al., 1991), presumably as a result of the reduction of sea ice formation. The reduction of transport to the deep and the impedance to gas exchange caused by increased melting may

also have a profound affect on the cycling of dissolved gases between the atmosphere and the ocean, but the interactions between dissolved gases and ice are not fully understood.

5.2 *The noble gases as tracers of the interactions between ice and water*

The noble gases have potential to be excellent tracers of the interactions between dissolved gases and ice, and the resulting interactions between ice and water. Noble gases are biogeochemically inert, and have a wide range of solubilities, solubility temperature dependencies, and diffusivities (Figure 1.1), making them powerful probes of the physical processes affecting dissolved gas concentrations. In addition, He and Ne are soluble in ice, while Ar and heavier gases are not, making the suite of noble gases unique tracers of the interactions between dissolved gases and ice formation.

It has been recognized for some time that the noble gases, He and Ne, and possibly H_2, should be soluble in the ice matrix, whereas gases with larger atomic radii are rejected from the matrix as ice freezes (Namoit and Bukhgalter, 1965; Kahane et al., 1969). The solubility of gases in liquids can be described by statistical mechanics (Pollack, 1991) and scaled particle theory (Pierotti, 1976), although several of the processes of solubility are not yet fully understood (Benson and Krause, 1980). The solubility of gases in ice can be examined using the same treatment. Solubility of gases in liquids occurs to establish an equilibrium condition such that the chemical potential for the solute is the same throughout the system . This processes can be described by two principle processes:

1) creation of a cavity in the solvent large enough to accommodate a solute molecule
2) introduction of the solute molecule into the liquid surface through the cavity and interaction with the surrounding solvent molecules.

The chemical potentials for the gas and solvent phases are given by:

$$\mu_2^g = k\,T \ln \rho_2^g \Lambda^3$$

and

$$\mu_2^l = k\,T \ln \rho_2^l \Lambda^3 + \mu^*$$

where

μ_2^g = chemical potential of the solute molecule in the gas phase

μ_2^l = chemical potential of the solute molecule in the liquid phase

k = Boltzman constant

ρ_2^g and ρ_2^l = number density of the gas and liquid

Λ = de Broglie thermal wavelength

μ^* = excess chemical potential - from the potential energy of solute-solvent and solvent-solvent interactions.

and μ^* = Gcav + Gint, the Gibbs free energies associated with the two principle processes of solubility described above.

The Gibbs free energy required to produce a cavity in a solvent can be calculated using scaled particle theory, which is used to determine the reversible work required to

introduce a hard-sphere molecule into a fluid consisting of hard core molecules. (for a complete discussion, see Pieroti, 1976).

In applying this approach to the solubility of gases in ice, it follows that if the atomic radius of the solute gas molecule is smaller than the cavities naturally present in the ice matrix , then the energy required to make a cavity in the solvent, Gcav, goes to zero, and the free energy associated with dissolving a gas molecule in ice becomes a function of the energy required to move the molecule into the cavity (Namoit, 1967). Since μ^* is thus lower for a gas dissolving in ice rather than water, the solubility of a gas molecule capable of fitting in the ice lattice is larger than its solubility in water.

Two sets of values exist for the solubility of He and Ne in ice (Namoit and Bukhgalter, 1965; Kahane et al., 1969). While the two studies are in agreement for the solubility value of He in ice, they disagree substantially for the solubility of Ne. Kahane et al. state that the solubility of neon in ice is greater than that in water, while Namoit and Bukhgalter suggest that it is less soluble in the ice relative to water. The results in the work of Namoit and Bukhgalter are explained in terms of clathrate formation of He and Ne in ice. However, clathrates of these noble gases do not exist in nature. The first He clathrate was made in a laboratory under extreme conditions in 1988 (Londono et al., 1988). For example, at temperatures near or slightly below the freezing point of water, a clathrate of He requires a pressure in excess of 2700 atmospheres for stability, while those of the heavier gases Kr and Ar require 10 atm and 50 atm, respectively (Davidson et

al., 1984). Clearly, the uptake of He and Ne observed at 300 atm by Namoit and Bukhgalter cannot be the result of clathrate formation. This discrepancy, however, may be one of definition of the term "clathrate". The solubility of He reported by Namoit and Bukhgalter is in excellent agreement with that measured by Kahane et al. (1969). In addition, Top et al. (1988) conducted a laboratory study of the effects of ice formation from salt water on the dissolved noble gases, and report good agreement with the values of Namoit and Bukgalter. However, there does not currently exist any definitive study to determine which of the sets of values is correct, and in this work, I use both sets of values to constrain the possible range of the effects of neon solubility in ice.

5.3 *Application of the noble gases as tracers of ice / water interactions:*

The noble gases could potentially provide useful and unique information in studies of ice / water interactions and dense water formation processes. The noble gas 'anomaly' would be particularly useful in shallow marginal basins or on continental shelves, where the dense water created by ice formation would sink without significant gas exchange with the atmosphere. The tracers most typically used to study these processes include temperature, salinity, and the oxygen isotopes. While much can be learned from these tracers, the information gained is often ambiguous. For example, dense water may be created by brine rejection during ice formation, or through open water convective processes (*i.e.* heat loss and evaporation), both of which serve to increase the salinity of the water. It is thus impossible with salinity alone to distinguish between these mechanisms, which may be important in terms of determining the origin of the formation

effect, and for constraining the potential of a system to create specific volumes or temperature and salinity characteristics of deep water masses. Similarly, the oxygen isotopes show large fractionation effects only for fresh water, and are not greatly affected by freezing and melting of seawater.

As an example of specific areas that may benefit from a tracer such as the noble gas anomaly, Aagaard et al. (1985) have shown that the Arctic Ocean may be an important source of dense water, and that a portion of this water is exported through the Fram Strait and into the North Atlantic. The dense water observed appears to be a mixture of dense, brine-enriched shelf water with water from the intermediate layers of the Arctic Ocean. Similarly, Jones et al. (1995) suggest that the major source of deep water of the Arctic Ocean is from density flows from the continental slope that are triggered by ice formation on the shelves and primarily consist of waters entrained from intermediate depths. Antarctic bottom water forms year round near the continental shelf break from deep and shelf waters. A portion of this water is derived from shelf water that has obtained its characteristics during ice formation, and has had little or no equilibration time with the atmosphere (Jacobs, 1986). Martin et al. (1992) suggest that 50-100% of the bottom water created in the Sea of Japan is the result of ice formation processes. These dense shelf waters that contribute to deep water formation and ventilation in the Arctic and Antarctic regions and in the polar marginal seas are likely to have noble gas concentrations that have been significantly altered by ice formation processes.

While the effects of ice formation on the noble gases have not been systematically studied in the ocean, the effects of melting glacial ice on the concentration of ^{4}He and its potential as a tracer of ice-water interactions has been investigated by Schlosser (1986). Schlosser (1986) states that the sensitivity of the noble gases as tracers of ice-water interactions is comparable with that of the stable isotopes. This study, however, did not recognize the effects of the solubility of helium in ice, and so defined the initial concentration of ^{4}He in the melt as a function of the dissolution of bubbles in the ice only. Using this calculation, Schlosser calculated the fraction of melt-water contained in Antarctic Ice Shelf Water to be approximately 1%, which is reasonably close to the 0.75% obtained using salt budget calculations. Using the parameterization of Schlosser (1986) and including a term for the ^{4}He in the ice matrix gives a melt-water fraction of approximately 0.87%, which brings the estimate in closer agreement with the salt budget estimate than the case with no ^{4}He from the ice. By using a more complete parameterization for helium in three phases and including neon and argon, the noble gases could indeed be powerful probes of ice-water interactions.

5.4 *Research strategy*:

I have measured the noble gases from a variety of ice formation environments in order to explore and characterize the interactions of the noble gases between ice and the water from which it is formed. The goals of this initial survey are to:

- determine if the noble gas anomaly exists on a clear and measurable scale in natural environments
- characterize and model the interactions of the gases and ice system
- use the noble gas anomaly as a tracer of local ice and hydrological processes
- determine the feasibility of application of the anomaly to oceanographic problems, and provide information to direct future investigations.

The environments sampled were ones in which the signal of the noble gas response to ice formation processes was expected to be strong. These include:

- Lake Fryxell, Antarctica - a permanently ice-covered fresh water lake
- Saroma-Ko Lagoon - a seasonally ice-covered salt water lagoon on the north shore of Hokkaido, Japan, connected to the Sea of Okhotsk via two inlets.
- Prydz Bay, Antarctica - an ice-covered bay in Antarctica with a permanent floating ice shelf (Amery Ice Shelf).

CHAPTER 6

Dissolved Gas Dynamics in Perennially Ice-Covered Lake Fryxell, Antarctica

E.M. Hood, B.L. Howes, and W.J. Jenkins (1997) Dissolved Gas Dynamics in Perennially Ice-Covered Lake Fryxell, Antarctica. *Limnology and Oceanography*, in press.

Lake Fryxell is a perennially ice-covered lake in the Dry Valley Region of southern Victoria Land, Antarctica. It is approximately 5km long, 1.6 km wide, and has a maximum depth of 18m. It is fed by glacial meltstreams from nearby Canada and Commonwealth glaciers, which discharge 1.6 x 10^9 l / yr into the lake, and has a volume of approximately 4.32 x 10^{10} liters (Green et al. 1988). The ice-cover has an average thickness of approximately 5m. Liquid water lakes exist in this desert region of Antarctica because thick ice-covers effectively insulate the water below from annual mean air temperatures of -20°C. The edge of the ice-cover melts during the brief

Antarctic summer, creating a moat a few meters wide through which sediments and meltwater enter the lake. Water is removed from the lake through ice formation at the base of the ice cover, ablation and sublimation from the ice surface, and to a lesser extent, evaporation at the moat. The ice-cover greatly restricts wind-generated mixing, as well as gas exchange with the atmosphere, and along with a salinity gradient that extends throughout the water column, creates a highly stable, amictic water column that is anoxic below about 10 meters (Fig. 1).

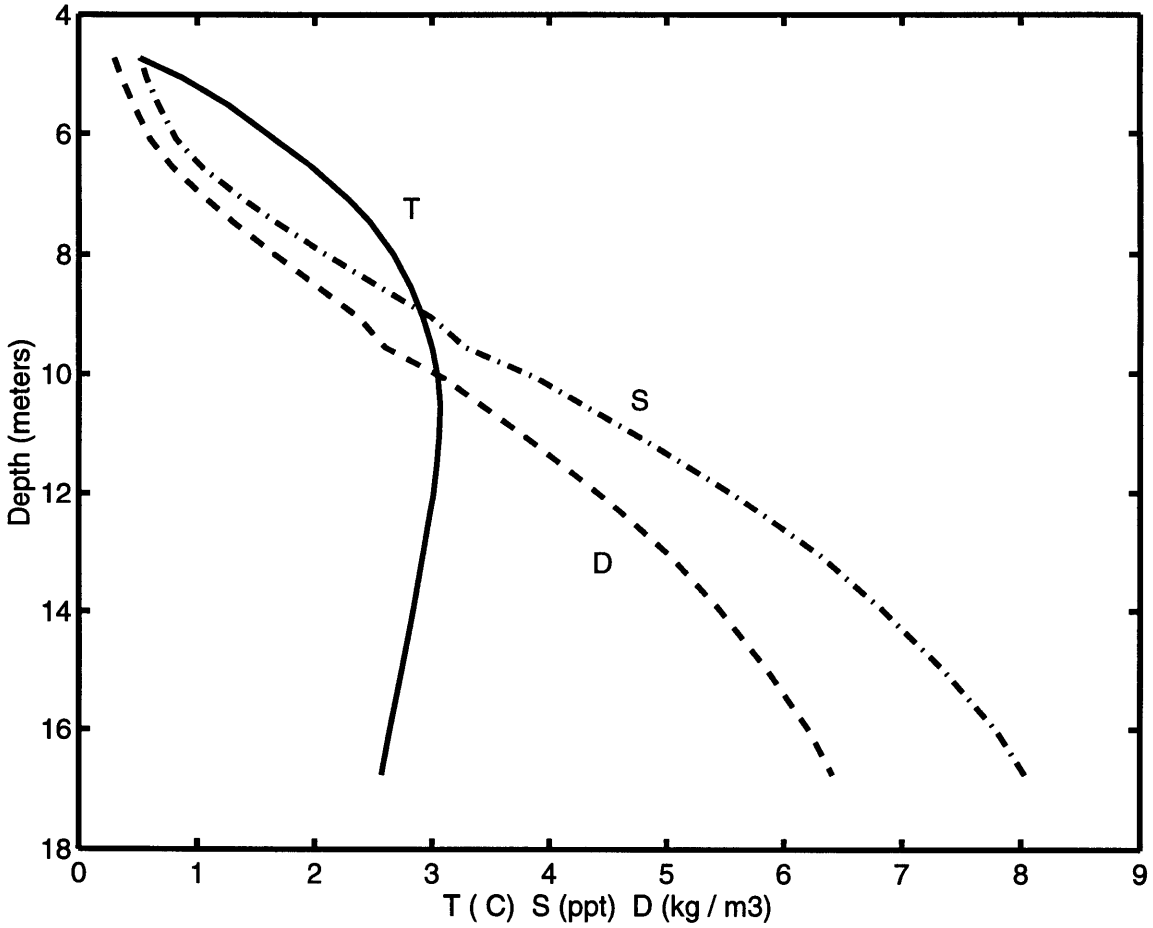

Figure 1 Profiles of temperature (line) in °C, salinity (dot-dashed line) in psu, and sigma theta in kg m^{-3} (dashed line).

Large supersaturations of several dissolved inert gases are observed at the ice-water interface of these lakes, due to the exclusion of the gases from the ice lattice as water freezes at the bottom of the ice cover (Burton 1981; Bari and Hallett 1974). As the dissolved gas concentrations in the water reach a critical supersaturation, bubbles form and become incorporated into the growing ice cover, and are eventually removed by ablation of the ice at the surface (Bari and Hallett 1974; Carte 1961). This is a major removal mechanism for gases from the lake.

The hydrological balances of these lakes are thought to be sensitive indicators of climate change on decadal timescales (Chinn 1993; Wharton et al. 1989), and because of the low vertical mixing rates and limited terrestrial inputs, the lakes provide model environments in which to study the biogeochemical cycles of carbon, methane, and sulfur in aquatic systems (Smith et al. 1993). However, the physical limnology of the lake, which impinges on the hydrological balances as well as the biogeochemical cycles, is not well understood. In this study we use the noble gases (He, Ne, Ar), helium isotopes, and tritium to examine the ventilation mechanisms and rates of Lake Fryxell and the physical processes affecting the dissolved gas cycles.

Methods

We measured the concentrations of the noble gases (He, Ne, and Ar) throughout the water column at 1 meter intervals at a station located over the deepest part of the lake basin. Multiple samples from each depth were collected from the center of the lake during the

1993-94 austral summer. Depths are referenced from the piezometric surface; i.e., the surface of the water in the drill hole. The ice-water interface is located at approximately 4.7m. Water samples for the helium isotopes and neon analyses were collected from Kemmerer bottles and stored in crimped copper tubes (Weiss 1969). Tritium samples were collected in 1 liter, treated Flint glass bottles fitted with high-density polyethylene caps. Argon was analyzed on site by gas chromatography, and has a measurement uncertainty of approximately 0.3%. Helium isotopes and concentrations were measured on a statically operated, magnetic sector, dual collecting mass spectrometer, and the Ne was measured by peak-height manometry using a quadrupole mass spectrometer (Lott and Jenkins 1984). Tritium was measured by the ^{3}He ingrowth technique (Clarke et al., 1976; Jenkins et al. 1983). Measurement uncertainties are ± 0.25% for Helium, ± 1% for Neon, and ± 0.01 T.U. for tritium.

Results

Dissolved Gases in the Upper Oxic Waters - Near the ice-water interface, argon is supersaturated with respect to solubility equilibrium with the atmosphere, similar to supersaturations of gases reported for other Antarctic lakes, (Craig et al. 1992; Wharton et al. 1993), while helium and neon are substantially undersaturated (Figs. 2a and 2b). We suggest that the latter is the result of the large partitioning of the sparingly soluble gases He and Ne between bubbles at the ice-water interface, coupled with the solubility of these gases within the ice itself (Kahane et al. 1969; Namoit and Bukhgalter 1965).

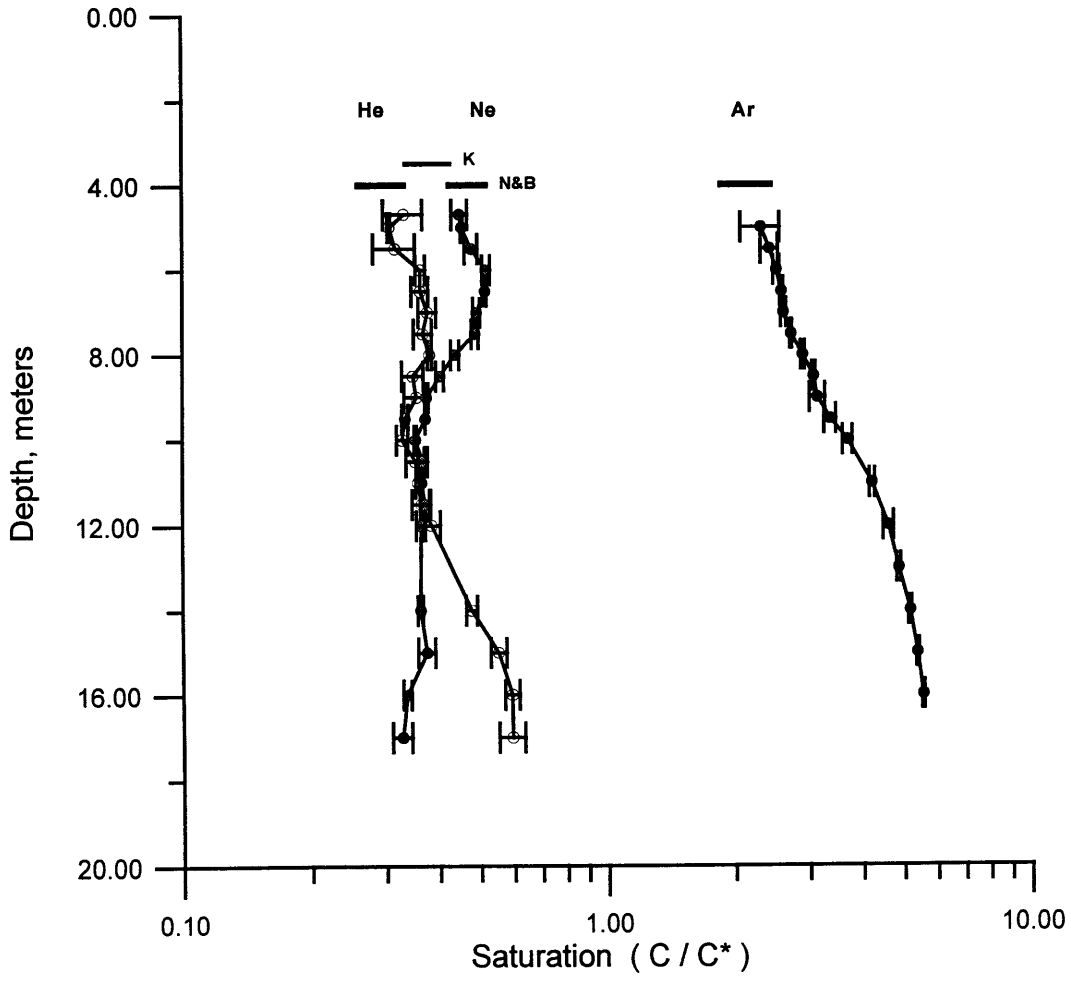

Figure 2a Profiles of He, Ne, and Ar, given as saturation with respect to solubility equilibrium (i.e. equilibrium = 1). Depth is referenced form the piezometric surface of the water. Saturations predicted by the 3-phase equilibrium distribution model at the ice-water are shown as bars at the top of each profile. For He and Ne, predictions using the solubility values of Namoit and Bukhgalter (1965) are shown. The uncertainties of the concentrations are calculated from the standard deviations of replicate samples for each depth. The partition coefficients were taken from the Bunsen solubility values reported by Weiss (1970 and 1971).

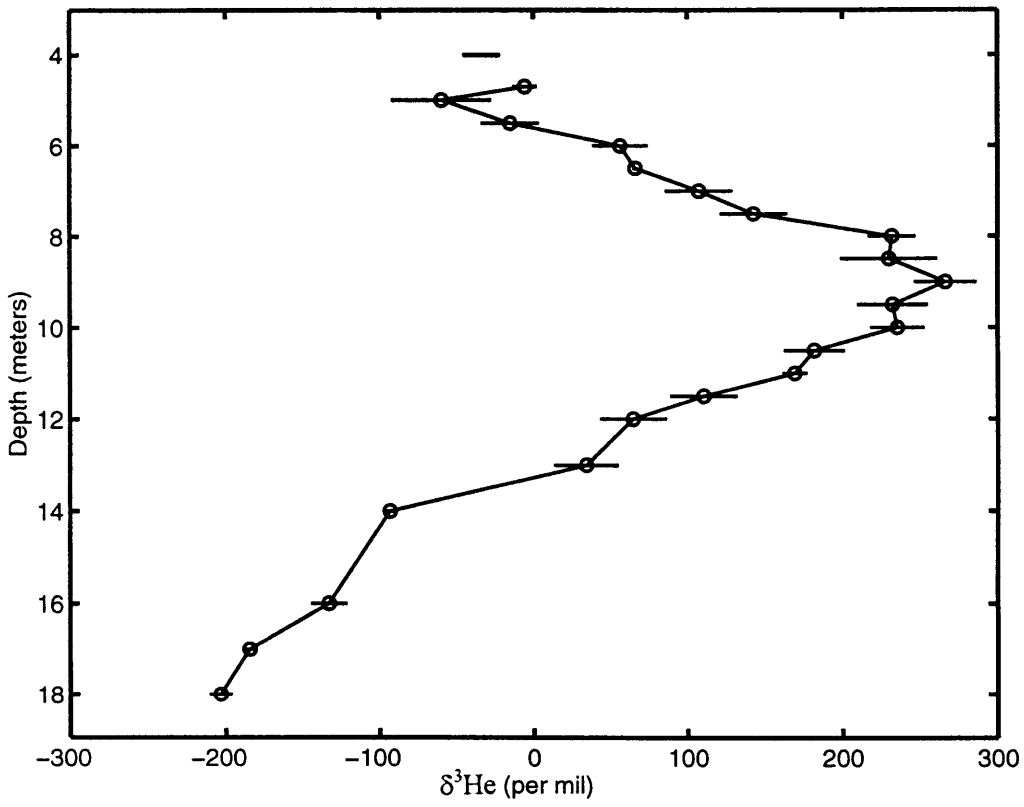

Figure 2b δ^3He profile: δ^3He=[(Rx/Ra)-1]*1000, where Rx=^{3}He/^{4}He sample, and Ra=^{3}He/^{4}He atmosphere. The model prediction of δ^3He at the ice-water interface is shown as a horizontal bar at the top of the profile. The helium isotope data is taken from Benson and Krause (1980).

In a relatively closed, three-phase system consisting of ice, air bubbles in the ice, and water, the water will become undersaturated in helium and neon with respect to solubility equilibrium with the atmosphere if it is not adequately ventilated. We propose that this is the case for helium and neon at the ice-water interface of Lake Fryxell.

Craig et al. (1992) measured the gas content of air bubbles within the ice-cover of neighboring Lake Hoare, and they presented a model calculation for the two-phase gas distribution for the gases at the ice-water interface. We extend the 2-phase equilibrium partitioning model to include a third phase of solution in ice for He and Ne, using the basic mass-balance equation:

$$C_{in}M_{in} = C_{rw}M_{rw} + C_iM_i + C_bV_b \qquad (6.1)$$

where M is the mass or volume of the reservoir and C is the concentration of the dissolved gas in the input water (C_{in}), the remaining input water (C_{rw}), the ice (C_i), and the air bubble (C_b). C_{in} is taken to be the equilibrium solubility of the gas with the atmosphere at 0°C.

The input volume of water to the Lake via meltstreams varies considerably from year to year (Lawrence and Hendy 1985). We thus present the masses and volumes of the system in relative terms that allow for calculations to be made without determining specific

volumes or masses. Approximately 80% of the incoming meltwater is frozen at the ice-water interface (Craig et al. 1992). We use a volume of bubbles in the ice equal to 14.2 $cm^3\ kg^{-1}$ of original input water, estimated using a gas partitioning of 20.6 cm^3 (STP) kg^{-1} of original input water (Craig et al. 1992), and corrected for an ambient pressure at the ice-water interface of 1.45 atm. The concentrations of the gases in each of the reservoirs are related by their equilibrium partition coefficients between the water, ice, and air bubbles in the ice (Table 1).

Partition	Argon	Neon (K)	Neon (N&B)	Helium
Bubble / Water	18.65	81.02	81.02	106.8
Bubble / Ice	∞	56.25	90.02	56.89
Ice / Water	0	1.4	0.9	1.9

Table 1. Equilibrium partition coefficients for He, Ne, and Ar in a three-phase system. Columns 2 and 3 show the coefficients calculated using the solubility values of Ne in ice from Kahane et al. (1969) and Namoit and Bukhgalter (1965), respectively. Partition coefficients were calculated using the Bunsen solubility coefficients of Weiss (1970 and 1971).

As far as we know, two sets of values for the solubility of helium and neon in ice are available. While the values of the solubility of helium in ice that are reported in these two references are in good agreement, the values for the solubility of neon in ice disagree. Kahane et al. (1969) report that, like helium, the ratio of the solubility of neon in ice to that in water is greater than one, while Namoit and Bukhgalter (1965) state that the ratio is slightly less than one. However, in this system, both sets of values predict the observations at the ice-water interface within the uncertainties of the mass balance calculation. We use both sets of solubility values throughout the work.

The partitioning of the gases between the three phases and the relation of the reservoirs as described by the mass balance equation provide a system of three equations that are solved to obtain the concentrations of the gases in each of the reservoirs. The dissolved gas concentrations at the ice-water interface predicted by this model for He, Ne, Ar, (Fig. 2a), and δ^3He (Fig. 2b) are in good agreement with the observed concentrations.

Table 2 contains model estimates of the gas saturations without dissolution in ice (removal by bubbles only) and without bubble formation (gas saturations prior to bubble formation), as well as a comparison of these estimates using different values of helium and neon solubility in ice.

	Observed	3 - phase (K)	3 - phase (N&B)	2 - phase	No Bubbles (K)	No Bubbles (N&B)
Helium	0.33 ± 0.04	0.30 ± 0.04	0.29 ± 0.04	0.63	0.54	0.51
Neon	0.45 ± 0.02	0.38 ± 0.05	0.47 ± 0.05	0.74	0.68	1.01
Argon	2.31 ± 0.005	2.15 ± 0.28	2.15 ± 0.28	2.15	5.0	5.0
Ne / He	1.36 ± 0.22	1.27 ± 0.31	1.62 ± 0.16			

Table 2. Comparison of observed gas saturations and model calculations. Saturations are reported as the ratio of the measured concentrations to the concentration at solubility equilibrium with the atmosphere. Column 1 shows the observed saturations at the ice-water interface. Columns 2 and 3 show the predicted three-phase system saturations using the solubility values of Ne in ice from Kahane et al. (1969) and Namoit and Bukhgalter (1965), respectively. Column 4 shows the predictions for the two-phase (bubble-water) case with no solubility of gases in ice. Columns 5 and 6 show the predicted saturations for freezing with no bubble formation.

The saturations of helium and neon are consistent with a three-phase equilibrium balance, while the two-phase systems substantially overpredict the saturations. We stress that this equilibrium partitioning process must be viewed as an annual net effect. During initial

ice formation, the gas saturations result from partitioning between ice and water. Upon nucleation of bubbles at the ice-water interface, the gases are further partitioned into the bubble phase. However, the strong, stable stratification of the lake and the tritium - ^{3}He age profile (Fig. 3a, discussed in more detail later) suggest little vertical mixing. The saturations generated at any stage of the annual freezing process are, therefore, unlikely to be mixed significantly below the interface, and the molecular diffusive timescales of the gases are not sufficient to transport the gases more than a fraction of a meter over the course of a year. We interpret the net annual partitioning of gases near the ice-water interface as an essentially closed system in which the initial meltwater input remains very near the ice-water interface throughout the freezing cycle. Additionally, because the partitioning of the gases into the bubble phase is dominant, the discrepancy between the two solubility values for Ne in the ice phase becomes indistinguishable within the uncertainties of the mass balance calculation.

We suggest that small variations in saturations seen in the profiles in the upper waters below the ice-water interface may be the result of changes in the meltwater input volume, freezing, the bubble volume in the ice, or melting of the ice at the interface. For instance, increases in Ne and He seen between 6-8 meters may be caused by melting of the ice cover, or a period of decreased freezing relative to meltwater input. Tritium-^{3}He ages show the 6-8 meter water to be approximately 10 years old. Chinn (1993) reports that the ice cover of Lake Fryxell thinned approximately 2m over a period approximately 10 ybp. However, the quality of the data presented here is not sufficient to discriminate between

these processes, and both long and short-term variability in the hydrological parameters of the lake can easily generate saturation changes of the sizes observed. Given the data and the constraints on the hydrological system at hand, we can only suggest that the general mechanism that controls the saturations of the inert gases at the ice-water interface appears to be the partitioning of the gases between the water, air bubbles in the ice, and for helium and neon, the ice matrix itself.

Dissolved Gases in the Anoxic Bottom Waters - We will focus first on the concentrations of Ar and Ne, and then discuss the helium concentrations, which respond to additional processes in the bottom waters. The Ar concentrations increase to approximately 5.75 times greater than solubility equilibrium, while the Ne concentrations decrease further to 0.33 times the solubility equilibrium. We calculate that the production of ^{40}Ar by the decay of ^{40}K in 230 meters of sediment below the lake is approximately 1×10^{7} atoms m^{-2} s^{-1} . The observed gradient of Ar in the bottom water implies a minimum upward flux (assuming the vertical mixing to be no greater than molecular diffusion) of approximately 7×10^{12} atoms m^{-2} s^{-1} , which is 5-6 orders of magnitude larger than can be supported by ^{40}K decay from the sediments.

The deep supersaturation of argon could be the result of bottom water that was created at some time in the past by slightly different freezing processes at the ice-water interface. We describe below one possible scenario for an alternative freezing processes at the ice-water interface, and constrain and support this scenario using the concentrations of the

dissolved gases and the balance between the hydrostatic pressure and total dissolved gas pressure; the latter determines whether and to what extent bubble formation will occur. The presence or absence of bubble formation in the ice is of paramount importance in these calculations, as it determines the extent to which gases will be concentrated and fractionated. The scenario has implications for changes in the hydrological balance of the system that are required to produce these observations, and these implications are discussed. We stress, however, that due to the unconstrained nature of the system and the limited data at hand, definitive explanations for the observations are not possible at this time.

To determine the total dissolved gas pressure for the system, it is necessary to include measurements of O_2 and N_2. Table 3 shows concentrations of the major and noble gases in the surface and bottom waters..

	Nitrogen	Oxygen	Argon	Ar / N_2	Neon
Surface	0.015 ± 0.004	0.029 ± 0.002	1.2×10^{-3} ± 1×10^{-4}		1.04×10^{-7} ± 2×10^{-9}
Saturation	0.8 ± 0.2	2.9 ± 0.2	2.3 ± 0.2	2.9 ± 0.8	0.45 ± 0.02
Deep	0.0318 ± 0.0007	0	2.46×10^{-3} ± 2×10^{-5}		8.15×10^{-8} ± 2×10^{-9}
Saturation	1.95 ± 0.04	0	5.64 ± 0.04	2.89 ± 0.06	0.33 ± 0.02

Table 3. Concentrations of the major dissolved gases in the surface and bottom waters. Concentrations are given in cc (STP) g^{-1}, and saturations are calculated as C / C*, where C is the concentration of the gas in the water, and C* is the concentration at solubility equilibrium with the atmosphere.

Nitrogen, oxygen, and argon constitute approximately 99% of the total dissolved gas load. The N_2 undersaturation at the ice-water interface could result from a combination

of biological processes and interactions with the ice, but will be the subject of a future paper and will not be discussed further here. We assume in our calculations that N_2 behaves as an inert gas that is not soluble in the ice. As discussed in the previous section, the He, Ne, and Ar are well -predicted by the 3 phase model, providing some confidence that the system is in approximate balance between the total dissolved gas pressure and the hydrostatic pressure at the ice-water interface. The hydrostatic pressure at the ice-water interface (~5 m) is approximately 1.45 atm. The equilibrium total dissolved gas pressure is determined by the hydrostatic pressure and the pressure required for heterogeneous bubble nucleation, which is often in slight excess of hydrostatic pressure in natural systems (Bari and Hallet 1974, Swanger and Rhines, 1972). Instead, we use the observed concentrations of the major gases at the ice-water interface to determine a "stability gas load" for the system, and use this as a reference equilibrium value at the ice-water interface. The total dissolved gas concentration at the ice-water interface is approximately 4.52×10^{-2} cc(STP) g^{-1}. If freezing were to continue, the total gas concentration in the water must remain at or near this stability gas load, with any excess due to increased freezing being removed by further bubble formation. The only way to increase inert gas concentrations in a closed system is to remove one or more of the major gases by another mechanism, thus lowering the total dissolved gas concentration and allowing the other gases to increase until the sum of the partial pressures of the remaining gases equals the stability gas load.

Comparison of surface and bottom water concentrations show a dramatic decrease in O_2 concentrations and a concomitant rise in concentrations of N_2 and Ar. One possible scenario to explain these observations begins with the assumption that at some point in the past, the ice-water interface was near the level of anoxia. Meltwater enters the lake with solubility equilibrium gas concentrations. Freezing begins, and the gases become concentrated until the critical dissolved gas pressure for bubble formation is reached. Bubbles form, and the gases are removed and fractionated according to their partition coefficients in the same manner described for current processes. The oxygen remaining is consumed or significantly reduced, and the total dissolved gas pressure decreases to below the critical dissolved gas pressure for bubble formation. Freezing thus continues with no bubble formation, creating the large saturations of Ar and N_2 observed in bottom water.

The surface and bottom water dissolved gas concentrations can be used to support and constrain this mechanism. In the bottom water, the O_2 concentrations go to zero, decreasing the total dissolved gas concentration to approximately 3.90×10^{-2} cc(STP) g^{-1}, which is not sufficient for bubble formation. The Ar / N_2 ratio has the same value in both surface and bottom waters, implying that the only fractionation mechanisms are those occurring presently at the ice-water interface. Taking the surface water concentrations of Ar and N_2 and calculating the amount of water that must be frozen with no bubble formation to produce the bottom water concentrations, we find that only an additional ~10% of the original meltwater input would have had to be frozen. Clearly, generating

the bottom water saturations in this manner does not require drastic changes to the current system.

An additional constraint is the concentration of Ne in the bottom water. While Ar and N_2 concentrations would simply increase due to freezing with no bubble formation, Ne would still be removed from the system due to its solubility in the ice. Using the above scenario and calculating the volume of ice formed from the additional freezing with no bubble formation, we estimate that the Ne concentration in the residual water should be approximately 33±2 % of solubility equilibrium (using the solubility values of Kahane et al. 1969), which is in excellent agreement with our observations (Table 3 and Fig. 2a). Using the solubility values of Namoit and Bukhgalter (1965), we estimate a Ne concentration of 42±2 % of solubility equilibrium, which is inconsistent with our observations.

While the required changes in the individual lake processes are not large, they do imply that the hydrological *balance* of the system has changed significantly over the history of the lake. For example, the requirement that the ice-water interface be near the level of anoxia at the time the bottom water concentrations were generated could be met in several ways. If conditions in the dry valleys were such that the ice cover became significantly covered with snow relative to present conditions, the albedo of the area would be reduced, and the meltwater entering the lake would decrease. Due to the imbalance of water input and freezing, the lake level would decrease and the ice thickness

would increase. The light penetrating the ice-cover would be reduced due to the increased thickness and snow cover, and the biological productivity of the lake would most likely decrease. These responses would serve to move the ice-water interface down toward the level of anoxia, currently at about 9 meters. The response of lake levels to changes in climate is very complex in the dry valleys areas (Chinn 1993), and the above scenario should only be viewed as an illustration of possible processes that could generate the observations.

The bathymetry of the lake also includes a pronounced shelf at the 9 meter level, which may indicate the level at which the ice-water interface rested at some time. This speculation is supported by paleoclimatic theories (Wilson 1964) that the lakes experienced a near-desiccation event, before re-expanding to their present size at about 1200 ybp. The re-expansion is presumed to have happened fairly rapidly, which would create an abrupt step-function in the concentrations of the dissolved gases between the homogeneous bottom waters and the new input water. This step function would, over time, diffuse into a profile resembling the observed shape of the argon and density profiles.

Additional mechanisms are required to explain the helium concentrations. Helium increases in the bottom water, rather than decreasing like neon as the model predicts, and the observed $^{3}He/^{4}He$ ratios (Fig. 2b) require a non-atmospheric helium flux into the

bottom of the lake. Assuming that vertical transport is limited to molecular diffusion (see below), we calculate a ^{4}He flux of at least $2.3 \pm 0.4 \times 10^8$ atoms m^{-2} s^{-1}, and a ^{3}He flux of approximately 2×10^2 atoms m^{-2} s^{-1}. We calculate that the ^{4}He flux can be supported by decay of U and Th in 230m of lake sediments, consistent with the thickness observed in the Dry Valley Drilling Project drill holes in the area (Purucker et al. 1981). However, the ^{3}He/^{4}He ratio is $9 \pm 1 \times 10^{-7}$, which is much greater than a radiogenic production ratio (Andrews 1985), thus requiring an additional source for the ^{3}He. We contend that the ^{3}He could be supported by loss of cosmogenic ^{3}He from the bottom sediment, which enters the lake with glacial meltwater during the summer. The cosmogenically produced ^{3}He concentration in Dry Valley sediments is $650 \pm 137 \times 10^6$ atoms/g (Brook and Kurz 1993). The observed flux of ^{3}He in the lake is consistent with a loss rate from the sediments of only 3% per million years, which is smaller than the predicted loss rate of 10% per million years (Trull et al. 1991). While the Dry Valley sediments analyzed may not be representative of those at the bottom of the lake, the above calculations and the pronounced ^{3}He gradient in the bottom water are consistent with input of ^{3}He from the sediment.

Ventilation Rates and Mechanisms - While the relatively homogeneous vertical profile of tritium in the upper water (Fig. 3b) is suggestive of rapid vertical mixing, it is most likely

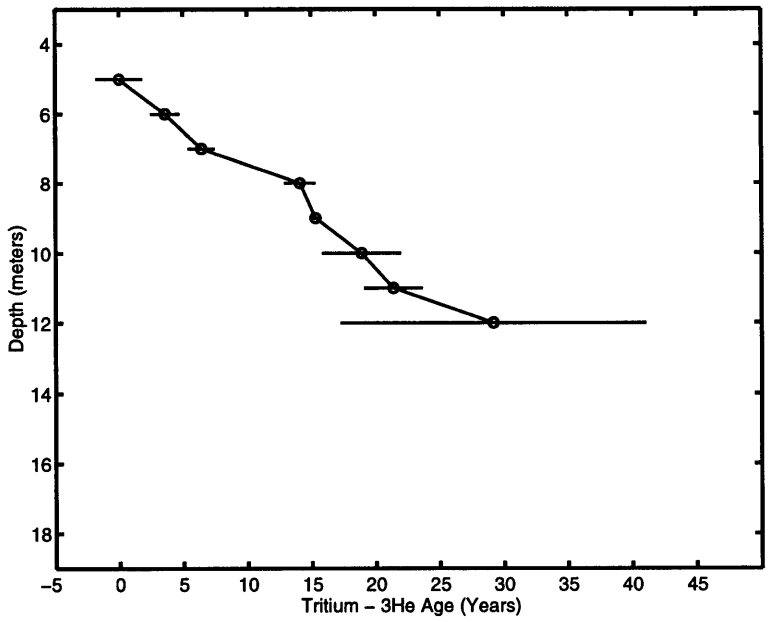

Figure 3a Tritium-^{3}Helium "age" = 17.96 ln(ξ / θ), where ξ is the sum of the tritium and the excess ^{3}He concentrations, and θ is the tritium concentration.

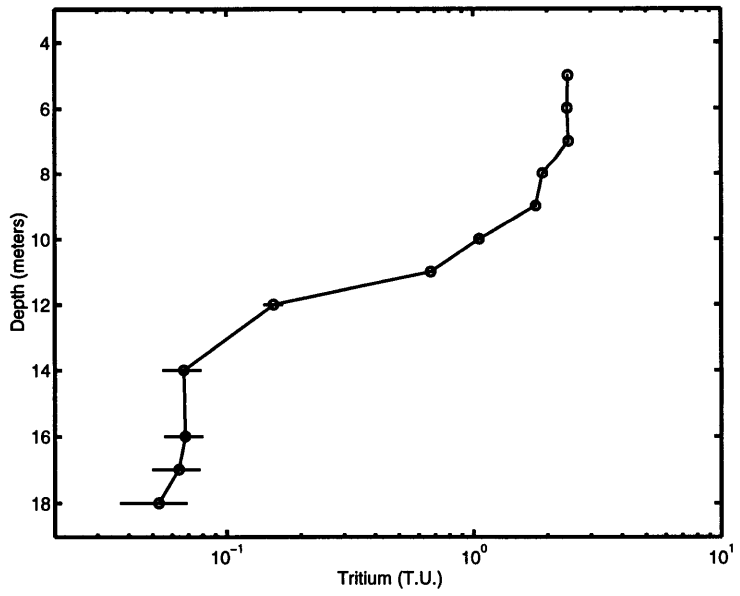

Figure 3b Tritium profile. 1 Tritium Unit (T.U.) = $^{3}H/^{1}H*10^{18}$. The scale height of the tritium concentration gradient is calculated using $(\kappa/\lambda)^{-½}$, where κ is the diffusion coefficient and λ is the decay constant for tritium.

the result of a temporal decrease in tritium input to the lake that is approximately equal to decay (half life = 12.43yrs). The pronounced vertical gradient in the tritium-^{3}He age profile (Fig. 3a) is inconsistent with rapid vertical mixing, and is qualitatively consistent with ventilation times of the upper lake ranging from a few years at the ice-water interface to several decades at the base of the oxic layer. Below this depth, it is not meaningful to date the water using the tritium-^{3}He age method. Green et al. (1989) estimate an age of a few thousand years for the bottom water of Lake Fryxell, based on the chloride budget for the lake. There is an abrupt change in the tritium concentration between the upper and lower layers of the lake, with a scale height of 1-2m, consistent with vertical mixing that is not much greater than molecular diffusion.

Within the anoxic waters, the average tritium concentration is 0.063 ± 0.007 T.U., more than 6 times the detection limit for the measurements and more than 25 times potential contamination levels (Jenkins et al. 1983). This relatively homogeneous vertical profile of tritium in the bottom water requires a mechanism that delivers tritium directly to the bottom water, yet does not disturb the diffusional gradients observed for the inert gases. This could be explained by a weak ventilation process which occurs when relatively dense water is created at shallow lake margins due to ice formation, where the residual dense water is trapped between the advancing ice front and the lake bottom, and becomes concentrated as freezing progresses. The ice around the margin of the lake grounds from the lake edge inward, causing the brine to move along the basin edges and sink to a level

of neutral buoyancy. Evidence of this type of haline circulation has been found in other Antarctic saline lakes (Ferris et al. 1991). To prevent significant disturbance of the gradients in the bottom water, this ventilation mechanism must be weak relative to the timescale of vertical exchange.

By reconstructing a time history of tritium in the surface water of the lake, we can estimate the ventilation rate for the deep water that is required to create the current concentrations of tritium in the bottom water. The meltwater input to the lake is predominantly from glacial meltwater, with a small additional volume from snow melt. The time history of tritium in the surface water is a function of the concentration of tritium of the glacier meltwater and the time history of tritium in local precipitation. We measured an average tritium concentration of 0.104 ± 0.02 T.U. for the Canada Glacier, and 2.51 ± 0.03 T.U. for the input (moat) water of Lake Fryxell. Precipitation in Antarctica has returned to background (pre-bomb) tritium concentrations (Jouzel et al. 1982), having an estimated value of approximately 23± 1 T.U. for the Dry Valleys. Using these values, we calculate an input water ratio of glacier meltwater to snow meltwater of approximately 10:1. The uncertainty in this estimate is on the order of 50%, based on variability in individual tritium measurements in precipitation from the South Pole (Jouzel et al., 1982). This variability is most likely due to seasonal variation in precipitation and deposition of tritium.

To a first approximation, the tritium concentration of the input water to the lake can be scaled to the history of tritium deposition at the South Pole, using the records of Jouzel et al. (1979), and the equation:

$$C_w^i = C_g \cdot \frac{V_g}{V_g + V_p} + C_w^0 \cdot \frac{D_{sp}^i}{D_{sp}^0} \tag{6.2}$$

where Cw is the concentration of tritium in the input water to the lake at time step i, Cg is the concentration of tritium in the glacier, Cw^0 is the concentration of tritium in the input water to the lake at steady-state (pre-bomb) tritium concentrations, and Dsp and D^0sp are the deposition of tritium (in meters x T.U./year) at the South Pole for time step i and at steady-state, respectively. We linearly interpolate the record from 1977 to 1995, using current (i.e. background) values of tritium in precipitation at the South Pole (Jouzel et al., 1982). The reconstructed time history of tritium in the input water to the lake is shown in Fig. 4. Based on the fractionation of hydrogen during freezing (Weston 1955), we estimate that tritium should be enriched in the ice relative to the water by approximately 4%. The input water values are adjusted for this effect prior to delivery to the bottom water. Because the concentration of tritium in the glaciers is only approximately 4% of the concentration of the input water, uncertainties in the estimate of the ratio of the volume of input water from glacial melt to the total volume of input water contributes an uncertainty to the input water concentration of about 2%. The overall uncertainty in the estimate of the time history of tritium in the input water to the lake is predominantly from the uncertainty in the measurements of the deposition of tritium at the South Pole, which is approximately 25%.

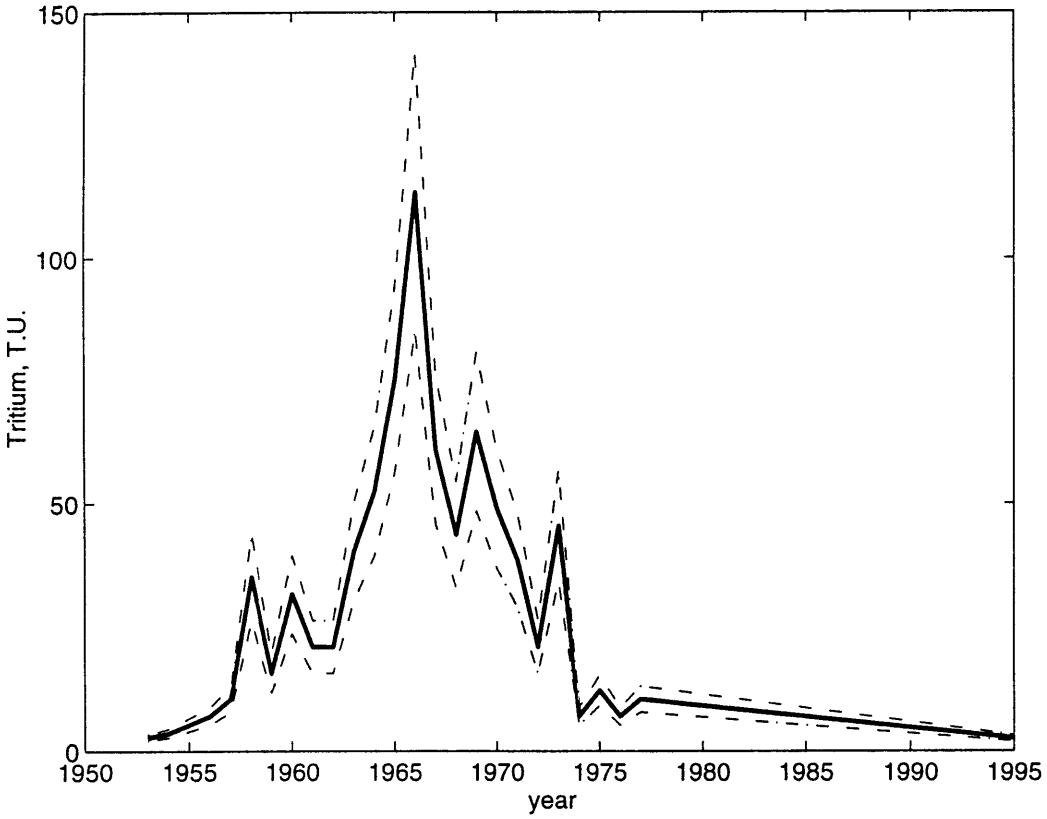

Figure 4 Constructed tritium history for the input water. Uncertainties are shown as dashed lines.

Time history of tritium in the bottom water- The tritium record in the bottom water of the lake is a function of the surface water concentration history, decay of tritium, and the turnover time, given by:

$$\frac{\partial C_b}{\partial t} = \frac{(C_s - C_b)}{\tau} - \lambda C_b \tag{6.3}$$

where C_b is the bottom water concentration, C_s is the surface water concentration corrected for fractionation effects, λ is the decay constant for tritium (0.0558 yr^{-1}), and

τ is the turnover time in years. To describe this process, we use a finite difference scheme:

$$C_b^{(i+1)} = (1-\lambda\Delta t)\cdot C_b^{(i)} + \frac{\Delta t}{\tau}\cdot(C_s^{(i)} - C_b^{(i)}) \tag{6.4}$$

where the superscripts (i) and (i+1) represent current and successive time-steps, and Δ t is 1 year. The concentration of the bottom water at steady state (pre-bomb) is given by:

$$C_b^0 = \frac{C_s^0}{1+\lambda\tau} \tag{6.5}$$

where Cb^0 and Cs^0 are the initial steady-state concentrations, with Cs^0 estimated from equation 5 for pre-bomb values of tritium in precipitation. The turnover time for the bottom water of the lake was determined by choosing the value of τ that results in the best approximation of the current tritium observations of 0.063 ± 0.007 T.U. The model was integrated from 1953, prior to bomb tritium reaching Antarctica, to the present in time increments of one year. Our calculations estimate a turnover time of 3800 years. By running the model with the maximum and minimum possible values of surface water tritium concentrations, we obtain a range of the turnover time from 2600 years to 5300 years. The turnover time should not be regarded as an age of the bottom layer of the lake, but rather the renewal time associated with one mechanism of ventilation that has been operating over at least the last 2-3 decades. Comparison of this time to age estimates of a few thousand years (Green et al. 1989) suggests that the ventilation of the bottom water may have changed considerably over time. The fact that the tritium profile in the bottom

water is relatively homogeneous is a reflection of the relative, evenly distributed, rates of ventilation as a function of density, rather than an indication of vertical mixing. The diffusion-length timescale associated with the development of the observed ^{4}He gradient is approximately 350 years, which is an order of magnitude faster than the estimated ventilation time, suggesting that this ventilation mechanism would not significantly disturb the dissolved gas gradients.

Using the estimate of the turnover time and an estimate of the volume of the bottom of the lake between 12-18 m, as taken from the bathymetry data of Lawrence and Hendy (1985), we estimate an upper limit for the yearly volume delivery to the bottom water via this ventilation process of approximately 5 x 10^5 liters. This volume must come from water remaining after freezing in the shallow margins of the lake. To estimate the original volume of water prior to freezing required by this ventilation mechanism, we use the salinity budget for the system. Green et al. (1988) report chloride concentrations of the inflow streams of 0.271mM, compared with concentrations at 17m of 102 mM. The bottom water concentration may be obtained by freezing approximately 99.75% of a volume of water at the stream inflow concentrations. We assume, as a first approximation, that the concentration of the residual brine in the shallow water is equal to that in the bottom of the lake, and we estimate that the volume of water required to produce the required volume of brine after freezing is approximately 2 x 10^8 liters. We estimate the volume of water shoreward of the 3 meter isobath, i.e. where grounding of

the ice is most likely to occur, to be approximately 5 x 10^9 liters. Thus, the proposed ventilation mechanism would require only about 4 % of this available volume.

Implicit in this calculation, however, is the assumption that the brine from the margins remains unmixed as it sinks to the bottom. This is clearly not a very realistic situation, and it implies that if mixing is occurring, the concentration of the brine in the margins would have to be substantially greater than that of the bottom water before sinking. Because the volume of the original water at stream input concentrations has already been reduced by approximately 99.75% to achieve the concentrations observed in the bottom water, a further increase in the brine concentration would most likely require multiple freezing stages, i.e. freezing water in shallow depressions of the margins that had already been concentrated by a prior freezing event. The bathymetry (Lawrence and Hendy 1985) indeed shows many shallow depressions around the periphery of the lake where such events could potentially occur, but more quantitative information about the likelihood of this mechanism is not possible with the present information. Additionally, the estimate assumes that the concentration of the brine in the bottom water is only the result of this dense water formation process in the margins of the lake and not residual brine from a prior desiccation event. With the available data and the volume constraints of the system, the proposed ventilation mechanism appears likely, but a more rigorous analysis is not possible at this time.

The consequence of this flux of water to the bottom of the lake is that there must be an upward advection of water to balance it. We calculate an upward advection of between 1 and 2 m kyr^{-1} near the top of the anoxic layer, which is not strong enough to greatly disturb the strong gradients within the lake, but which may partly explain the observed curvature in the dissolved gas profiles.

Summary and Conclusions

The lack of significant vertical mixing within Lake Fryxell provides a unique environment in which the noble gases and tritium can be used to examine the current physical processes affecting dissolved gas cycles and ventilation rates, and also to reconstruct processes that may have affected the lake over hundreds to thousands of years ago. The oxic layer is ventilated on the timescale of several decades. The linear trend of the tritium - ^3He age profile indicates that the water column is highly stratified, even in the upper few meters of the water column below the ice. This information, along with the 3- phase equilibrium partitioning model presented can be used to characterize the cycles of the noble gases in this system, which can provide constraints on the cycles of other dissolved gases, such as N_2 and O_2, as well as provide the framework for future investigations of primary productivity in the lake.

To the best of our knowledge, the effects of the combined processes of uptake by bubbles and solubility of He and Ne in ice have never been observed on such a large scale in

nature. These effects are quite dramatic here due to the unique, insulated nature of a permanently ice-covered, highly stratified lake. The undersaturations of He and Ne at the ice-water interface provide a striking contrast to the supersaturations of the heavier gases. Top et al (1983) first recognized ice formation effects on the noble gases in natural aquatic systems, and they suggested that this anomaly may have applications as a water mass tracer. Schlosser (1986) demonstrated the potential of using supersaturations of ^4He from the melting of ice as a tracer of ice-water interactions. These same processes of equilibrium distribution control the dissolved gas cycles in all aquatic systems where ice formation occurs, but the anomaly may vary between systems due to differences in the environment and ice structure.

In the bottom water, the lack of information about the system prevents more definitive conclusions, but our proposed scenario appears consistent with the available information. For a more complete treatment, it would be necessary to estimate the budgets of O_2 and carbon in the lake under the proposed conditions in order to determine if a limited amount of biological productivity or a chemical sink could remove a significant portion of the O_2 entering the system with fresh meltwater input. It would also be necessary to determine whether the lowering ice-water interface was from an increase in the ice thickness, or a total lowering of the entire ice-lake water system. This would have bearing on the hydrostatic pressure at the ice-water interface, which determines whether or not bubbles will form and fractionate the gases. In general, we suggest the bottom water dissolved

gas concentrations are largely relict concentrations that resulted from a hydrological balance of the system quite different than that operating today.

Chapter 7

Dissolved Gas / Ice Interactions in Saroma-Ko Lagoon

7.1 *Introduction*

Recent work (Schlosser, 1986; Top et al., 1988; Schlosser et al., 1990; Hood et al., 1997) suggests that the noble gases (He, Ne, and Ar) have potential as tracers of the interactions between dissolved gases and ice, and as tracers of water masses that have been influenced by the formation or melting of ice. Such tracers would provide unique and important information into processes such as dense water formation processes, ventilation processes in ice-covered areas, and the transport pathways and fluxes of biogeochemically important gases such as CO_2, CH_4, O_2, and DMS.

The purpose of this study of the dissolved gases in the Saroma-Ko lagoon during the ice-covered season is to explore the potential of the noble gases as a tracers of the

interactions between dissolved gases and ice in the ocean environment. This study is a preliminary survey to determine if anomalous noble gas concentrations are in fact present in the lake during the ice-covered period, and if these concentrations can be directly linked to interactions with the ice. Using this information, further studies can be planned to more completely characterize the exact nature of the process, which is necessary before the anomaly could be fully utilized as a tracer.

In order to characterize the interactions of dissolved gases and ice, it is necessary to examine these processes in a type of natural laboratory, where the signals are likely to be strong, and where the factors affecting the system can be estimated and quantified. While laboratory measurements of these effects may provide useful information (Top et al., 1988), it is vitally important to study the dissolved gas - ice interactions in the natural environment, where parameters such as the freezing rate and composition of the ice and water are representative of the oceanic environment. Saroma-Ko lagoon offers such an environment.

The Saroma-Ko lagoon is located on the Okhotsk sea coast of Hokkaido, Japan (Figure 7.1). It has a surface area of approximately 150 km^2, with a maximum depth of 19.5 meters, and an average depth of 14.5 meters (Shirasawa et al., 1992). The lagoon has a total volume of approximately 1.3 x 10^9 m^3, and is connected to the Sea of Okhotsk by two inlets. Approximately 90% of the tidal exchange occurs through the first inlet. Twenty two rivers drain into the lagoon, with an annual discharge of 3 x $10^8 m^3$ yr^{-1}.

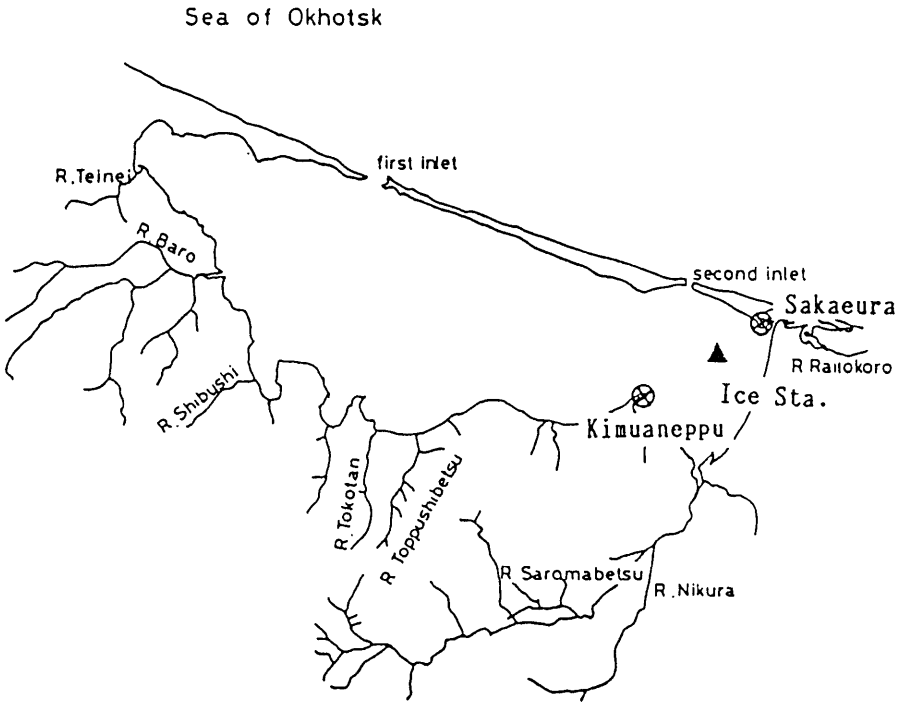

Figure 7.1 Map of Saroma-Ko Lagoon; adapted from Shirasawa et al. (1992).

In the summer, the lagoon is strongly stratified and eutrophic, and the fresh water discharge into the lake has a vertical influence of less than 3 meters across the lagoon. The tidal interchange for the average tidal range of 1meter is approximately 1 x $10^8 m^3$ through the first channel, and 1 x 10^7 m^3 through the second. The average residence time of water in the lagoon is 2-3 weeks (Takeuchi, 1993).

The lagoon is ice-covered from early February until early April most years. The Sea of Okhotsk adjacent to the coast (measured within a 30 nautical mile radius from the lagoon) is also ice-covered for this period. The duration of ice coverage between the lagoon and

the coast is highly correlated, and differs by only a few days (Shirasawa, 1993). The average ice thickness is 50cm. The maximum tidal range during the ice-covered period is 0.8 meters. The tidal cycle varies over the ice-covered period, from a typically semi-diurnal tide to a completely diurnal signal. The average current speed below the ice is approximately 4.2 cm/s with little variability. Sudden, regular changes in direction are synchronous with diurnal high tide. The overall circulation pattern changes continually over the ice-covered period, with current direction changes exhibiting a slow, steady counter-clockwise rotation (Shirasawa et al., 1992).

In the spring and summer months, the water mass structure is strongly affected by exchange with the Sea. In the spring, the Soya Warm Water is dominant along the coast, and the bottom water of the lagoon shows variations similar to coastal conditions. In the fall, the Sakhaline water, with a temperature of 15°C and salinity of 34 psu enters the lagoon. During the ice-covered period, the lagoon is less affected by coastal water masses, and maintains a stable Winter Water Mass, with a temperature of -1.7° C and 32 psu (Fujiyoshi et al., 1993).

7.2 *Results*

Samples were taken by Kunio Shirasawa, Mitsuo Ikeda, Masao Ishikawa, and Tohru Takatsuka of the Sea Ice Research Laboratory, Hokkaido University, on March 25th, 1996 from Station 1, located at 44°06.8' N, 143°57.7'E. The water depth at the station is

6.97 meters, and the ice thickness was 0.59 meters, with a freeboard of 0.55 meters. Tables 7.1a, 7.1b, 7.1c, and Figure 7.2 show the concentrations and saturations of He, Ne, and Ar in Saroma-Ko.

depth, m	Helium	+/-	Neon	+/-	Argon	+/-
0	5.21e-8	7e-10	2.31e-7	3e-9	4.89e-4	3e-6
1	4.42e-8	1e-10	1.928e-7	5e-10	4.09e-4	2e-6
2	4.63e-8	7e-10	2.00e-7	3e-9	4.12e-4	4e-6
3	4.37e-8	7e-10	1.91e-7	3e-9	4.07e-4	4e-6
4	4.54e-8	1e-9	1.97e-7	3e-9	4.17e-4	3e-6
5	4.41e-8	7e-10	1.94e-7	3e-9	4.07e-4	4e-6

Table 7.1a. Concentrations of dissolved He, Ne, and Ar in Saroma-ko. Concentrations are given in cc (STP) / g. Uncertainties represent the standard deviation of the mean of the replicate samples at each depth. Where only one sample is available, the uncertainty is the average of the sample standard deviations of the set of samples.

depth, m	Helium	+/-	Neon	+/-	Argon	+/-
0	1.09	0.01	1.05	0.01	1.009	0.006
1	1.083	0.002	1.055	0.003	1.033	0.005
2	1.13	0.02	1.10	0.02	1.05	0.01
3	1.08	0.02	1.05	0.02	1.04	0.01
4	1.12	0.02	1.09	0.02	1.066	0.008
5	1.09	0.02	1.07	0.02	1.04	0.01

Table 7.1b. Saturations of He, Ne, and Ar in Saroma-ko. Saturation is defined as the measured concentrations divided by the concentration of the gas at solubility equilibrium with the atmosphere. Solubility values are from Weiss (1970, 1971).

Cast	Bottle	Depth	He e-8 cc/g	Ne e-7 cc/g	Ar e-4 cc/g	comments
1	1	1	4.43	1.93	4.11	
1	2	1	4.41	1.92	4.07	
2	1	2	4.63	2.00	4.12	
2	2	2	N/A	N/A	N/A	leak
3	1	3	N/A	N/A	N/A	system failure
3	2	3	4.37	1.91	4.07	
4	1	4	4.64	2.00	4.20	
4	2	4	4.44	1.94	4.14	
5	1	5				tube broke
5	2	5	4.41	1.94	4.07	
6	1	0	5.14	2.28	4.87	
6	2	0	5.28	2.34	4.93	

Table 7.1c. Concentrations of dissolved He, Ne, and Ar in Saroma-Ko for all samples analyzed. Concentrations are given in cc (STP) / g. Uncertainties for individual measurements are approximately 0.2%. Uncertainties reported in Table 1a represent the standard deviation of replicate samples at each depth. Where only one sample was analyzed, the uncertainty is the average of the standard deviation of all replicate samples.

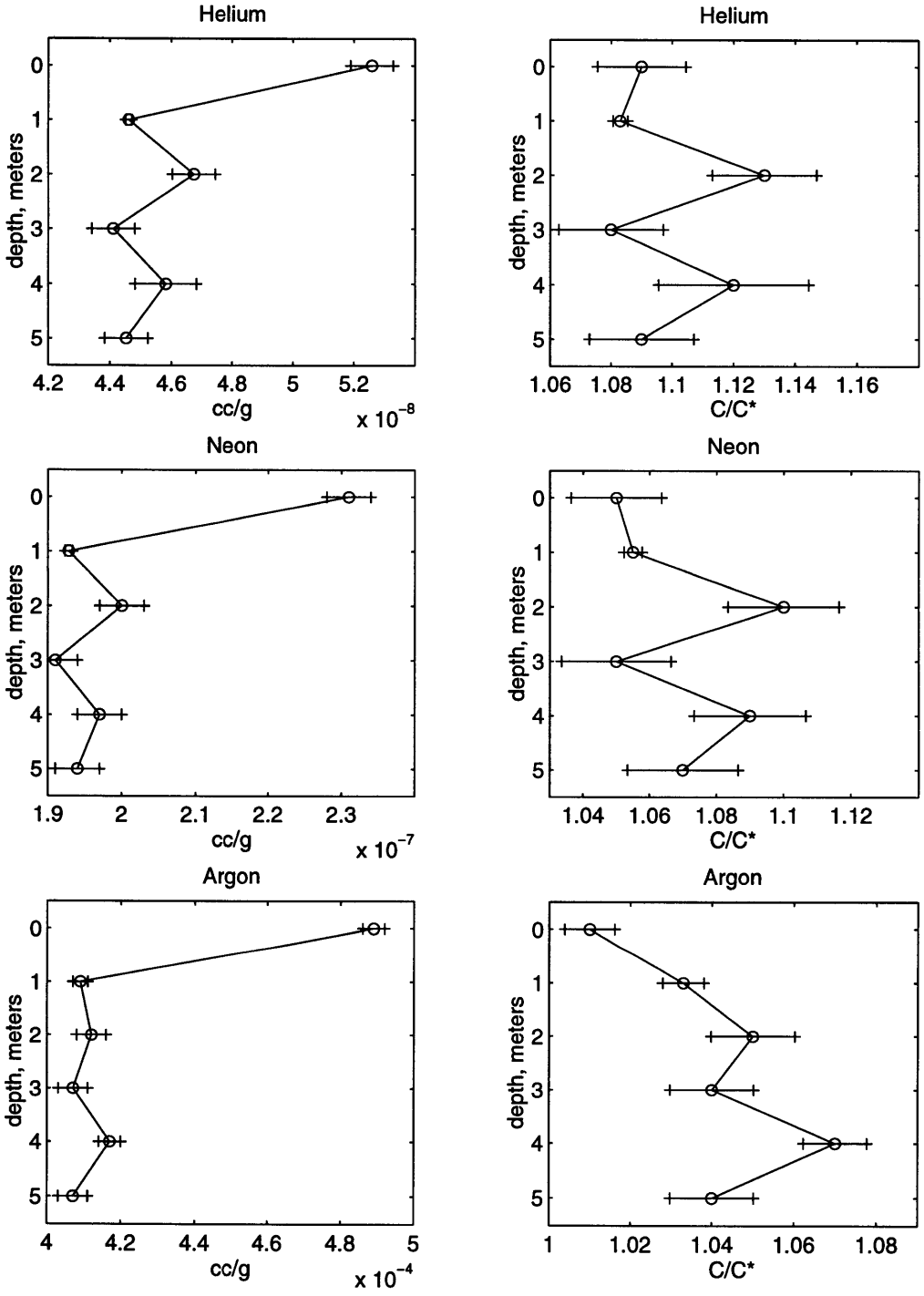

Figure 7.2 Concentrations and Saturations of He, Ne, and Ar in Saroma-Ko Lagoon. Saturations are expressed as C/C*, where C = the measured concentration, and C* is the concentration at solubility equilibrium with the atmosphere at the in situ temperature and salinity.

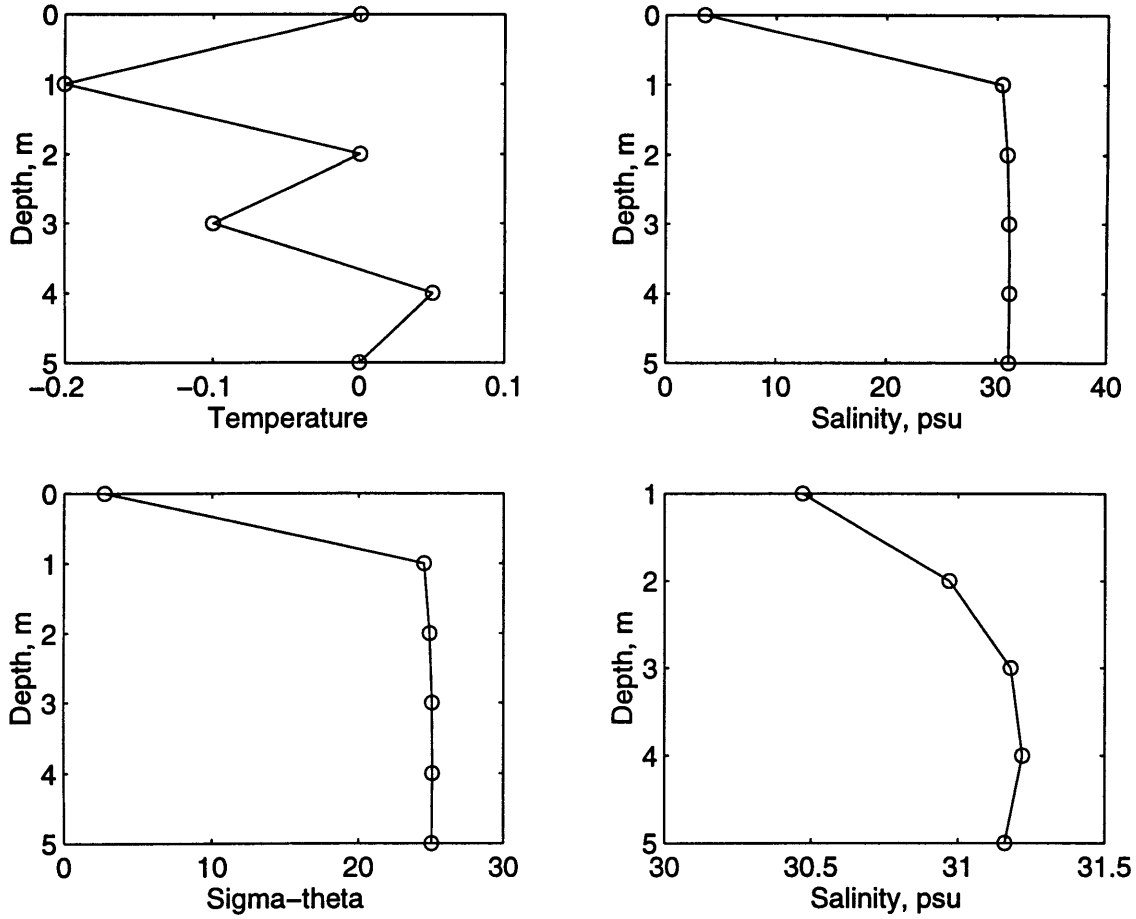

Figure 7.3 Temperature, Salinity, and Density of Saroma-Ko Lagoon. Panel d shows the salinity below 1 meter to illustrate the relative salinity structure at depth.

The error bars reflect the standard deviation of replicate samples at each depth. Figure 7.3 shows the temperature, salinity, and density profiles at the sample site when the samples were taken. The gases in the lake are supersaturated with respect to solubility equilibrium with the atmosphere. Typical springtime saturations for the Sea of Okhotsk near Hokkaido are approximately 3.5% for He, 2.8% for Ne, and 1% for Ar (W. Jenkins, pers. comm.). Thus the saturations in the lake are quite high compared to periods of no ice cover. The concentration profiles show a striking inverse correlation to the salinity

profile, with the values at the ice-water interface being approximately 15% higher than the average lake water concentrations. While the error bars of the concentration profiles are large in relation to the implied profile structure, the structure shows a strong correspondence to the temperature profile structure (Figure 7.4), suggesting that the structure is real and not an artifact of sampling or analysis.

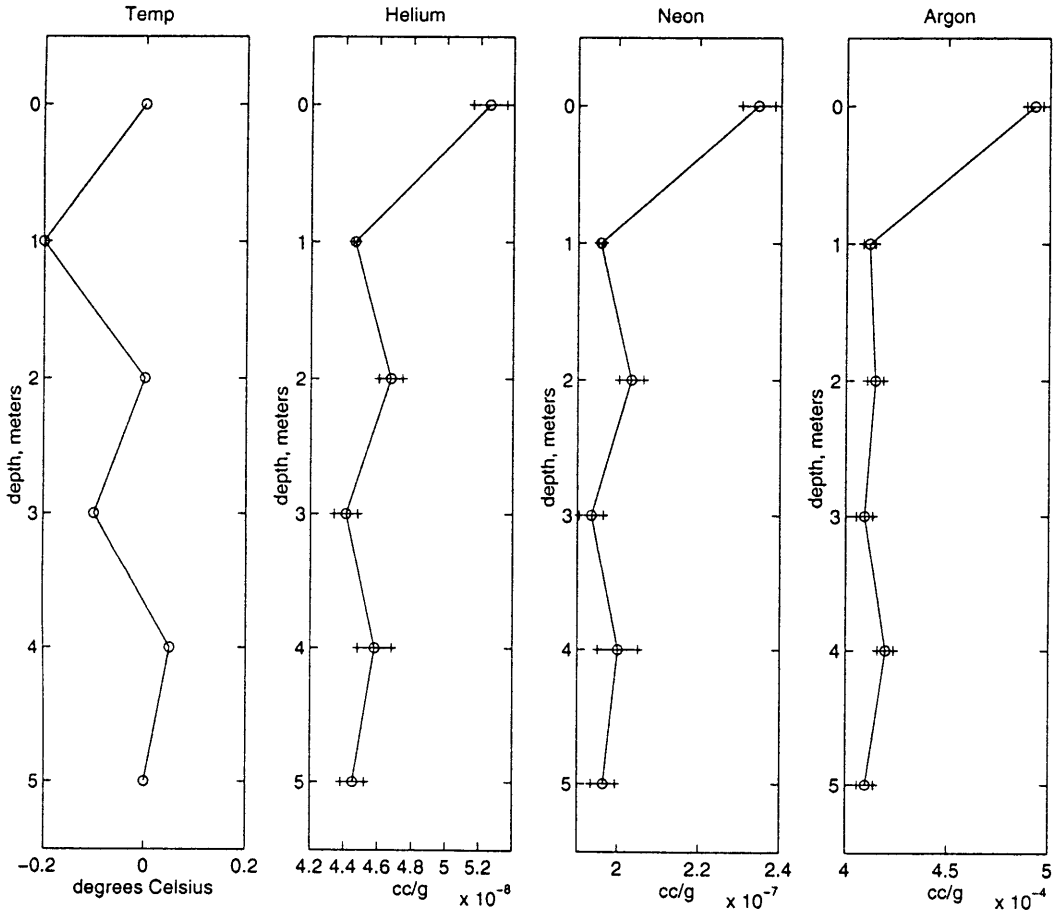

Figure 7.4 Temperature and noble gas concentration profiles showing similar structure through the water column.

7.3 *Discussion and Interpretation*

The salinity profile, with a salinity of 3.5 psu at the ice-water interface and an average salinity of 31 psu below, is suggestive of melting of the ice. The concentrations of the gases in this lens of fresher water are also qualitatively consistent with an input of the dissolved gases from the ice cover. In 1996, the lake experienced complete freeze-up on February 1st, and break-up of the ice occurred on April 16th (Shirasawa et al., 1997). Figure 7.5 shows a time series of temperature and salinity at the ice-water interface for 1996 at a nearby station.

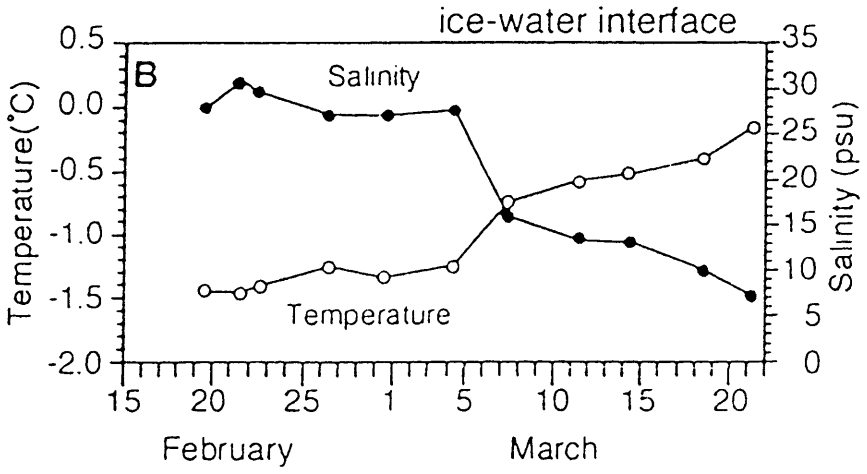

Figure 7.5 Time series of temperature and salinity of the water at the ice-water interface adapted from Hamasaki et al., 1997.

A dramatic decrease in salinity at the ice-water interface, accompanied by an increase in temperature marks the beginning of ice melt, which occurred more than a month before complete break-up of the ice cover. At the time of sampling on March 25th, the temperature at the ice-water interface was 0°C, while the salinity was 3.5 psu, which is consistent with the trend shown in the temperature-salinity time series. While these

records clearly show a lens of fresh melt-water developing at the ice-water interface, current meter records show no increase in circulation between the lake and the adjacent Sea of Okhotsk until after break-up of the ice cover. This suggests that during the ice-covered period, melting prior to the ice-cover break up creates a stable lens of fresh water at the interface that is not significantly disturbed by tidal mixing with the Sea of Okhotsk at the sample location. Because of the diurnal tide during the ice-covered period, however, the bottom waters of the lake almost certainly are influenced by exchange with the adjacent sea.

In order to characterize the melting processes that may be responsible for the observations of the gas saturations, it is necessary to know something of the gas concentrations in the ice . However, without specific information about the gas concentrations in the ice, we are faced with the task of constructing a model of the ice and the concentrations of the gases in the various reservoirs of the ice, the brine, and the bubbles in the ice. With this information, we can then explore how the ice could be melted in a way that would satisfy the observed salinity budget and the dissolved gas budgets of all three gases.

Hood et al. (1997) demonstrated that for a closed system, a model of noble gas partitioning between the various phases of an ice-water system during freezing could be constructed to predict the dissolved concentration values at the ice-water interface. While this model calculation was an empirical parameterization of the processes occurring in a permanently ice-covered lake, the basic mechanisms for the gas behavior in a three-phase

system should be applicable to other aquatic environments. Unlike the Lake Fryxell study, however, we have no information on the volume of bubbles in the ice cover of Saroma-Ko, and have the additional reservoir of brine within the ice. In addition, sea ice has a very different crystal structure than fresh water ice, which may affect the way in which the dissolved gases interact with this ice composition. To assess these effects and estimate the volumes of the necessary reservoirs from information provided about the ice at Saroma-Ko, we use information from several studies of sea ice composition and dissolved gas concentrations in bubbles in sea ice to model the ice.

Examining first the nature of the ice phase in the sea ice composition, it has been shown that there is no significant substitution of constituents from the salt solution into the solid structure of the ice (Weeks and Ackley, 1982). The ice can thus be considered to be a pure phase. This has bearing not only on the solubility of the gases in the ice, but on the "salinity" of each phase, which is important for establishing a salinity budget for the system. There are no estimates of the solubility of He and Ne in sea ice, although Top et al. (1988) report good agreement between the values observed in laboratory tests using salt water solutions and the solubility values of Namoit and Bukhgalter (1965). For this study, the values of both Kahane et al. (1969), and Namoit and Bukhgalter (1965) will be used.

The crystal structure of sea-ice is considerably different than ice formed from fresh water. Because the ice crystals must dissipate both heat and solute, they assume a shape of

maximum efficiency, having the form of a hexagonal dendritic star with a discoidal center (Weeks and Ackely, 1982). The result of this pattern is that the brine rejected from the ice lattice during freezing often becomes trapped between the spires of the dendritic formations, and becomes incorporated into the ice sheet as freezing continues. This process is responsible for giving sea-ice its salinity.

7.4 *Ice Model*

We treat the lake during freezing as a closed system, and do not consider interactions of the gases from the river input or from the Sea of Okhotsk. We first establish the mass balance equation that must be satisfied:

$$C_w V_w = C_i V_i + C_b V_b + C_{br} V_{br} + C_{rw} V_{rw} \qquad (7.1)$$

where:

V's = volumes of each of the reservoirs, in cm^3

C's = concentrations of the gasses in each of the reservoirs , in cc (STP)/cm^3

and

w = initial water

i = ice

b = bubbles

br = brine

rw = residual water after freezing

The volume of the ice is estimated by multiplying the thickness of the ice at the sample site by the surface area of the lake. The initial volume of water is taken to be the volume of the lake. Using measurements from previous years of the ice temperature, salinity, and density (Shirasawa et al., 1992; Taguchi et al., 1992), it is possible to calculate the volume of the brine in the ice, the salinity of the brine, and the volume of the bubbles in the ice (Cox and Weeks, 1983). The residual water is estimated to be the initial water volume minus the amount of water frozen and the amount of water taken up as brine. These volumes are given in Table 7.2.

Reservoir	Volume cm^3
Initial water	1.3e15
Ice	7.1e13
Brine	1.3e13
Bubbles	1.8e12
Residual water	1.2e15

Table 7.2 Volumes of reservoirs for Saroma-Ko ice model.

Prior to freezing, the salinity of the lake water was approximately 31 psu, and the temperature was approximately -1.5°C. Using these values of temperature and salinity, we calculate the concentrations of the gases at solubility equilibrium with the atmosphere. We assume the gas saturations prior to complete freezing to be in solubility equilibrium with the atmosphere. This assumption is based on the fact that a non-consolidated mixture of ice crystal forms on the lake several weeks prior to complete freeze-up, through which gases may equilibrate, and which also serves to dampen wave action that might inject bubbles into the water.

The remaining concentrations are calculated by relating the concentrations of the various reservoirs by their equilibrium partitioning values between the various phases. The equilibrium partitioning values are calculated as the inverse of the Bunsen solubility coefficient (Weiss, 1970; Weiss, 1971) at the temperature and salinity of the reservoir. These partition coefficients for the Saroma-Ko ice model are shown in Table 7.3.

	He	Ne (a)	Ne (b)	Ar
Ice / Water *	1.8	1.4	0.9	0
Bubble / Water	125	96	96	22
Bubble / Brine	128	100	100	23
Bubble / Ice	69.4	68.5	107	inf

* also used for Ice / Brine partitioning

Table 7.3 Equilibrium Partition Coefficients for Saroma-Ko system.

With the mass balance equation, estimates of the reservoir volumes, the equilibrium partitioning coefficients, and initial concentrations of the gases in the system, it is possible to solve the system of equations to obtain the concentration of the gases in each of the reservoirs. Table 7.4 shows the concentrations of the gases in each reservoir, along with the percent of the gas residing in each reservoir.

While the model is necessarily based on several assumptions, the gases in the resulting model ice composition can be compared to measurements of gases in sea ice to determine if the model is producing a realistic ice composition.

	He cc(stp)/cm3		cc's gas in reservoir	% of total
Ci	6.4e-8		4.5e6	8.0
Cb	4.5e-6	bub./air = .86	7.9e6	13.9
Cbr	3.5e-8		4.7e5	.83
Crw	3.6e-8	S_{He}=.86	4.4e7	77.3
Cinit	4.37e-8		5.68e7	100

	Ne_a cc(stp)/cm3		reservoir cc's	% of total
Ci	2.3e-7		1.7e7	6.5
Cb	1.6e-5	bub./air = .89	2.9e7	11.3
Cbr	1.6e-7		2.2e6	.86
Crw	1.7e-7	S_{Ne} = .90	2.1e8	81.4
Cinit	1.96e-7		2.5e8	100

	Ne_b cc(stp)/cm3		reservoir cc's	% of total
Ci	1.5e-7		1.1e7	4.26
Cb	1.7e-5	bub./air = .94	2.9e7	11.6
Cbr	1.7e-7		2.2e6	.88
Crw	1.7e-7	S_{Ne} = .92	2.1e8	83.3
Cinit	1.96e-7		2.5e8	100

	Ar cc(stp)/cm3		reservoir cc's	% of total
Ci	0		0	0
Cb	9.7e-3	bub./air = 1.04	1.7e10	3.1
Cbr	4.2e-4		5.6e9	1.0
Crw	4.3e-4	S_{Ar} = 1.04	5.3e11	95.9
Cinit	4.25e-4		5.5e11	100

Table 7.4 Ice Model Concentrations

Because measurements of He and Ne in the bubbles of sea-ice do not exist (to the best of our knowledge), we ran the model for N_2 and O_2 for the comparisons. We compare the model output to measured concentrations of N_2, O_2, and Ar in 6 sea-ice samples from the

North Pacific and Sea of Okhotsk from Matsuo and Miyake, 1966. The comparisons are shown in Figure 7.6.

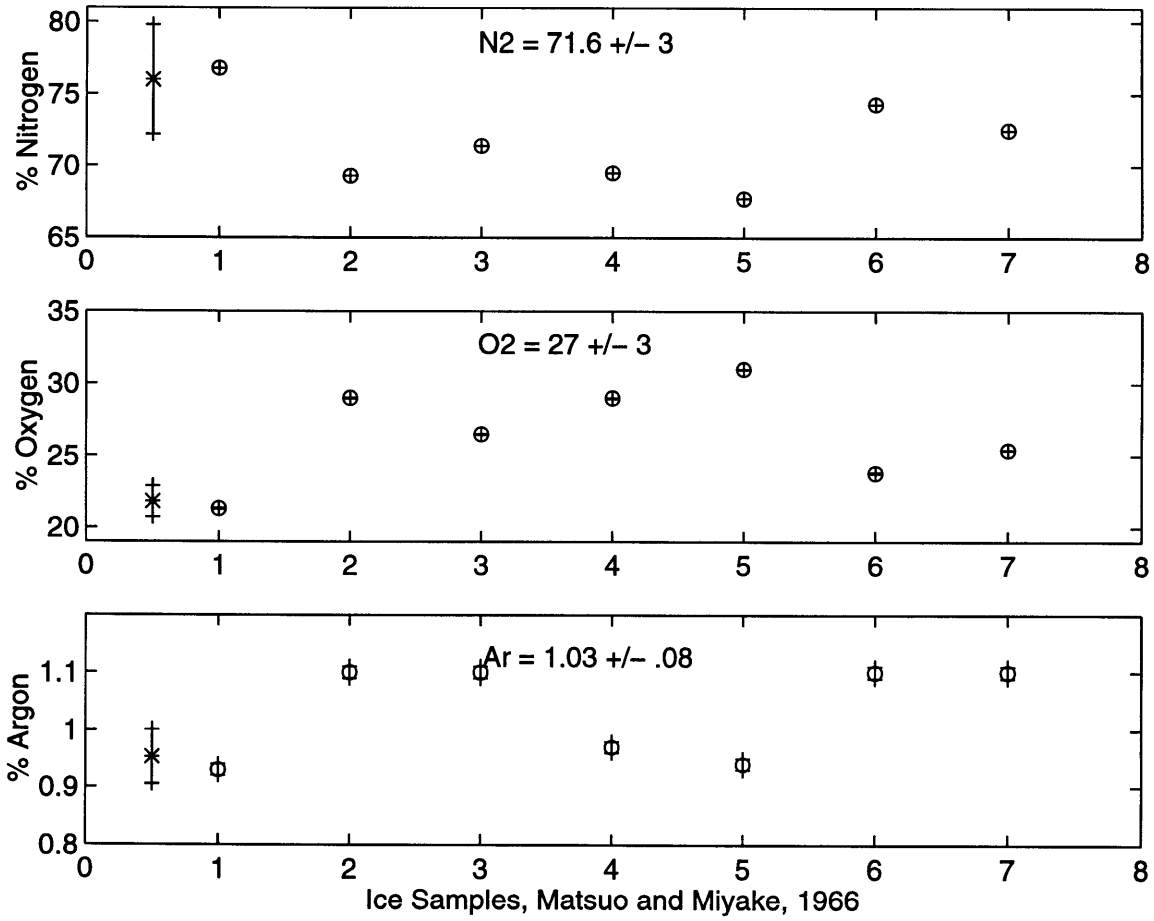

Figure 7.6 Comparison of the gas composition of bubbles in the ice predicted by the ice model (stars) and measurements of gases in ice from Matsuo and Miyake, 1966.

The model values show excellent agreement with one particular ice sample, and within the uncertainties of the measurements and the model calculations, the model results are consistent with the averages of the sea ice samples for N_2 and Ar. The model result for O_2 is a bit lower than the measured values, although not significantly so. We believe this discrepancy may result from biological O_2 production in the ice (Hamasaki et al., 1997), which is not accounted for in the model. From this analysis, we feel that the modeled ice

composition is reasonably representative of a typical ice cover that would be formed under the stated conditions.

7.5 *Ice Melting Model*

Our approach is to calculate the initial concentrations of the noble gases in the undiluted melt-water from the ice, and use those values as tracers of ice-water interactions. This approach has been used by Schlosser (1986) and Schlosser et al. (1990) for ^{4}He from glacial melt-water addition to seawater.

The mass balance equation that describes the concentration of the gases in the undiluted melt-water is:

$$C_m = \frac{C_i V_i + C_b V_b + C_{br} V_{br}}{V_m} \tag{7.2}$$

where C and V are concentrations (in cc (STP) / cm^3) and volumes (in cm^3), respectively, and the subscripts m, i, b, and br are melt, ice, bubbles, and brine, respectively. Using the reservoir volumes from the ice model described above, we have:

$$V_b = 0.025\ V_i$$

$$V_{br} = 0.18\ V_i$$

Using an average ice density of 0.91g /cm^3, we relate V_i and V_m, and the equation thus reduces to:

$$C_m = C_i\,(1.1) + C_b\,(0.025)(1.1) + C_{br}\,(0.18)(1.1) \tag{7.3}$$

The concentrations of the gases in each reservoir are taken from the ice model, and the concentration of each gas in the undiluted melt is calculated. Table 7.5 shows the concentrations and saturations at 0°C, 0 psu in the undiluted melt-water.

	cc (STP) / g	C / C*	Melt %
Helium	1.94×10^{-7}	4.15	2.1
Neon (K)	7.30×10^{-7}	3.43	1.6
Neon (N&B)	6.41×10^{-7}	3.01	1.8
Argon	3.42×10^{-4}	0.73	1.3

Table 7.5 Undiluted meltwater concentrations and meltwater fraction to the ice-water interface. The saturations of the undiluted melt are relative to 0°C, 0ppt.

Using the observations at the ice-water interface and the concentrations of the gases in the undiluted melt, we calculate the percentage of melt-water added to water at solubility equilibrium with the atmosphere required to produce the observations at the ice-water interface. The predicted values are shown in Table 7.5. All three gases are in relatively good agreement, and predict a melt-water addition to the ice-water interface of about 1.5-2.0%.

The bottom water concentrations can be explained by a smaller melt-water addition, or mixing with the water at the ice-water interface. The concentration profiles (Figure 7.2 and Table 7.1a) show high concentrations at the ice-water interface that decrease sharply to the lower concentrations in the bottom waters. The decrease in concentration from the ice-water interface to the bottom waters is approximately 15% for all three gases, suggesting mixing and a melt-water contribution of approximately 0.26%. The coastal area of the Sea of Okhotsk connected to the lagoon also experiences ice formation, and

the period of ice cover for the lagoon and the Sea of Okhotsk are highly correlated (Shirasawa, 1993). Thus, this melt-water addition or dilution could occur in the Sea of Okhotsk before the water enters the lagoon. The structure observed in the temperature profile and the concentrations of the dissolved gases in the bottom waters (Figure 7.4) is also seen in the percentage of melt-water addition at each depth, with higher melt-water fractions corresponding to warmer temperatures.

7.6 *Summary and Conclusions*

The concentrations and saturations of the noble gases in this sea-ice environment show large deviations from solubility equilibrium with the atmosphere, and the concentration gradients between the ice-water interface and the bottom waters are consistent with ice melt. Using estimates of the temperature, salinity, and density of the ice, and the temperature and salinity of the lagoon water prior to freezing, a model of the ice composition can be constructed to predict the concentrations of the noble gases in the various phases of the ice. The predicted concentrations of gases in the bubbles in the ice are in excellent agreement with measured values. This model can then be used to calculate the noble gas concentrations in undiluted melt-water, which can be used to trace the interactions between ice and water. Using this model, all three gases predict consistent melt-water fraction additions to the ice-water interface. The bottom water concentrations show smaller melt-water fractions, possibly from inflowing water masses from the adjacent Sea of Okhotsk that more actively dilute the melt-water from the ice cover of the sea.

The results of this initial survey provide confidence that the noble gas anomaly indeed has potential as a tracer of the interactions between dissolved gases, water, and ice, and while much of the interpretation of the data is of a qualitative nature only, we believe that the results are sufficient to merit further study and can be used to direct future investigations. In order to more completely characterize the interactions of the noble gases with the ice, a time-series of the gases over a complete cycle of freezing and melting in Saroma-Ko would provide the necessary information about the magnitude and temporal evolution of these anomalies.

Chapter 8

Dissolved Noble Gases in Prydz Bay, Antarctica

8.1 *Introduction*

In Chapter 6, I described the properties and interactions between the dissolved noble gases and ice that make them unique tracers in freshwater systems, and in Chapter 7, I extended this work to demonstrate that the noble gas are also being affected by interactions with ice in seawater environments. A summary of the important features of the interactions between the noble gases and ice is listed below:

- He and Ne are soluble in ice; Ar is rejected from the ice matrix as water freezes.
- With information about the volume of ice formed, the volume of bubbles in the ice, and the relative volume of residual water that remains after freezing, a three-

phase equilibrium partitioning model of the gases can be constructed to quantitatively predict the dissolved noble gas concentrations in the residual water.

- Noble gas saturation anomalies due to interaction with ice are also present in seawater environments.
- With estimates of the ice temperature, salinity, and density, and an estimate of the mixed layer depth in contact with the ice as the water freezes, a model of the ice composition can be constructed (i.e. bubble volume, brine volume, and the concentrations of gases in each of the reservoirs), and the concentrations of the noble gases in the melt-water of this ice can be estimated.
- The noble gas concentrations in sea ice melt-water can be used as tracers of the volume of melt-water addition to water masses in contact with the ice.

Here, I extend this work further to examine the interactions between ice and the dissolved noble gases in the more open and active environment of a large bay on the continental shelf of Antarctica. The premise of this study is that water masses that have been influenced by either ice formation or melting should have unique noble gas "tags" that can be used to distinguish the water masses from those not significantly influenced by interactions with ice. Further, these tags may potentially be used to distinguish between water masses from different ice formation areas, such as water masses formed in the various continental shelf regions of Antarctica, since the interaction between the water mass and ice is likely to vary in different environments.

Prydz Bay, the third largest bay in Antarctica, is situated between Mac Robertson Land and Princess Elizabeth Land in the Indian Ocean sector of the Antarctic continental shelf. Figure 8.1, taken from Nunes Vaz and Lennon (1996), shows the bathymetry of the bay.

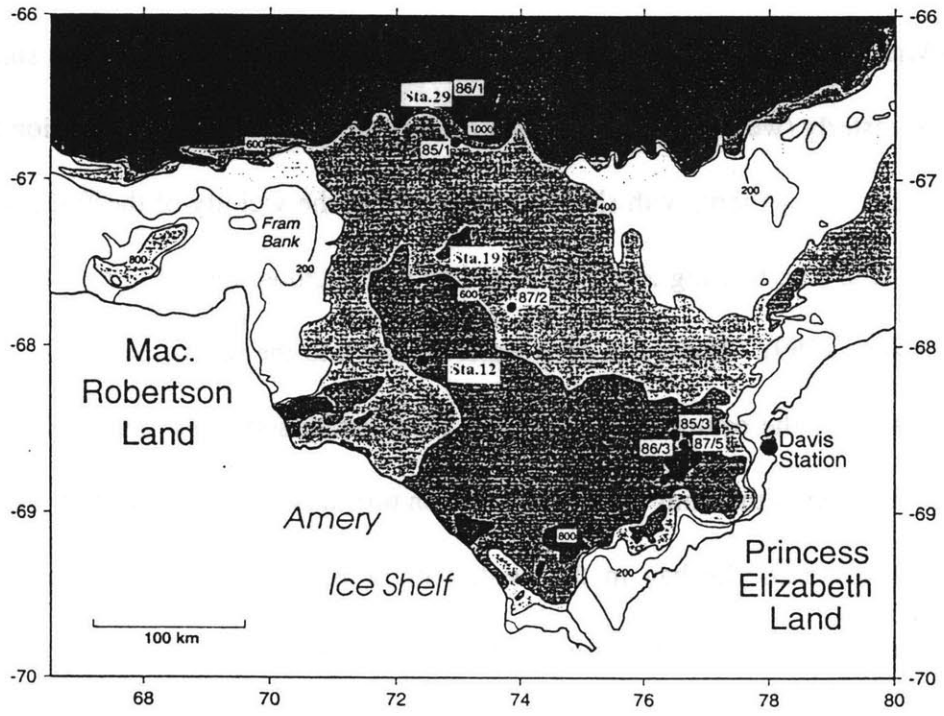

Figure 8.1 Bathymetry and station locations of Prydz Bay, adapted from Nunes-Vaz and Lennon, 1996.

The depth of the bay is about 500-600 meters with a deep basin in the inner part of the bay that has a depth of 800 meters in some places. The depths adjacent to the Amery Ice Shelf are about 1085 meters. There is a sill between 68° S and 67° S at 400-500 meters. Seaward of this sill, the depth increases to 600 meters at the edge of the continental shelf.

The waters of the bay are in contact with a floating ice shelf, the Amery Ice Shelf, in the southwestern part of the bay.

Sea ice covers more than 70% of the bay from April until December, and freezing is active during most of the year, with significant fractions of open water occurring only in January (Middleton and Humphries, 1989). The wind stress during the austral summer is zonal, with easterly (west-going) winds over the bay area. The coastal circulation follows a general clockwise pattern, with shallow inflows from the vicinity of the West Ice Shelf in the east of the bay, flowing along the coastline in a southwesterly direction (Middleton and Humphries, 1989). There is a deep water inflow into the bay across the shelf break just to the west of the center of the bay, and flows south-southeast. Both shallow and deep flows proceed to the limit of the bay and then turn west and flow beneath the Amery Ice Shelf. Flow exits the bay in the west, with some recirculation of the westward flowing current back into the bay (Nunes Vaz and Lennon, 1996).

There are basically 5 principle water masses within Prydz Bay. A temperature and salinity diagram of the water masses found within the bay is shown in Figure 8.2, taken from Nunes Vaz and Lennon (1996). There is a fresher, warmer surface layer in the upper 50 meters over the shelf area during the spring and summer, referred to as Antarctic Shelf Water (ASW), which is formed by mixing of Low Salinity Shelf Water (LSSW), melting of ice, and solar warming. LSSW and High Salinity Shelf Water (HSSW) have

temperatures close to the freezing point at the surface, and the two types are determined by their salinities, having a separation at 34.6 ppt.

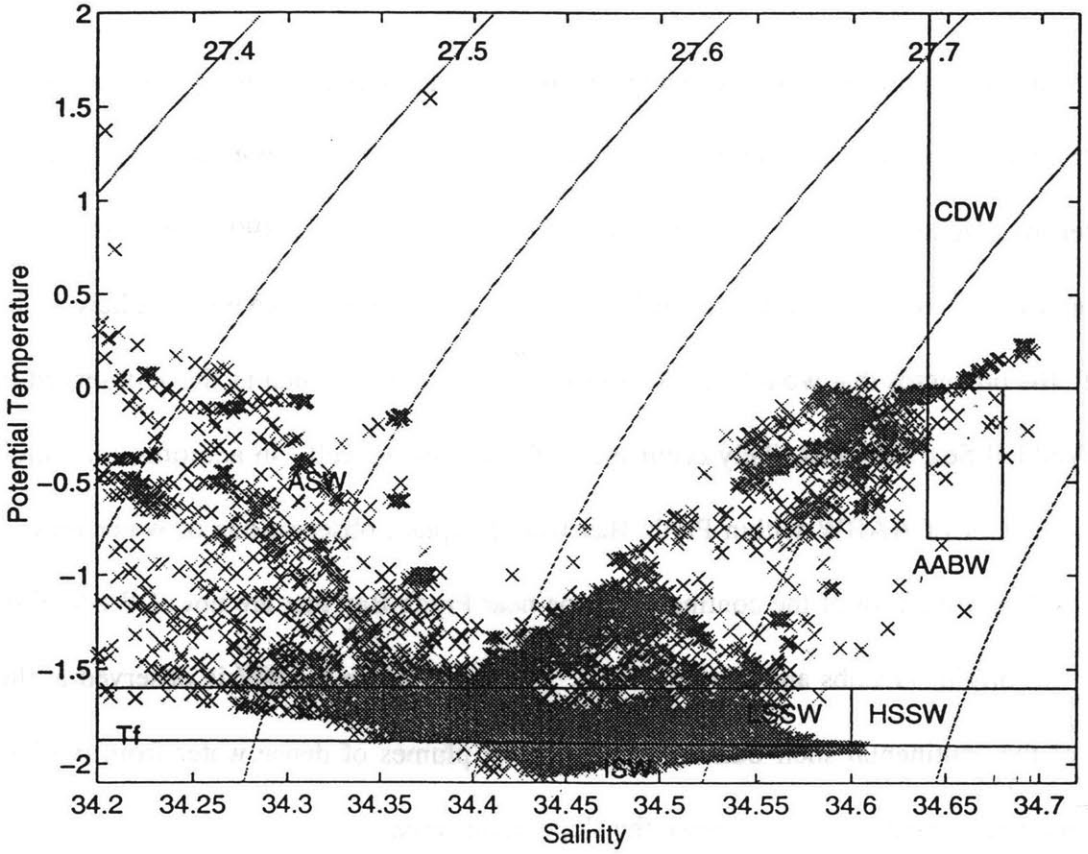

Figure 8.2 θ-S diagram of the water masses in Prydz Bay, adapted from Nunes-Vaz and Lennon, 1996.

HSSW, which covers the floor of the shelf, is generated by brine rejection during sea-ice formation (Nunes Vaz and Lennon, 1996). Ice Shelf Water (ISW) has a temperature that is lower than the freezing point at the surface, indicating interaction with the ice shelf at depth. Circumpolar Deep Water (CDW) is generally much warmer than the shelf water masses, and has a salinity > 34.65 ppt. Winter Water (WW) is a colder, lower salinity

water mass that lies above CDW below at about 200 meters. Winter Water is formed by winter convection.

The primary purpose of most hydrographic studies of the region has been to determine if Prydz Bay contributes to Antarctic Bottom Water (AABW) formation. The general consensus (Nunes Vaz and Lennon, 1996; Smith and Treguer, 1994; Middleton and Humphries, 1989) is that while contribution from Prydz Bay to AABW is likely to be small, the processes that would lead to bottom water formation, such as those observed in the Weddell Sea, are most likely occurring in Prydz Bay as well. In addition, formation of a precursor of AABW within Prydz Bay would explain observations of water masses observed near the foot of the continental slope near Prydz Bay that are not of Weddell or Ross Sea origins (Jacobs and Georgi, 1977). However, while AABW is observed at the base of the continental shelf outside of Prydz Bay, plumes of dense water from the bay have not been observed moving down the slope in this area.

8.2 *The Data*

Samples were obtained from a three-station transect extending from the inner bay, north of the Amery Ice Shelf, to the continental slope during the 1997 *Aurora Australis* voyage #5 (station locations are shown in Figure 8.1). Profiles from each of the three stations consist of six depths, evenly spaced from 10 meters to the bottom. Figures 8.3a, b, c and d and Tables 8.1, 8.2 and 8.3 show the temperature and salinity profiles and the concentration and saturation profiles for He, Ne, and Ar.

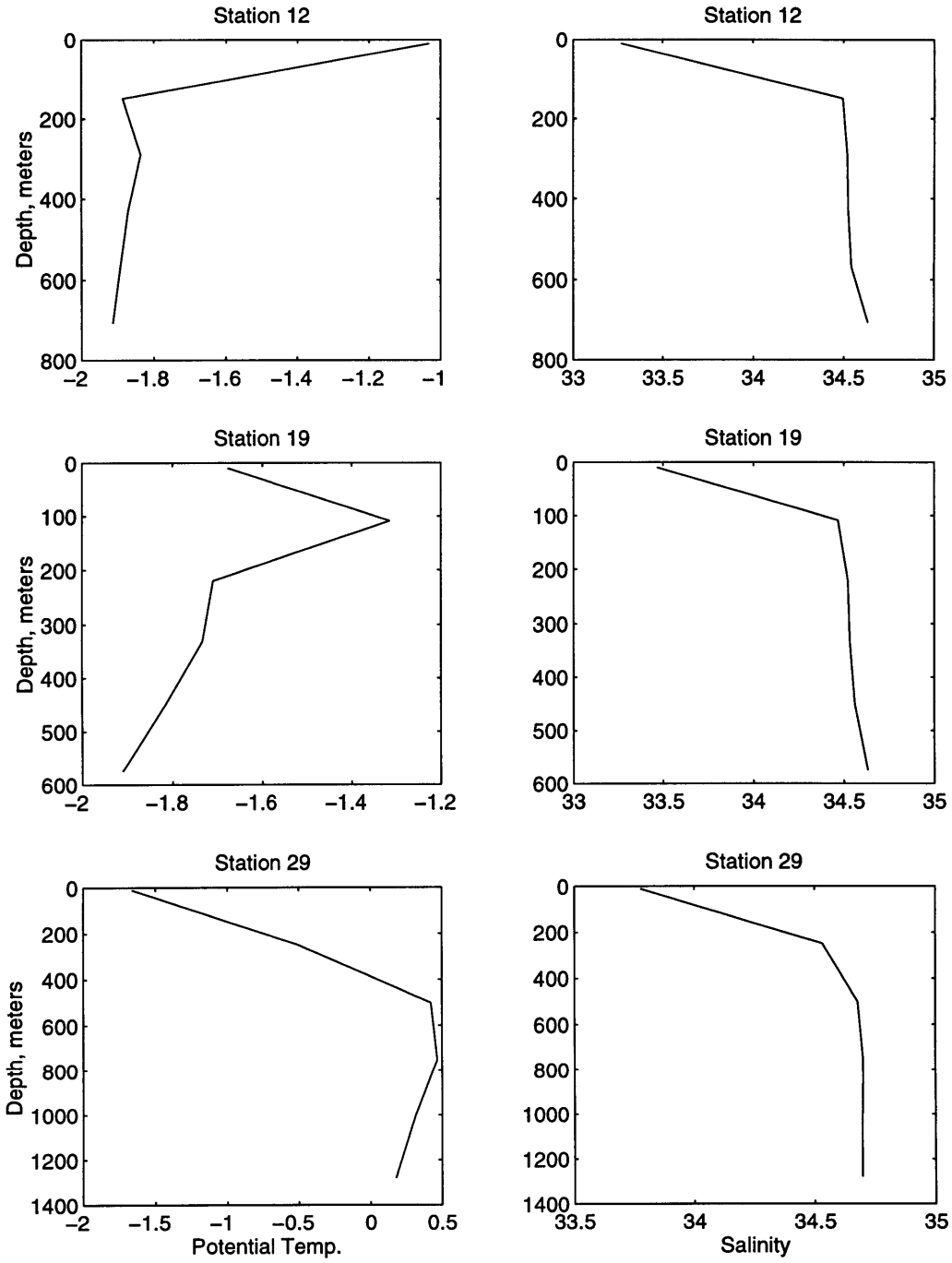

Figure 8.3a Temperature and salinity profiles of Stations 12, 19, and 29 in Prydz Bay.

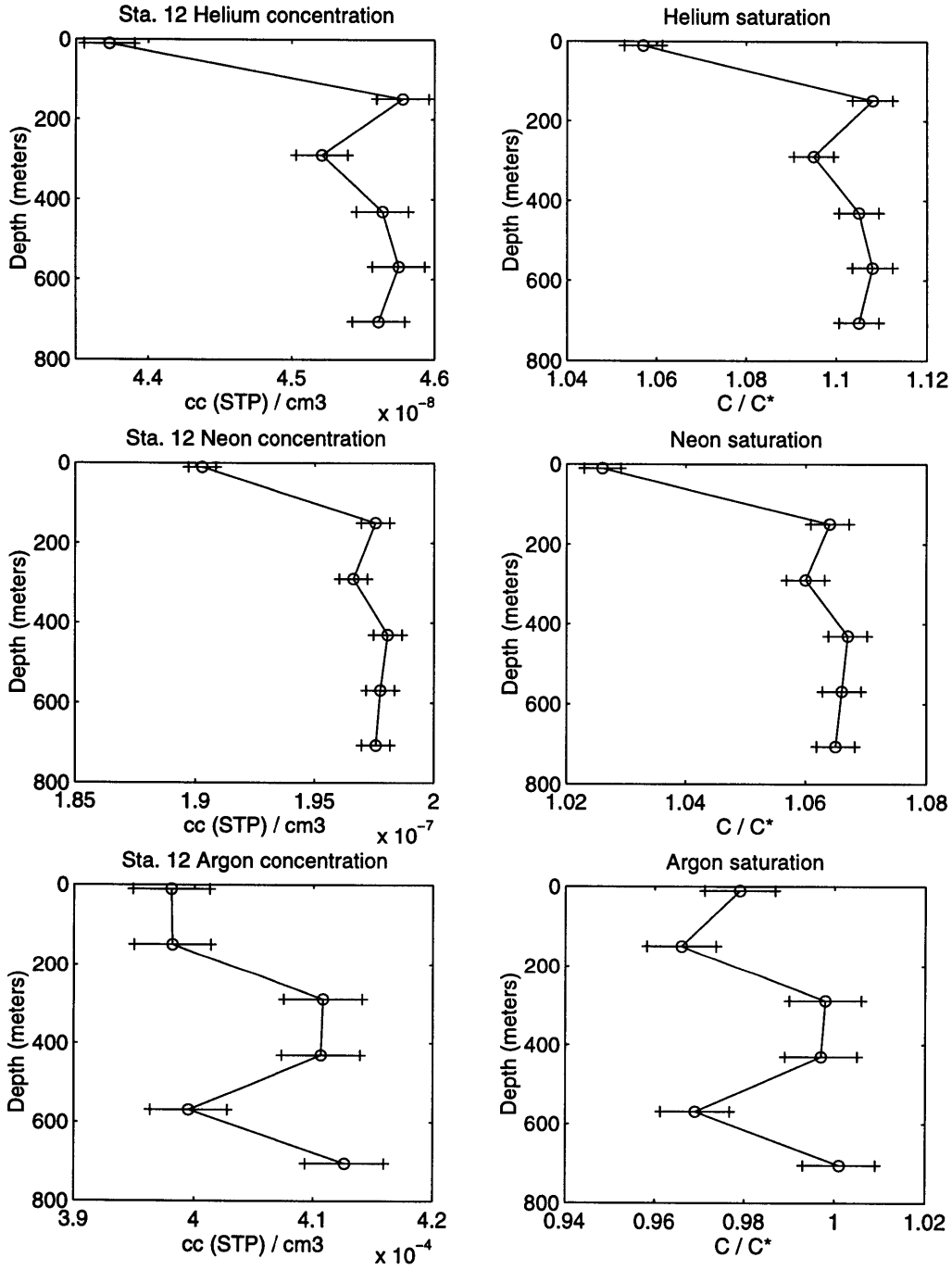

Figure 8.3b He, Ne, and Ar concentrations and saturations from **Station 12**. Saturations are given as C/C*, where C is the measured concentration, and C* is the concentration of solubility equilibrium with the atmosphere at the in situ temperature and salinity. The data is shown in Table 8.1 Uncertainties are the standard deviation of replicate samples.

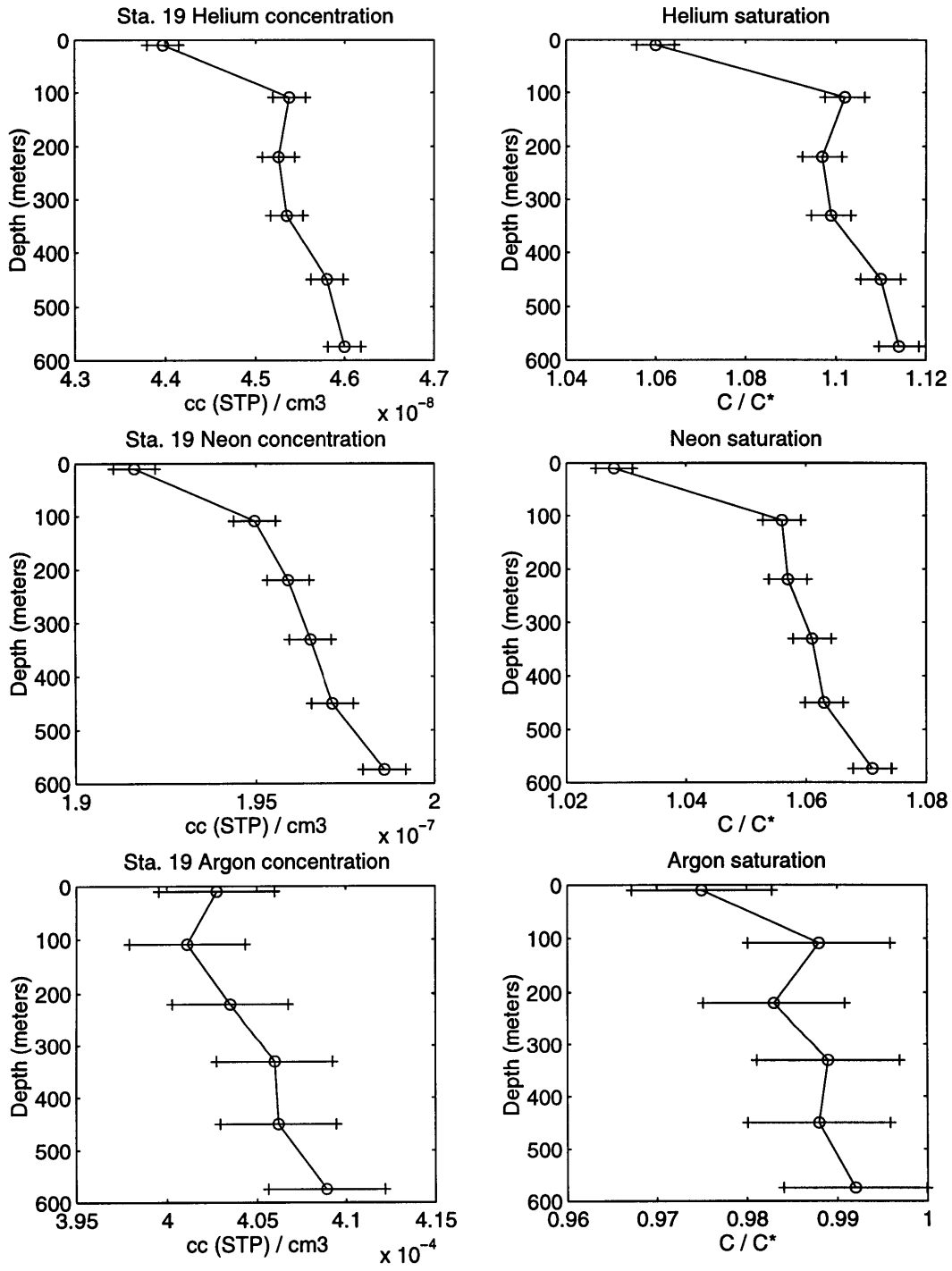

Figure 8.3c He, Ne, and Ar concentrations and saturations from **Station 19**. Saturations are given as C/C*, where C is the measured concentration, and C* is the concentration of solubility equilibrium with the atmosphere at the in situ temperature and salinity. The data is shown in Table 8.2. Uncertainties are the standard deviation of replicate samples.

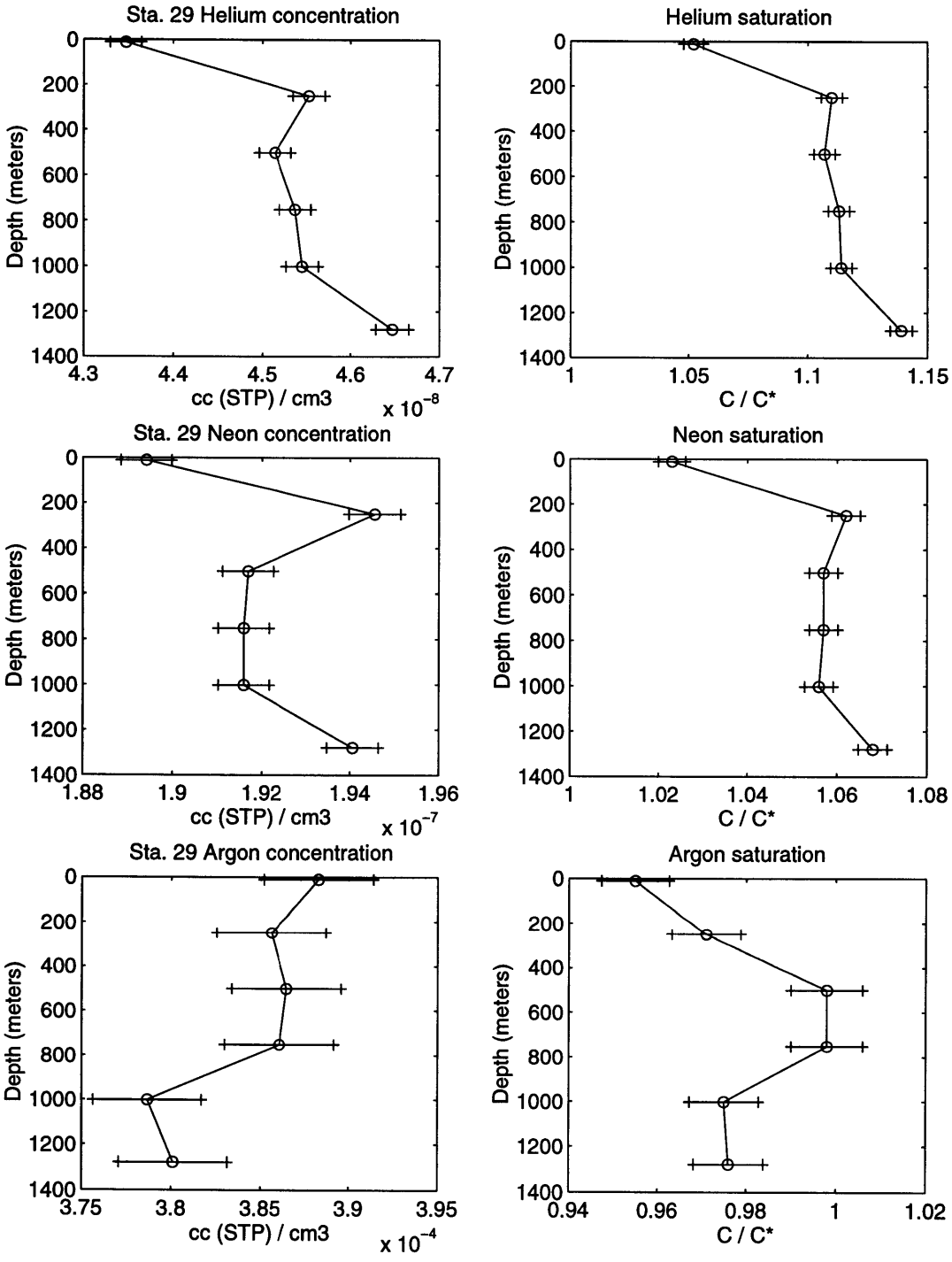

Figure 8.3d He, Ne, and Ar concentrations and saturations from **Station 29**. Saturations are given as C/C*, where C is the measured concentration, and C* is the concentration of solubility equilibrium with the atmosphere at the in situ temperature and salinity. The data is shown in Table 8.3. Uncertainties are the standard deviation of replicate samples.

Depth m	θ	S	He ncc / cm^3	He C / C*	Ne ncc / cm^3	Ne C / C*	Ar µcc /cm^3	Ar C / C*
10	-1.0321	33.2680	43.7	1.057	190.3	1.026	398.1	0.979
150	-1.8862	34.4966	45.8	1.108	197.5	1.064	398.2	0.966
290	-1.8370	34.5206	45.2	1.095	196.6	1.060	410.8	0.998
430	-1.8716	34.5263	45.6	1.105	198.1	1.067	410.6	0.997
570	-1.8935	34.5434	45.8	1.108	197.8	1.066	399.5	0.969
710	-1.9143	34.6346	45.6	1.105	197.6	1.065	412.6	1.001

Table 8.1 Station 12, Prydz Bay: S 68° 11.5' E 73° 17.6'

Depth m	θ	S	He ncc /cm^3	He C / C*	Ne ncc /cm^3	Ne C / C*	Ar µcc /cm^3	Ar C / C*
10	-1.6765	33.4676	44.0	1.060	191.6	1.028	402.8	0.975
109	-1.3146	34.4683	45.4	1.102	195.0	1.056	401.1	0.988
220	-1.7101	34.5219	45.3	1.097	195.9	1.057	403.5	0.983
330	-1.7339	34.5331	45.4	1.099	196.5	1.061	406.0	0.989
450	-1.8154	34.5601	45.8	1.110	197.1	1.063	406.2	0.988
575	-1.9107	34.6328	46.0	1.114	198.6	1.071	408.9	0.992

Table 8.2 Station 19, Prydz Bay: S 67° 36.8' E 73° 18.7'

Depth m	θ	S	He ncc / cm^3	He C / C*	Ne ncc / cm^3	Ne C / C*	Ar µcc / cm^3	Ar C / C*
12	-1.1662	33.7775	43.5	1.052	189.4	1.023	388.3	0.955
250	-0.5049	34.5315	45.5	1.110	194.6	1.062	385.6	0.971
500	0.4229	34.6785	45.1	1.107	191.7	1.057	386.5	0.998
750	0.4665	34.7002	45.4	1.113	191.6	1.057	386.1	0.998
1000	0.3149	34.6976	45.5	1.114	191.6	1.056	378.7	0.975
1280	0.1770	34.6974	46.5	1.139	194.1	1.068	380.1	0.976

Table 8.3 Station 29, Prydz Bay: S 66° 30.0' E 72° 17.2'

Uncertainties are calculated from the standard deviation of replicate samples, which were taken from at least one depth per profile, and are 0.4%, 0.3%, and 0.8% for He, Ne, and Ar, respectively. In general, the shelf station profiles show lower concentrations at the surface that increase with depth. He and Ne are greatly supersaturated with respect to

solubility equilibrium with the atmosphere, while Argon is at or below saturation by almost 3% at certain depths.

The temperature-salinity diagram for the samples obtained is shown in Figure 8.4. The three shelf water types, LSSW, HSSW, and modified Antarctic Surface Water (ASW) are clearly shown from the two shelf stations, and CDW is seen in the slope station. Also observed in two samples is mixing between CDW and a lower salinity component of LSSW (see Figure 8.2).

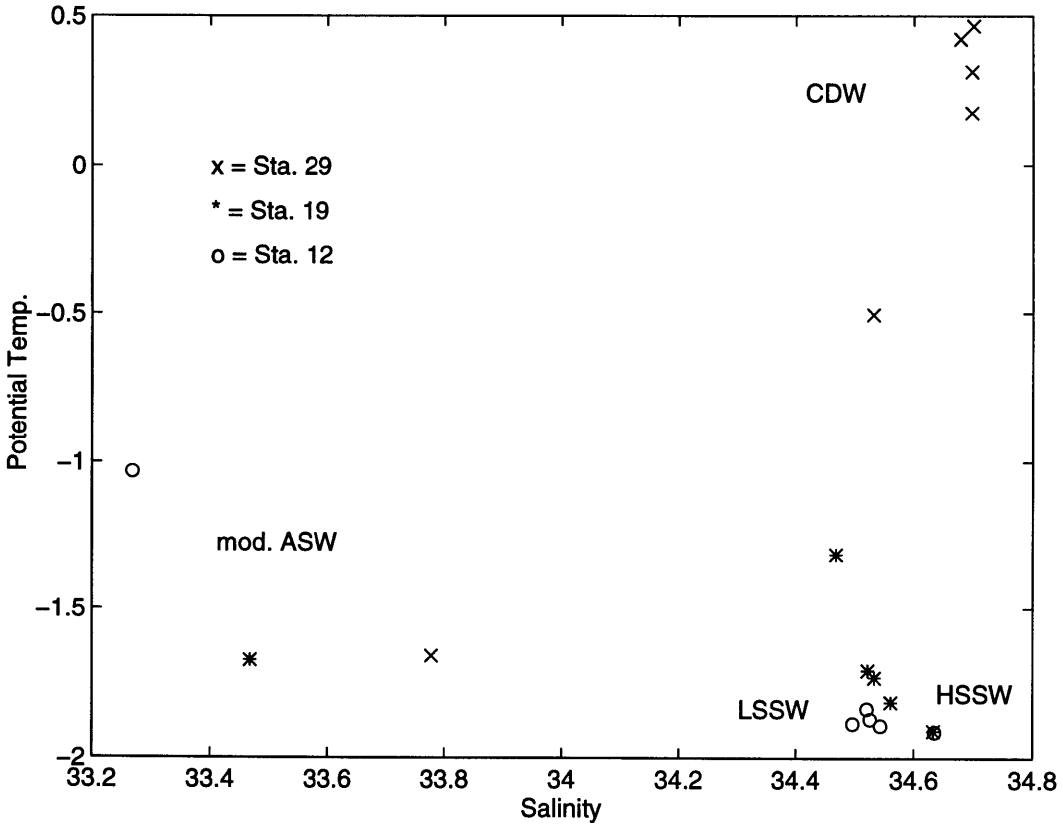

Figure 8.4 θ-S diagram of water masses sampled from Stations 12, 19, and 29.

8.3 *Noble gas - Ice interactions*

Although the dynamics of the system are too complex to predict *a priori* the concentrations that the noble gases would have in brine or in melt-water, the ratios of the noble gas saturations can be used to constrain the processes responsible for the observations. To determine if the noble gases in the Prydz Bay region are affected by interactions with ice, I focus the analysis on two water mass types: the shelf water masses, consisting of LSSW and HSSW, and the slope water mass, CDW. The samples that showed mixing between LSSW and CDW have been removed from the analysis. Table 8.4 lists the average concentrations and saturations of the shelf and slope water masses.

	Prydz Bay Shelf Waters	**Circumpolar Deep Water**
He cc (STP) / cm^3	$4.561 \times 10^{-8} \pm 9 \times 10^{-11}$	$4.56 \times 10^{-8} \pm 3 \times 10^{-10}$
Ne cc (STP) / cm^3	$1.973 \times 10^{-7} \pm 3 \times 10^{-10}$	$1.923 \times 10^{-7} \pm 6 \times 10^{-10}$
Ar cc (STP) / cm^3	$4.063 \times 10^{-4} \pm 2 \times 10^{-6}$	$3.829 \times 10^{-4} \pm 2 \times 10^{-6}$
He saturation C / C*	1.105 ± 0.002	1.118 ± 0.007
Ne saturation C / C*	1.06 ± 0.06	1.060 ± 0.003
Ar saturation C / C*	0.987 ± 0.004	0.987 ± 0.007

Table 8.4 Noble gas concentrations and saturations in the shelf and slope waters of the Prydz Bay region. Shelf waters (LSSW and HSSW) are shown in column 1, and CDW is shown in column 2. Saturations are given in C / C*, where C is the measured concentration, and C* is the concentration of the gas at solubility equilibrium with the atmosphere at the measured temperature and salinity.

The saturations of the noble gases in the two water mass types show the same general trend, with high saturations of He and Ne, and undersaturations for Ar. Undersaturations of Ar can occur through equilibration with the atmosphere at low atmospheric pressure, rapid cooling of the water without sufficient time for gas equilibration prior to sinking, or

interaction with ice. The first two mechanisms would reduce the saturations of He and Ne in the same manner (although to a much lesser extent), while melt-water addition would act to supersaturate the water with He and Ne while decreasing the Argon saturation. Figure 8.5 shows a vector diagram of the processes that can influence the saturations of He and Ar.

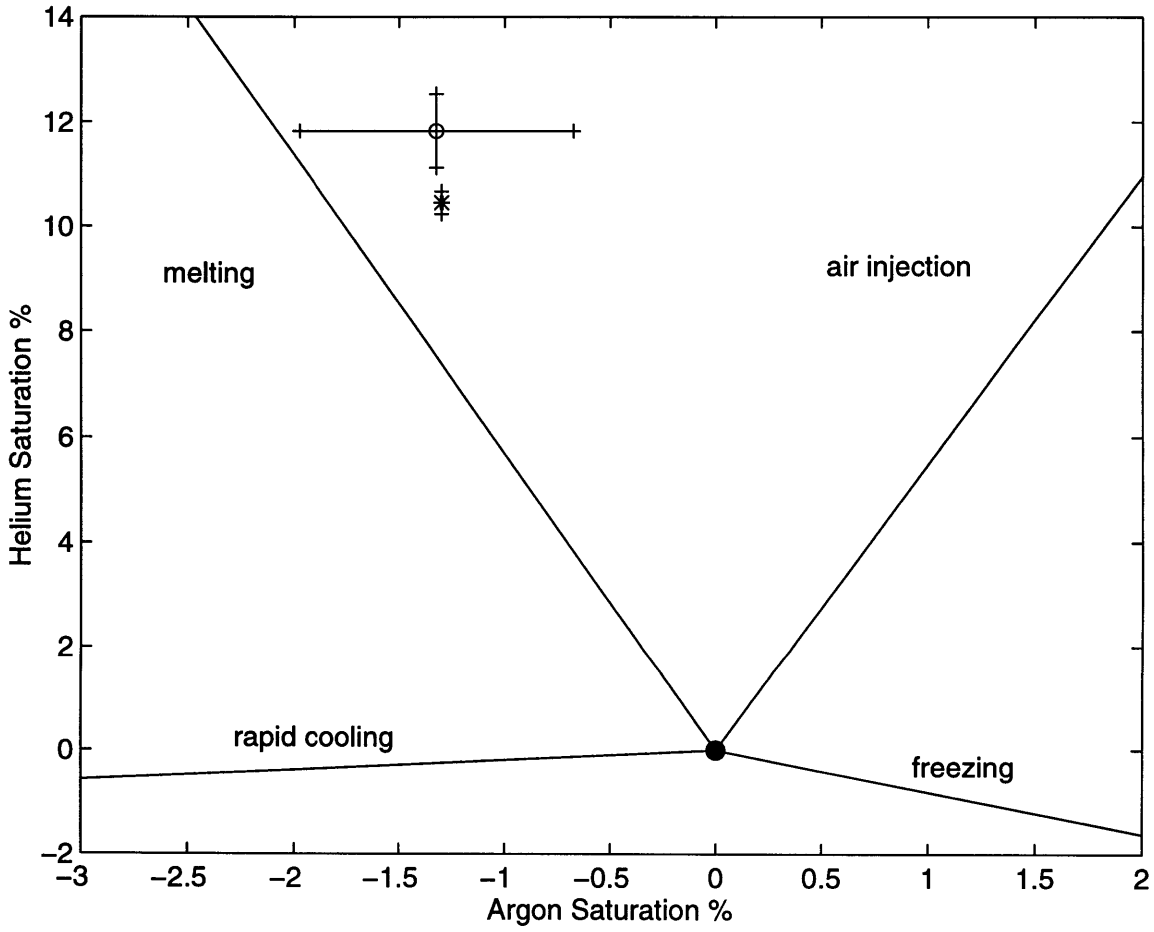

Figure 8.5 Vector diagram of He and Ar deviations from solubility equilibrium (0% saturation) due to sea-ice formation, sea-ice melting, air injection, and rapid cooling of the water with no gas exchange with the atmosphere. Shown also are the average He and Ar saturation values and standard deviations from the means of CDW and SW.

The major influences, air injection, freezing, melting, and rapid cooling, affect the ΔHe / ΔAr ratio in very distinct ways, making the ΔHe / ΔAr ratio an excellent diagnostic of these processes. The air injection vector is calculated from the saturations that would result from complete dissolution of a parcel of air in the water, modeled as:

$$\frac{\Delta_a}{\Delta_b} = \frac{\beta_b}{\beta_a}$$

where β is the Bunsen solubility coefficient of the gas, and Δ is the resulting saturation. The freezing and melting vectors are calculated using the sea-ice composition model constructed for the Saroma-Ko Lagoon (Chapter 7, Table 7.4). The rapid cooling without equilibration vector is created by calculating the solubility ratio of the two gases in water cooled from 0°C to -2° C. Atmospheric pressure influences will affect the saturations of the gases uniformly in positive and negative directions.

From a starting point of solubility equilibrium with the atmosphere, it becomes clear that the mechanism primarily responsible for the observed ΔHe / ΔAr ratio in both water mass types is melt-water addition. Melt-water can be incorporated into non-surface water masses in several ways. A water mass above the freezing temperature that flows beneath surface sea-ice will loose heat to the ice, which can create a more dense water mass containing some fraction of melt-water (Moore and Wallace, 1988; Moore and Spitzer, 1990). Martin et al. (1992) describe a process of dense water formation in the ice-covered Tatarskiy Strait in the Sea of Japan involving the formation of a polynya by storms, followed by upwelling of warm water, ice melt, rapid heat loss, refreezing, and

dense water formation. From the melting vector in Figure 8.5, the ΔHe / ΔAr ratio in the water masses must also have minor influences from air injection, gas exchange, or freezing. Correlations of the noble gas saturations and salinity should exist between water masses affected by melt-water and those not significantly affected. However, this relation would be complicated by the fact that the noble gas - salinity relation would become decoupled at the surface if air injection or gas exchange processes were occurring. It is not possible to examine this affect in the present study, since both water masses show evidence of melt-water influence, and the salinities of the two water mass types differ by less than ~ 0.1 ppt. Without further information to constrain these processes, it is impossible to make quantitative estimates of the amount of each process (*i.e.* melting, air injection, freezing) responsible for the observations. However, this analysis indicates qualitatively that the mechanism primarily responsible for the noble gas saturations in this region is the melting of sea ice..

8.4 *Noble Gas Concentrations of Individual Water Masses*

While the saturations of the noble gases in SW and CDW are very similar, the concentrations differ significantly. Saturations of gases are affected by changes in temperature and salinity (which affect the solubility of the gas), whereas the concentrations of the gases are only affected by source and sink mechanisms such as air injection and interaction with ice, and are generally conservative properties. By plotting the concentrations of the noble gases against one another, it becomes apparent that there are distinct concentrations of the noble gases for the different water masses. Figures 8.6a,

b, c, and d show plots of the concentrations of He versus Ne and He versus Ar in the shelf water masses (LSSW and HSSW), the slope water mass (CDW) and the surface waters of all three stations. Figures 8.6 c and d were made by taking the mean and standard deviation of the mean values within each water mass defined by the cluster of data points.

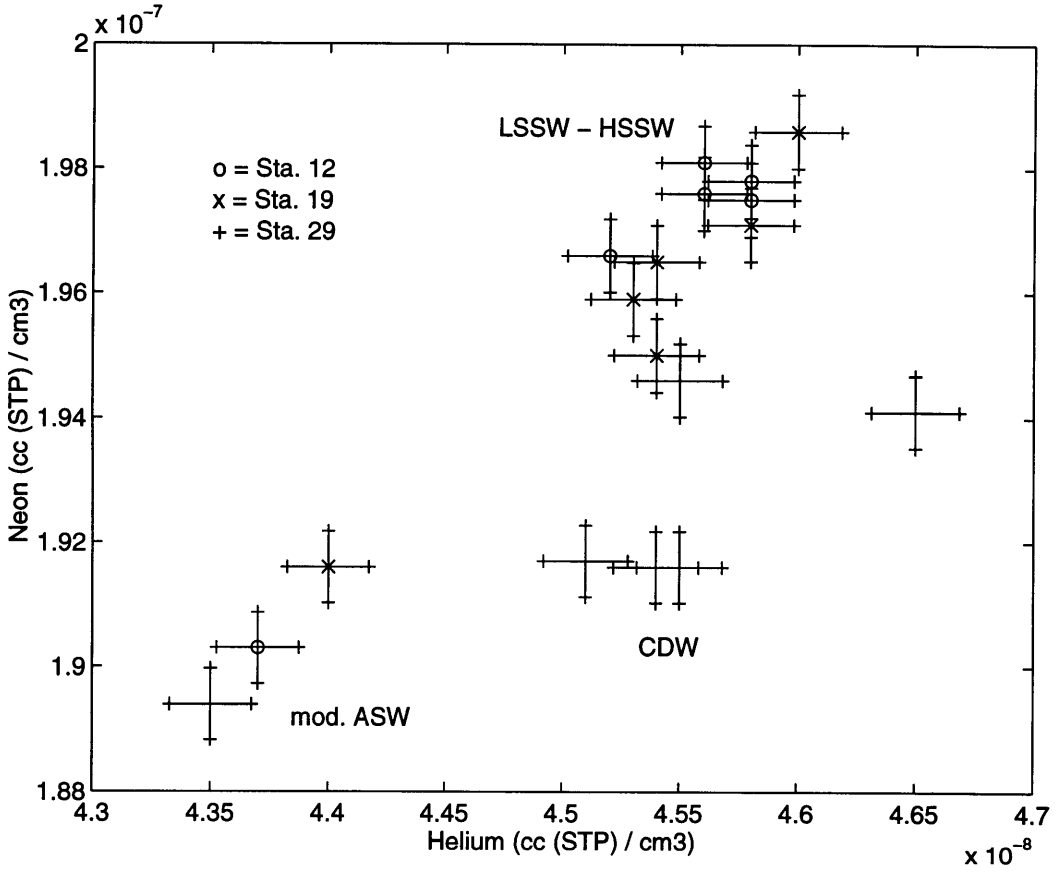

Figure 8.6a He and Ne concentrations in the water masses in Prydz Bay defined by the θ-S relations. Uncertainties are standard deviations from replicate samples.

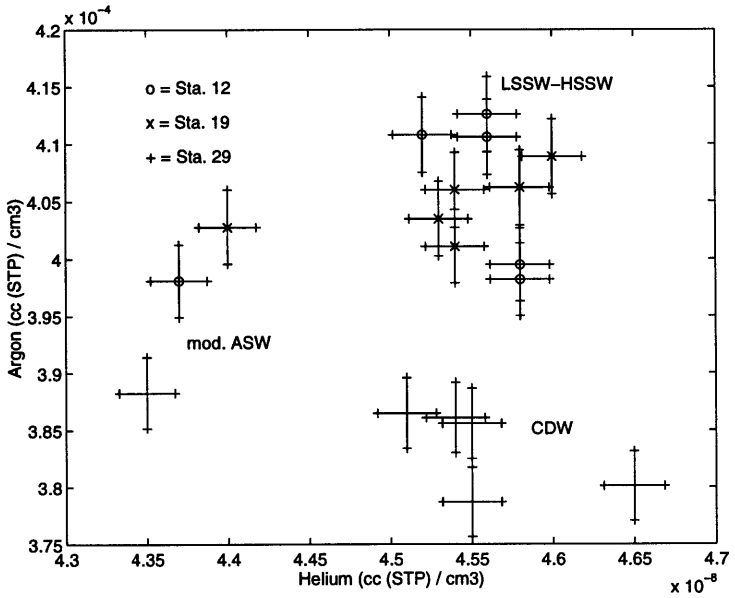

Figure 8.6b He and Ar concentrations in the water masses in Prydz Bay defined by the θ-S relations. Uncertainties are standard deviations from replicate samples.

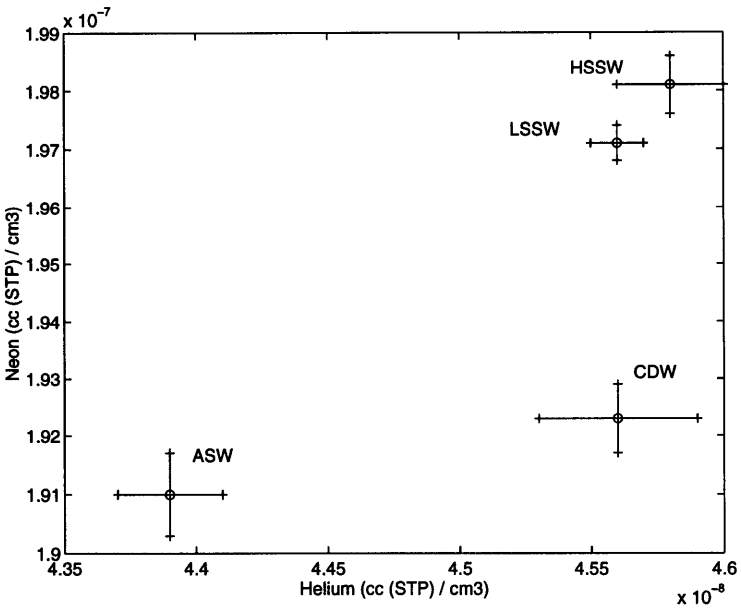

Figure 8.6c Average He and Ne concentrations of the water masses in Prydz Bay. Uncertainties are the standard deviations from the mean of the individual measurements shown in Figure 8.6a.

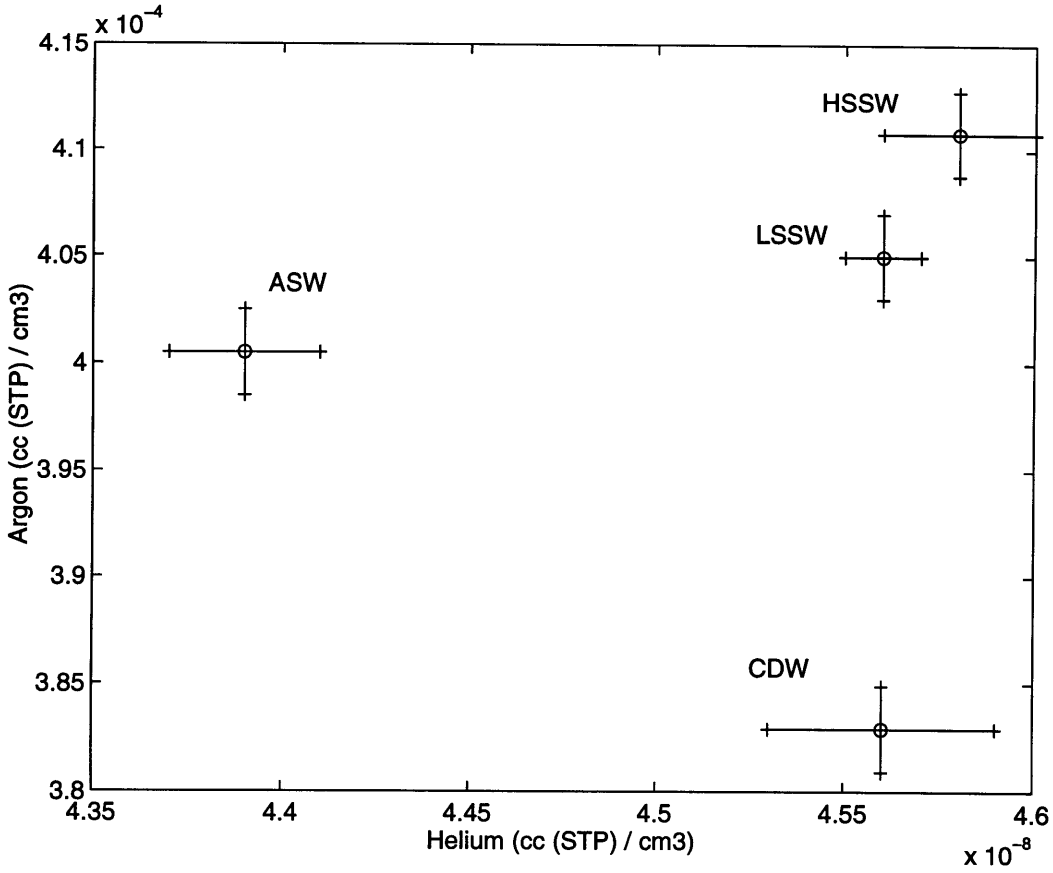

Figure 8.6d Average He and Ar concentrations of the water masses in Prydz Bay. Uncertainties are the standard deviations from the mean of the individual measurements shown in Figure 8.6b.

While the earlier analysis indicated that both water mass types are affected by melt-water, the distinct noble gas signatures of each water mass indicate that the water masses are affected by melt-water in significantly *different* ways, either through differences in the type of ice melted *(i.e.* sea ice or glacial ice), the volume of ice melted, or the influence of other processes such as air injection or gas exchange. While the distinctions between the two shelf water masses are not very significant, the distinctions between the shelf water masses and CDW are strong. The differences between SW and CDW are not apparent in

the He concentrations alone, but are clearly seen when using all three gases. Neon concentrations vary by approximately 2.5% between the two water mass types, while the concentrations of Ar vary by more than 6%. While the noble gases may not provide the sensitivity of other water mass tracers such as salinity and temperature, they can provide unique information about the composition of the water that may allow a source region or formation mechanism of a water mass to be better constrained.

8.5 *Conclusions*

These distinctions provide further evidence that the noble gases are being influenced by interactions with ice, and that the unique noble gas signatures of individual water masses may indeed be useful tracers of the interactions of water masses in these environments. By defining the noble gas concentrations in the unmixed, core water masses of interest, the noble gases could provide unique insights into the circulation and mixing pathways of water masses in these areas. The noble gas signatures of the water masses may change over time, both seasonally and annually, due to changes in interactions with ice. It has been suggested that recent decreases in ice formation rates and increases in melt-water input to the surface ocean have slowed dense water formation in many areas of the world's oceans (Wadhams, 1995). It may be speculated that trends in the annual changes of the noble gas signatures in areas such as the Antarctic continental shelves may be sensitive indicators of changes in the cycles of ice melt and formation.

CHAPTER 9

Summary

9.1 *Analytical Developments*

I have developed a technique for measuring He, Ne, and Ar in seawater by quadrupole mass spectrometry using cryogenic separation of the gases and ion current manometry. This technique can be used to measure the concentrations of the dissolved noble gases with an analytical uncertainty of ~ 0.25%. The reproducibility of replicate samples is approximately 0.3% for all three gases. Preliminary experiments indicate that a modification of this technique may be used to measure the noble gas concentrations in water samples as small as 1 milliliter.

9.2 *The Effects of Gas Exchange and Air Injection Processes on the Seasonal Cycles of Dissolved Gases*

I have modified a 1-D upper ocean bulk mixed-layer model to simulate the seasonal cycles of the dissolved noble gases in the upper ocean. I used a 2 year time series of He, Ne, and Ar in the upper ocean near Bermuda to constrain and validate the simulations, and quantitatively estimated the processes of vertical mixing, air injection, gas exchange, and the mode of bubble trapping. The seasonal cycles of the dissolved gases and temperature were well-simulated by the model, and the magnitude of the deviations between the model simulation and data observations were of the same order as the total measurement uncertainty in the data for most constraint equations. This study demonstrated that the gas exchange formulation of Wanninkhof (1992) is in good agreement with the observations, while the formulation of Liss and Merlivat (1986) underpredicts the required gas exchange flux by a factor of 1.7 ± 0.6. The air injection formulation of Monahan and Torgersen (1991) was used, and the average air entrainment velocity required by the model was 3.0 cm s^{-1}, which is consistent with previous findings from laboratory simulations (Keeling, 1993; Asher et al., 1992). This study demonstrated that over the timescale of a year, the flux of gas into the upper ocean from bubbles is largely the result of partial bubble trapping, which is consistent with the work of Jenkins (1988). However, this study also suggests that the dominant mode of bubble trapping varies seasonally, with gas flux from bubbles that dissolve completely being more important in the winter at Bermuda. Future work will examine the influence of this

seasonally-varying bubble trapping mode on the parameterization of the total gas exchange process.

9.3 *Design and Development of a Moorable, Sequential Noble Gas Sampler*

In order to obtain a quantitative understanding of gas flux from bubbles, it is necessary to observe the behavior of the dissolved gases as they respond to air injection processes. It is thus necessary to sample at a frequency that is sufficient to resolve the air injection event, but current techniques and obvious logistical problems prevent sampling of this frequency during storm events, when the air injection process is most active. An automated, moorable noble gas sampler has been developed that can obtain a high-frequency time series of the noble gases over periods of several weeks to one year. The sampler employs membrane introduction techniques to obtain samples of the dissolved gas by equilibration of the dissolved gases in seawater across a gas permeable membrane. The samples are stored in specially-designed sample chambers that prevent significant contamination of the gases over periods of 3-4 months. Preliminary tests indicate that one milliliter of water is sufficient for the analysis of the noble gases, and that the reproducibility of replicate samples is ~0.6%, which can be improved significantly by increasing the initially flushing volume of the fill water from the chambers prior to sampling. Further tests are needed to determine the accuracy of the samples taken by the sampler, by comparison with samples taken by conventional methods.

9.4 *The interactions between dissolved gases and ice in aquatic systems*

Using measurements of He, Ne, and Ar in a permanently ice-covered Antarctic lake, I described the process of the solubility of He and Ne in ice, which, to the best of my knowledge, has never been observed before on such a large scale in nature. I developed a 3-phase equilibrium partitioning model of the system, and quantitatively estimated the effects that the solubility of He and Ne in ice have on the concentrations of the dissolved gases in the water in contact with the ice. The fractionation that occurs between He, Ne, and Ar due to differing interactions with the ice makes the noble gases potentially useful tracers of the interactions between ice and water. These interactions impinge on issues of water mass formation, large scale circulation, ventilation, and tracer distributions in the high latitude oceans and polar marginal seas. To extend this work, I studied the effects of the interactions between the dissolved noble gases and ice in a quiescent, seasonally ice-covered, salt-water lagoon connected to the Sea of Okhotsk, and also in a large ice-covered bay on the Antarctic continental shelf. Results of these studies demonstrated that the concentrations of the dissolved noble gases in ice formation areas are being influenced by interactions with sea ice. Further, the noble gas concentrations were shown to be tracing individual water masses in the Prydz Bay region, and this work suggested that the noble gases may provide unique tags of water masses formed in various areas that may be used to constrain the origins of water masses as well as circulation and mixing in these areas. With the available data, it was not possible to quantitatively determine the nature of the influence of ice interaction on the dissolved gases of the individual water masses, although it was qualitatively demonstrated that interaction with ice, namely

meltwater addition, was most likely the process responsible for the anomalous saturations. Future work must include a time series of the noble gases in an area such as the Saroma-Ko lagoon over a complete cycle of freezing and melting to quantitatively study these interactions. The type and quality of information that could be obtained from the use of the noble gases as tracers of the interactions between ice and water could then be more fully explored.

CHAPTER 10

References

Aagaard, K., and E.C. Carmack (1989) The role of sea ice and other fresh water in the Arctic circulation. *J. Geophys. Res.*, **94**, 14485-14498.

Aagaard, K., J.H. Swift, and E.C. Carmack (1985) Thermohaline circulation in the Arctic Mediterranean seas. *J. Geophys. Res.*, **90**, 4833-4846.

Anderson, M.L, and B.D. Johnson (1992) Gas Transfer: A gas tension method for sutdying equilibration across a gas-water interface. *J. Geophys. Res.*, **97**, 17899-17904.

Andrews, J.N. (1985) The isotopic composition of radiogenic helium and its use to study groundwater movement in confined aquifers. *Chemical Geology*, **49**, 339-351.

Asher, W.E., P.J. Farley, R. Wanninkhof, E.C. Monahan, and T.S. Bates (1992) Laboratory and field experiments on the correlation of fractional area whitecap coverage with air/sea gas transport, in *Precipitation Scavenging and Atmosphere-*

Surface Exchange, 2, S.E. Schwartz and W.G.N.Slinn, eds., Hemisphere Publishing Corp., Washington, D.C., 815-825.

Bari, S.A. and J. Hallett (1974) Nucleation and growth of bubbles at an ice-water interface, *Journal of Glaciology*, **13**, 489-520.

Bauch, D., P. Schlosser, and R.G. Fairbanks (1995) Freshwater balance and the sources of deep and bottom waters in the Arctic Ocean inferred from the distribution of $H_2{}^{18}O$. *Prog. Oceanog.*, **35**, 53-80.

Bedard, P., D. Hillaire-Marcel, and P. Page (1981) ^{18}O modeling of freshwater in Baffin Bay and Canadian coastal waters. *Nature*, **293**, 287-289.

Benson, B.B., and D. Kraus, Jr. (1980) Isotopic fractionation of helium during solution: a probe for the liquid state. *J. Solution Chem.*, **9**, 895-909.

Bieri, R.H. (1971) Dissolved noble gases in marine waters. *Earth and Planetary Science Letters*, **10**, 329-333.

Birchfield, G.E. and W.S. Broecker (1990) A salt oscillator in the glacial Atlantic? A scale analysis model. *Paleoceanography*, **5**, 835-843.

Blanchard, D.C. and A.H. Woodcock (1957) Bubble formation and modification in the sea and its meteorological significance. *Tellus*, **9**, 145-158.

Broecker, H.Ch., and W.Siems (1984) The role of bubbles for gas transfer from water to air at higher windspeeds. Experiiments in the wind-wave facility in Hamburg, in *Gas Transfer at Water Surfaces*, W. Brutsaert and G.H. Jirka, eds., D. Reidel Publishing Co., 229-236.

Broecker, W.S. (1990) Salinity history of the northern Atlantic during the last deglaciation. *Paleoceanography*, **5**, 459-467.

Broecker, W.S. and G.H. Denton (1989) The role of ocean-atmosphere reorganizations in glacial cycles. *Geochimica et Cosmochimica Acta*, **53**, 2465-2501.

Broecker, W.S. and T.H. Peng (1974) Gas exchange rates between air and sea. *Tellus*, **26**, 21-35.

Brook, E.J., and M.D. Kurz (1993) Surface exposure chronology using in situ cosmogenic 3He in Antarctic quartz sandstone boulders. *Quaternary Research*, **39**, 1-10.

Bunker, A.F. (1976) Computations of surface energy flux and annual air-sea interaction cycles of the North Atlantic Ocean. *Mon. Weather Rev.*, **104**, 1122-1140.

Burton, H.R. (1981) Chemistry, physics and evolution of Antarctic saline lakes, *Hydrobiologia*, **82**, 339-362.

Carte, A.E. (1961) Air bubbles in ice. *Proc. of the Phys. Soc. Lond.*, **77**, 757-768.

Chinn, T.J. (1993) Physical hydrology of the Dry Valley Lakes *In* Physical and Biochemical Processes in Antarctic Lakes, Antarctic Research Series, vol. 59, pp 1-52.

Chou, J.Z. (1985) Numerical modeling of oxygen cycling in the upper ocean. WHOISSF report no. 42 (unpublished), 50 pp.

Clift, R., J.R. Grace, and M.E. Weber (1978) *Bubbles, Drops and Particles*. Academic Press, NY.

Cooks, R.G., and T. Kotiaho (1992) Membrane introduction mass spectrometry in environmental analysis, in *Pollution Prevention in Industrial Processes*, Amer. Chem. Soc., 127-154.

Cox, G.F.N. and W.F. Weeks (1982) Equations for determining the gas and brine volumes in sea ice samples. *USA Cold Regions Research and Engineering Laboratory Report 82-30*. Hanover, New Hampshire.

Craig, H. and T. Hayward (1987) Oxygen supersaturations in the ocean : biological vs. physical contributions. *Science*, **235**, 199-202.

Craig, H., and R.F. Weiss (1971) Dissolved gas saturation anomalies and excess helium in the ocean. *Earth and Planetary Science Letters*, **10**, 289-296.

Craig, H., R.A.Wharton, Jr., and C.P. McKay (1992) Oxygen supersaturation in ice-covered Antarctic lakes: biological versus physical contributions. *Science*, **255**, 218-221.

Crawford, G.B. and D.M. Farmer (1987) On the spatial distribution of ocean bubbles. *Journal of Geophysical Research*, **92**, 8231-8243.

Davidson, D.W., Y.P. Handa, C.I. Ratcliffe, and J.S. Tse (1984) The ability of small molecules to form clathrate hydrates of structure II. *Nature*, **311**, 142-143.

Deacon, E.L. (1977) Gas transfer to and across an air-water interface. *Tellus*, **29**, 363-374.

Emerson, S., P.D. Quay, C. Stump, D. Wilbur, and R. Schudlich (1995) Chemical tracers of productivity and respiriation in the subtropical Pacific Ocean. *J. Geophys. Res.*, **100**, 15873-15887.

Erickson, D.J., J.T. Merril, and R.A. Duce (1986) Seasonal estimates of global oceanic whitecap coverage. *J. Geophys. Res.*, **91**, 12975-12977.

Etcheto, J. and L. Merlivat (1988) Satellite determination of the carbon dioxide exchange coefficient at the ocean-atmosphere interface: A first step. *J. Geophys. Res.*, **93**, 15669-15678.

Farmer, D.M., C.L. McNeil, and B.D. Johnson (1993) Evidence for the importance of bubbles in increasing air-sea gas flux. *Nature,* **361**, 620-623.

Ferris, J.M, J.A.E. Gibson, and H.R. Burton. (1991) Evidence of density currents with the potential to promote meromixis in ice-covered saline lakes. *Palaeogeography, Palaeoclimatology, Palaeoecology*, **84**, 99-107.

Frankignoul, C. (1981) Low-frequency temperature fluctuations off Bermuda. *J.Geophys. Res.*, **86**, 6522-6528.

Frew, N.M., E.J. Bock, W.R. McGillis, A.V. Karachintsev, T. Hara, T. Munsterer, and B. Jähne (1995) Variation of air-water gas transfer with wind stress and surface viscoelasticity, in *Air-Water Gas Transfer.* AEON Verlag & Studio, Hanau, Germany, 529-541.

Fuchs, G., W. Roether, and P. Schlosser (1987) Excess ^{3}He in the ocean surface. *J. Geophys. Res.*, **92**, 6559-6568.

Fujiyoshi, Y., S.I. Shibanuma, and M. Kajiwara (1993) Variability in water mass characteristics in Lake Saroma. *Bulletin of Plankton Society of Japan*, **39**, 151-175.

Gargett, A.E. (1984) Vertical eddy diffusivity in the ocean interior. *J. Mar. Res.*, **42**, 359-393.

Green, W.J., M.P. Angle, and K.E. Chave (1988) The geochemistry of Antarctic streams and their role in the evolution of four lakes of the McMurdo Dry Valleys, *Geochimica et Cosmochimica Acta*, **52**, 1265-1274.

Green, W.J., T.J. Gardner, T.G. Ferdelman, M.P. Angle, L.C. Varner, and P. Nixon (1989) Geochemical processes in the Lake Fryxell basin (Victoria Land, Antarctica), *Hydrobiologia*, **172**, 129-148.

Hamasaki et al. (1997) Seasonal variation of the size fractionated chlorophyll A biomass in relation to ice algae and ice coverage in Mombetsu Harbor, Hokkaido, Japan. *The Twelfth International symposium on Okhotsk Sea and Sea Ice Abstracts*, Okhotsk Sea and Cold Ocean Research Association, Hokkaido, Japan, 103-105.

Hara, T., E.J. Bock, N.M. Frew, and W.R. McGillis (1995) Relationship between air-sea gas transfer velocity and surface roughness, in *Air-Water Gas Transfer.* AEON Verlag & Studio, Hanau, Germany, 611-616.

Hood, E.M., B.L. Howes, and W.J. Jenkins (1997) Dissolved gas dynamics in perennially ice-covered Lake Fryxell, Antarctica. *Limnology and Oceanography (in press).*

Hwang, P.A., Y.H.L. Hsu, and J. Wu (1990) Air bubbles produced by breaking wind waves: A laboratory study. *J. Phys. Ocean.*, **20**, 19-28.

Jacobs, S.S., R.G. Fairbanks, and Y. Horibe (1985) Origin and evolution of water masses near the Antarctic continental margin: Evidence from $H_2{}^{18}O/H_2{}^{16}O$ ratios in seawater, in *Oceanology of the Antarctic Continental Shelf*, Antarct. Res. Ser. 43, S.S. Jacobs, ed., AGU, Washington, D.C.

Jacobs, S.S. and D.T. Georgi (1977) Observations on the southwest Indian/Antarctic Ocean. in: A voyage of discovery, M. Angel, ed., G.E. Deacon 70th Anniv. Supplement to *Deep-Sea Res.*, 43-84.

Jähne, B. and E.C. Monahan, eds. (1995) *Air-Water Gas Transfer.* AEON Verlag & Studio, Hanau, Germany.

Jähne, B. et.al. (1984) A new optical bubble measuring device; A simple model for bubble contribution to gas exchange. in *Gas Transfer at Water Surfaces.* Brutsaert and Jirka, eds., D. Reidel Pub. Co., Dordrecht, Holland. 237-246.

Jähne, B. et.al. (1985) He and Rn gas exchange measurements in the large wind-wave facility of IMST. *J. Geophys. Res.*, **90**, 11989-11997.

Jähne, B., K.O. Munnich, R. Bosinger, A. Dutzi, W. Huber, and P. Libner (1987) On parameters influencing air-water gas exchange. *J. Geophys. Res.*, **92**, 1937-1949.

Jenkins, W.J. (1988) The use of anthropogenic tritium and helium-3 to study subtropical gyre ventilation and circulation. *Phil. Trans. R. Soc. Lond.* A, **325**, 43-61.

Jenkins, W.J. and J.C. Goldman (1985) Seasonal oxygen cycling and primary production in the Sargasso Sea. *J. Mar. Res.*, **43**, 465-491.

Jenkins, W.J., and D.W.R. Wallace (1992) Tracer based inferences of new primary production in the sea, in *Primary Productivity and Biogeochemical Cycles in the Sea*, P.G. Falkowski and A.D. Woodhead, eds., Plenum Press, NY, 299-316.

Jenkins, W.J., D.E. Lott, M.W. Pratt, and R.D. Boudreau (1983) Anthropogenic tritium in South Atlantic Bottom Water, *Nature*, **305**, 45-46.

Jenkins, W.J. (1982) On the climate of a subtropical ocean gyre: decade time-scale variations in water mass renewal in the Sargasso Sea. *J. Mar. Res.*, **40** (Supp.), 265-290.

Johannessen, O.M., M. Miles, and E. Bjorgo (1995) The Arctic's shrinking sea ice. *Nature*, **376**, 126-127.

Johnson, B.C. and R.C. Cooke (1979) Bubble populations and spectra in coastal waters: A photographic approach. *J.Geophys. Res.*, **84**, 3761-3766.

Jones, E.P., and A.R. Coote (1981) Oceanic CO_2 produced by the precipitation of $CaCO_3$ from brines in sea ice. *J. of Geophys. Res.*, **86**, 11041-11043.

Jones, E.P., B. Rudels, and L.G. Anderson (1995) Deep waters of the Arctic Ocean: origins and circulation. *Deep-Sea Res.*, **42**, 737-760.

Jones, G.A. (1991) A stop-start ocean conveyer. *Nature*, **349**, 364-365.

Jouzel, J., L. Merlivat, D. Mazaudier, M. Pourchet, and C. Lorius (1982) Natural tritium deposition over Antarctica and estimation of the mean global production rate. *Geophysical Research Letters*, **9**, 1191-1194.

Jouzel, J., L. Merlivat, M. Pourchet, and C. Lorius (1979) A continuous record of artificial tritium fallout at the South Pole (1954-1978). *Earth and Planetary Science Letters*, **45**, 188-200.

Kahane, A., J. Klinger, and M. Philippe (1969) Dopage selectif de la glace monocristalline avec de l'helium et du neon. *Solid State Communications*, **7**, 1055-1056.

Kalnay, E., et al. (1996) The NCEP/NCAR reanalysis project. *Bull. Am. Meteorol. Soc.*, **77**, 437-471.

Kanwisher, J. (1963) On the exchange of gases between the atmosphere and the sea. *Deep-Sea Research*, **10**, 195-207.

Keeling, R.F. (1993) On the role of large bubbles in air-sea gas exchange and supersaturation in the ocean. *J. Mar. Res.*, **51**, 237-271.

Keeling, R.F., S.C. Piper, and M. Heimann (1996) Global and hemispheric CO2 sinks deduced from changes in atmospheric O_2 concentration. *Nature*, **381**, 218-221.

Keigwin, L.D., G.A. Jones, S.J. Lehman, and E.A. Boyle (1991) Deglacial meltwater discharge, North Atlantic deep circulation, and abrupt climate change. *J. Geophys. Res.*, **96**, 16811-16826.

Kephart, L.A., J.G. Dulak, G.A. Slippy, and S. Dheandhanoo (1992) On-line analysis of liquid streams using a membrane interface and a quadrupole mass spectrometer, in *Pollution Prevention in Industrial Processes*, Amer. Chem. Soc., 178-189.

Kolovayev, D.A. (1976) Investigation of the concentration and statistical size distribution of wind produced bubbles in the near-surface ocean layer. *Oceanology*, **15**, 659-661.

Kotiaho, T., F.R. Lauritsen, T.K. Choudhury, and R.G. Cooks (1991) Membrane introduction mass spectrometry. *Anal. Chem.*, **63**, 875-883.

Kraus, E.B. (1972) *Atmosphere-Ocean Interaction*, Clarendon Press, Oxford, England.

Lauritsen, F.R., T.K. Choudhury, L.E. Dejarme and R.G. Cooks (1992) Microporous membrane introduction mass spectrometry with solvent chemical ionization and glow discharge for the direct detection of volatile organic compounds in aqueous solution. *Analytica Chimica Acta*, **266**, 1-12.

Lawrence, M.J.F. and C.H. Hendy (1985) Water column and sediment characteristics of Lake Fryxell, Taylor Valley, Antarctica, *New Zealand Journal of Geology and Geophysics*, **28**, 543-552.

Ledwell, J.R. (1984) The variation of the gas transfer coefficient with molecular diffusivity, in *Gas Transfer at Water Surfaces*, Brutsaert and Jirka, eds., D. Reidel, Hingham, MA., 293-302.

Ledwell, J.R., A.J. Watson, and C.S. Law (1993) Evidence for slow mixing across the pycnocline from an open-ocean tracer-release experiment. *Nature*, **364**, 701-703.

Levich, V.G. (1962) *Physicochemical Hydrodynamics*. Prentice-Hall Pub., N.J.

Liss, P.S. and L. Merlivat (1986) Air-Sea gas exchange rates: Introduction and synthesis. in: *The Role of Air-Sea Gas Exchange in Geochemical Cycling*, P.Buat-Menard, ed., D. Reidel Pub., Dordrecht, Holland, 113-127.

Liss, P.S. and R.A. Duce (1997) *The sea surface and global change*. Cambridge University Press., Cambridge, U.K.

Londono, D., W.F. Kuhs, and J.L. Finney (1988) Enclathration of helium in ice II: the first helium hydrate. *Nature*, **332**, 141-142.

Lott, D.E. and W.J. Jenkins (1984) An automated cryogenic charcoal trap system for helium isotope mass spectrometry. *Rev. Sci. Instrum.*, **55**(12), 1982-1988.

Martin, P.J. (1986) Testing and comparison of several mixed-layer models. Technical Report, *Nav. Ocean Res. and Develop. Activ.*, Natl. Space Technol. Lab., MS

Martin, S. E. Munoz, and R. Drucker (1992) The effect of severe storms on the ice cover of the Norther Tatarskiy Strait. *J. Geophys. Res.*, **97**, 17753-17764.

Matsuo, S. and Y. Miyake (1966) Gas composition in ice samples from Antarctica. *J. Geophys. Res.*, **71**, 5235-5241.

McGillis, W.R., E.J. Bock, and N.M. Frew (1995) Mass transfer from gas bubbles in fresh and seawater, in *Air-Water Gas Transfer*. AEON Verlag & Studio, Hanau, Germany, 611-616.

Medwin, H. (1970) *In situ* acoustic measurements of bubble populations in coastal ocean water. *J.Geophys. Res.*, **75**, 599-611.

Medwin, H. and N.D. Breitz (1989) Ambient and transient bubble spectral densities in quiescent seas and under spilling breakers. *J.Geophys.Res.*, **94**, 12751-12759.

Merlivat, L. and L. Memery (1983) Gas exchange across an air-water interface: Experimental results and modeling of bubble contribution to transfer. *J.Geophys. Res.*, **88**, 707-724.

Merlivat, L., L. Memery, and J. Boutin (1993) Gas exchange at the air-sea interface: present status. Case of CO_2 , in *Abstract Volume, 4th International Conference on CO_2*, Carquerainne, France, September 13-17.

Middleton, J.H., and S.E. Humphries (1989) Thermohaline structure and mixing in the region of Prydz Bay, Antarctica. *Deep-Sea Res.*, **36**, 1255-1266.

Monahan, E.C. and T. Torgersen (1991) Enhancement of air-sea gas exchange by oceanic whitecapping, in *Air-Water Mass Transfer*, Second International Symposium on Gas Transfer at Water Surfaces, ASCE, NY., 608-617.

Moore, R.M. and D.W.R. Wallace (1988) A relationship between heat transfer to sea ice and temperature-salinity properties of Arctic Ocean waters. *J. Geophys. Res.*, **93**, 565-571.

Moore, R.M. and W. Spitzer (1990) Heat transfer from Atlantic waters to sea ice in the Arctic ocean: Evidence from dissolved argon. *Geophys. Res. Let.*, **17**, 2149-2152.

Musgrave, D.L., J. Chou, and W.J. Jenkins (1988) Application of a model of upper-ocean physics for studying seasonal cycles of oxygen. *J. Geophys. Res.*, **93**, 15679-15798.

Namoit, A., and E.B. Bukhgalter (1965) Clathrates formed by gases in ice. *Journal of Structural Chemistry*, **6**, 911-912.

Namoit, A.Y. (1967) Reasons for the small solubility of nonpolar gases in water. *Zhurnal Strukturnoi Khimii,* **8**, 408-412.

Nunes Vaz, R.A. and G.W. Lennon (1996) Physical oceanography of the Prydz Bay region of Antarctic waters. *Deep-Sea Res.*, 43, 603-641.

Oberhuber, J.M. (1988) An atlas based on 'COADS' data set. *Tech. Rep.* **15**, Max-Planck Instutut fur Meteorologie. Data obtained from LDEO Climate Group Data Library, *http://rainbow.ldeo.columbia.edu/AT-DataLibraryquery.html.*

Paulson, C.A. and J.J. Simpson (1977) Irradiance measurements in the upper ocean. *J. Phys. Oceanogr.*, **7**, 952-956.

Peng, T.H., et.al. (1979) Radon evasion rates in the Atlantic and Pacific oceans as determined during the GEOSECS programme. *J.Geophys. Res.*, **84**, 2471-2486.

Pierotti, R.A. (1976) A scaled particle theory of aqueous and nonaqueous solutions. *Chemical Reviews*, **76**, 717-726.

Pollack, G.L. (1991) Why gases dissolve in liquids. *Science*, **251**, 1323-1330.

Price, J.F. (1979) Observations of a rain-formed mixed layer. *J. Phys. Oceanogr.*, **9**, 643-649.

Price, J.F., C.N.K. Mooers, and J.C. Van Leer (1978) Observation and simulation of storm-induced mixed-layer deepening. *J. Phys. Oceanogr.*, **8**, 582-599.

Price, J.F., R.A. Weller, and R. Pinkel (1986) Diurnal cycling: Observations and models of the upper ocean response to diurnal heating, cooling, and wind mixing. *J. Geophys. Res.*, **91**, 8411-8427.

Purucker, M.E., D.P. Elston, and S.L. Bressler (1981) Magnetic stratigraphy of Late Cenozoic glaciogenic sediments from drill cores, Taylor Valley, Transantarctic

Mountains, Antarctica. *Dry Valley Drilling Project*, Antarctic Research Series, **3**, 109-129, American Geophysical Union, Washington, D.C.

Sarmiento, J.L. and E.T. Sundquist (1992) Revised budget for the oceanic uptake of anthropogenic carbon dioxide. *Nature*, **356**, 589-593.

Schlosser, P. (1986) Helium: a new tracer in Antarctic oceanography. *Nature*, **321**, 233-235.

Schlosser, P., B. Kromer, G. Ostlund, B. Ekwurzel, G. Bonisch, H.H. Loosli, and R. Purtschert (1994) On the 14C and 39Ar distribution in the central Arctic Ocean: implications for deep water formation. *Radiocarbon*, **36**, 327-343.

Schlosser, P., G. Bonisch, M. Rhein, and R. Bayer (1991) Reduction of deepwater formation in the Greenland Sea during the 1980s: evidence from tracer data. *Science*, **251**, 1054-1056.

Schlosser, P., R. Bayer, A. Flodvik, T. Fammelsrod, G. Rohardt, and K.O. Munnich (1990) Oxygen 18 and helium as tracers of ice shelf water and water/ice interaction in the Weddell Sea. *J. Geophys. Res.*, **95**, 3253-3263.

Schudlich, R. and S. Emerson (1996) Gas supersaturation in the surface ocean: The roles of heat flux, gas exchange, and bubbles. *Deep-Sea Res.*, **43**, 569-589.

Seto et al. (1997) Population dynamics of algae in the seasonal sea ice at Saroma-Ko Lagoon. *The Twelfth International symposium on Okhotsk Sea and Sea Ice Abstracts*, Okhotsk Sea and Cold Ocean Research Association, Hokkaido, Japan, 108-111.

Shirasawa et al. (1992) Atmospheric and oceanographic data report for Saroma-Ko Lagoon of the SARES (Saroma-Resolute Studies) Project, 1992. *Low Temperature Science*, **Ser. A, 52**, 69-167.

Shirasawa et al. (1997) Sea ice conditions and meteorological observations at Saroma-Ko Lagoon, Hokkaido, December 1995-November 1996. *Low Temp. Sci.*, **55**, 48-77.

Shirasawa, K (1993) Variations in atmospheric conditions and ice formations in Lake Saroma. *Bulletin of Plankton Society of Japan*, **39**, no. 2, 156-158.

Siegenthaler, U. and J.L. Sarmiento (1993) Atmospheric carbon dioxide and the ocean. *Nature*, **365**, 119-125.

Smith, N.R. and P. Treguer (1994) Physical and chemical oceanography in the vicinity of Prydz Bay, Antarctica, in *Southern ocean ecology, the BIOMASS perspective*, El-Sayed S., editor, Cambridge University Press, Cambridge, 25-41.

Smith, R.L., L.G. Miller, and B.L. Howes (1993) The geochemistry of methane in Lake Fryxell, an amictic, permanently ice-covered, antarctic lake. *Biochemistry*, 21, 95-115.

Spitzer, W.S. (1989) Rates of vertical mixing, gas exchange and new production : Estimates from seasonal gas cycles in the upper ocean near Bermuda. Ph.D. Thesis, MIT-WHOI Joint Program in Oceanography and Ocean Engineering. WHOI89-30. 161pp.

Spitzer, W.S. and W.J. Jenkins. (1989) Rates of vertical mixing, gas exchange and new production : Estimates from seasonal gas cycles in the upper ocean near Bermuda. *J. Mar. Res.*, **47**, 169-196.

Swanger, L.A. and W.C. Rhines. (1972) On the necessary conditions for homogeneous nucleation of gas bubbles in liquids. *Journal of Crystal Growth*, **12**, 323-326.

Taguchi et al. (1992) Biological data report for the Saroma-ko site of the SARES (Saroma-Resolute Studies) Project, February-March, 1992. *Low Temperature Science*, **Ser. A., 53**, 67-163.

Takeuchi (1993) Freshwater input and bottom materials in Lake Saroma. Bulletin of Plankton Society of Japan, **39**, 151-175.

Tan, F.C., and P.M. Strain (1980) The distribution of sea ice meltwater in the eastern Canadian Arctic. *J. Geophys. Res.*, **85**, 1925-1932.

Tans, P.P., I.Y. Fung, and T. Takahashi (1990) Observational constraints on the global atmospheric CO_2 budget. *Science*, **247**, 1431-1438.

Thorpe, S.A. (1982) On the clouds of bubbles formed by breaking wind-waves in deep water, and their role in air-sea gas transfer. *Phil. Trans. R. Soc. Lond.* A, **304**, 155-210.

Thorpe, S.A. (1984) The role of bubbles produced by breaking waves in supersaturating the near-surface ocean mixing layer with oxygen. *Annales Geophysicae* v**2**, 53-56.

Thorpe, S.A. (1986) Measurements with an automatically recording inverted echo sounder; ARIES and the bubble clouds. *J. Phys. Oceanogr.*, **16**, 1462-1478.

Thorpe, S.A. and A.J. Hall (1983) The characteristics of breaking waves, bubble clouds, and near-surface currents observed using side-scan sonar. *Cont. Shelf Res.*, **1**, 353-384.

Top, Z., S.Martin, and P. Becker (1988) A laboratory study of dissolved noble gas anomaly due to ice formation. *Geophysical Research Letters*, **15**, 796-799.

Top, Z., W.B. Clarke, and R.M. Moore (1983) Anomalous Neon-Helium ratios in the Arctic Ocean. *Geophysical Research Letters*, **10**, 1168-1171.

Trull, T.W., M.D. Kurz, and W.J. Jenkins (1991) Diffusion of cosmogenic 3He in olivine and quartz: implications for surface exposure dating. *Earth and Planetary Science Letters*, **103**, 241-256.

Wadhams, P. (1995) Arctic sea ice extent and thickness. *Phil. Trans. R. Soc. Lond.* A, **352**, 301-319.

Wallace, D.W.R. and C.D. Wirick (1992) Large air-sea gas fluxes associated with breaking waves. *Nature*, **356**, 694-696.

Walsh, A.L. and P.J. Mulhearn (1987) Photographic measurements of bubble populations from breaking wind waves at sea. *J. Geophys. Res.*, **92**, 14553-14565.

Wanninkhof, R. (1992) Relationship between wind speed and gas exchange over the ocean. *J. Geophys. Res.*, **97**, 7373-7382.

Wanninkhof, R., and L.F. Bliven (1991) Relationship between gas exchange, wind speed, and radar backscatter in a large wind-wave tank. *J. Geophys. Res.*, **96**, 2785-2796.

Wanninkhof, R., J.R. Ledwell, and W.S. Broecker (1985) Gas exchange-wind speed relation measured with sulfur hexafluoride on a lake. *Science*, **227**, 1224-1226.

Wanninkhof, R., W. Asher, R. Weppernig, H. Chen, P. Schlosser, C. Langdon, and R. Sambrotto (1993) Gas transfer experiment on Georges Bank using two volatile deliberate tracers. *J. Geophys. Res.*, **98**, 20237-20248.

Watson, A., R. Upstill-Goddard, and P.S. Liss (1991) Air-sea exchange in rough and stormy seas, measured by a dual tracer technique. *Nature*, **349**, 145-147.

Watson, A.J. et.al. (1991) Air-sea gas exchange in rough and stormy seas measured by a dual-tracer technique. *Nature*, **349**, 145-147.

Weart, S.R. (1997) The discovery of the risk of global warming. *Physics Today*, **50**, 34-40.

Weeks, W.F. and S.F. Ackley (1982) The growth, structure, and properties of sea ice. USA Cold Regions Research and Engineering Laboratory, Monograph 82-1.

Weiss, R.F. (1969) Piggyback sampler for dissolved gas studies on sealed water samples. *Deep-Sea Research*, **15**, 695-699.

Weiss, R.F. (1971) Solubility of Helium and Neon in water and seawater. *Journal of Chemical and Engineering Data*, **16**, 235-241.

Weston, R.E.Jr. (1955) Hydrogen isotope fractionation between ice and water. *Geochimica et Cosmochimica Acta*, **8**, 281-284.

Wharton, R.A. Jr., W.B. Lyons, and D.J. Des Marais (1993) Stable isotopic biogeochemistry of carbon and nitrogen in a perennially ice-covered Antarctic lake. *Chemical Geology* (Isotope Geoscience Section), **107**, 159-172.

Wharton, R.A.Jr., G.M. Simmons,Jr., and C.P. McKay (1989) Perennially ice-covered Lake Hoare, Antarctica: physical environment, biology, and sedimentation. *Hydrobiologia*, **172**, 305-320.

Wilson, A.T. (1979) Geochemical problems of the Antarctic dry areas. *Nature*, **280**, 205-208.

Woods, J.D., and W. Barkmann (1986) A lagrangian mixed layer model of Atlantic 18°C water formation. *Nature*, **319**, 574-576.

Woolf, D.K. (1993) Bubbles and the air-sea transfer velocity of gases. *Atmosphere-Ocean*, **31**, 517-540.

Woolf, D.K. and S.A. Thorpe (1991) Bubbles and the air-sea exchange of gases in near-saturation conditions. *J. Mar. Res.*, **49**, 435-466.

Worthington, L.V. (1976) On the North Atlantic circulation. The Johns Hopkins Oceanographic Studies, vol. 6, Johns Hopkins Univ. Press, Baltimore, 110 pp.

Wu, J. (1981) Bubble populations and spectra in the near-surface ocean: Summary and review of field measurements. *J. Geophys. Res.*, **86**, 457-463.

3118-70